SAPIENZA
UNIVERSITÀ DI ROMA

Sapienza University of Rome

Faculty of Civil and Industrial Engineering
Department of Mechanical and Aerospace Engineering

Thesis For The Degree Of Doctor Of Philosophy
in Aeronautics and Space Engineering

Modeling and Control for Multi-Quadrotor Cooperative Load Transportation

Supervisor
Prof. Guido De Matteis

Correlatore
Prof. Alessandro Zavoli

PhD Candidate
Giovanni Di Monaco

Academic Year 2025-2026 (XXXVIII cycle)

Sapienza University of Rome

© 2025 Giovanni Di Monaco. All rights reserved

Written with LaTeX

Email of the author: giovanni.dimonaco@uniroma1.it

Abstract

This research addresses the problem of a cooperative transportation system consisting of multiple quadrotors carrying a slung load. It presents a comprehensive methodology that encompasses the entire development process, from mathematical modeling to controller synthesis. Two distinct mathematical models are developed: one based on the Udwadia–Kalaba formulation and another based on an embedded Lagrangian formulation defined directly on the configuration manifold. For effective cooperative load transport, reliable models of individual agents, as well as their coupled behavior, are essential. The Udwadia-Kalaba formulation allows one to first model the full dynamics of each subsystem, including actuators dynamics, saturations, delays, and external disturbances, and then impose the constraint forces in closed form. To guarantee the safety and effectiveness of the transportation system, the control laws must account for factors such as load distribution, swing control, and collision avoidance, possibly incorporating coupling effects between the dynamics of rigid payload, flexible cables, and multiple quadrotors into control system design. The embedded Lagrangian formulation provides a compact representation of the coupled dynamics, making it particularly suitable for controller synthesis. Moreover, it admits analytical linearization along reference trajectories, thereby enabling the systematic design of linear controllers. Two different control strategies are proposed. In the first, a time-varying LQR is designed based on the linearized dynamics of the coupled system, with feasible quadrotor trajectories generated by exploiting the system differential flatness. To reduce dependence on an accurate model of the constrained dynamics and to eliminate the need for additional sensing or estimation algorithms, a second control strategy is proposed, in which the agents are controlled to maintain a fixed formation. The control scheme employs a cascade architecture, where the payload is treated as an external disturbance acting on the formation. Robustness against unmodeled constraint forces is achieved by utilizing INDI-based inner loops. An obstacle avoidance strategy for the entire formation–payload system is also proposed, in which a Control Barrier Function (CBF) acts on the virtual leader to generate safe trajectories. Additional CBFs are implemented at the quadrotor level to prevent inter-agent collisions. Simulation results confirm the effectiveness of the proposed approaches, while the formation controller has been experimentally validated using Parrot Bebop 2 quadrotors and a motion capture system.

Contents

List of Figures **iv**

List of Tables **vi**

1 Introduction **1**
1.1 Research Motivation . . . 1
1.2 Research Framework . . . 3
1.2.1 Slung-Load Modeling . . . 3
1.2.2 Trajectory Planning . . . 6
1.2.3 Load-Leading Control . . . 7
1.2.4 Fixed-Formation Control . . . 8
1.3 Main Objectives and Original Contributions . . . 10
1.4 Structure of the Work . . . 14

2 Modeling **15**
2.1 Multi-UAV Slung-Load System . . . 15
2.2 Configuration Space . . . 16
2.3 Udwadia-Kalaba Formulation . . . 18
2.3.1 Numerical Issues . . . 24
2.3.2 Quadrotor Model . . . 27
2.3.3 Load Model . . . 30
2.3.4 Cable Model . . . 32
2.4 Differential Geometry . . . 33
2.4.1 Special Orthogonal Group $SO(3)$ . . . 37
2.4.2 Two-Sphere S^2 . . . 42
2.5 Lagrangian Dynamics on Manifold . . . 44

3 Control **50**
3.1 Load-Leading Control Architecture . . . 50
3.1.1 Linearized Dynamics . . . 51
3.1.2 Differential Flatness . . . 52
3.1.3 Time-Varying LQR Control . . . 58
3.2 Formation-Centered Control Architecture . . . 59
3.2.1 Communication Topology . . . 61
3.2.2 Formation Control . . . 62
3.2.3 Linear Acceleration Control . . . 66
3.2.4 Attitude Control . . . 69
3.3 Collision/Obstacle Avoidance . . . 73

4 Results and Discussions **77**
4.1 Trim in Hovering . . . 78
4.2 Load-Leading Control . . . 82
4.2.1 Payload Stabilization . . . 83
4.2.2 Trajectory Tracking . . . 85
4.3 Formation-Centered Control . . . 89
4.3.1 Trajectory Tracking . . . 91
4.3.2 Take-off and Landing . . . 98
4.3.3 Wind Gust Rejection . . . 102
4.3.4 Obstacle/Collision Avoidance . . . 104
4.4 Flight Tests . . . 106
4.4.1 Results . . . 109

5 Conclusions **114**
5.1 Slung-Load Modeling . . . 114
5.2 Cooperative Control . . . 115
5.3 Future Work . . . 117

Bibliography **119**

Appendix A **129**
A.1 Moore-Penrose Inverse . . . 129
A.1.1 Computation via SVD . . . 131
A.1.2 Solution of Linear Systems . . . 132
A.2 Proof of the Udwadia-Kalaba Equation (Eq. (2.7)) . . . 132
A.3 Mass and Constraint Matrices in the Multi-Element Cable Model . . . 134
A.4 Expression of matrix C in Eq. (2.55) . . . 135

Appendix B **136**
B.1 Hat Operator . . . 136
B.2 Lagrangian . . . 136
B.3 Derivatives of the Lagrangian . . . 138
B.4 Derivation of Lagrange equations of motion . . . 141

Appendix C **145**
C.1 Expressions of ${}^{b_i}\dot{\boldsymbol{\omega}}_i$ and ${}^{b_i}\boldsymbol{\omega}_i$ from Differential Flatness . . . 145
C.2 First-Order Approximation of Configuration Errors on $SO(3)$ and S^2 . . . 146
C.2.1 Linearized error on SO(3) . . . 147
C.2.2 Linearized error on S^2 . . . 148
C.3 Linearized Dynamics . . . 148

List of Figures

2.1 Multi–quadrotor payload system with flexible cables 16
2.2 Orientation of the reference frame $\mathcal{F}_{b_i}$ and (right) directions of rates ω_k and torques τ_k 27
2.3 Orientation of frame $\mathcal{F}_{b_l}$, and location and numbering of attachment points . 31

3.1 Load-Leading Control Architecture 51
3.2 Cable geometries in static equilibrium for different values of the free parameter z 55
3.3 Reconstruction of system states and inputs through differential flatness . . . 58
3.4 Cascaded control architecture for a formation of $N > 2$ agents and a virtual leader 60
3.5 Middle control loop 69
3.6 Inner control loop 72

4.1 Geometry of the i-th cable in Π_{i_Z} 80
4.2 Time history of load position error 83
4.3 Time history of load attitude error 84
4.4 Time-histories of cables attitude errors 84
4.5 Time-histories of quadrotors attitude errors 84
4.6 Time-histories of quadrotor thrust commands 85
4.7 Time-histories of quadrotor pitch angles 85
4.8 Sanpshot of the stabilization maneuver 85
4.9 Coordinates of payload and quadrotor c.g. vs. time, $\omega = 0.2\pi$ rad/s; the dashed black line indicates reference values 87
4.10 Velocity components of payload and quadrotors vs. time, $\omega = 0.2\pi$ rad/s; the dashed black line indicates reference values 87
4.11 Time-history of load position error for varying ω 88
4.12 Time-histories of cables attitude errors for varying ω 88
4.13 Time-histories of quadrotors attitude errors for varying ω 88
4.14 Time-histories of load position error in presence of model uncertainties . . . 88
4.15 Communication scheme 89
4.16 Coordinates of virtual leader (#1) and agent c.g. vs. time, $\omega = 0.2\pi$ rad/s; the dashed black line indicates reference values 92
4.17 Velocity components of virtual leader (#1) and agents vs. time, $\omega = 0.2\pi$ rad/s; the dashed black line indicates reference values 92
4.18 Snapshots of the maneuver, $\omega = 0.2\pi$ 93
4.19 Tensile forces on the agents, $\omega = 0.2\pi$ 94
4.20 Time-histories of mean formation error at different values of ω 95
4.21 Time-histories of mean leader-follower error at different values of ω 95
4.22 Time-histories of trajectory tracking error at different values of ω 95

4.23 Comparison of cable tension time-histories for vertical and inclined cable configurations . . . 97
4.24 Snapshot of the maneuver with inclined cables, $\omega = 0.2\pi$ . . . 98
4.25 Snapshots of the maneuver with inclined cables at $t = 5.5$ s (left), and $t = 10.5$ s (right), $\omega = 0.2\pi$ . . . 99
4.26 Payload Euler angles, $\omega = 0.2\pi$ . . . 99
4.27 Time-histories of cable tensions during take-off . . . 100
4.28 Time-histories of formation errors during take-off . . . 100
4.29 Sanpshots of the take-off maneuver . . . 101
4.30 Time-histories of cable tensions during landing . . . 101
4.31 Time-histories of formation error during landing . . . 102
4.32 Sanpshots of the landing maneuver . . . 102
4.33 Gust response: time-histories of formation error . . . 103
4.34 Gust response: time-histories of formation error . . . 103
4.35 Gust response: time-histories of tensile forces . . . 103
4.36 Sanpshot of the gust disturbance rejection . . . 104
4.37 Distances between virtual leader (#1), agents (#2 and #3), payload, and obstacle vs. time . . . 105
4.38 Snapshots of the avoidance maneuver . . . 105
4.39 Snapshots of the collision avoidance maneuver . . . 106
4.40 Experimental setup [1] . . . 107
4.41 Cascade control architecture . . . 108
4.42 Case 1: Quadrotor trajectories . . . 110
4.43 Case 1: time-histories of formation error . . . 111
4.44 Case 1: time-histories of leader-follower formation error . . . 111
4.45 Case 1: Video frame of the test . . . 112
4.46 Case 2: quadrotor and load (purple line) trajectories . . . 112
4.47 Case 2: time-histories of formation error . . . 113
4.48 Case 2: Video frame of the test . . . 113

List of Tables

4.1 System parameters 78

Chapter 1

Introduction

1.1 Research Motivation

This thesis focuses on the mathematical modeling and control system design of a transportation system composed of multiple quadrotors carrying a suspended load.

The use of quadrotors has gained significant attention from academic and governmental research groups worldwide in recent years, due to their exceptional maneuverability and mobility, particularly in challenging three-dimensional environments. Their versatility led to their adoption in various applications, including surveillance [2], aerial refueling [3], exploration of unexplored areas [4], and Search and Rescue (SAR) operations [5]. More recently, interest is growing in the use of quadrotors in multi-agent systems, which involve a group of agents working cooperatively to achieve a given task. Among the others, aerial vehicle applications of multi-agent systems include flight formation [6], surveillance [7], aerial construction [8], and load transportation [9]. At present, quadrotors have largely proven their effectiveness in cooperative load-transportation tasks. Using multiple Unmanned Aerial Vehicles (UAVs) offers several advantages, including carrying larger payloads, improving oscillation control, distributing weight more evenly, and providing redundancy in case of mechanical or technical failures [10, 11]. Therefore, it is of interest to conduct research and attain a deep understanding of the challenges inherent in cooperative load transportation using multiple quadrotors.

Developing a mathematical model of the UAVs-load system suitable for control design and implementation is a challenging task, as it involves the combination of the dynamics of UAVs, cables, and load. The model should be able to capture the realistic behavior of the

system while remaining computationally efficient, sufficiently simple to enable analysis, offline and hardware-in-the-loop (HITL) simulations, and control design. When multiple UAVs are used to carry a single load, the interactions are not only associated with information sharing between agents but also with the physical coupling between them.

Among the different approaches to aerial manipulation, cable-suspended systems are particularly appealing due to their lightweight design and mechanical simplicity [10]. In this configuration, each quadrotor is attached to the payload at distinct points via cables, allowing a group of three or more vehicles to control the entire pose of the suspended load simply by coordinating their relative positions. This strategy removes the necessity for additional actuation mechanisms, such as robotic arms or complex grippers.

When a load is transported through cables, the payload is dynamically coupled to the quadrotor through a single attachment point, which allows the vehicle to maintain its rotational degrees of freedom (DoFs). However, connections between agents introduce additional dynamics that reduce maneuverability and induce stability problems and disturbances such as oscillations.

To guarantee the safety and effectiveness of the transportation system, the control laws must account for factors such as load distribution, swing control, and collision avoidance, possibly incorporating coupling effects between the dynamics of rigid payload, flexible cables, and multiple quadrotors into control system design. During outdoor missions, UAVs are often exposed to significant gusts caused by atmospheric turbulence. Moreover, even a uniform wind can produce a highly non-uniform flow field in urban environments due to interactions with buildings and other obstacles [12]. Indoor operations are also affected by aerodynamic disturbances, for instance those generated by the vehicle own propeller backwash when flying near walls. In addition, wind gusts can directly act on the suspended payload, inducing oscillations. Therefore, the controller must be robust to external aerodynamic disturbances to ensure stable and precise transportation. During flight, payload swing directly affects the dynamic characteristics of the UAV. It is therefore crucial to suppress or minimize the payload oscillations to maintain stability and improve control performance. Furthermore, when dealing with multiple agents systems, the trajectory generation should also guarantee that the UAVs will not collide during flight.

Control approaches for cooperative transport can be considered with reference to two categories: payload trajectory tracking, often referred to as load-leading control, [13, 14], in which agents adjust their positions and velocities to achieve the desired trajectory of the

load, and fixed formation approaches [9, 15], where the synchronization of agents along the specified path determines the position and attitude of the load. The first approach typically relies on a centralized control architecture [16], in which a central unit computes the reference trajectories for all agents to achieve the overall motion objective of the payload. While this centralized method allows for precise coordination among agents and for agile maneuvers, it also requires significant computational effort, accurate estimation of the system state, and may limit scalability as the number of agents increases. In contrast, fixed-formation control is usually implemented through a decentralized control architecture [9], where each agent computes its control actions based only on locally available information or limited communication with neighboring agents. This decentralized structure enhances scalability and robustness, making it suitable for systems with limited onboard sensing and computing capabilities, although it may provide less precise payload control compared to centralized approach, and is limited to low velocity trajectories.

The generation of dynamically feasible trajectories for a system composed of multiple quadrotors transporting a suspended payload is challenging, since the overall system is highly underactuated [17]. In fact, the number of available control inputs is smaller than the total number of DoFs of the coupled system. Specifically, a system composed of N quadrotors carrying a rigid-body payload through cables has $4N$ inputs and exhibits $6 - N + 2N$ degree of under-actuation (DoA). As a result, planning dynamically feasible trajectories for all vehicles and the payload is a nontrivial problem, because not every desired trajectory in the state space can be realized through admissible control inputs. For fully actuated systems, where each DoF is directly controlled, trajectory generation is more straightforward, as dynamically feasible trajectories can be defined for all the states variables.

1.2 Research Framework

1.2.1 Slung-Load Modeling

A first modeling decision concerns the representation of the cables connecting the payload to the quadrotors. Several methods have been proposed in the literature. The review by Estavez *et al.* [18] provides an extensive and exhaustive overview of the methodologies for the mathematical modeling of cables in individual and collaborative transport systems based on multirotor. In many studies dealing with small, lightweight UAV systems the cable is

represented by a straight and inelastic bar while the load may be a point mass [19, 20] or a 6-DoF body [21]. Other authors model the cable as flexible, assuming that it is composed of rigid links of equal [22] or varying mass and length [23], or formed by a series of extensible elements, each treated as a point mass, connected via a chain of springs and dampers [24]. As a general comment on the approaches to the mathematical description of the cable in single- or multiple-lift systems, the rigid massless model is widely adopted for simplicity and lower computational load, although it requires dealing with the complexity of collision. Since the single-element cable model does not inherently account for the fact that cables can only withstand tensile forces, a switching dynamics approach is required. The so-called cable collapse and collisions (CCC), that is, switching dynamics, are handled when the cable state changes instantaneously from taut to slack and vice versa, the collisions being modeled using the conservation of momentum. In [25], the interconnected slung load system using one or two small-scale helicopters is modeled assuming perfectly rigid and massless cables, and a switching dynamics is introduced to account for cables slacking and tightening. A hybrid dynamical system is proposed in [26] to account for the switching dynamics experienced by four agents starting to lift a load. In the studies [27, 28], where the lift maneuver of a single agent is decomposed into three dynamic modes, namely, setup, pull, and raise, the cable is massless and not extensible, the load is modeled as point-mass, and a trajectory tracking problem is solved for the hybrid and geometrically flat system. The detection and resolution of CCC are also considered in [29] for a four-agent formation carrying a point-mass load via single-element cables, and the collision response is modeled by the momentum method [25]. However, in CCC situations, the success of switching dynamics is taken almost for granted, while it depends on the number N of agents, particularly if it is $N \leqslant 4$ or $N > 4$, as discussed in [30]. In the same study, it is shown that, if a rigid-body payload is considered, it is necessary to impose strict conditions also on the feasible geometries of attachment points and/or load. Moreover, imposing that the multibody system is rigid (an equality constraint on the distance between the cable attachment points holds) results in an unrealistic model of the constraint forces on the agents and the load when dealing with the control action because, from a theoretical point of view, the cable can be compressed. Switching dynamics have so far limited the application of the single-element cable model to smooth low-velocity flight conditions ruling out, to some extent, the consideration of take-off and landing phases for formations of four or more agents, including aggressive maneuvers.

The dynamics of interconnected robot systems subjected to constraints can be formulated

in two different ways, that is, in augmented, or embedded formulations. In the augmented formulation, the system is described in terms of redundant coordinates, and the constraints are imposed through additional equations. In this case, the equations of motion are derived either with the Newton-Euler formalism or with the Lagrange formulation, with the constraints incorporated through Lagrange multipliers. In the embedded formulation, generalized coordinates that parametrize the admissible configuration space are used. In this case, the constraints are used to eliminate some configuration variables thereby yielding the minimum number of variables needed to describe the system. As a result, constraint forces do not appear explicitly, and the obtained set of equations of motion is minimal. An embedded formulation is based either on the Newton-Euler approach, or the Lagrangian framework, by applying D'Alembert's principle of virtual work, or the Kane's method. A more recent development within the embedded formulation consists in applying the Lagrangian formalism directly on the configuration manifold of the system, without relying on local coordinates [31]. The resulting equations admit a more compact and elegant representation, avoiding the use of cumbersome trigonometric expressions.

An alternative to Newtonian or Lagrangian mechanics for describing constrained systems is the Gauss's principle of least constraint. It states that the actual accelerations of a system are those that minimize the deviation of the unconstrained accelerations from the accelerations required to satisfy the constraints. Building on Gauss's principle, Udwadia and Kalaba [32] derived an explicit closed-form expression for the constrained acceleration, known as the Udwadia-Kalaba equation (UKE). In this formulation, the system is expressed in redundant coordinates, but no explicit constraint equations are added. Instead, the constraint forces are obtained in closed form, yielding an explicit expression for the constrained dynamics.

The UKE has been widely adopted in applications with aerial [33], ground [34] and underwater [35] formations of unmanned vehicles. In [22] a single quadrotor is considered and the dynamic equations are derived using UKE to estimate cable length and payload mass by a frequency analysis. The study [23] deals with the dynamics and control of an arbitrary number of quadrotors transporting a rigid-body load and presents a coordinate-free form of the equations of motion derived according to Lagrange mechanics on a nonlinear manifold for the full dynamic model. The influence of cable flexibility on trim, stability, and handling qualities, in the model of a full-scale helicopter with external load, established via Kane's method is investigated in Ref. [24]. In [36] the focus is again on the dynamics of the rigid-body payload, connected to the agents via massless rigid links. As with [23], a

global formulation of the nonlinear configuration manifold is presented, and the position and attitude of the payload are controlled to avoid collision with obstacles in complex terrain where agile response is required. In [25], the interconnected slung load system using one or two small-scale helicopters is modeled assuming perfectly rigid and massless cables and using UKE to take advantage of the possibility of removing and adding constraints in modeling cable slacking and tightening. The system dynamics is described in [26] by the Newton-Euler approach, and geometric control is used to track a desired trajectory.

1.2.2 Trajectory Planning

The trajectory planning problem for underactuated system is significantly simplified if the system is differentially flat, meaning that all the states and control inputs can be expressed as analytic functions of a limited set of flat outputs and a finite number of their derivatives [37]. This property allows the generation of dynamically consistent trajectories by specifying only the evolution of the flat outputs, and computing all other quantities accordingly. In this way, the trajectory planning problem is decoupled from the subsequent control design, which can then focus on tracking these feasible reference trajectories.

In [38], the differential-flatness property of a quadrotor with a cable-suspended point-mass load connected through a rigid and massless cable is established, with the load position and the quadrotor yaw serving as flat outputs. In [39], this property is extended to different configurations, including a single quadrotor with a load suspended through a flexible cable, a point-mass load suspended from multiple quadrotors through flexible cables, and a rigid-body load suspended from multiple quadrotors through flexible cables. In both works, the differential flatness property is established under the assumptions of negligible aerodynamic effects and zero offset between the quadrotor center of gravity (c.g.) and the cable attachment point. In [40], the differential flatness property for a quadrotor carrying a point-mass load suspended from an offset through a rigid and massless cable is also demonstrated, again neglecting aerodynamic effects.

The notion of a differentially flat hybrid system is introduced in [41] and [42] for, respectively, single and multiple quadrotors carrying a cable-suspended load to enable aggressive trajectory generation and tracking, handling the case when the cable tension goes to zero.

1.2.3 Load-Leading Control

In the load-leading approach, the control objective is formulated with respect to the desired motion of the payload rather than the individual quadrotors. A reference trajectory for the load is first specified, and the corresponding cable tensions required to generate the desired load accelerations are obtained from the inverse dynamics of the coupled system [43]. The quadrotors are then controlled to produce the thrust forces and orientations that realize the desired cable tensions. In this approach, accurate knowledge of the cable tensions is required. Such information can be obtained either from direct tension measurements, for example by employing a six-axis force/moment transducer as in [44], or from a dynamic model of the coupled system, as in [45], where a spring-damper model of the cable is used. In this context, accurate measurement of the load position is essential. Common approaches include motion capture systems [46], which restrict applicability to indoor laboratory environments, optical-based methods such as visual detection [47], as well as onboard sensing solutions based on GPS or IMU units mounted directly on the payload. The inclusion of additional sensing hardware increases the overall system complexity, cost, and integration effort. Moreover, as discussed in [48], existing sensing solutions often suffer from high size, weight, accuracy and power requirements. Model-based approaches depend strongly on accurate knowledge of numerous system parameters and high-fidelity dynamic models, and require accurate state-estimation algorithms. An estimation strategy based on the Fading Gaussian Deterministic Filter (FGDF) has been proposed to estimate payload swing angles and angular rates using only onboard accelerometer data, and is integrated into a proportional feedback controller for payload oscillation stabilization [49]. In [46], a modified version of the extended Kalman filter is derived to estimate states on S^2 and is validated using a motion capture system.
Both nonlinear and linear control strategies have been investigated in the literature to regulate the payload dynamics. For instance, in [42, 50, 51], geometric nonlinear controllers, which accounts for the coupled effects between the dynamics of payload, cables, and quadrotors, are applied so that the load asymptotically follows given trajectories. In [45] and [52] a hierarchical system features a top-level trajectory control law for the payload, while lower-level controllers on a team of autonomous helicopters generate the individual commands required to realize the desired payload motion. In [16], a hierarchical load-leading control strategy is proposed, where the payload acts as the leader, computing the required net wrench to follow a desired trajectory and distributing the corresponding cable tension com-

mands to each vehicle. The approach includes a convex optimization formulation for cable force allocation and demonstrates real-time implementation through both indoor and outdoor flight experiments. In [53], an optimization-based cable force allocation for geometric control is proposed, using cascaded quadratic programs to compute collision-free cable forces in real time. In [39], a linearized model of a quadrotor transporting a suspended payload through a flexible cable is derived using a variation-based approach, and a Linear Quadratic Regulator (LQR) controller is designed to track the desired payload trajectory. In [54], an LQR controller is developed from a variation-based linearization of the nonlinear dynamics to coordinate multiple quadrotors transporting a flexible hose.

1.2.4 Fixed-Formation Control

In the fixed-formation approach, the control objective is defined in terms of the relative configuration of the quadrotors rather than the payload motion. The quadrotors are commanded to maintain a desired geometric formation, so that, under the assumption of taut cables, and provided that at least three quadrotors are employed and the cable attachment points on the load are not collinear, the payload position and orientation are uniquely determined by the instantaneous formation geometry and the cable lengths [9]. Consequently, the load trajectory can be inferred from the collective motion of the formation. Among the large body of literature concerning multi-agent formation control, the reviews in [55] and [56] provide a comprehensive description and cataloging of control strategies. Among these, consensus-based algorithms represent one of the most widely adopted frameworks. In these approaches, consensus is achieved when all agents asymptotically converge to the same values of certain state variables, typically position, velocity, or heading, through local information exchange. Each agent updates its control input using relative state information from its neighbors, according to the communication topology defined by an interaction graph. Under appropriate connectivity assumptions, local consensus guaranties global coordination of the entire network. For a detailed analysis of distributed consensus control for multi-agent systems, refer to [57].

The consensus mechanism can be exploited to maintain a desired spatial configuration among agents by defining suitable relative state constraints [57]. Moreover, consensus is also achieved with respect to the motion of a leader, ensuring that all vehicles in the team converge to the reference state defined by the leader. To enhance robustness, feedback from

the followers to the leader can be incorporated into the consensus law, enabling adaptation of the leader motion to the actual formation state [57]. As a result, the leader evolves at its nominal speed when the consensus error is small and slows down adaptively as the error increases.

Consensus-based strategies have been extensively applied in the formation control of quadrotors. Among several studies, [58] presents a cooperative formation control algorithm validated through simulations and experimental tests using multiple small commercial UAVs. A distributed consensus-based formation control strategy is presented in [59], assuming a double integrator model for the agents. The paper includes a stability analysis, as well as numerical simulations and experimental results based on the Parrot Bebop 2 vehicles in an indoor laboratory setting. A formation control strategy based on a virtual structure approach is illustrated in [60], where a simplified mathematical model of the Parrot Bebop 2 quadrotor identified using a least-mean-square error procedure, is used to design high-level controllers. The proposed controller is again evaluated through experiments conducted in an indoor laboratory. A consensus-based formation control protocol is presented in [61] for quadrotor swarm systems to achieve a given time-varying formation. Each quadrotor is modeled as a double integrator, and control system validation is carried out through numerical simulations and flight tests. In [62], a robust leader-following consensus protocol for multi-agent systems is discussed, based on a Lyapunov approach and an optimal H_∞ criterion, which guarantees that all agents can follow a virtual leader in spite of communication faults and external disturbances. In [63] a centralized formation controller based on a virtual structure, which generates reference velocity commands for a team of three UAVs, is proposed. Each UAV is equipped with an individual dynamic compensator that tracks the assigned reference velocity. The effectiveness of the approach is validated through experimental tests on Bebop2 quadrotors. In [64], a leader–follower consensus algorithm is designed and implemented to coordinate the heading and altitude of a group of Bebop2 quadrotors. While simulations show satisfying control performance, a non-negligible sensitivity to aerodynamic disturbances generated by the agents in close formation is apparent in the flight tests.

When designing a formation controller for cooperative load transportation, two main approaches can be followed: explicitly accounting for the constraint forces in the controller synthesis, or treating the payload as an external disturbance. To explicitly account for the constraint forces in the formation control design, either a direct measurement or an accurate model of the cable tensile forces is required. For example, a formation-centered

controller based on exact dynamic inversion is presented in [65] where, assuming taut cables, the constraint forces are calculated using the UKE formulation. However, errors in the measurements of agent and load positions may compromise the precise calculation of constraint forces, which limits the controller performance. An alternative approach is to treat the payload as an external disturbance acting on the formation and design the controller to be robust against unmodeled external forces [9, 66].

Several control methodologies for single and collaborative teams of multicopters are discussed in [18], also considering the use of robotic arms and grasping for payload transportation. A cooperative control architecture is discussed in [19] for a team of multirotor-type UAVs to lift a suspended payload, where a path generation algorithm minimizes the variation of load drag among the agents for smooth operations. Each agent is synchronized along the trajectory and features a robust path-following controller designed by the back-stepping technique. A cooperative transportation task performed by a formation of multiple UAVs is analyzed in [9], considering unknown environmental disturbances and using a passivity-based control strategy to develop a position-based controller for coordinating the agents. The strategy proposed in [26] combines passivity-based formation control to create a formation capable of reducing control effort and geometric control to track the desired trajectory. In [29] a decentralized controller based on a sub-optimal LQR-PID is presented for the linearized model of each UAV to guarantee a fixed formation during the cooperative load transportation. Distance-based formation-motion control is proposed in [66] to generate acceleration signals to be tracked by a team of quadrotors using Incremental Nonlinear Dynamic Inversion (INDI) controllers for attitude and thrust commands. A leader-follower consensus algorithm is employed in [67] to coordinate the flight of a formation of quadcopters and to ensure the payload tracks the virtual leader. The control strategy integrates an adaptive Robust Integral of the Sign of the Error (RISE) controller [68] to improve robustness. The effectiveness of the proposed approach is demonstrated through simulations and laboratory flight experiments.

1.3 Main Objectives and Original Contributions

The main goals of this work are

- To develop a mathematical model of the UAVs-load system able to capture the real-

istic behavior of the system, suitable for dealing with a wide range of motions and maneuvers, including take-off and landing, while remaining computationally efficient, sufficiently simple to enable analysis, off-line and HITL simulations, and control design

- To investigate different control approaches for cooperative transportation, with a focus on understanding their advantages and limitations

In order to develop a mathematical model of the multi-UAV load transportation system, the first step concerns the definition of an appropriate cable model. To overcome the drawbacks of single-element cable models, particularly the reliance on switching dynamics to capture cable slackening and tightening phenomena, while preserving simplicity and computational efficiency, a multi-element cable model is adopted.

Once the constraint model, that is, the cable representation, has been defined, the dynamics of the constrained multi-body system are derived accordingly. Among the various formulations available in the literature, two approaches are considered: the Udwadia–Kalaba formulation and the Lagrangian formulation defined directly on the configuration manifold. The augmented formulation is instead not considered here due to the increased complexity associated with the use of Lagrange multipliers.

Each of these two approaches offers distinct advantages. The Udwadia–Kalaba formulation, providing a closed-form expression for the constrained accelerations, is simple to implement and to adapt whenever the agent dynamics changes. Moreover, it allows the unconstrained dynamics of each agent, including actuator dynamics, saturation effects, and external disturbances, to be modeled and incorporated explicitly before enforcing the constraints, which is generally more cumbersome in a purely Lagrangian framework. Furthermore, explicit knowledge of the constraint forces enables analysis of the maximum allowable stresses. However, because it is formulated at the acceleration level and relies on pseudo-inverses, analytic linearization is generally not possible, and numerical integration may introduce drift in the cables length, thus requiring the use of correction schemes [69]. On the other hand, the Lagrangian formulation, when expressed directly on the configuration manifold, provides a more compact and elegant representation of the system dynamics. This formulation avoids cumbersome trigonometric expressions and does not rely on local coordinates, thereby eliminating the singularities associated for example with Euler angles. Moreover, it allows for analytic linearization around equilibrium points or along desired trajectories, thereby supporting the design of linear controllers. As a final remark, both formulations are well suited

for large-scale systems and scale efficiently with the number of quadrotors and cable links.
Concerning the second objective, that is the definition of suitable control approaches for cooperative transportation, the analysis considers both load-centered and formation-centered approaches. In the context of payload-centered control, a linear control strategy is adopted to achieve accurate tracking of dynamically feasible payload trajectories while maintaining design simplicity and ease of implementation. Nonlinear controllers can capture the full system dynamics, but they are strongly model-dependent, complex to design, non-intuitive, and often difficult to implement in real time [70]. Linear control techniques, on the other hand, rely on well-established synthesis methods, are computationally efficient, and are easily re-tuned for systems with different parameters. Motivated by the successful application of LQR control to a single quadrotor transporting a suspended payload [39], and to multiple quadrotors collaboratively carrying a flexible hose [54], an LQR is designed here for the cooperative transportation of a rigid-body payload by multiple quadrotors.
In the context of formation-centered control, a cascaded control architecture is here adopted. In this framework, the outer loop is responsible for governing the formation by generating reference accelerations, while the inner loops are tasked with accurately tracking these references. To enable the formation to follow a desired reference trajectory, a leader–follower strategy has been implemented in the outer loop. Within this architecture, the leader is assigned to track the reference trajectory, whereas the followers maintain the prescribed formation by regulating their relative motion with respect to the leader and to each others. In cooperative transportation tasks, where agents are physically coupled through a shared payload, precise motion synchronization is essential to avoid load oscillation and cable slackening. Assigning a physical agent as the leader may induce asymmetric behaviors, since only the designated leader directly tracks the reference trajectory while the others follow it with a delay. A more effective approach is to adopt a virtual leader that has the same dynamic model as the other agents and is controlled to follow the reference trajectory.
To enhance synchronization among the agents, the most effective approach is to have the virtual leader directly communicate with each follower, with its dynamics implemented at a central location and broadcast to every vehicle in the team. This ensures a uniform and prompt response of all agents to the leader motion but introduces a centralized structure. A more scalable and fully distributed alternative is to introduce a hierarchical architecture that includes a consensus layer on the virtual leader state, as proposed in [57]. In this approach, the virtual leader states are reconstructed by the followers through a distributed

consensus-based observer.

To reduce the dependence on precise mathematical modeling and to avoid the need for additional sensors for estimating the tension or internal state of the payload, the constraint forces are not explicitly included in the control synthesis. Instead, robustness to these unmodeled interaction forces is achieved through the use of INDI-based inner loops.

INDI provides a sensor-based control framework capable of compensating for external forces and moments [12, 66, 71, 72]. By directly using the measured specific forces and angular rates from the onboard IMU, INDI estimates and rejects the effect of unknown disturbances, such as aerodynamic and payload-induced constraint forces, in real time, thus providing a robust and adaptive control action. The key idea behind INDI is that the measured acceleration/angular acceleration inherently includes the effects of all forces and moments acting on the vehicle, including aerodynamic, and constraint forces. The control law is expressed in incremental form, where the control input is updated to compensate for the discrepancy between the desired and the measured linear and angular accelerations, effectively counteracting the combined influence of unmodeled dynamics and external disturbances. Because the control input in INDI is updated incrementally from its previous value, the method inherently retains memory of past control actions. This feature provides an effect analogous to integral action, allowing the controller to reject constant or slowly varying disturbances without the need for an explicit integral term, therefore avoiding the potential drawbacks typically associated with integral control, such as increased overshoot, longer settling times, or reduced stability margins.

The original contribution of this work are as follows: (i) the integration of a multi–element cable model within the UKE formulation resulting in a modeling framework suitable for dealing with a wide range of motions and maneuvers, including take-off and landing, unlike typical UKE applications to cooperative load transportation systems that employ single-element cable model; (ii) the extension of the mathematical model developed in [73], derived by applying the Lagrangian formulation directly on the configuration manifold, to include aerodynamic effects and non–barycentric cable attachment points on the quadrotors; (iii) the development of two control strategies that takes into account realistic requirements; (iv) the application of the variation-based linearization method developed in [70] to the system composed of multiple-quadrotors carrying a suspended rigid body payload and the design of a linear controller to stabilize the linearized error dynamics defined on the configuration manifold. This framework has been successfully applied to different dynamical systems, such as a

single quadrotor transporting a point-mass payload through flexible cables [39], and multiple quadrotors collaboratively carrying a flexible hose [54]. However, to the best of the author's knowledge, it has not yet been applied to the case of multiple quadrotors transporting a rigid-body payload through flexible cables; (v) the development of a distributed cascade control architecture for cooperative transportation, in which the outer loop governs formation and trajectory tracking through a virtual leader–follower consensus-based approach, the design of which is carried out neglecting the load, while robustness to constraint forces is achieved through the INDI-based loops; (vi) the implementation of an obstacle avoidance strategy for the entire formation-payload system within the framework of the formation-centered control approach.

1.4 Structure of the Work

The organization of the thesis is briefly illustrated in this section.
In Chapter 2, the derivation of the two mathematical models for the multi-UAV slung-load system, one based on the Udwadia–Kalaba formulation and the other based on a Lagrangian formulation on the configuration manifold, is presented.
In Chapter 3, the design of both the centralized linear load-leading controller and the distributed formation controller is presented.
In Chapter 4, the performance and suitability of the proposed approaches are evaluated through numerical simulations and flight tests.
Finally, in Chapter 5 the conclusions and the major contributions of this thesis are presented.

Chapter 2

Modeling

In this chapter, the mathematical model of a multi-UAV slung-load system is developed according to the Udwadia-Kalaba approach and the Lagrangian formulation on the configuration manifold.

2.1 Multi-UAV Slung-Load System

The multi-UAV slung-load system consists of N quadrotors connected to a suspended load via N inelastic flexible cables, attached to specific points of the vehicles and the load, in general not coinciding with the c.g., so that the attitude dynamics of all the bodies are affected by cable tension. The cables are modeled as a series of serially connected rectilinear elements represented by point masses $m_{p_{ij}}$ with $j = 1, \ldots, P$, being $m_{p_{ij}}$ the mass of the j-th element of the i-th cable, which for simplicity are assumed to be concentrated at the outboard end of the link. The direction of each cable element is represented by the unit vector $\boldsymbol{n}_{ij}$. A schematic representation of the multi–quadrotor payload system is provided in Fig. 2.1

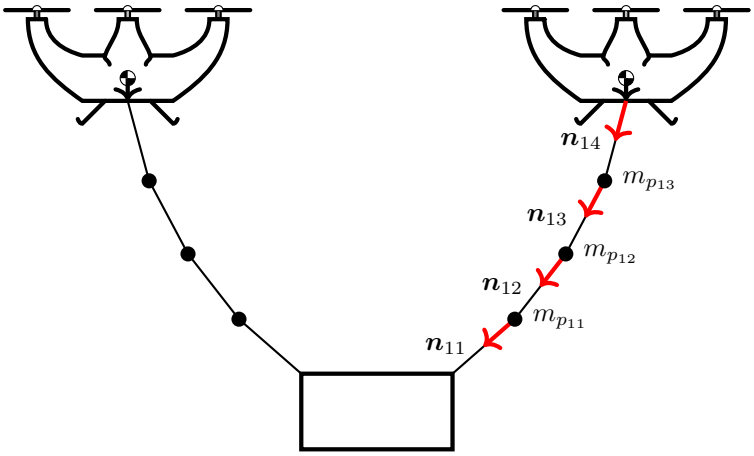

Figure 2.1: Multi–quadrotor payload system with flexible cables

The dynamics of the systems are expressed in two reference frames, namely a North-East-Down (NED) reference frame $\mathcal{F}_e$, and a body-fixed reference frame $\mathcal{F}_b$. Each body, namely, the vehicles and the load, is considered a 6 DoF rigid body with translational and rotational dynamics described in $\mathcal{F}_e$ and in $\mathcal{F}_B$, respectively.

North-Est-Down (NED) Reference Frame

The NED reference frame is assumed inertial under the hypothesis of flat, non-rotating Earth. It has the origin located in an arbitrary point on Earth's surface and is oriented with the x-axis pointing in the direction of the North, the z-axis is perpendicular to the x-axis and oriented along the local vertical pointing downward, and the y-axis completes the right-hand frame. A generic variable measured in this frame is denoted as ${}^{e}(\cdot)$.

Body-Fixed Reference Frame

The body-fixed reference frame is fixed to the principal axes of inertia of the vehicle, assumed rigid, with origin in the c.g. The x-axis is along the vehicle longitudinal axis, the z-axis is in the plane orthogonal to the x-axis pointing downward, while the y-axis completes the right-handed frame. A generic variable measured in this frame is denoted as ${}^{b}(\cdot)$.

2.2 Configuration Space

In classical mechanics, the set of variables that define the configuration of a system are called generalized coordinates (often denoted by $\boldsymbol{q}$), and the space defined by these coordinates is

called the configuration space of the mechanical system. The dimension of the configuration space determines the number of DoF of the system.

For example, for a point mass, the configuration space is the set of all admissible positions. If the mass moves freely in the three-dimensional space, then the configuration space is simply $\mathbb{R}^3$. If, instead, the point mass is constrained by a rigid and massless link fixed to a point in space, its motion is restricted to be on the surface of a sphere, and in this case its configuration space is the subset of coordinates in $\mathbb{R}^3$ that define points on the sphere $S^2 = \{(x, y, z) \in \mathbb{R}^3 \mid x^2 + y^2 + z^2 = 1\}$. For a rigid-body, the configuration is determined by the position of its c.g., and by the orientation of a body-fixed reference frame with respect to an inertial reference frame. The orientation is represented by a rotation matrix $\mathcal{R}_{eb} \in \mathbb{R}^{3\times3}$ that is orthogonal if both reference frames are orthonormal. When the two frames have the same orientation (e.g., both right-handed), then $\mathcal{R}_{eb}$ belongs to the special orthogonal group $SO(3) = \{\mathcal{R}_{eb} \in \mathbb{R}^{3\times3} \mid \mathcal{R}_{eb}^T\mathcal{R}_{eb} = \mathcal{I}, \det(\mathcal{R}_{eb}) = 1\}$.

Both the sphere S^2 and the special orthogonal group $SO(3)$ are examples of configuration spaces that are not Euclidean. As will be discussed later, they are smooth manifold. Roughly speaking, a manifold is a space that locally resembles an open subset of the Euclidean space, so that points on a manifold can be represented as objects in $\mathbb{R}^n$ by introducing local coordinates. In practice, such spaces are often described using local coordinates; for instance, Euler angles or quaternions are commonly used for $SO(3)$, while polar coordinates are used for S^2. For a given manifold there are many possible choices of local coordinates, each providing a valid local identification. However, equations expressed in a particular coordinate system may change when switching to another, and geometric features such as angles or distances may not be preserved under a change of coordinates. Instead, by working directly on the manifold without relying on a particular coordinate system, all constructions remain coordinate-invariant or intrinsic, and the geometric properties of the configuration space are satisfied.

The configuration manifold of the multi-UAV slung-load system described in Sec. 2.1 is

$$M = \left(SO(3) \times \mathbb{R}^3\right) \times \left(S^2\right)^{NP} \times SO(3)^N \tag{2.1}$$

where $SO(3) \times \mathbb{R}^3$ describes the configurations of the payload, $(S^2)^{NP}$ the configurations of the NP cable elements, and $SO(3)^N$ the attitude of the N quadrotors. Only the rotational configurations of each quadrotor are considered, since their positions are fully determined

by the payload position and the cable directions.

In the Udwadia–Kalaba formulation, the system is expressed in redundant coordinates, namely in terms of the position and attitude of the payload, the positions of the intermediate point masses, and the position and attitude of each quadrotor. The admissible motions are enforced through additional holonomic constraints, and the attitude of each rigid body is locally parameterized using Euler angles. Conversely, the Lagrangian formulation developed on the configuration manifold M is written directly in terms of the generalized coordinates, that is, the position and attitude of the payload, the orientations of the cable links, and the attitudes of the quadrotors. In this case, the equations evolve intrinsically on the constrained manifold without the need for explicit constraint equations.

2.3 Udwadia-Kalaba Formulation

An unconstrained mechanical system is described using Newtonian or Lagrangian mechanics as

$$\boldsymbol{M}\ddot{\boldsymbol{q}}_u = \boldsymbol{Q} \tag{2.2}$$

where $\boldsymbol{M} \in \mathbb{R}^{n\times n}$ is the positive-definite symmetric generalized mass matrix, $\boldsymbol{q}_u \in \mathbb{R}^n$ is the vector of generalized coordinates of the unconstrained system, and $\boldsymbol{Q} \in \mathbb{R}^n$ is the generalized force vector. The generalized acceleration of the unconstrained system, denoted by $\boldsymbol{a}$, is defined as $\boldsymbol{a} = \ddot{\boldsymbol{q}}_u = \boldsymbol{M}^{-1}\boldsymbol{Q}$. Consider m constraints acting on the system, which do not have to be linearly independent, and can be either holonomic or non holonomic

$$\boldsymbol{\eta}(\boldsymbol{q}, t) = 0 \tag{2.3}$$

$$\boldsymbol{\eta}(\boldsymbol{q}, \dot{\boldsymbol{q}}, t) = 0 \tag{2.4}$$

where $\boldsymbol{q} \in \mathbb{R}^n$ represents the generalized coordinate vector of the constrained system. If the constraints are sufficiently smooth, i.e. $\boldsymbol{\eta} \in C^2$, Eqs. (2.4) and (2.3) are differentiated once or twice, respectively, to yield

$$\boldsymbol{A}(\boldsymbol{q}, \dot{\boldsymbol{q}}, t)\ddot{\boldsymbol{q}} = \boldsymbol{b}(\boldsymbol{q}, \dot{\boldsymbol{q}}, t) \tag{2.5}$$

where $\boldsymbol{A} \in \mathbb{R}^{m \times n}$ and $\boldsymbol{b} \in \mathbb{R}^{m}$ are the Jacobian of the constraint function and the acceleration-independent component of the constraint equation, respectively. Equation (2.5) encompasses a wide variety of constraints, provided that they are linear with respect to generalized accelerations or that they are reducible in that form.

The equations of motion for the constrained system are written as [32]

$$\boldsymbol{M}\ddot{\boldsymbol{q}} = \boldsymbol{Q} + \boldsymbol{Q}_c \tag{2.6}$$

being $\boldsymbol{Q}_c \in \mathbb{R}^n$ the vector of generalized forces due to the constraints. Using the Gauss' Principle of Least Constraint gives

$$\boldsymbol{Q}_c = \boldsymbol{K}\left(\boldsymbol{b} - \boldsymbol{A}\boldsymbol{M}^{-1}\boldsymbol{Q}\right) = \boldsymbol{K}\left(\boldsymbol{b} - \boldsymbol{A}\boldsymbol{a}\right) \tag{2.7}$$

where $\boldsymbol{K} = \boldsymbol{M}^{\frac{1}{2}}\left(\boldsymbol{A}\boldsymbol{M}^{\frac{1}{2}}\right)^{+}$, and the symbol $(\cdot)^{\dagger}$ indicates the More-Penrose inverse. Details on the More-Penrose inverse, and on how to derive the Udwadia-Kalaba equation (Eq. (2.7)) from the Gauss' Principle of Least Constraint are reported in Appendix A.1, and A.2, respectively.

In order to give an interpretation of Eq. (2.6), Eq. (2.7) is substituted into Eq. (2.6)

$$\ddot{\boldsymbol{q}} = \boldsymbol{a} + \boldsymbol{M}^{-1}\boldsymbol{K}\left(\boldsymbol{b} - \boldsymbol{A}\boldsymbol{a}\right) \tag{2.8}$$

which is rewritten as

$$\Delta\boldsymbol{a} = \boldsymbol{K}_1\boldsymbol{e} \tag{2.9}$$

where $\Delta\boldsymbol{a} = \ddot{\boldsymbol{q}} - \boldsymbol{a}$ is the difference between the constrained and unconstrained acceleration, $\boldsymbol{e} = (\boldsymbol{b} - \boldsymbol{A}\boldsymbol{a})$ denotes the residual by which the acceleration of the unconstrained system deviate from those required to satisfy the constraint equations, and $\boldsymbol{K}_1 = \boldsymbol{M}^{-1}\boldsymbol{K}$.

Equation (2.9) states that the motion of a constrained system evolves such that, at each time instant, the difference between the constrained and unconstrained acceleration, $\Delta\boldsymbol{a}$, is directly proportional through $\boldsymbol{K}_1$ to the residual by which the unconstrained acceleration at that instant fails to satisfy the constraint equations ($\boldsymbol{e}$).

Equation (2.6) for a swarm-load system with N agents and with the cables composed of

rectilinear elements is written as

$$\boldsymbol{M}_m \, \ddot{\boldsymbol{q}}_m = \boldsymbol{Q}_m + \boldsymbol{Q}_{c_m} \tag{2.10}$$

where the second derivative of the generalized coordinates vector $\boldsymbol{q}_m$ is given by

$$\ddot{\boldsymbol{q}}_m = \left[\ddot{\boldsymbol{q}}_{m_1}^T, \quad \cdots, \quad \ddot{\boldsymbol{q}}_{m_i}^T, \quad \cdots, \quad \ddot{\boldsymbol{q}}_{m_N}^T, \quad {}^e\ddot{\boldsymbol{p}}_l^T, \quad {}^{b_l}\dot{\boldsymbol{\omega}}_l^T \right]^T \tag{2.11}$$

being

$$\ddot{\boldsymbol{q}}_{m_i} = \left[{}^e\ddot{\boldsymbol{p}}_i^T, \quad {}^{b_l}\dot{\boldsymbol{\omega}}_i^T, \quad {}^e\ddot{\boldsymbol{p}}_{p_{i1}}^T, \quad \cdots, \quad {}^e\ddot{\boldsymbol{p}}_{p_{ij}}^T, \quad \cdots, \quad {}^e\ddot{\boldsymbol{p}}_{p_{iP}}^T \right]^T \tag{2.12}$$

and the mass matrix $\boldsymbol{M}_m$ is reported in Appendix A.3. In order to obtain the constraint forces and moments vector $\boldsymbol{Q}_{cm}$, it is necessary to calculate the matrix $\boldsymbol{A}$ and the vector $\boldsymbol{b}$, as shown in Eq. (2.7).

The constraint on the constant length of each cable link l_{ij} is expressed in terms of the norm of the vector ${}^e\boldsymbol{L}_{ij}$, which connects the two endpoints of the link, as

$$\eta_{ij} = \| {}^e\boldsymbol{L}_{ij} \|^2 - l_{ij}^2 = 0 \tag{2.13}$$

Differentiating twice Eq. (2.13) yields

$$\dot{\eta}_{ij} = 2 \, {}^e\boldsymbol{L}_{ij}^T \, {}^e\dot{\boldsymbol{L}}_{ij} = 0 \tag{2.14}$$

$$\ddot{\eta}_{ij} = 2 \, {}^e\dot{\boldsymbol{L}}_{ij}^T \, {}^e\dot{\boldsymbol{L}}_{ij} + 2 \, {}^e\boldsymbol{L}_{ij}^T \, {}^e\ddot{\boldsymbol{L}}_{ij} = 0 \tag{2.15}$$

Finally, Eq. (2.15) is recast into the standard form of Eq. (2.5), which makes it possible to evaluate the matrix $\boldsymbol{A}$ and the vector $\boldsymbol{b}$ required for evaluating the constraint forces in Eq. (2.7).

The definition of ${}^e\boldsymbol{L}_{ij}$ depends on the specific type of connection. In the case of the first link, which connects the UAV to the first mass of the cable, the corresponding link vector is given by

$${}^e\boldsymbol{L}_{i1} = {}^e\boldsymbol{p}_{i1} - ({}^e\boldsymbol{p}_i + \mathcal{R}_{eb_i} \, {}^{b_i}\boldsymbol{r}_{a_i}) \tag{2.16}$$

where ${}^{b_i}\boldsymbol{r}_{a_i}$ is the position vector of the cable attachment point on the i-th agent expressed in the agent body reference frame. The derivatives of the link vector are given by

$$\dot{\boldsymbol{L}}_{i1} = {}^{e}\dot{\boldsymbol{p}}_{i1} - ({}^{e}\dot{\boldsymbol{p}}_i + \dot{\mathcal{R}}_{eb_i}\,{}^{b_i}\boldsymbol{r}_{a_i}) \tag{2.17}$$

$$\ddot{\boldsymbol{L}}_{i1} = {}^{e}\ddot{\boldsymbol{p}}_{i1} - ({}^{e}\ddot{\boldsymbol{p}}_i + \ddot{\mathcal{R}}_{eb_i}\,{}^{b_i}\boldsymbol{r}_{a_i}) \tag{2.18}$$

The time derivatives of the rotation matrix are given by

$$\dot{\mathcal{R}}_{eb_i} = \mathcal{R}_{eb_i}\,{}^{b_i}\widehat{\boldsymbol{\omega}}_i \tag{2.19}$$

$$\ddot{\mathcal{R}}_{eb_i} = \dot{\mathcal{R}}_{eb_i}\,{}^{b_i}\widehat{\boldsymbol{\omega}}_i + \mathcal{R}_{eb_i}\,{}^{b_i}\dot{\widehat{\boldsymbol{\omega}}}_i = \mathcal{R}_{eb_i}\,{}^{b_i}\widehat{\boldsymbol{\omega}}_i\,{}^{b_i}\widehat{\boldsymbol{\omega}}_i + \mathcal{R}_{eb_i}\,{}^{b_i}\dot{\widehat{\boldsymbol{\omega}}}_i \tag{2.20}$$

where the hat operator is defined in App. B.1. Substituting Eqs. (2.19), and (2.20) into Eqs. (2.17), and (2.18) gives

$$\dot{\boldsymbol{L}}_{i1} = {}^{e}\dot{\boldsymbol{p}}_{i1} - ({}^{e}\dot{\boldsymbol{p}}_i + \mathcal{R}_{eb_i}\,{}^{b_i}\widehat{\boldsymbol{\omega}}_i\,{}^{b_i}\boldsymbol{r}_{a_i}) \tag{2.21}$$

$$\ddot{\boldsymbol{L}}_{i1} = {}^{e}\ddot{\boldsymbol{p}}_{i1} - ({}^{e}\ddot{\boldsymbol{p}}_i + \mathcal{R}_{eb_i}\,{}^{b_i}\widehat{\boldsymbol{\omega}}_i\,{}^{b_i}\widehat{\boldsymbol{\omega}}_i\,{}^{b_i}\boldsymbol{r}_{a_i} + \mathcal{R}_{eb_i}\,{}^{b_i}\dot{\widehat{\boldsymbol{\omega}}}_i\,{}^{b_i}\boldsymbol{r}_{a_i}) \tag{2.22}$$

Finally, exploiting the antisymmetric property of the cross product, Eq. (2.22) becomes

$$\ddot{\boldsymbol{L}}_{i1} = {}^{e}\ddot{\boldsymbol{p}}_{i1} - ({}^{e}\ddot{\boldsymbol{p}}_i + \mathcal{R}_{eb_i}\,{}^{b_i}\widehat{\boldsymbol{\omega}}_i\,{}^{b_i}\widehat{\boldsymbol{\omega}}_i\,{}^{b_i}\boldsymbol{r}_{a_i} - \mathcal{R}_{eb_i}\,{}^{b_i}\widehat{\boldsymbol{r}}_{a_i}\,{}^{b_i}\dot{\boldsymbol{\omega}}_i) \tag{2.23}$$

The explicit form of the second derivative of the constraint equation for the first links is obtained by substituting Eqs. (2.21), and (2.23) into Eq. (2.15). Rearranging as in Eq. (2.5) yields

$$\boldsymbol{A}_{i1}\ddot{\boldsymbol{q}}_{i1} = \boldsymbol{b}_{i1} \tag{2.24}$$

where $\boldsymbol{A}_{i1}$, and $\boldsymbol{b}_{i1}$ are given by

$$\boldsymbol{A}_{i1} = 2\,{}^{e}\boldsymbol{L}_{i1}^{T}\begin{bmatrix}\boldsymbol{0}_{3\times\mu(i-1)} & -\boldsymbol{\mathcal{I}} & \mathcal{R}_{eb_i}\,{}^{b_i}\widehat{\boldsymbol{r}}_i & \boldsymbol{\mathcal{I}} & \boldsymbol{0}_{3\times\mu(N-i)+6}\end{bmatrix} \tag{2.25}$$

$$\boldsymbol{b}_{i1} = -2\,{}^{e}\dot{\boldsymbol{L}}_{i1}^{T}\,{}^{e}\dot{\boldsymbol{L}}_{i1} + 2\,{}^{e}\boldsymbol{L}_{i1}^{T}\left(\mathcal{R}_{eb_i}\,{}^{b_i}\widehat{\boldsymbol{\omega}}_i\,{}^{b_i}\widehat{\boldsymbol{\omega}}_i\,{}^{b_i}\boldsymbol{r}_i\right) \tag{2.26}$$

with $\mu = 6 + 3P$. For the intermediate links, connecting two adjacent cable masses, the

corresponding link vectors and their time derivatives are

$$
{}^{e}\boldsymbol{L}_{ij} = {}^{e}\boldsymbol{p}_{i(j+1)} - {}^{e}\boldsymbol{p}_{ij} \tag{2.27}
$$

$$
{}^{e}\dot{\boldsymbol{L}}_{ij} = {}^{e}\dot{\boldsymbol{p}}_{i(j+1)} - {}^{e}\dot{\boldsymbol{p}}_{ij} \tag{2.28}
$$

$$
{}^{e}\ddot{\boldsymbol{L}}_{ij} = {}^{e}\ddot{\boldsymbol{p}}_{i(j+1)} - {}^{e}\ddot{\boldsymbol{p}}_{ij} \tag{2.29}
$$

with $j \neq 1, N$. Substituting Eqs. (2.28), and (2.29) into Eq. (2.15) gives

$$
\boldsymbol{A}_{ij} = 2\,{}^{e}\boldsymbol{L}_{i}^{T}\begin{bmatrix}\boldsymbol{0}_{3\times\mu(i-1)+3(j-1)} & -\boldsymbol{\mathcal{I}} & \boldsymbol{\mathcal{I}} & \boldsymbol{0}_{3\times\mu(N-i)+3(P-(j+1))+6}\end{bmatrix} \tag{2.30}
$$

$$
b_{ij} = -2\,{}^{e}\dot{\boldsymbol{L}}_{ij}^{T}\,{}^{e}\dot{\boldsymbol{L}}_{ij} \tag{2.31}
$$

Finally, for the last link, connecting the last mass of the cable to the load, the link vector is given by

$$
{}^{e}\boldsymbol{L}_{iP} = ({}^{e}\boldsymbol{p}_{l} + \mathcal{R}_{eb_l}\,{}^{b_l}\boldsymbol{r}_{al_i}) - {}^{e}\boldsymbol{p}_{iP} \tag{2.32}
$$

being ${}^{b_l}\boldsymbol{r}_{al_i}$ the position vector of the i-th cable attachment point on the load expressed in the load body frame. The derivatives of the link vector are given by

$$
{}^{e}\dot{\boldsymbol{L}}_{iP} = ({}^{e}\dot{\boldsymbol{p}}_{l} + \mathcal{R}_{eb_l}\,{}^{b_l}\widehat{\boldsymbol{\omega}}_{l}\,{}^{b_l}\boldsymbol{r}_{al_i}) - {}^{e}\dot{\boldsymbol{p}}_{iP} \tag{2.33}
$$

$$
{}^{e}\ddot{\boldsymbol{L}}_{iP} = ({}^{e}\ddot{\boldsymbol{p}}_{l} + \mathcal{R}_{eb_l}\,{}^{b_l}\widehat{\boldsymbol{\omega}}_{l}\,{}^{b_l}\widehat{\boldsymbol{\omega}}_{l}\,{}^{b_l}\boldsymbol{r}_{al_i} + \mathcal{R}_{eb_l}\,{}^{b_l}\dot{\widehat{\boldsymbol{\omega}}}_{l}\,{}^{b_l}\boldsymbol{r}_{al_i}) - {}^{e}\ddot{\boldsymbol{p}}_{iP} \tag{2.34}
$$

where the derivatives of the rotation matrix have been used. The second derivative of the constraint equations for the last links are given by

$$
\boldsymbol{A}_{iP} = 2\,{}^{e}\boldsymbol{L}_{iP}^{T}\begin{bmatrix}\boldsymbol{0}_{3\times\mu(i-1)+3(P-1)} & -\boldsymbol{\mathcal{I}} & \boldsymbol{0}_{3\times\mu(N-i)} & \boldsymbol{\mathcal{I}} & \mathcal{R}_{eb_l}\,{}^{b_l}\widehat{\boldsymbol{r}}_{l_i}\end{bmatrix} \tag{2.35}
$$

$$
b_{iP} = -2\,{}^{e}\dot{\boldsymbol{L}}_{iP}^{T}\,{}^{e}\dot{\boldsymbol{L}}_{iP} + 2\,{}^{e}\boldsymbol{L}_{iP}^{T}\left(\mathcal{R}_{eb_l}\,{}^{b_l}\widehat{\boldsymbol{\omega}}_{l}\,{}^{b_l}\widehat{\boldsymbol{\omega}}_{l}\,{}^{b_l}\boldsymbol{r}_{l_i}\right) \tag{2.36}
$$

The constraint equations for the whole system, according to Eq. (2.5), are given by

$$
\boldsymbol{A}_{m}\ddot{\boldsymbol{q}}_{m} = \boldsymbol{b}_{m} \tag{2.37}
$$

where

$$\boldsymbol{A}_m = \begin{bmatrix} \boldsymbol{A}_{m_1} \\ \vdots \\ \boldsymbol{A}_{m_i} \\ \vdots \\ \boldsymbol{A}_{m_n} \end{bmatrix} \qquad \boldsymbol{b}_m = \begin{bmatrix} b_{m_1} \\ \vdots \\ b_{m_i} \\ \vdots \\ b_{m_N} \end{bmatrix} \tag{2.38}$$

and

$$\boldsymbol{A}_{m_i} = \begin{bmatrix} \boldsymbol{A}_{i1} \\ \vdots \\ \boldsymbol{A}_{ij} \\ \vdots \\ \boldsymbol{A}_{iP} \end{bmatrix} \qquad \boldsymbol{b}_{m_i} = \begin{bmatrix} b_{i1} \\ \vdots \\ b_{ij} \\ \vdots \\ b_{iP} \end{bmatrix} \tag{2.39}$$

The generalized constraint force and moment vector is

$$\boldsymbol{Q}_{c_m} = \boldsymbol{M}_{\boldsymbol{m}}^{\frac{1}{2}} \left(\boldsymbol{A}_{\boldsymbol{m}} \boldsymbol{M}_{\boldsymbol{m}}^{-\frac{1}{2}} \right)^{+} \left(\boldsymbol{b}_m - \boldsymbol{A}_m \boldsymbol{M}_{\boldsymbol{m}}^{-1} \boldsymbol{Q}_m \right) \tag{2.40}$$

where

$$\boldsymbol{Q}_{c_m} = \begin{bmatrix} \boldsymbol{Q}_{c_{m_1}} \\ \vdots \\ \boldsymbol{Q}_{c_{m_i}} \\ \vdots \\ \boldsymbol{Q}_{c_{m_N}} \\ \boldsymbol{Q}_{c_{m_l}} \end{bmatrix} \tag{2.41}$$

and

$$\boldsymbol{Q}_{c_{m_i}} = \begin{bmatrix} {}^{e}\boldsymbol{F}_{c_{m_i}} \\ {}^{b_i}\boldsymbol{G}_{c_{m_i}} \\ {}^{e}\boldsymbol{F}_{c_{m_{i1}}} \\ \vdots \\ {}^{e}\boldsymbol{F}_{c_{m_{ij}}} \\ \vdots \\ {}^{e}\boldsymbol{F}_{c_{m_{iP}}} \end{bmatrix} \qquad \boldsymbol{Q}_{c_{m_l}} = \begin{bmatrix} {}^{e}\boldsymbol{F}_{c_{m_l}} \\ {}^{b_l}\boldsymbol{G}_{c_{m_l}} \end{bmatrix} \tag{2.42}$$

with ${}^{e}\boldsymbol{F}_{c_{m_{i,l}}}$ and ${}^{b_i}\boldsymbol{G}_{c_{s_{i,l}}}$ the constraint forces and moments, respectively, acting on the i-th agent and the load, and ${}^{e}\boldsymbol{F}_{c_{m_{ij}}}$ the constraint force acting on $m_{p_{ij}}$.
Finally, the initial conditions ($\boldsymbol{q}_m(0) = \boldsymbol{q}_{m0}, \dot{\boldsymbol{q}}_m(0) = \dot{\boldsymbol{q}}_{m0}$) for the system in Eq. (2.10) need to be assigned such that Eqs. (2.13) and (2.14) are satisfied.

2.3.1 Numerical Issues

A well-known problem of the UKE formulation is the constraint drift, which results in a slow variation of cable length. This issues originates from the fact that constraints are enforced in terms of acceleration (Eq. (2.5)) and not directly in terms of velocity and position (Eqs. (2.13), (2.14)). As a result, numerical integration may induce a cumulative error in velocity and position states, which can grow unbounded depending on the integration scheme and step size adopted. To mitigate this behavior, corrective strategies must be employed to account for numerical errors. In the following, three possible correction methods from the literature are recalled.

Baumgarte Method

In the Baumgarte method [74], a state feedback mechanism is introduced in Eq. (2.5) in order to stabilize the constraint dynamics

$$\ddot{\boldsymbol{\eta}} + 2\alpha\dot{\boldsymbol{\eta}} + \beta^2\boldsymbol{\eta} = 0 \tag{2.43}$$

$$\boldsymbol{A}\ddot{\boldsymbol{q}} = \boldsymbol{b} - 2\alpha\dot{\boldsymbol{\eta}} - \beta^2\boldsymbol{\eta} \tag{2.44}$$

The system in Eq. (2.44) is asymptotically stable for $\alpha, \beta > 0$, that is $\boldsymbol{\eta} \to 0$, as $t \to \infty$. Equation (2.8) thus becomes

$$\ddot{\boldsymbol{q}} = \boldsymbol{a} + \boldsymbol{M}^{-1}\boldsymbol{K}\left(\boldsymbol{b} - 2\alpha\dot{\boldsymbol{\eta}} - \beta^2\boldsymbol{\eta} - \boldsymbol{A}\boldsymbol{a}\right) \tag{2.45}$$

A careful choice of the constants α and β is essential, as unsuitable values can modify the original dynamics of the system.

Spring-Damper Method

An alternative approach is the one introduced in [75]. It is similar to the Baumgarte method, but it acts directly on the equation of motion by introducing an additional acceleration term $\boldsymbol{a}_n$, which represents the effect of a fictitious spring–damper system acting in parallel with each cable link. As a result, whenever the link length tends to increase, the corrective contribution $\boldsymbol{a}_n$ counteracts the deviation, thereby restoring the link to its nominal length, according to

$$\ddot{\boldsymbol{q}} = \boldsymbol{a} + \boldsymbol{M}^{-1}\boldsymbol{K}\left(\boldsymbol{b} - \boldsymbol{A}\boldsymbol{a}\right) + \boldsymbol{a}_n \tag{2.46}$$

As an example, consider two masses connected by a rigid and massless link. In this case, the acceleration $\boldsymbol{a}_{n1}$ for the first body is

$$\boldsymbol{a}_{n1} = \frac{1}{m_1}\left[\boldsymbol{F}_{m1} + \boldsymbol{F}_{s1}\right] \tag{2.47}$$

where

$$\boldsymbol{F}_{m1} = \boldsymbol{k}_m\boldsymbol{\eta}\boldsymbol{N}_1 \tag{2.48}$$

$$\boldsymbol{F}_{s1} = -\boldsymbol{k}_s\dot{\boldsymbol{\eta}}\boldsymbol{N}_1 \tag{2.49}$$

with $\boldsymbol{k}_m$ and $\boldsymbol{k}_s$ characterizing the spring and damper, respectively, and $\boldsymbol{N}_1$ being the unit vector representing the link direction.

Braun-Goldfarb Method

In the Braun-Goldfarb method [76], the system in Eq. (2.8) is rewritten in the first-order form

$$\begin{cases} \dot{\boldsymbol{q}} &= \boldsymbol{v} + \boldsymbol{K}_1 \left(\tilde{\boldsymbol{b}} - \boldsymbol{A}\boldsymbol{v} - \frac{\boldsymbol{\eta}}{dt} \right) \\ \dot{\boldsymbol{v}} &= \boldsymbol{a} + \boldsymbol{K}_1 \left(\boldsymbol{b} - \boldsymbol{A}\boldsymbol{a} - \frac{\dot{\boldsymbol{\eta}}}{dt} \right) \end{cases} \tag{2.50}$$

where $\tilde{\boldsymbol{b}}$ is the part independent of $\dot{\boldsymbol{q}}$ that arises from the first derivative of the constraint. The corrective terms $\frac{\boldsymbol{\eta}}{dt}$ and $\frac{\dot{\boldsymbol{\eta}}}{dt}$ come from the Taylor expansion of $\boldsymbol{\eta}$ and $\dot{\boldsymbol{\eta}}$ as

$$\boldsymbol{\eta}(t + dt) = \boldsymbol{\eta}(t) + (\boldsymbol{A}\dot{\boldsymbol{q}} - \tilde{\boldsymbol{b}})dt + \boldsymbol{\mathcal{O}}(dt^2) \tag{2.51}$$

$$\dot{\boldsymbol{\eta}}(t + dt) = \dot{\boldsymbol{\eta}}(t) + (\boldsymbol{A}\ddot{\boldsymbol{q}} - \boldsymbol{b})dt + \boldsymbol{\mathcal{O}}(dt^2) \tag{2.52}$$

By imposing $\boldsymbol{\eta}(t + dt) = 0$ and $\dot{\boldsymbol{\eta}}(t + dt) = 0$, it follows

$$\boldsymbol{A}\dot{\boldsymbol{q}} = \tilde{\boldsymbol{b}} - \frac{\boldsymbol{\eta}}{dt} \tag{2.53}$$

$$\boldsymbol{A}\ddot{\boldsymbol{q}} = \boldsymbol{b} - \frac{\dot{\boldsymbol{\eta}}}{dt} \tag{2.54}$$

From a numerical perspective, dt corresponds to the integration step size. The corrective terms are such that they minimize, in terms of both acceleration and kinetic energy, their own effect on the system dynamics.

In this work, the Braun-Goldfarb method is used. For the system in Eq. (2.10), Eq. (2.50) reads

$$\begin{cases} \boldsymbol{C}\dot{\boldsymbol{e}} = \boldsymbol{v} + \boldsymbol{K}_{1_m} \left(\tilde{\boldsymbol{b}}_m - \boldsymbol{A}_m\boldsymbol{v} - \frac{\boldsymbol{\eta}}{dt} \right) \\ \dot{\boldsymbol{v}} = \boldsymbol{a}_m + \boldsymbol{K}_{1_m} \left(\boldsymbol{b}_m - \boldsymbol{A}_m\boldsymbol{v} - \frac{\dot{\boldsymbol{\eta}}}{dt} \right) \end{cases} \tag{2.55}$$

where $\boldsymbol{a}_m$ is the unconstrained acceleration of the system, $\boldsymbol{v} = \dot{\boldsymbol{q}}_m$, $\boldsymbol{K}_{1_m} = \boldsymbol{M}_m^{-\frac{1}{2}}(\boldsymbol{A}_m\boldsymbol{M}_m^{\frac{1}{2}})^+$, the constraint vector $\boldsymbol{Q}_{c_m}$ is again evaluated by Eq. (2.7), and

$$\boldsymbol{e} = \left[\boldsymbol{e}_1^T, \quad \cdots, \quad \boldsymbol{e}_i^T, \quad \cdots, \quad \boldsymbol{e}_N^T, \quad {}^e\boldsymbol{p}_l^T, \boldsymbol{\Phi}_l^T \right]^T \tag{2.56}$$

with

$$\boldsymbol{e}_i = \left[{}^e\boldsymbol{p}_i^T, \quad \boldsymbol{\Phi}_i^T, \quad {}^e\boldsymbol{p}_{p_{i1}}^T, \quad \cdots, \quad {}^e\boldsymbol{p}_{p_{ij}}^T, \quad \cdots, \quad {}^e\boldsymbol{p}_{p_{iP}}^T \right]^T \tag{2.57}$$

where $\boldsymbol{\Phi}_{i,l}$ represents the attitude of the i-th quadrotor, and the load, respectively. The matrix $\boldsymbol{C}$ is reported in Appendix A.4.

2.3.2 Quadrotor Model

The unconstrained dynamics of each quadrotor, which are required to formulate the constrained equations of motion via the Udwadia–Kalaba approach, are introduced.
Each quadrotor is modeled as a 6 DoF rigid body with the translational dynamics described in $\mathcal{F}_e$ and the rotational dynamics in $\mathcal{F}_{b_i}$ (Fig. 2.2). The orientation of $\mathcal{F}_b$ with respect to $\mathcal{F}_e$ is expressed through the Euler angles of roll (ϕ), pitch (θ), and yaw (ψ). The quadrotor has four rotors, the rotation axes of which are parallel to z_{b_i}.

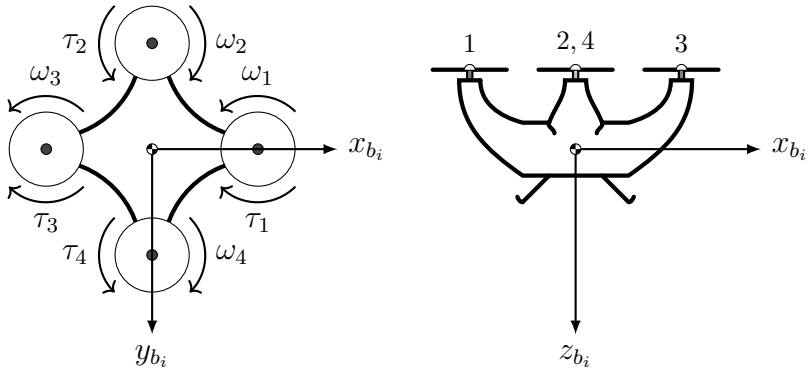

Figure 2.2: Orientation of the reference frame $\mathcal{F}_{b_i}$ and (right) directions of rates ω_k and torques τ_k

The governing equations read [77]

$${}^e\ddot{\boldsymbol{p}} = {}^e\boldsymbol{g} + \frac{1}{m}\,{}^e\boldsymbol{F} \tag{2.58}$$

$${}^b\dot{\boldsymbol{\omega}} = {}^b\boldsymbol{I}^{-1}\left({}^b\boldsymbol{G} - {}^b\boldsymbol{\omega} \times {}^b\boldsymbol{I}\,{}^b\boldsymbol{\omega}\right) \tag{2.59}$$

where the subscript i is omitted for the sake of clarity, ${}^e\boldsymbol{g} = [0, 0, g]^T$ is the gravity acceleration vector, ${}^b\boldsymbol{I} = \mathrm{diag}\{I_{xx}, I_{yy}, I_{zz}\}$ is the inertia tensor assumed constant [77] and diagonal

in the body reference frame. The attitude kinematics is written as

$$\dot{\Phi} = \boldsymbol{T}\,{}^{b}\boldsymbol{\omega} \tag{2.60}$$

where $\boldsymbol{\Phi} = [\phi, \theta, \psi]^T$, and the matrix $\boldsymbol{T}(\phi, \theta, \psi)$ is defined as [77]

$$\boldsymbol{T}(\phi, \theta, \psi) = \begin{bmatrix} 1 & \sin(\phi)\tan(\theta) & \cos(\psi)\tan(\theta) \\ 0 & \cos(\phi) & -\sin(\psi) \\ 0 & \sin(\psi)\sec(\theta) & \cos(\phi)\sec(\theta) \end{bmatrix} \tag{2.61}$$

The total external force ${}^{e}\boldsymbol{F}$ and moment ${}^{b}\boldsymbol{G}$ on the quadrotor are

$${}^{e}\boldsymbol{F} = {}^{e}\boldsymbol{F}_T + {}^{e}\boldsymbol{F}_A + {}^{e}\boldsymbol{F}_{c_m} \tag{2.62}$$

$${}^{b}\boldsymbol{G} = {}^{b}\boldsymbol{G}_L + {}^{b}\boldsymbol{G}_T + {}^{b}\boldsymbol{G}_{c_m} \tag{2.63}$$

where the subscripts indicate thrust (T), aerodynamic (A), and gyroscopic (L) terms, and the constraints (c). The aerodynamic moment generated by the airframe is disregarded because, for a quadrotor, the distance l from the c.g. to the airframe aerodynamic center is typically small compared to the arm length, that is, the distance between any rotor and the c.g. Also, the damping effect due to the variation of induced velocity on the rotors during rotational motion is neglected.

The airframe drag is obtained using the equivalent flat-plane concept, so that the force vector is expressed as, in the body frame

$${}^{b}\boldsymbol{F}_A = -\frac{1}{2}\rho \begin{bmatrix} A_x|(u-u_W)|(u-u_W) \\ A_y|(v-v_W)|(v-v_W) \\ A_z|(w-w_W)|(w-w_W) \end{bmatrix} \tag{2.64}$$

where A_x, A_y, and A_z are the equivalent flat-plane drag areas, $[u, v, w]^T = \mathcal{R}_{be}\,{}^{e}\boldsymbol{v}$ is the inertial velocity vector in body-axes, $[u_w, v_w, w_w]^T = \mathcal{R}_{be}\,{}^{e}\boldsymbol{v}_w$ is the instantaneous wind velocity vector in the same frame, and $\mathcal{R}_{be}$ is the transformation matrix from $\mathcal{F}_b$ to $\mathcal{F}_e$ [77]. The airframe force is written in the inertial frame as ${}^{e}\boldsymbol{F}_A = \mathcal{R}_{eb}\,{}^{b}\boldsymbol{F}_A$, being $\mathcal{R}_{eb} = \mathcal{R}_{be}^T$. Each rotor generates a thrust force T_k, $k = 1, ..., 4$, directed along z_{b_i} and a reaction torque τ_k in the opposite direction of the rotor rate ω_k. Figure 2.2 shows the directions of the rotor

angular velocities and the signs of the reaction torques. It is ${}^{e}\boldsymbol{F}_T = \mathcal{R}_{eb}\,[0, 0, -T]^T$, where $T = T_1 + T_2 + T_3 + T_4$ is the total thrust force, being $T_k = b\omega_k^2$, with b the thrust coefficient. The thrust moment is

$$ {}^{b}\boldsymbol{G}_T = \begin{bmatrix} l(T_2 - T_4) \\ l(T_1 - T_3) \\ \tau_1 - \tau_2 + \tau_3 - \tau_4 \end{bmatrix} \tag{2.65} $$

where $\tau_k = d\omega_k^2$, d is the torque coefficient, and l is the distance etween each rotor and the quadrotor c.g. The gyroscopic moment is ${}^{b}\boldsymbol{G}_L = {}^{b}\boldsymbol{\omega} \times {}^{b}\boldsymbol{I}_r\, {}^{b}\boldsymbol{\omega}_r$, where ${}^{b}\boldsymbol{I}_r = \text{diag}\{I_r, I_r, J_r\}$ is the inertia tensor of the single rotor, and ${}^{b}\boldsymbol{\omega}_r = [0, 0, \omega_r]^T$ is the overall rotor rate, with $\omega_r = -\omega_1 + \omega_2 - \omega_3 + \omega_4$. Finally, the constraint force (${}^{e}\boldsymbol{F}_{c_m}$) and moment $\left({}^{b}\boldsymbol{G}_{c_m} = \left[L_{c_m}^T, M_{c_m}^T, N_{c_m}^T\right]^T\right)$ are defined in Eq. (2.42). The model reads, in scalar form [78]

$$
\begin{aligned}
\ddot{x} &= -\tfrac{1}{m}\left[-U_1\Big(\cos(\phi)\sin(\theta)\cos(\psi)+\sin(\phi)\sin(\psi)\Big)+F_{A_x}+F_{c_{m_x}}\right]\\
\ddot{y} &= -\tfrac{1}{m}\left[-U_1\Big(\cos(\phi)\sin(\theta)\sin(\psi)-\sin(\phi)\cos(\psi)\Big)+F_{A_y}+F_{c_{m_y}}\right]\\
\ddot{z} &= g-\tfrac{1}{m}\left[-U_1\Big(\cos(\phi)\cos(\theta)\Big)+F_{A_z}+F_{c_{m_z}}\right]\\
\dot{p} &= \left(\tfrac{I_{yy}-I_{zz}}{I_{xx}}\right)qr+\tfrac{1}{I_{xx}}\left(J_r\omega_r q+L_{c_m}+U_2\right)\\
\dot{q} &= \left(\tfrac{I_{zz}-I_{xx}}{I_{yy}}\right)pr+\tfrac{1}{I_{yy}}\left(-J_r\omega_r p+M_{c_m}+U_3\right)\\
\dot{r} &= \left(\tfrac{I_{xx}-I_{yy}}{I_{zz}}\right)pq+\tfrac{1}{I_{zz}}\left(N_{c_m}+U_4\right)\\
\dot{\phi} &= p+\sin(\phi)\tan(\theta)q+\cos(\phi)\tan(\theta)r\\
\dot{\theta} &= \cos(\phi)q-\sin(\phi)r\\
\dot{\psi} &= \tfrac{1}{\cos(\theta)}\left[\sin\phi q+\cos(\phi)r\right]
\end{aligned}
\tag{2.66}
$$

where the pseudo-control vector, $\boldsymbol{U}=[U_1,\,U_2,\,U_3,\,U_4]^T$, is expressed as

$$
\boldsymbol{U}=\begin{bmatrix} b & b & b & b\\ 0 & lb & 0 & -lb\\ -lb & 0 & lb & 0\\ d & -d & d & -d\end{bmatrix}\begin{bmatrix}\omega_1^2\\ \omega_2^2\\ \omega_3^2\\ \omega_4^2\end{bmatrix}
\tag{2.67}
$$

2.3.3 Load Model

The load is a cuboid box of dimension $l_x \times l_y \times l_z$ modeled as a 6 DoF rigid body with, again, the translational dynamics described in $\mathcal{F}_e$ and the rotational dynamics in $\mathcal{F}_{b_l}$. The orientation of the body-fixed frame is shown in Fig. 2.3, where the numbering of cable attachment points for $N = 4$ is also visible.

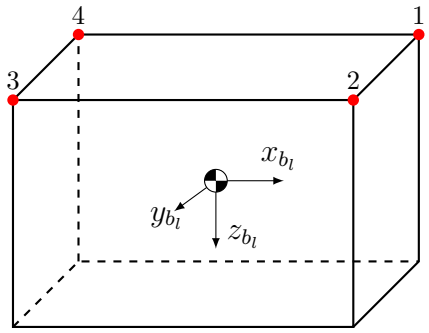

Figure 2.3: Orientation of frame $\mathcal{F}_{b_l}$, and location and numbering of attachment points

The equations of motion of the load read

$$ {}^{e}\ddot{\boldsymbol{p}}_l = {}^{e}\boldsymbol{g} + \frac{1}{m_l}\,{}^{e}\boldsymbol{F}_l \tag{2.68} $$

$$ {}^{b_l}\dot{\boldsymbol{\omega}} = {}^{b_l}\boldsymbol{I}^{-1}\left({}^{b_l}\boldsymbol{G} - {}^{b_l}\boldsymbol{\omega}_l \times {}^{b_l}\boldsymbol{I}\,{}^{b_l}\boldsymbol{\omega}_l\right) \tag{2.69} $$

where ${}^{b_l}\boldsymbol{I} = \mathrm{diag}\{I_{xx_l}, I_{yy_l}, I_{zz_l}\}$ is the inertia tensor assumed to be diagonal in the body reference frame. The same kinematic equation, as in Eq. (2.60), applies to the attitude dynamics of the load. The total external force ${}^{e}\boldsymbol{F}$ and moment ${}^{b}\boldsymbol{G}$ on the load are

$$ {}^{e}\boldsymbol{F}_l = {}^{e}\boldsymbol{F}_{A_l} + {}^{e}\boldsymbol{F}_{c_l} \tag{2.70} $$

$$ {}^{b_l}\boldsymbol{G}_l = {}^{b}\boldsymbol{G}_{c_l} \tag{2.71} $$

where the subscripts have the same meaning as before, and again the aerodynamic moment generated by the drag is disregarded. The aerodynamic force reads, in the body-frame

$$ {}^{b_l}\boldsymbol{F}_{A_l} = -\frac{1}{2}\rho C_{d_l}\begin{bmatrix} S_{x_l}|(u_l - u_W)|(u_l - u_W) \\ S_{y_l}|(v_l - v_W)|(v_l - v_W) \\ S_{z_l}|(w_l - w_W)|(w_l - w_W) \end{bmatrix} \tag{2.72} $$

with C_{d_l} the drag coefficient, and the elements of $\boldsymbol{S}_l = \begin{bmatrix} S_{x_l} & S_{y_l} & S_{z_l} \end{bmatrix}^T$ are the reference areas associated with the three body axes, namely the areas of the faces of the parallelepiped orthogonal to x_l, y_l, and z_l, respectively. The vector $[u_l, v_l, w_l]^T = \mathcal{R}_{be_l}\,{}^{e}\boldsymbol{v}_l$ is the inertial velocity vector in body-axes, and $[u_w, v_w, w_w]^T = \mathcal{R}_{be}\,{}^{e}\boldsymbol{v}_w$ is the instantaneous wind velocity vector in the same frame. The aerodynamic force is written in the inertial frame as ${}^{e}\boldsymbol{F}_{A_l} = \mathcal{R}_{eb_l}\,{}^{b_l}\boldsymbol{F}_{A_l}$. Finally, the constraint force and moment are the elements of vector $\boldsymbol{Q}_{c_{m_l}}$ in

Eq. (2.42). The model reads in scalar form

$$
\begin{aligned}
\ddot{x}_l &= \tfrac{F_{Ax_l}}{m_l} + \tfrac{F_{cx_l}}{m_l} \\
\ddot{y}_l &= \tfrac{F_{Ay_l}}{m_l} + \tfrac{F_{cy_l}}{m_l} \\
\ddot{z}_l &= \tfrac{F_{Az_l}}{m_l} + \tfrac{F_{cz_l}}{m_l} + g \\
\dot{p}_l &= \tfrac{(I_{yy_l} - I_{zz_l})}{I_{xx_l}} q_l r_l + \tfrac{G_{cL_l}}{I_{xx_l}} \\
\dot{q}_l &= \tfrac{(I_{zz_l} - I_{xx_l})}{I_{yy_l}} p_l r_l + \tfrac{G_{cM_l}}{I_{yy_l}} \\
\dot{r}_l &= \tfrac{(I_{xx_l} - I_{yy_l})}{I_{zz_l}} p_l q_l + \tfrac{G_{cN_l}}{I_{zz_l}} \\
\dot{\phi}_l &= p_l + q_l \sin(\phi_l) \tan(\theta_l) + r_l \cos(\phi_l) \tan(\theta_l) \\
\dot{\theta}_l &= q_l \cos(\phi_l) - r_l \sin(\phi_l) \\
\dot{\psi}_l &= q_l \sin(\phi_l) \sec(\theta_l) + r_l \cos(\phi_l) \sec(\theta_l)
\end{aligned}
\tag{2.73}
$$

2.3.4 Cable Model

The translational dynamics of the point mass elements of the i-th cable are written in $\mathcal{F}_e$ for each of the $j = 1, \cdots, P$ masses, distributed such that they form $P + 1$ segments of equal length, as

$$
{}^{e}\ddot{\boldsymbol{p}}_{p_{ij}} = {}^{e}\boldsymbol{g} + \frac{1}{m_{p_{ij}}} {}^{e}\boldsymbol{F}_{A_{m_{ij}}} + \frac{1}{m_{p_{ij}}} {}^{e}\boldsymbol{F}_{c_{m_{ij}}} \tag{2.74}
$$

where ${}^{e}\boldsymbol{F}_{c_{m_{ij}}}$ is a vector element of the generalized constraint force $\boldsymbol{Q}_{c_{m_i}}$ as given in Eq. (2.42), and ${}^{e}\boldsymbol{F}_{A_{m_{ij}}}$ is the aerodynamic drag computed as

$$
{}^{e}\boldsymbol{F}_{A_{m_{ij}}} = -\frac{1}{2}\rho A_s C_{d_s} || \, {}^{e}\dot{\boldsymbol{p}}_{p_{ij}} - \boldsymbol{v}_w || ({}^{e}\dot{\boldsymbol{p}}_{p_{ij}} - {}^{e}\boldsymbol{v}_w) \tag{2.75}
$$

where A_s is the reference area for drag computation, C_{d_s} is the drag coefficient of a sphere, and ${}^e\boldsymbol{v}_w$ is the wind velocity in $\mathcal{F}_E$.

2.4 Differential Geometry

To formulate equations directly on configuration spaces, the notion of calculus, which is well established in $\mathbb{R}^n$ or in open subsets of it, must be extended to manifolds [79]. A fundamental requirement for this extension is that the manifold be smooth, so that smooth functions and derivatives can be consistently defined in a coordinate-independent way. The reminder of this section recalls basic definitions and facts from differential geometry that will be used in the sequel. Further details and references can be found in [79, 80].
The introduction of smooth manifolds rely on the preliminary notions of topological spaces, charts, and atlases.

Definition 1 (Topological space)**.** *A topological space is a pair (M, τ), where M is a set and τ is a collection of subsets of M, called open sets, such that*

1. *both M and the empty set $\varnothing$ are open;*
2. *the union of any collection of open subsets is open;*
3. *the intersection of finitely many open subsets is open.*

A local chart is a homeomorphism from an open subset of the topological space to an open subset of Euclidean space. It provides a local parametrization that allows the identifications of points on the topological space to be represented in $\mathbb{R}^n$.

Definition 2 (Local chart)**.** *A local chart is a pair (U, ϕ) with $U \subset M$ open and $\phi : U \subset M \to V \subset \mathbb{R}^n$ a homeomorphism. Given $p \in U$, the local coordinate of p are defined by $\phi(p) = [x_1(p), x_2(p), \cdots, x_n(p)]^T$.*

A collection of charts that covers the entire space, while satisfying certain overlap conditions, is called atlas. Since the focus here is on smooth manifolds, the notion of a C^∞ atlas is introduced.

Definition 3 (C^∞ atlas)**.** *A C^∞ atlas $A = \{(U_1, \phi_1), (U_2, \phi_2), ...\}$ is a collection of local charts such that if (U_α, ϕ_α) and (U_β, ϕ_β) are local charts with $U_\alpha \cap U_\beta \neq 0$ there exist a*

transition map $\phi_{\beta\alpha} := \phi_\beta \circ \phi_\alpha^{-1}$ *from* $\phi_\alpha(U_\alpha \cap U_\beta) \subset V_\alpha \to \phi_\beta(U_\beta \cap U_\alpha) \subset V_\beta$ *that is* C^∞*. A smooth atlas* A *on* M *is maximal if it is not properly contained in any larger smooth atlas.*

The condition on the overlaps ensures that different coordinate representations describe the same underlying geometric object on M.
Having introduced topological spaces, charts, and atlases, it is now possible to define a smooth manifold.

Definition 4 (Smooth manifold)**.** *A smooth manifold is a Hausdorff, second-countable, topological space* (M, τ) *equipped with a maximal* C^∞ *atlas.*

In Lagrangian mechanics, the state of a system is described by configurations and velocities. Configurations lie on the configuration manifold, while velocities are elements of a separate geometric space, called tangent bundle. The tangent bundle is the set of all tangent vectors at all points of a manifold, and can be interpreted as the space of admissible positions and velocities. In differential geometry, a velocity is not an independent object, but is always defined as a tangent vector at a specific point of the manifold. In Lagrangian mechanics, when the configuration space of a system is a manifold, the equations of motion are formulated on its tangent bundle. The notion of curves on manifolds is now introduced, as it provide the foundation for defining tangent vectors and the tangent bundle.

Definition 5 (Smooth function on a manifold)**.** *A function* $f : (M, A) \to \mathbb{R}$ *is said* C^∞ *if* $f \circ \phi^{-1}$ *is* $C^\infty \; \forall \; (U, \phi) \; \in A$*. The set of all such functions is denoted by* $C^\infty(M)$*.*

The differentiability of a function on a manifold is analyzed by expressing the function in local coordinates, and studying the differentiability of its coordinate representation.

Definition 6 (Tangent vector)**.** *Let* M *be a smooth manifold, and let* p *be a point of* M*. A linear map* $v : C^\infty(M) \to \mathbb{R}$ *is called a derivation at* p *if it satisfies* $v \cdot (fg) = (v \cdot f)g(p) + f(p)(v \cdot g) \quad \forall f, g \in C^\infty(M)$*. The set of all derivations of* $C^\infty(M)$ *at* p*, is denoted by* T_pM*, and is called the tangent space to* M *at* p*. An element of* T_pM *is called a tangent vector at* p*.*

Proposition 1. *Let* M *be a smooth* n*-manifold, and let* $p \in M$*. Then for any smooth chart* $(U, (\phi^i))$ *containing* p*, the coordinate vectors*

$$\left.\frac{\partial}{\partial \phi^1}\right|_p, \ldots, \left.\frac{\partial}{\partial \phi^n}\right|_p \tag{2.76}$$

form a basis for T_pM.

A tangent vector at a point of a smooth curve can be regarded as a derivation on $C^\infty(M)$ that differentiates smooth functions along the curve. In $\mathbb{R}^n$, the velocity of a smooth parametrized curve is given by the derivatives of its component functions, so tangent vectors can naturally be interpreted as velocities of curves.

Proposition 2 (Tangent vectors as velocities of curves)**.** *Let $\gamma : J \subseteq \mathbb{R} \to M$ be a smooth curve with $\gamma(t_0) = p \in M$, and $f \in C^\infty(M)$. Then, $\frac{\partial}{\partial t}\gamma(t)\big|_{t_0} \in T_pM$.*

Definition 7 (Tangent bundle)**.** *Let M be a smooth manifold. The tangent bundle of M*

$$TM = \bigsqcup_{p \in M} T_pM \tag{2.77}$$

is the disjoint union of all tangent spaces. The natural projection is the map $\pi : TM \to M$ defined by $\pi(v_p) = p$, with $v_p \in T_pM$.

For example, the tangent bundle of a sphere is the set of planes tangent to the sphere at each point.
The tangent bundle TM is itself a smooth manifold, and so is possible to define charts on it.

Definition 8 (Trivial tangent bundle)**.** *Let M be a smooth manifold of dimension n. The tangent bundle TM is said to be trivializable if there exists a isomorphism $TM \simeq M \times \mathbb{R}^n$. In this case TM is called a trivial tangent bundle.*

Locally, every tangent bundle is trivializable via a chart ϕ, since $TM|_U \simeq V \times \mathbb{R}^n \simeq U \times \mathbb{R}^n$. However, this local triviality does not in general extend to a global trivialization.
The trivialization of the tangent bundle is important for writing the equations of motion in global coordinates. If TM is trivial, then $TM \simeq M \times \mathbb{R}^n$ and one can introduce global coordinates $(\boldsymbol{q}^i, \boldsymbol{v}^i) \in TM$ that describe positions and velocities on the whole manifold. This allows the equations of motion to be expressed globally in a single coordinate system. If TM is not trivial, only local trivializations exist, and the equations must be written in local coordinates. In this case their intrinsic meaning is guaranteed by the smooth compatibility of the coordinate representations on chart overlaps.
After introducing the configuration manifold, which describes the set of admissible configurations of a mechanical system, and its tangent bundle, which represents configurations

together with velocities, the next step in formulating the equations of motion is to describe the system dynamics. This means specifying how states evolve in time. Given a point $(\boldsymbol{q}, \boldsymbol{v}) \in TM$, the equations of motion determine the instantaneous rate of change of this state. Geometrically, this corresponds to assigning to each state $(\boldsymbol{q}, \boldsymbol{v}) \in TM$ a tangent vector in $T_{(\boldsymbol{q},\boldsymbol{v})}TM$.
Since TM is itself a smooth manifold, the general notions introduced for manifolds apply to it as well.

Definition 9 (Vector field)**.** *A vector field on a manifold M is defined as a map $X : M \to TM$ such that $X(p) = X_p \in T_pM$ for each $p \in M$. A C^∞ vector field is such that $X \in C^\infty$.*

For example, in $\mathbb{R}^n$, a vector field is expressed in coordinates as

$$X_x = v_1(x)\frac{\partial}{\partial x_1}\Big|_x + v_2(x)\frac{\partial}{\partial x_2}\Big|_x + \cdots + v_n(x)\frac{\partial}{\partial x_n}\Big|_x,$$

where the coefficients $v_j : \mathbb{R}^n \to \mathbb{R}$ are smooth functions. The vector bundle $X(M)$ is the set of all vector fields in M, and is defined as

$$X(M) := \{X : M \to TM | X_x \in T_xM \quad \forall x \in M\} \tag{2.78}$$

Vector fields can also be regarded as derivations of $C^\infty(M)$. In particular, $X \in Der(C^\infty(M))$ if $X : C^\infty(M) \to C^\infty(M)$ s.t., for $f, g \in C^\infty$,

1. $X(\lambda f + \mu g) = \lambda Xf + \mu Xg$
2. $X(fg) = (Xf)g + f(Xg)$

Vector fields are closed under addition, multiplication by smooth functions, and the Lie bracket, also called matrix commutator ($[\cdot, \cdot]$). In particular, let $V_1, V_2 \in \mathrm{Der}(\mathcal{C}^\infty(M))$, and $\phi \in \mathcal{C}^\infty(M)$, then

1. $V_1 + V_2 : \mathcal{C}^\infty(M) \to \mathcal{C}^\infty(M)$ s.t. $(V_1 + V_2)f = V_1 f + V_2 f$.
2. $\phi X : \mathcal{C}^\infty(M) \to \mathcal{C}^\infty(M)$ s.t. $(\phi X)f = \phi(Xf)$
3. $[X_1, X_2] : \mathcal{C}^\infty(M) \to \mathcal{C}^\infty(M)$ s.t. $[X_1, X_2]f = X_1(X_2 f) - X_2(X_1 f)$

The Lie bracket satisfies the following identities

1. Bilinearity:

$$[\lambda_1 X_1 + \lambda_2 X_2, Y] = \lambda_1 [X_1, Y] + \lambda_2 [X_2, Y]$$
$$[X, \mu_1 Y_1 + \mu_2 Y_2] = \mu_1 [X, Y_1] + \mu_2 [X, Y_2]$$

2. Antisymmetry:

$$[X, Y] = -[Y, X]$$

3. Jacobi identity:

$$[X, [Y, Z]] = [[X, Y], Z] + [Y, [X, Z]]$$

2.4.1 Special Orthogonal Group $SO(3)$

The special orthogonal group $SO(3)$ is a Lie group, in the sequel referred to as G, that is, a smooth manifold endowed with a group structure for which both multiplication and inversion are smooth maps [79, 80]. In this case, the underlying manifold is the set of 3×3 orthogonal matrices with determinant one, and the group operation is matrix multiplication.
The tangent space of a Lie group G at the identity element $\boldsymbol{e} \in G$ is called the Lie algebra and is denoted by $\mathfrak{g} := T_e G$. For Lie groups, $\mathfrak{g}$ can be naturally identified with the set of left-invariant vector fields on G, equipped with the Lie bracket $[\cdot, \cdot] : \mathfrak{g} \times \mathfrak{g} \to \mathfrak{g}$.
To formalize this, consider the left and right translation maps, defined for $\boldsymbol{g}, \boldsymbol{h} \in G$ as

$$\boldsymbol{L}_h : G \to G, \quad \boldsymbol{L}_h(\boldsymbol{g}) = \boldsymbol{h}\boldsymbol{g}, \qquad \boldsymbol{R}_h : G \to G, \quad \boldsymbol{R}_h(\boldsymbol{g}) = \boldsymbol{g}\boldsymbol{h} \tag{2.79}$$

Given $\boldsymbol{\xi} \in \mathfrak{g}$, the associated left-invariant vector field is defined as

$$\boldsymbol{X}_\xi : G \to TG \quad \boldsymbol{X}_\xi(\boldsymbol{g}) = \boldsymbol{T}_e \boldsymbol{L}_g \cdot \boldsymbol{\xi} \tag{2.80}$$

where $\boldsymbol{T}_e \boldsymbol{L}_g : T_e G \to T_g G$. By construction, $\boldsymbol{X}_\xi$ is left-invariant, since

$$\boldsymbol{T}_g \boldsymbol{L}_h \cdot \boldsymbol{X}_\xi(\boldsymbol{g}) = (\boldsymbol{T}_g \boldsymbol{L}_h \cdot \boldsymbol{T}_e \boldsymbol{L}_G) \cdot \boldsymbol{\xi} = (\boldsymbol{T}_e \boldsymbol{L}_{hg}) \cdot \boldsymbol{\xi} = \boldsymbol{X}_\xi(\boldsymbol{h}\boldsymbol{g}) \tag{2.81}$$

The introduction of left translation map is crucial because it provides a canonical way to transport tangent vectors from the identity to any point of the group. In particular, the differential $\boldsymbol{T}_e\boldsymbol{L}_g : T_eG \to T_gG$ allows elements of the Lie algebra $\mathfrak{g}$ to be extended uniquely to left-invariant vector fields on the whole group. This establishes a fundamental link between the local structure encoded in the Lie algebra and the global geometry of the Lie group.
An important consequence is that the tangent bundle TG can be identified with $G \times \mathfrak{g}$ through left trivialization.
In this context, identification means providing an isomorphism of smooth bundles, i.e., a bijective correspondence between the two spaces that is smooth and has a smooth inverse. For convenience, the bijection is first given in the reverse direction, namely from $G \times \mathfrak{g}$ to TG

$$G \times \mathfrak{g} \to TG \tag{2.82}$$

Given $\boldsymbol{g} \in G$ and $\boldsymbol{\xi} \in \mathfrak{g}$, the corresponding tangent vector at $\boldsymbol{g}$ is obtained by transporting $\boldsymbol{\xi}$ from the identity to $\boldsymbol{g}$ through left multiplication

$$(\boldsymbol{g}, \boldsymbol{\xi}) \mapsto (\boldsymbol{T}_e\boldsymbol{L}_g) \cdot \boldsymbol{\xi} = \boldsymbol{g}\boldsymbol{\xi} = \dot{\boldsymbol{g}} \tag{2.83}$$

where $\boldsymbol{T}_e\boldsymbol{L}_g$ is the differential. It can be shown that this map is an isomorphism, in fact, it is possible to evaluate the inverse as

$$TG \to G \times \mathfrak{g} \tag{2.84}$$

An element of TG is a tangent vector at some point of the group. Thus, if $\dot{\boldsymbol{g}} \in T_gG$ is a tangent vector at G in $\boldsymbol{g}$, is possible to associate to it the pair $(\boldsymbol{g}, \boldsymbol{T}_g\boldsymbol{L}_{g^{-1}} \cdot \dot{\boldsymbol{g}})$, where the second component belongs to the Lie algebra

$$\dot{\boldsymbol{g}} \in T_gG \mapsto (\boldsymbol{g}, \boldsymbol{T}_g\boldsymbol{L}_{g^{-1}} \cdot \dot{\boldsymbol{g}}) \tag{2.85}$$

For $SO(3)$, this identification reads

$$(\mathcal{R}, \dot{\mathcal{R}}) = \boldsymbol{T}_e\boldsymbol{L}_{\mathcal{R}}(\boldsymbol{\xi}) = \mathcal{R}\boldsymbol{\xi} \tag{2.86}$$

for $\boldsymbol{\xi} \in \mathfrak{so}(3)$, where $\mathfrak{so}(3)$ is the Lie algebra of $SO(3)$, consisting of all skew-symmetric 3×3 matrices. There exists an isomorphism between $\mathfrak{so}(3)$ and $\mathbb{R}^3$, given by the hat map

$$^\wedge : \mathbb{R}^3 \to \mathfrak{so}(3), \qquad \boldsymbol{\omega} \mapsto \hat{\boldsymbol{\omega}} \tag{2.87}$$

Therefore, any element $\boldsymbol{\xi} \in \mathfrak{so}(3)$ can be uniquely represented as $\boldsymbol{\xi} = \hat{\boldsymbol{\omega}}$ for some $\boldsymbol{\omega} \in \mathbb{R}^3$. The vector $\boldsymbol{\omega}$ is called the angular velocity of the rigid body, expressed in the body-fixed frame. Hence, the tangent bundle $TSO(3)$ is identified with $TSO(3) \simeq SO(3) \times \mathfrak{so}(3) \simeq SO(3) \times \mathbb{R}^3$. The kinematic equation for the rotation matrix is thus written as

$$\dot{\mathcal{R}} = \mathcal{R}\hat{\boldsymbol{\omega}} \tag{2.88}$$

There exists a local diffeomorphism from a neighborhood of zero in $\mathfrak{g}$ onto a neighborhood of $\boldsymbol{e}$ in G, called the exponential map $\exp : \mathfrak{g} \to G$, defined as

$$\exp(\boldsymbol{\xi}) = \boldsymbol{\gamma}_\xi(1) \tag{2.89}$$

where $\boldsymbol{\gamma}_\xi$ is the integral curve of the left-invariant vector field $\boldsymbol{X}_\xi$ defined as

$$\begin{cases} \dot{\boldsymbol{\gamma}}_\xi(t) = \boldsymbol{X}_\xi(\boldsymbol{\gamma}_\xi(t)) \\ \boldsymbol{\gamma}_\xi(0) = \boldsymbol{e} \end{cases} \tag{2.90}$$

In the case of the Lie group $SO(3)$, the exponential map goes from $\mathfrak{so}(3)$ to $SO(3)$, that is, it establishes a relation between skew-symmetric matrices and orthogonal matrices, in the sense that an orthogonal matrix can be expressed in terms of a skew-symmetric matrix. In particular, for every orthogonal matrix there exists a skew-symmetric matrix such that the orthogonal matrix is written as

$$\mathcal{R} = e^{\boldsymbol{\xi}} = \sum_{n=0}^{\infty} \frac{\boldsymbol{\xi}^n}{n!} \tag{2.91}$$

The exponential map plays a central role in the definition of variations of functions with values in a Lie group. Let $\boldsymbol{g} : [t_0, t_f] \to G$ be a smooth curve on a Lie group G. A variation of $\boldsymbol{g}$ is defined by a smooth map $\boldsymbol{g}^\epsilon(t) : (-c, c) \times [t_0, t_f] \to G$, such that $\boldsymbol{g}^0(t) = \boldsymbol{g}(t)$, and

$\boldsymbol{g}^{\epsilon}(t_0) = \boldsymbol{g}(t_0)$, $\boldsymbol{g}^{\epsilon}(t_f) = \boldsymbol{g}(t_f)$ $\forall \epsilon$. The infinitesimal variation of $\boldsymbol{g}$ is defined as

$$\delta \boldsymbol{g}(t) = \left. \frac{d}{d\varepsilon} \right|_{\varepsilon=0} \boldsymbol{g}^{\varepsilon}(t) \ \in \ T_{g(t)}G \tag{2.92}$$

A convenient way to parametrize variations on a Lie group is through the exponential map. Variations are introduced in the Lie algebra $\mathfrak{g}$, which is a linear vector space. These infinitesimal perturbations are then transported to a generic point of the group by means of the exponential map, ensuring that the perturbed curves remain in the Lie group. This construction is the analogue of writing $\boldsymbol{g}^{\varepsilon}(t) = \boldsymbol{g}(t) + \varepsilon \boldsymbol{h}(t)$ in $\mathbb{R}^n$. Specifically, given a smooth curve $\boldsymbol{\eta} : [t_0, t_f] \to \mathfrak{g}$, with $\boldsymbol{\eta}(t_0) = \boldsymbol{\eta}(t_f) = 0$, a variation of $\boldsymbol{g}$ is defined as

$$\boldsymbol{g}^{\epsilon}(t) = \boldsymbol{g}(t) \, \exp\big(\varepsilon \, \hat{\boldsymbol{\eta}}(t)\big) \tag{2.93}$$

and the corresponding infinitesimal variation is given by

$$\delta \boldsymbol{g}(t) = \left. \frac{d}{d\varepsilon} \right|_{\varepsilon=0} \boldsymbol{g}^{\varepsilon}(t) = \left. \frac{d}{d\varepsilon} \right|_{\varepsilon=0} \big(\boldsymbol{g}(t) \exp(\varepsilon \hat{\boldsymbol{\eta}}(t))\big) \tag{2.94}$$

$$= \boldsymbol{T}_e \boldsymbol{L}_{g(t)} \left(\left. \frac{d}{d\varepsilon} \right|_{\varepsilon=0} \exp(\varepsilon \hat{\boldsymbol{\eta}}(t)) \right) \tag{2.95}$$

$$= \boldsymbol{T}_e \boldsymbol{L}_{g(t)} \big(\hat{\boldsymbol{\eta}}(t)\big) = \boldsymbol{g}(t) \hat{\boldsymbol{\eta}}(t) \tag{2.96}$$

In the case of the Lie group $SO(3)$ this leads to

$$\delta \mathcal{R} = \mathcal{R} \hat{\boldsymbol{\eta}} \tag{2.97}$$

with $\boldsymbol{\eta} \in \mathbb{R}^3$. The variation of the angular velocity $\boldsymbol{\omega}$ is obtained by substituting Eq. (2.97) into Eq. (2.88)

$$\mathcal{R} \hat{\boldsymbol{\omega}} \hat{\boldsymbol{\eta}} + \mathcal{R} \dot{\hat{\boldsymbol{\eta}}} = \mathcal{R} \hat{\boldsymbol{\eta}} \hat{\boldsymbol{\omega}} + \mathcal{R} \delta \hat{\boldsymbol{\omega}} \tag{2.98}$$

using the property of the hat map in App. B.1 it follows

$$\delta \boldsymbol{\omega} = \dot{\boldsymbol{\eta}} + \boldsymbol{\omega} \times \boldsymbol{\eta} \tag{2.99}$$

which represent the infinitesimal variation of the angular velocity.

In order to control a system evolving on a configuration manifold, it is necessary to introduce the configuration errors. Given a desired attitude $\mathcal{R}_d \in SO(3)$, the scalar configuration error on $SO(3) \times SO(3)$ is defined as [80]

$$\Psi(\mathcal{R}, \mathcal{R}_d) = \tfrac{1}{2} \operatorname{tr}[\mathcal{I} - \mathcal{R}_d^T \mathcal{R}] \tag{2.100}$$

where the matrix $\mathcal{R}_d^T \mathcal{R} \in SO(3)$ represents the relative rotation that maps the desired frame into the current one.
Using the axis-angle representation $\mathcal{R}_d^T \mathcal{R} = \exp(\theta\, \hat{\boldsymbol{u}})$, with rotation angle $\theta \in [0, \pi]$ and unit axis $\hat{\boldsymbol{u}} \in S^2$, the relation $\operatorname{tr}(\mathcal{R}_d^T \mathcal{R}) = 1 + 2\cos\theta$ yields

$$\Psi(\mathcal{R}, \mathcal{R}_d) = 1 - \cos\theta \tag{2.101}$$

Thus, Ψ is positive definite about the desired attitude

$$\Psi(\mathcal{R}, \mathcal{R}_d) \geqslant 0, \qquad \Psi(\mathcal{R}, \mathcal{R}_d) = 0 \text{ iff } \mathcal{R} = \mathcal{R}_d \tag{2.102}$$

Its value increases monotonically with the rotation angle θ and reaches a maximum of $\Psi = 2$ when the current and desired attitudes differ by 180° ($\theta = \pi$). At this configuration, the gradient of Ψ vanishes, corresponding to a critical point of the error function; therefore, the configuration associated with $\Psi = 2$ ($\theta = \pi$) is excluded from the region of interest.
The attitude error vector is then obtained as the gradient of the scalar error function with respect to variations on SO(3) [81], that is

$$\frac{\partial \Psi}{\partial \mathcal{R}} \cdot \delta\mathcal{R} = -\frac{1}{2} \operatorname{tr}[\mathcal{R}_d^T \mathcal{R} \hat{\boldsymbol{\eta}}] = \frac{1}{2} \operatorname{tr}[\mathcal{R}_d^T \mathcal{R} - \mathcal{R}^T \mathcal{R}_d]^\vee \cdot \boldsymbol{\eta} \tag{2.103}$$

where the hat properties in App. (B.7) are used. Thus

$$\boldsymbol{e}_{\mathcal{R}} = \frac{1}{2} \operatorname{tr}[\mathcal{R}_d^T \mathcal{R} - \mathcal{R}^T \mathcal{R}_d]^\vee \tag{2.104}$$

In addition to the attitude error, it is necessary to define the angular velocity error. The actual angular velocity ${}^b\boldsymbol{\omega} \in \mathbb{R}^3$ is expressed in the current body frame, while the desired angular velocity ${}^{b_d}\boldsymbol{\omega}_d \in \mathbb{R}^3$ is expressed in the desired body frame. In order to compare them, both vectors must be represented in the same frame. The relative rotation $\boldsymbol{E} = \mathcal{R}^T \mathcal{R}_d \in$

$SO(3)$ maps vectors from the desired body frame to the current one, and the angular velocity error is therefore defined as

$$\boldsymbol{e}_\omega = {}^b\boldsymbol{\omega} - \mathcal{R}^T\mathcal{R}_d\ {}^{b_d}\boldsymbol{\omega}_d \tag{2.105}$$

2.4.2 Two-Sphere S^2

The two-sphere S^2 is a smooth manifold but not a Lie group, and its tangent bundle is not globally trivializable. Nevertheless, the dynamics in S^2 admits a global description thanks to its homogeneous structure. In fact, the rotation group $SO(3)$ acts transitively on S^2, that is, for any $\boldsymbol{n}_1, \boldsymbol{n}_2 \in S^2$ there exists $\mathcal{R} \in SO(3)$ such that $\boldsymbol{n}_2 = \mathcal{R}\boldsymbol{n}_1$. This symmetry implies that all points of the sphere are geometrically equivalent, which allows the construction of global equations. Since $\boldsymbol{n} \in S^2$ is constrained to remain on the sphere, its velocity $\dot{\boldsymbol{n}}$ must be orthogonal to $\boldsymbol{n}$, and thus lie in the plane tangent to the sphere at $\boldsymbol{n}$. The tangent space of S^2 at $\boldsymbol{n}$ is therefore defined as $T_nS^2 = \{\boldsymbol{\xi} \in \mathbb{R}^3 \mid \boldsymbol{n} \cdot \boldsymbol{\xi} = 0\}$. Every tangent vector at $\boldsymbol{n}$ can be thus expressed as the cross product between $\boldsymbol{n}$ and some vector $\boldsymbol{\omega} \in \mathbb{R}^3$. This leads to the kinematic equation

$$\dot{\boldsymbol{n}} = \boldsymbol{\omega} \times \boldsymbol{n} \tag{2.106}$$

where $\boldsymbol{\omega}$ can be interpreted as an angular velocity vector satisfying $\boldsymbol{n} \cdot \boldsymbol{\omega} = 0$. In addition, the time derivative of the angular velocity satisfies $\boldsymbol{n} \cdot \dot{\boldsymbol{\omega}} = 0$.

Let $\boldsymbol{n} : [t_0, t_f] \to S^2$ be a smooth curve in S^2. The variation of $\boldsymbol{n}$ is a smooth map $\boldsymbol{n}^\epsilon(t) : (-c, c) \times [t_0, t_f] \to S^2$ for $c > 0$, such that $\boldsymbol{n}^0(t) = \boldsymbol{n}(t)$, and $\boldsymbol{n}^\epsilon(t_0) = \boldsymbol{n}_i(t_0)$, $\boldsymbol{n}_i^\epsilon(t_f) = \boldsymbol{n}_i(t_f)\ \forall \epsilon \in (-c, c)$. Since the special orthogonal group $SO(3)$ acts transitively on S^2, the variation of $\boldsymbol{n}(t)$ can be expressed using the exponential map on $SO(3)$. In fact, every tangent vector on the two-sphere can be identified with the infinitesimal action of an element of the Lie algebra $\mathfrak{so}(3)$; that is, each tangent variation on S^2 arises from an infinitesimal rotation in $SO(3)$. Specifically, given a smooth curve $\boldsymbol{\eta} : [t_0, t_f] \to \mathfrak{so}(3)$, with $\boldsymbol{\eta}(t_0) = \boldsymbol{\eta}(t_f) = 0$, a variation of $\boldsymbol{n}$ is defined as

$$\boldsymbol{n}^\epsilon(t) = \exp\big(\epsilon\boldsymbol{\eta}(t)\big)\boldsymbol{n}(t) \tag{2.107}$$

The corresponding infinitesimal variation is given by

$$\delta \boldsymbol{n}(t) = \left. \frac{d}{d\epsilon} \right|_{\epsilon=0} \boldsymbol{n}^{\epsilon}(t) = \boldsymbol{\eta}(t)\boldsymbol{n}(t) \tag{2.108}$$

which can be rewritten as

$$\delta \boldsymbol{n}(t) = \hat{\boldsymbol{\xi}}(t)\boldsymbol{n}(t) \tag{2.109}$$

for $\boldsymbol{\xi} \in \mathbb{R}^3$. Since the variation and the differentiation commute, the expression for the infinitesimal variation of $\dot{\boldsymbol{n}}(t)$ is

$$\delta \dot{\boldsymbol{n}}(t) = \dot{\hat{\boldsymbol{\xi}}}(t)\boldsymbol{n}(t) + \hat{\boldsymbol{\xi}}(t)\dot{\boldsymbol{n}}(t) \tag{2.110}$$

On S^2, a suitable scalar error function can be defined as [82]

$$\Psi(\boldsymbol{n}, \boldsymbol{n}_d) = 1 - \boldsymbol{n} \cdot \boldsymbol{n}_d, \tag{2.111}$$

which is nonnegative and vanishes if and only if $\boldsymbol{n} = \boldsymbol{n}_d$. As in the case of $SO(3)$, the error vector is obtained as the gradient of the scalar error function with respect to admissible variations on S^2 [82]

$$\frac{\partial \Psi}{\partial \boldsymbol{n}} \cdot \delta \boldsymbol{n} = -(\boldsymbol{\xi} \times \boldsymbol{n}) \cdot \boldsymbol{n}_d = (\boldsymbol{n}_d \times \boldsymbol{n}) \cdot \boldsymbol{\xi}. \tag{2.112}$$

It follows that the configuration error vector on S^2 is defined as

$$\boldsymbol{e}_n = \boldsymbol{n}_d \times \boldsymbol{n} \tag{2.113}$$

Finally the angular velocity error is defined. Since $\boldsymbol{\omega}$ generates a tangent vector in $T_n S^2$ while $\boldsymbol{\omega}_d$ generates one in $T_{n_d} S^2$, the desired angular velocity must be projected onto the tangent space at $\boldsymbol{n}$ in order to be comparable with $\boldsymbol{\omega}$. Using the projection operator $P(\boldsymbol{n}) = \mathcal{I} - \boldsymbol{n}\boldsymbol{n}^T$ [83], the angular velocity error on S^2 is defined as

$$\boldsymbol{e}_\omega = \boldsymbol{\omega} - (\mathcal{I} - \boldsymbol{n}\boldsymbol{n}^T)\,\boldsymbol{\omega}_d \tag{2.114}$$

2.5 Lagrangian Dynamics on Manifold

Once the configuration manifold and its tangent bundle are defined, together with the associated kinematic relations and geometric properties, the Euler–Lagrange equations of motion for the constrained multi-body system are derived following the coordinate-free approach of [84]. Unlike previous formulations [73], the model is extended to account for the offset between the cable attachment point and the c.g. of the quadrotor [40], and to incorporate aerodynamic drag forces acting on the payload, the vehicles, and the intermediate masses.
Instead of introducing explicit algebraic constraints for the positions of the attachment points and the particles along the cables, as in the Udwadia-Kalaba formulation, the constrained motion is modeled directly on the product of two-sphere manifolds $(S^2)^P$. Consequently, the direction of the j-th link of the i-th cable, pointing downward, is defined by the unit vector $\boldsymbol{n}_{ij} \in S^2$.
In the following, a notation consistent with that of [84] is intentionally adopted, since the developments in this section build directly upon the theoretical framework reported in that book. This choice facilitates the understanding of the present work and allows readers to easily refer to their extensive literature for further details and background.
The position of the i-the quadrotor c.g. is related to the load position and attitude, and to the links direction through

$$ {}^{e}\boldsymbol{p}_i = {}^{e}\boldsymbol{p}_l + \mathcal{R}_{eb_l}\, {}^{b_l}\boldsymbol{r}_{l_i} - \sum_{j=1}^{P} l_{ij}\boldsymbol{n}_{ij} - \mathcal{R}_{eb_i}\, {}^{b_i}\boldsymbol{r}_i \tag{2.115} $$

where ${}^{b_l}\boldsymbol{r}_{l_i}$, and ${}^{b_i}\boldsymbol{r}_i$ are the offset vectors, expressed in the body frame, of the cables attachment points from the payload and quadrotors c.g., respectively. The configuration space M of the system is given in Eq. (2.1). The system has $6 + 3N + 2NP$ degrees of freedom, 6 for the rigid-body payload (3 for the position of its c.g., and 3 for its attitude), 3 for the attitude of each quadrotor, and 2 for the attitude of each cable link.
The equations of motion are obtained through the Lagrange-d'Alembert principle [84], which states that the variation of the action integral must equal the negative of the virtual work of the external forces and moments, for any admissible variation with fixed endpoints

$$ \delta\mathcal{B} = -\delta W \tag{2.116} $$

The action integral is defined as the time integral of the Lagrangian along the system trajectory [31], $\mathcal{B} = \int_{t_0}^{t_f} \mathcal{L} dt$. The Lagrangian is a real-valued function defined on the tangent bundle TM of the configuration manifold M, $\mathcal{L} : TM \to \mathbb{R}$. The tangent bundle associated with the configuration manifold M is

$$TM \simeq (SO(3) \times \mathbb{R}^3 \times \mathbb{R}^3 \times \mathbb{R}^3) \times (SO(3) \times \mathbb{R}^3)^N \times (S^2 \times TS^2)^{NP} \tag{2.117}$$

where the identification $TSO(3) \simeq SO(3) \times \mathfrak{so}(3) \simeq SO(3) \times \mathbb{R}^3$ is used as discussed in Sec. 2.4. The Lagrangian is defined as $\mathcal{L} = \mathcal{K} - \mathcal{U}$, where $\mathcal{K}$ and $\mathcal{U}$ denote, respectively, the total kinetic and potential energy of the system. The explicit expression is reported in Appendix B.2.

The variation of the action integral is expressed in terms of the configuration variables as

$$\begin{aligned}\delta\mathcal{B} = \int_{t_0}^{t_f} \Big(&\frac{\partial \mathcal{L}}{\partial\, {}^{e}\boldsymbol{p}_l} \cdot \delta\, {}^{e}\boldsymbol{p}_l + \frac{\partial \mathcal{L}}{\partial\, {}^{e}\dot{\boldsymbol{p}}_l} \cdot \delta\, {}^{e}\dot{\boldsymbol{p}}_l + \sum_{i=1}^{N} \sum_{j=1}^{P-1} \frac{\partial \mathcal{L}}{\partial \boldsymbol{n}_{ij}} \cdot \delta \boldsymbol{n}_{ij} + \sum_{i=1}^{N} \sum_{j=1}^{P-1} \frac{\partial \mathcal{L}}{\partial \dot{\boldsymbol{n}}_{ij}} \cdot \delta \dot{\boldsymbol{n}}_{ij} \\ &+ \frac{\partial \mathcal{L}}{\partial \mathcal{R}_{eb_l}} \cdot \delta \mathcal{R}_{eb_l} + \frac{\partial \mathcal{L}}{\partial\, {}^{b_l}\boldsymbol{\omega}_l} \cdot \delta\, {}^{b_l}\boldsymbol{\omega}_l + \sum_{i=1}^{N} \frac{\partial \mathcal{L}}{\partial \mathcal{R}_{eb_i}} \cdot \delta \mathcal{R}_{eb_i} + \frac{\partial \mathcal{L}}{\partial\, {}^{b_i}\boldsymbol{\omega}_i} \cdot \delta\, {}^{b_i}\boldsymbol{\omega}_i \Big) dt\end{aligned} \tag{2.118}$$

By substituting the expressions for the variations on S^2 and $SO(3)$ defined in Eqs. (2.97) and (2.109), and applying the mixed product identity $\boldsymbol{a} \cdot (\boldsymbol{b} \times \boldsymbol{c}) = -(\boldsymbol{b} \times \boldsymbol{a}) \cdot \boldsymbol{c} = (\boldsymbol{c} \times \boldsymbol{a}) \cdot \boldsymbol{b}$, with $\boldsymbol{a}, \boldsymbol{b}, \boldsymbol{c} \in \mathbb{R}^n$, it follows that

$$\frac{\partial \mathcal{L}}{\partial \boldsymbol{n}_{ij}} \cdot \delta \boldsymbol{n}_{ij} = \frac{\partial \mathcal{L}}{\partial \boldsymbol{n}_{ij}} \cdot (\boldsymbol{\xi}_{ij} \times \boldsymbol{n}_{ij}) = \boldsymbol{n}_{ij} \times \frac{\partial \mathcal{L}}{\partial \boldsymbol{n}_{ij}} \cdot \boldsymbol{\xi}_{ij} \tag{2.119}$$

$$\frac{\partial \mathcal{L}}{\partial\, {}^{b_l}\boldsymbol{\omega}_l} \cdot \delta\, {}^{b_l}\boldsymbol{\omega}_l = \frac{\partial \mathcal{L}}{\partial\, {}^{b_l}\boldsymbol{\omega}_l} \cdot (\dot{\boldsymbol{\eta}}_l + {}^{b_l}\boldsymbol{\omega}_l \times \boldsymbol{\eta}_l) = \frac{\partial \mathcal{L}}{\partial\, {}^{b_l}\boldsymbol{\omega}_l} \cdot \dot{\boldsymbol{\eta}}_l - {}^{b_l}\hat{\boldsymbol{\omega}}_l \frac{\partial \mathcal{L}}{\partial\, {}^{b_l}\boldsymbol{\omega}_l} \cdot \boldsymbol{\eta}_l \tag{2.120}$$

Furthermore, the terms involving the attitude variations can be expressed as an inner product with the variation parameter $\boldsymbol{\eta} \in \mathbb{R}^3$ as

$$\frac{\partial \mathcal{L}}{\partial \mathcal{R}} \cdot \delta \mathcal{R} = \frac{\partial \mathcal{L}}{\partial \mathcal{R}} \cdot \mathcal{R}\hat{\boldsymbol{\eta}} = \nabla_L \mathcal{L}(\mathcal{R}) \cdot \boldsymbol{\eta}, \tag{2.121}$$

where $\nabla_L \mathcal{L}(\mathcal{R}) \in \mathbb{R}^3$ denotes the left-trivialized derivative of $\mathcal{L}$ at $\mathcal{R}$ [84], defined in Eq. (B.18) of Appendix B.3.

Applying the integration by parts rule to Eq. (2.118)

$$\int_{t_0}^{t_f} f(t)\cdot\dot{g}(t)dt = \Big[f(t)\cdot g(t)\Big]_{t_0}^{t_f} - \int_{t_0}^{t_f}\dot{f}(t)\cdot g(t)dt \tag{2.122}$$

and recalling that the variations vanish at the integration boundaries by definition, it follows that

$$\begin{aligned}\delta\mathcal{B} = \int_{t_0}^{t_f}\Big[&\Big(\frac{\partial\mathcal{L}}{\partial\,{}^{e}\boldsymbol{p}_l} - \frac{d}{dt}\Big(\frac{\partial\mathcal{L}}{\partial\,{}^{e}\dot{\boldsymbol{p}}_l}\Big)\Big)\cdot\delta\,{}^{e}\boldsymbol{p}_l\\ &+\sum_{i=1}^{N}\sum_{j=1}^{P-1}\hat{\boldsymbol{n}}_{ij}\Big(\frac{\partial\mathcal{L}}{\partial\boldsymbol{n}_{ij}} - \frac{d}{dt}\Big(\frac{\partial\mathcal{L}}{\partial\dot{\boldsymbol{n}}_{ij}}\Big)\Big)\cdot\boldsymbol{\xi}_{ij}\\ &+\nabla_L\mathcal{L}(\mathcal{R}_{eb_l})\cdot\boldsymbol{\eta}_l - \frac{d}{dt}\Big(\frac{\partial\mathcal{L}}{\partial\,{}^{b_l}\boldsymbol{\omega}_l}\Big)\cdot\boldsymbol{\eta}_l - {}^{b_l}\hat{\boldsymbol{\omega}}_l\frac{\partial\mathcal{L}}{\partial\,{}^{b_l}\boldsymbol{\omega}_l}\cdot\boldsymbol{\eta}_l\\ &+\sum_{i=1}^{N}\nabla_L\mathcal{L}(\mathcal{R}_{eb_i})\cdot\boldsymbol{\eta}_i - \frac{d}{dt}\Big(\frac{\partial\mathcal{L}}{\partial\,{}^{b_i}\boldsymbol{\omega}_i}\Big)\cdot\boldsymbol{\eta}_i - {}^{b_i}\hat{\boldsymbol{\omega}}_i\frac{\partial\mathcal{L}}{\partial\,{}^{b_i}\boldsymbol{\omega}_i}\cdot\boldsymbol{\eta}_i\Big]dt\end{aligned} \tag{2.123}$$

The virtual work associated with external forces and moments is

$$\delta W = \int_{t_0}^{t_f}\sum_{i=1}^{N}\sum_{j=1}^{P-1}\Big[({}^{e}\boldsymbol{F}_{T_i} + {}^{e}\boldsymbol{F}_{A_i})\cdot\delta({}^{e}\boldsymbol{p}_i) + {}^{e}\boldsymbol{F}_{A_{m_{ij}}}\cdot\delta({}^{e}\boldsymbol{p}_{ij}) + {}^{e}\boldsymbol{F}_{A_l}\cdot\delta({}^{e}\boldsymbol{p}_l) + {}^{b}\boldsymbol{G}_{T_i}\cdot\boldsymbol{\eta}_i\Big] \tag{2.124}$$

Substituting the expression of ${}^{e}\boldsymbol{p}_i$, and ${}^{e}\boldsymbol{p}_{p_{ij}}$ in terms of the configuration variables gives

$$\begin{aligned}\delta W = \int_{t_0}^{t_f}\sum_{i}^{N}\sum_{j=1}^{P-1}\Big[&({}^{e}\boldsymbol{F}_{T_i} + {}^{e}\boldsymbol{F}_{A_i})\cdot\delta({}^{e}\boldsymbol{p}_l + \mathcal{R}_{eb_l}\,{}^{b_l}\boldsymbol{r}_{l_i} - \sum_{a=1}^{P} l_{ia}\boldsymbol{n}_{ia} - \mathcal{R}_{eb_i}\,{}^{b_i}\boldsymbol{r}_i)\\ &+ {}^{e}\boldsymbol{F}_{A_{m_{ij}}}\cdot\delta({}^{e}\boldsymbol{p}_l + \mathcal{R}_{eb_l}\,{}^{b_l}\boldsymbol{r}_{l_i} - \sum_{a=1}^{j} l_{ia}\boldsymbol{n}_{ia})\\ &+ {}^{e}\boldsymbol{F}_{A_l}\cdot\delta({}^{e}\boldsymbol{p}_l) + {}^{b}\boldsymbol{G}_{T_i}\cdot\boldsymbol{\eta}_i\Big]\end{aligned} \tag{2.125}$$

The operator δ is linear with respect to addition and satisfies the product rules for the dot and cross products as well as for matrix–vector and matrix–matrix multiplications. It follows

that

$$\begin{aligned}\delta W = \int_{t_0}^{t_f} \sum_{i}^{N} \sum_{j=1}^{P-1} \Big[&({}^{e}\boldsymbol{F}_{T_i} + {}^{e}\boldsymbol{F}_{A_i}) \cdot \delta({}^{e}\boldsymbol{p}_l) + {}^{e}\boldsymbol{F}_{A_{m_{ij}}} \cdot \delta({}^{e}\boldsymbol{p}_l) + {}^{e}\boldsymbol{F}_{A_l} \cdot \delta({}^{e}\boldsymbol{p}_l) \\ &- \sum_{a=1}^{P} \hat{\boldsymbol{n}}_{ia}({}^{e}\boldsymbol{F}_{T_i} + {}^{e}\boldsymbol{F}_{A_i}) \cdot l_{ia}\boldsymbol{\xi}_{ia} - \sum_{a=1}^{j} \hat{\boldsymbol{n}}_{ia}\, {}^{e}\boldsymbol{F}_{A_{m_{ij}}} \cdot l_{ia}\boldsymbol{\xi}_{ia} \\ &+ {}^{b_l}\hat{\boldsymbol{r}}_{l_i}\mathcal{R}_{eb_l}^{T}({}^{e}\boldsymbol{F}_{T_i} + {}^{e}\boldsymbol{F}_{A_i}) \cdot \boldsymbol{\eta}_l + {}^{b_l}\hat{\boldsymbol{r}}_{l_i}\mathcal{R}_{eb_l}^{T}\, {}^{e}\boldsymbol{F}_{A_{m_{ij}}} \cdot \boldsymbol{\eta}_l \\ &- {}^{b_i}\hat{\boldsymbol{r}}_{i}\mathcal{R}_{eb_i}^{T}({}^{e}\boldsymbol{F}_{T_i} + {}^{e}\boldsymbol{F}_{A_i}) \cdot \boldsymbol{\eta}_i + {}^{b}\boldsymbol{G}_{T_i} \cdot \boldsymbol{\eta}_i \Big] \end{aligned} \tag{2.126}$$

Finally, the Euler–Lagrange equations of motion are obtained by applying the fundamental lemma of the calculus of variations [84]. In the Euclidean case $\mathbb{R}^n$, the lemma states that if

$$\int_{t_0}^{t_f} \boldsymbol{f}(t) \cdot \delta\boldsymbol{x}(t) dt = 0 \tag{2.127}$$

for all continuous variations $\delta\boldsymbol{x}(t)$ with fixed endpoints, then necessarily $\boldsymbol{f}(t) = 0$. For variations on a smooth manifold, the corresponding result is that

$$\int_{t_0}^{t_f} \boldsymbol{f}(t) \cdot \boldsymbol{\xi}(t) dt = 0 \tag{2.128}$$

which implies that $\boldsymbol{f}(t)$ must be orthogonal to the admissible variation $\boldsymbol{\xi}(t)$, that is $\boldsymbol{f}(t) \cdot \boldsymbol{\xi} = 0$. In the case of S^2, since the admissible variations $\boldsymbol{\xi}$ are, by definition, orthogonal to $\boldsymbol{n}$, this condition requires that the integrand $\boldsymbol{f}(t)$ must be aligned with $\boldsymbol{n}$, that is $\hat{\boldsymbol{n}}\boldsymbol{f}(t) = 0$. The Euler-Lagrange equations read

$$\frac{d}{dt}\left(\frac{\partial \mathcal{L}}{\partial\, {}^{e}\dot{\boldsymbol{p}}_l}\right) - \frac{\partial \mathcal{L}}{\partial\, {}^{e}\boldsymbol{p}_l} = \sum_{i=1}^{N} \sum_{j=1}^{P-1} {}^{e}\boldsymbol{F}_{T_i} + {}^{e}\boldsymbol{F}_{A_i} + {}^{e}\boldsymbol{F}_{A_{m_{ij}}} + {}^{e}\boldsymbol{F}_{A_l} \tag{2.129}$$

$$\widehat{\boldsymbol{n}}_{ij}^{2}\left(\frac{d}{dt}\left(\frac{\partial \mathcal{L}}{\partial \dot{\boldsymbol{n}}_{ij}}\right) - \frac{\partial \mathcal{L}}{\partial \boldsymbol{n}_{ij}}\right) = -l_{ij}\widehat{\boldsymbol{n}}_{ij}^{2}({}^{e}\boldsymbol{F}_{T_i} + {}^{e}\boldsymbol{F}_{A_i} + {}^{e}\boldsymbol{F}_{A_{m_{ij}}}) \tag{2.130}$$

$$\frac{d}{dt}\left(\frac{\partial \mathcal{L}}{\partial\, {}^{b_l}\boldsymbol{\omega}_l}\right) + {}^{b_l}\boldsymbol{\omega}_l \times \frac{\partial \mathcal{L}}{\partial\, {}^{b_l}\boldsymbol{\omega}_l} - \nabla_L \mathcal{L}(\mathcal{R}_{eb_l}) = \sum_{i=1}^{N} \sum_{j=1}^{P-1} {}^{b_l}\widehat{\boldsymbol{r}}_{l_i}\mathcal{R}_{eb_l}^{T}({}^{e}\boldsymbol{F}_{T_i} + {}^{e}\boldsymbol{F}_{A_i} + {}^{e}\boldsymbol{F}_{A_{m_{ij}}}) \tag{2.131}$$

$$\frac{d}{dt}\left(\frac{\partial \mathcal{L}}{\partial\, {}^{b_i}\boldsymbol{\omega}_i}\right) + {}^{b_i}\boldsymbol{\omega}_i \times \frac{\partial \mathcal{L}}{\partial\, {}^{b_i}\boldsymbol{\omega}_i} - \nabla_L \mathcal{L}(\mathcal{R}_{eb_i}) = -\,{}^{b_i}\widehat{\boldsymbol{r}}_{i}\mathcal{R}_{eb_i}^{T}({}^{e}\boldsymbol{F}_{T_i} + {}^{e}\boldsymbol{F}_{A_i}) + {}^{b}\boldsymbol{G}_{T_i} \tag{2.132}$$

where the derivatives of the Lagrangian are defined in Appendix B.3. The thrust force vector is ${}^{e}\boldsymbol{F}_T = \mathcal{R}_{eb}\,[0, 0, -T]^T$, while the thrust moment, aerodynamic forces acting on the quadrotor, payload, and cable are reported in Eqs. (2.65), (2.64), (2.72), (2.75), respectively.

In this model, the control inputs are defined as the total thrust magnitude and the control moments. Since the control effectiveness matrix, introduced in Eq. (2.67), is invertible, it can be directly used to map these control inputs into the corresponding rotor angular velocities, while the actuator dynamics are neglected. The equations of motion are then rewritten in terms of the links angular velocity in order to have the system in standard form $\dot{\boldsymbol{x}} = f(\boldsymbol{x}, \boldsymbol{u})$. A detailed derivation of the Lagrange equations is provided in Appendix B.4. The final set of equations of motion, including the translational dynamics of the payload c.g. (Eq. 2.133), the link attitude dynamics (Eq. 2.134), the payload rotational dynamics (Eq. 2.135), and the quadrotor rotational dynamics (Eq. 2.136), is given by

$$
\begin{aligned}
&m_t\, {}^{e}\ddot{\boldsymbol{p}}_l - \sum_{i=1}^{N} m_{iT} \mathcal{R}_{eb_l}\, {}^{b_l}\hat{\boldsymbol{r}}_{l_i}\, {}^{b_l}\dot{\boldsymbol{\omega}}_l + \sum_{i=1}^{N} m_i\, \mathcal{R}_{eb_i}\, {}^{b_i}\hat{\boldsymbol{r}}_i\, {}^{b_i}\dot{\boldsymbol{\omega}}_i + \sum_{i=1}^{N}\sum_{j=1}^{P} m_{0ij} l_{ij} \hat{\boldsymbol{n}}_{ij} \dot{\boldsymbol{\omega}}_{ij} \\
&= \sum_{i=1}^{N} m_{iT} \mathcal{R}_{eb_l}\, {}^{b_l}\hat{\boldsymbol{\omega}}_l\, {}^{b_l}\hat{\boldsymbol{r}}_{l_i}\, {}^{b_l}\boldsymbol{\omega}_l - \sum_{i=1}^{N} m_i \mathcal{R}_{eb_i}\, {}^{b_i}\hat{\boldsymbol{\omega}}_i\, {}^{b_i}\hat{\boldsymbol{r}}_i\, {}^{b_i}\boldsymbol{\omega}_i - \sum_{i=1}^{N}\sum_{j=1}^{P} m_{0ij} l_{ij} \|\boldsymbol{\omega}_{ij}\|^2 \boldsymbol{n}_{ij} \\
&\quad + m_t g\, \boldsymbol{e}_3 + \sum_{i=1}^{N} {}^{e}\boldsymbol{F}_{T_i} + \sum_{i=1}^{N} {}^{e}\boldsymbol{F}_{A_i} + \sum_{i=1}^{N}\sum_{j=1}^{P-1} {}^{e}\boldsymbol{F}_{A_{m_{ij}}} + {}^{e}\boldsymbol{F}_{A_l}
\end{aligned}
\tag{2.133}
$$

$$
\begin{aligned}
&\sum_{k=1,k\neq j}^{P} m_{0ij} l_{ij} l_{ik} \hat{\boldsymbol{n}}_{ij} \hat{\boldsymbol{n}}_{ik}\, \dot{\boldsymbol{\omega}}_{ik} + m_{0ij} l_{ij}^2 \dot{\boldsymbol{\omega}}_{ij} + m_{0ij} l_{ij} \hat{\boldsymbol{n}}_{ij}\, {}^{e}\ddot{\boldsymbol{p}}_l - m_{0ij} l_{ij} \hat{\boldsymbol{n}}_{ij} \mathcal{R}_{eb_l} ({}^{b_l}\hat{\boldsymbol{r}}_{l_i}\, {}^{b_l}\dot{\boldsymbol{\omega}}_l) \\
&\quad + m_i l_{ij} \hat{\boldsymbol{n}}_{ij} \mathcal{R}_{eb_i} ({}^{b_i}\hat{\boldsymbol{r}}_i\, {}^{b_i}\dot{\boldsymbol{\omega}}_i) = -m_{0ij} l_{ij} g \hat{\boldsymbol{n}}_{ij} \boldsymbol{e}_3 - \sum_{k\neq j} m_{0ij} l_{ij} l_{ik}\, \|\boldsymbol{\omega}_{ik}\|^2 \hat{\boldsymbol{n}}_{ij} \boldsymbol{n}_{ik} \\
&\quad + m_{0ij} l_{ij} \hat{\boldsymbol{n}}_{ij} \mathcal{R}_{eb_l} ({}^{b_l}\hat{\boldsymbol{\omega}}_l\, {}^{b_l}\hat{\boldsymbol{r}}_{l_i}\, {}^{b_l}\boldsymbol{\omega}_l) - m_i l_{ij} \hat{\boldsymbol{n}}_{ij} \mathcal{R}_{eb_i} ({}^{b_i}\hat{\boldsymbol{\omega}}_i\, {}^{b_i}\hat{\boldsymbol{r}}_i\, {}^{b_i}\boldsymbol{\omega}_i) \\
&\quad + l_{ij}\, \hat{\boldsymbol{n}}_{ij} ({}^{e}\boldsymbol{F}_{T_i} + {}^{e}\boldsymbol{F}_{A_i} + {}^{e}\boldsymbol{F}_{A_{m_{ij}}})
\end{aligned}
\tag{2.134}
$$

$$
\begin{aligned}
&\bar{\boldsymbol{J}}_l\, {}^{b_l}\dot{\boldsymbol{\omega}}_l + \sum_{i=1}^{N} m_{iT}\, {}^{b_l}\hat{\boldsymbol{r}}_{l_i}\, \mathcal{R}_{eb_l}^T\, {}^{e}\ddot{\boldsymbol{p}}_l + \sum_{i=1}^{N} m_i\, {}^{b_l}\hat{\boldsymbol{r}}_{l_i}\, \mathcal{R}_{eb_l}^T \mathcal{R}_{eb_i}\, {}^{b_i}\hat{\boldsymbol{r}}_i\, {}^{b_i}\dot{\boldsymbol{\omega}}_i \\
&\quad + \sum_{i=1}^{N}\sum_{j=1}^{P} m_{0ij}\, {}^{b_l}\hat{\boldsymbol{r}}_{l_i}\, \mathcal{R}_{eb_l}^T\, l_{ij}\, \hat{\boldsymbol{n}}_{ij}\, \dot{\boldsymbol{\omega}}_{ij} = \sum_{i=1}^{N}\sum_{j=1}^{P-1} {}^{b_l}\hat{\boldsymbol{r}}_{l_i}\, \mathcal{R}_{eb_l}^T ({}^{e}\boldsymbol{F}_{T_i} + {}^{e}\boldsymbol{F}_{A_i} + {}^{e}\boldsymbol{F}_{A_{m_{ij}}}) \\
&\quad - \sum_{i=1}^{N}\sum_{j=1}^{P} m_{0ij}\, {}^{b_l}\hat{\boldsymbol{r}}_{l_i}\, \mathcal{R}_{eb_l}^T\, l_{ij}\, \|\boldsymbol{\omega}_{ij}\|^2 \boldsymbol{n}_{ij} + \sum_{i=1}^{N} m_{iT} g\, {}^{b_l}\hat{\boldsymbol{r}}_{l_i}\, \mathcal{R}_{eb_l}^T \boldsymbol{e}_3 - {}^{b_l}\hat{\boldsymbol{\omega}}_l \bar{\boldsymbol{J}}_l\, {}^{b_l}\boldsymbol{\omega}_l
\end{aligned}
\tag{2.135}
$$

$$
\begin{aligned}
&({}^{b_i}\boldsymbol{I} + m_i\,{}^{b_i}\hat{\boldsymbol{r}}_i^2)\,{}^{b_i}\dot{\boldsymbol{\omega}}_i + m_i\,{}^{b_i}\hat{\boldsymbol{r}}_i\mathcal{R}_{eb_i}^T\,{}^{e}\ddot{\boldsymbol{p}}_l + m_i\,{}^{b_i}\hat{\boldsymbol{r}}_i\mathcal{R}_{eb_i}^T\sum_{j=1}^{P} l_{ij}\hat{\boldsymbol{n}}_{ij}\dot{\boldsymbol{\omega}}_{ij} - m_i\,{}^{b_i}\hat{\boldsymbol{r}}_i\mathcal{R}_{eb_i}^T\mathcal{R}_{eb_l}\,{}^{b_l}\hat{\boldsymbol{r}}_{l_i}\,{}^{b_l}\dot{\boldsymbol{\omega}}_l \\
&= {}^{b_i}\widehat{\boldsymbol{r}}_i\mathcal{R}_{eb_i}^T\,({}^{e}\boldsymbol{F}_{T_i} - {}^{e}\boldsymbol{F}_{A_i}) - {}^{b}\boldsymbol{G}_i + m_i g\,{}^{b_i}\hat{\boldsymbol{r}}_i\mathcal{R}_{eb_i}^T\boldsymbol{e}_3 - m_i\,{}^{b_i}\hat{\boldsymbol{\omega}}_i({}^{b_i}\boldsymbol{I} + {}^{b_i}\hat{\boldsymbol{r}}_i^2)\,{}^{b_i}\boldsymbol{\omega}_i \\
&\quad - m_i\,{}^{b_i}\hat{\boldsymbol{r}}_i\mathcal{R}_{eb_i}^T\sum_{j=1}^{P} l_{ij}\|\boldsymbol{\omega}_{ij}\|^2\boldsymbol{n}_{ij}
\end{aligned}
\tag{2.136}
$$

together with the kinematic relations in Eqs. (2.88) and (2.106).

Chapter 3

Control

In this chapter, the control system for the multi-UAV cooperative transportation system is developed. Two distinct control strategies are investigated, the load-leading and the formation-fixed approaches.

3.1 Load-Leading Control Architecture

In this section, the design of a centralized linear controller for payload trajectory tracking is presented.

To this end, the nonlinear equations of motion obtained from the Lagrangian formulation (Eqs. (2.133)–(2.136)) are linearized using the variation–based method [70]. This methodology allows the system dynamics to be linearized along nominal trajectories evolving on the manifold, thereby preserving the intrinsic geometric structure of the original nonlinear model. The resulting linearized model is then employed for the synthesis of a time-varying LQR. Exploiting the differential flatness property of the underlying nonlinear system [39], the desired state trajectories and the corresponding feedforward control terms are analytically computed. Since the system is formulated directly on the configuration manifold, configuration errors, as described in sections 2.4.1, 2.4.2, are employed for feedback control. The overall control architecture is illustrated in Fig. 3.1.

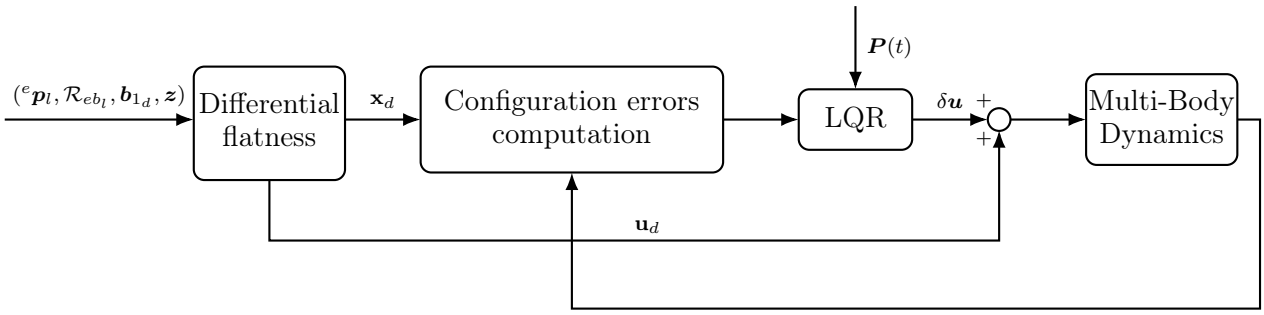

Figure 3.1: Load-Leading Control Architecture

3.1.1 Linearized Dynamics

The nonlinear equations of motion in Eqs. (2.133)–(2.136), are linearized along a prescribed, dynamically feasible reference trajectory, to obtain a linear time-varying (LTV) system, which serves as the basis for the subsequent feedback control design. To linearize the system along a reference trajectory, it is necessary to introduce variations of all state variables and control inputs with respect to the nominal trajectory. For the variables evolving in $\mathbb{R}^3$, namely the payload position and velocity, variations are defined as $\delta\boldsymbol{x} = \boldsymbol{x}_d - \boldsymbol{x}$. For the variables evolving on $SO(3)$ and S^2, admissible variations must instead be introduced in the corresponding tangent spaces [82]. The explicit expressions of the admissible variations for variables evolving on $SO(3)$ and S^2 are reported in Eqs. (2.97), (2.109). For the Euclidean variables, the variations coincide with the errors, while for the variables that evolves on $SO(3)$, and S^2, the variations do not coincide globally with the configuration errors, but they provide a first-order approximation of them [70], as is also demonstrated in Appendix C.2.
The linearized dynamics is obtained following the variation-based method detailed in [70]. In this approach, the variational operator $\delta(\cdot)$ is applied to both sides of the nonlinear equations of motion, and the resulting expressions are then evaluated along the reference trajectory. The operator $\delta(\cdot)$ is linear with respect to addition and satisfies the standard product rules for inner and cross products, as well as for matrix–vector and matrix–matrix multiplications [70].
By applying this procedure to the system in Eqs. (2.133)–(2.136), the linearized equations of motion are obtained. Due to their length, the full expressions are reported in Appendix C.3. Let $\delta\mathbf{x}(t)$ denote the collection of the variations of all the state variables (see sections 2.4.1,

2.4.2), and $\delta\mathbf{u}$ the variations of the inputs

$$\delta\mathbf{x} = [\delta\,{}^{e}\boldsymbol{p}_l, \boldsymbol{\xi}_{ij}, \delta\,{}^{e}\dot{\boldsymbol{p}}_l, \boldsymbol{\eta}_l, \delta\,{}^{b_l}\boldsymbol{\omega}_l, \delta\boldsymbol{\omega}_{ij}, \boldsymbol{\eta}_i, \delta\,{}^{b_i}\boldsymbol{\omega}_i] \tag{3.1}$$

$$\delta\mathbf{u} = [\delta T_i, \delta\,{}^{b_i}\boldsymbol{G}_{T_i}] \tag{3.2}$$

the linearized equations of motion are written as

$$\delta\dot{\mathbf{x}}(t) = \boldsymbol{A}(\mathbf{x}_d(t), \mathbf{u}_d(t))\delta\mathbf{x}(t) + \boldsymbol{B}(\mathbf{x}_d(t), \mathbf{u}_d(t))\delta\mathbf{u}(t) \tag{3.3}$$

which is a linear time varying system that represents the linearized error dynamics of the nonlinear system. The matrices $\boldsymbol{A}(\mathbf{x}_d(t), \mathbf{u}_d(t))$ and $\boldsymbol{B}(\mathbf{x}_d(t), \mathbf{u}_d(t))$ are obtained by collecting the coefficients of $\delta\mathbf{x}$ and $\delta\mathbf{u}$ from the linearized equations reported in Appendix C.3. For variables evolving on the unit sphere S^2, variations must satisfy the algebraic constraint $\boldsymbol{\xi} \cdot \mathbf{n}_d = 0$. Since this condition must hold for all time, its time derivative must also vanish, that is $\frac{d}{dt}(\boldsymbol{\xi} \cdot \mathbf{n}_d) = 0$, which lead to the differential constraint $-\boldsymbol{\omega}_d^T \hat{\mathbf{n}}_d \boldsymbol{\xi} + \mathbf{n}_d^T(\delta\boldsymbol{\omega}) = 0$. Applying these two constraints for all links yields the constraint matrix expressed as

$$\mathbf{C}(\mathbf{x}_d(t))\delta\mathbf{x}(t) = \mathbf{0} \tag{3.4}$$

where, for each link, the corresponding block has the form

$$\begin{bmatrix} \mathbf{n}_{ij_d}^T & \mathbf{0}_{1\times 3} \\ -\boldsymbol{\omega}_{ij_d}^T \hat{\mathbf{n}}_{ij_d} & \mathbf{n}_{ij_d}^T \end{bmatrix} \begin{bmatrix} \boldsymbol{\xi}_{ij} \\ \delta\boldsymbol{\omega}_{ij} \end{bmatrix} = \mathbf{0}. \tag{3.5}$$

As shown in [70], the constraint matrix $\mathbf{C}(\mathbf{x}_d(t))$ in Eq. (3.4) is time-invariant. Therefore, if the initial condition of the linearized state satisfies the constraint $\mathbf{C}(\mathbf{x}_d(0))\,\delta\mathbf{x}(0) = \mathbf{0}$, it will remain satisfied for all $t \geqslant 0$. Consequently, the system trajectory constrained by Eq. (3.4) evolves within the same subspace as the unconstrained linearized dynamics described in Eq. (3.3).

3.1.2 Differential Flatness

In this section, the system state reconstruction process based on the differential flatness property is presented. In [39], the authors demonstrate that the system composed of multiple quadrotors carrying a rigid-body payload through flexible cables is differentially flat

under the assumptions that the cable attachment points coincide with the quadrotor centers of gravity and that aerodynamic forces are neglected. In [40], the authors show that a system composed of a single quadrotor carrying a point-mass load through a rigid and massless link with an offset attachment point is also differentially flat, under the assumptions of small quadrotor angular accelerations and negligible aerodynamic forces. Here, these two results are combined and extended to the case of multiple quadrotors with nonzero attachment offsets carrying a rigid-body payload through flexible cables, while also accounting for aerodynamic forces.

Definition 10. *Differential Flatness [37]: A control system of the form $\dot{x} = f(x, u)$, with state $x \in \mathbb{R}^n$ and input $u \in \mathbb{R}^m$, is said to be differentially flat if there exists a set of outputs y that can be written as $y = y(x, u, \dot{u}, \ldots, u^{(p)})$, such that both the states and the inputs can be reconstructed from y and a finite number of its time derivatives as $x = x(y, \dot{y}, \ldots, y^{(q)})$ and $u = u(y, \dot{y}, \ldots, y^{(q)})$, for some finite integers p and q.*

The differential flatness property enables to write the state $[{}^e\boldsymbol{p}_i,\ {}^e\dot{\boldsymbol{p}}_i,\ \mathcal{R}_{eb_i},\ {}^{b_i}\boldsymbol{\omega}_i,\ \boldsymbol{n}_{ij},\ \boldsymbol{\omega}_{ij}]^T$ and the inputs $[T_i,\ {}^{b_i}\boldsymbol{G}_{T_i}]$ as algebraic functions of p selected flat outputs and a finite number of their derivatives. The flat outputs are the payload position ${}^e\boldsymbol{p}_l$, the payload attitude $\mathcal{R}_{eb_l}$, and the direction of the x-body axis b_{1_i}, as in [39]. To reconstruct the system state from the flat outputs, it is convenient to look at the equations of motion written in terms of generalized coordinates using the Newton-Euler formalism such that the constraint forces of the system appear explicitly (see Sec. 2.5)

$$m_i\,{}^e\ddot{\boldsymbol{p}}_i = {}^e\boldsymbol{F}_T - \mathcal{R}_{eb_i}(\tfrac{1}{2}\rho\mathbf{A}_i|\mathcal{R}_{eb_i}^T\,{}^e\dot{\boldsymbol{p}}_i|\mathcal{R}_{eb_i}^T\,{}^e\dot{\boldsymbol{p}}_i) + m_i\,{}^e\boldsymbol{g} + t_{iP}\boldsymbol{n}_{iP} \tag{3.6}$$

$${}^{b_i}\boldsymbol{I}_i\,{}^{b_i}\dot{\boldsymbol{\omega}}_i + {}^{b_i}\boldsymbol{\omega}_i\,{}^{b_i}\boldsymbol{I}_i\,{}^{b_i}\boldsymbol{\omega}_i = {}^{b_i}\boldsymbol{G}_i + {}^{b_i}\hat{\boldsymbol{r}}_i\big(-\mathcal{R}_{eb_i}t_{iP}\boldsymbol{n}_{iP}\big) \tag{3.7}$$

$$m_{ij}\,{}^e\ddot{\boldsymbol{p}}_{ij} = -\tfrac{1}{2}\rho A_s C_{d_s}\|\,{}^e\dot{\boldsymbol{p}}_{ij}\|\,{}^e\dot{\boldsymbol{p}}_{ij} + m_{ij}\,{}^e\boldsymbol{g} - t_{i(j+1)}\boldsymbol{n}_{i(j+1)} + t_{ij}\boldsymbol{n}_{ij} \tag{3.8}$$

$$m_l\,{}^e\ddot{\boldsymbol{p}}_l = -\mathcal{R}_{eb_l}(\tfrac{1}{2}\rho\boldsymbol{C}_{d_l}\mathbf{S}_l|\mathcal{R}_{eb_l}^T\,{}^e\dot{\boldsymbol{p}}_l|\mathcal{R}_{eb_l}^T\,{}^e\dot{\boldsymbol{p}}_l) + m_l\,{}^e\boldsymbol{g} - \sum_{i=1}^{N} t_{i1}\boldsymbol{n}_{i1} \tag{3.9}$$

$${}^{b_l}\boldsymbol{I}_l\,{}^{b_l}\dot{\boldsymbol{\omega}} + {}^{b_l}\hat{\boldsymbol{\omega}}\,{}^{b_l}\boldsymbol{I}_l\,{}^{b_l}\boldsymbol{\omega}_l = \sum_{i=1}^{N} {}^{b_l}\hat{\boldsymbol{r}}_{l_i}\big(-\mathcal{R}_{eb_l}t_{i1}\boldsymbol{n}_{i1}\big) \tag{3.10}$$

where t_{ij} is the modulus of the tensile force on the j-th link of the i-th cable. From Eqs. (3.9), (3.10) the tensile forces in the cable elements directly connected to the payload ($\boldsymbol{n}_{i1}$)

are obtained solving an under-determined linear system of the form

$$\boldsymbol{A}\boldsymbol{t} = \boldsymbol{b} \tag{3.11}$$

where

$$\boldsymbol{A} = \begin{bmatrix} I & I & \cdots & I \\ {}^{b_l}\hat{\boldsymbol{r}}_{l_1} & {}^{b_l}\hat{\boldsymbol{r}}_{l_2} & \cdots & {}^{b_l}\hat{\boldsymbol{r}}_{l_N} \end{bmatrix} \tag{3.12}$$

$$\boldsymbol{b} = -\begin{bmatrix} \mathcal{R}_{eb_l} m_l \Big({}^{e}\ddot{\boldsymbol{p}}_l + \mathcal{R}_{eb_l}\big(\tfrac{1}{2}\rho \boldsymbol{C}_{d_l}\mathbf{S}_l | \mathcal{R}_{eb_l}^T\, {}^{e}\dot{\boldsymbol{p}}_l | \mathcal{R}_{eb_l}^T\, {}^{e}\dot{\boldsymbol{p}}_l\big) - {}^{e}\boldsymbol{g}\Big) \\ {}^{b_l}\boldsymbol{I}\, {}^{b_l}\dot{\boldsymbol{\omega}} + {}^{b_l}\hat{\boldsymbol{\omega}}\, {}^{b_l}\boldsymbol{I}\, {}^{b_l}\boldsymbol{\omega}_l \end{bmatrix} \tag{3.13}$$

Suppose that $\boldsymbol{A} \in \mathbb{R}^{6\times 3N}$ has full row rank equal to six, which corresponds to the case where at least three cables are present and the attachment points are not collinear. In this case, the general solution of Eq. (3.11), as shown in Appendix A.1.2, is given by

$$\boldsymbol{t} = \boldsymbol{A}^{\dagger}\boldsymbol{b} + \boldsymbol{N}\,\boldsymbol{z} \tag{3.14}$$

where $\boldsymbol{N} \in \mathbb{R}^{3N\times(3N-6)}$ is a full column rank matrix whose columns span $\ker(\boldsymbol{A})$ so that $\boldsymbol{A}\boldsymbol{N} = 0$, and $\boldsymbol{z} \in \mathbb{R}^{3N-6}$ is a free vector. In Eq. (3.14), $\boldsymbol{t} = \boldsymbol{A}^{\dagger}\boldsymbol{b}$ is the minimum norm solution, and $\boldsymbol{N}\boldsymbol{z}$ is an additional term that lies in the null space of $\boldsymbol{A}$, so it does not change the equilibrium condition $\boldsymbol{A}\boldsymbol{t} = \boldsymbol{b}$, since $\boldsymbol{A}\boldsymbol{N}\boldsymbol{z} = 0$, but can be used to impose constraints on the links tension. The minimum norm solution guarantees that the desired net force an moment acting on the payload c.g. are satisfied by minimizing the total cable forces. The null–space component then redistributes these forces among the attachment points without changing the net force and moment on the payload. The free vector $\boldsymbol{z}$ can therefore be chosen to shape the tension distribution in the links. A convenient basis for the null space of $\mathbf{A}$ can be constructed by considering internal forces that act in equal and opposite pairs [17]. For any unordered pair of attachment points (i, j), define the unit vector

$$\boldsymbol{u}_{ij} = \frac{{}^{b_l}\boldsymbol{r}_{l_j} - {}^{b_l}\boldsymbol{r}_{l_i}}{\| {}^{b_l}\boldsymbol{r}_{l_j} - {}^{b_l}\boldsymbol{r}_{l_i} \|} \tag{3.15}$$

which represents the direction vector pointing from attachment point i to attachment point

j. The null–space matrix $\boldsymbol{N}$ is then formed as

$$\boldsymbol{N} = [\boldsymbol{n}_{12},\ \boldsymbol{n}_{13},\ \cdots,\ \boldsymbol{n}_{ij},\ \cdots] \tag{3.16}$$

where each column $\boldsymbol{n}_{ij}$ has the form

$$\boldsymbol{n}_{ij} = [\mathbf{0}, \cdots, \mathbf{0},\ \boldsymbol{u}_{ij},\ \mathbf{0}, \cdots, \mathbf{0},\ -\boldsymbol{u}_{ij},\ \mathbf{0}, \cdots, \mathbf{0}]^T \tag{3.17}$$

that is, the position corresponding to the i-th attachment point contains u_{ij}, the position corresponding to the j-th attachment point contains $-\boldsymbol{u}_{ij}$, and all other positions are zero. By construction, the total force is zero, because $\boldsymbol{u}_{ij} + (-\boldsymbol{u}_{ij}) = 0$. The total moment is also zero, since

$$^{b_l}\boldsymbol{r}_{l_i} \times \boldsymbol{u}_{ij} + {}^{b_l}\boldsymbol{r}_{l_j} \times (-\boldsymbol{u}_{ij}) = ({}^{b_l}\boldsymbol{r}_{l_i} - {}^{b_l}\boldsymbol{r}_{l_j}) \times \boldsymbol{u}_{ij} = 0 \tag{3.18}$$

since the vector $\boldsymbol{u}_{ij}$ is parallel to ${}^{b_l}\boldsymbol{r}_{l_j} - {}^{b_l}\boldsymbol{r}_{l_i}$. Each $\boldsymbol{n}_{ij}$ therefore belongs to $\ker(\boldsymbol{A})$ and represents a self–equilibrated internal force mode. The free parameter vector $\boldsymbol{z}$ then collects the coefficients weighting these modes.

For example, in the static equilibrium configuration ($\mathcal{R}_{eb_l} = \mathcal{I}$, ${}^e\boldsymbol{p}_l = \text{const}$), for $N = 4$, the minimum-norm solution yields cable forces aligned with the vertical axis (Fig. 3.2a). By setting $\boldsymbol{z} = [\, z_{12},\, 0,\, 0,\, 0,\, 0,\, z_{34}\,]^T$ with $z_{12} = z_{34} = \frac{1}{4} m_l g \tan(\theta)$, the cables become inclined by an angle θ with respect to the vertical (Fig. 3.2b).

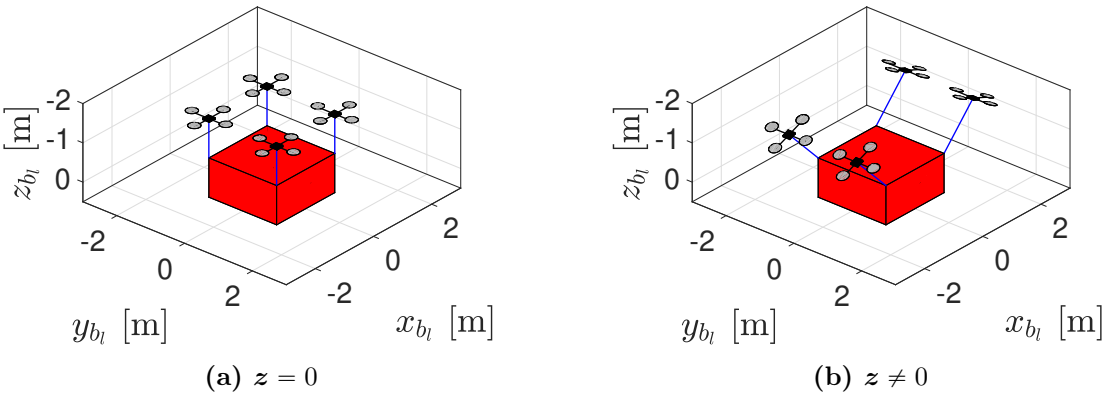

(a) $\boldsymbol{z} = 0$ **(b)** $\boldsymbol{z} \neq 0$

Figure 3.2: Cable geometries in static equilibrium for different values of the free parameter $\boldsymbol{z}$

Given ${}^e\boldsymbol{p}_l$, $\mathcal{R}_{eb_l}$, and $\boldsymbol{z}$, and their higher order derivatives, the tensions in the cable elements directly connected to the payload are evaluated. Once the vectors $t_{i1}\boldsymbol{n}_{i1}$ are obtained, the

unit direction of the first element of each cable and the corresponding tension magnitude are computed as

$$\boldsymbol{n}_{i1} = \frac{t_{i1}\boldsymbol{n}_{1i}}{\|t_{i1}\boldsymbol{n}_{i1}\|} \tag{3.19}$$

$$t_{i1} = t_{1i}\boldsymbol{n}_{i1} \cdot \boldsymbol{n}_{i1} \tag{3.20}$$

Knowing the directions of the first links, it is possible to compute the positions of the first cable masses as

$${}^{e}\boldsymbol{p}_{i1} = {}^{e}\boldsymbol{p}_{l} + \mathcal{R}_{eb_l}\,{}^{b_l}\boldsymbol{r}_{l_i} - l_{i1}\boldsymbol{n}_{i1} \tag{3.21}$$

By differentiating twice, and recalling that the time derivative of a unit vector is given by

$$\|\dot{\boldsymbol{a}}\| = \frac{\boldsymbol{a}^T \cdot \boldsymbol{a}}{\|\boldsymbol{a}\|} \tag{3.22}$$

${}^{e}\ddot{\boldsymbol{p}}_{i1}$ are obtained. The tensions in the following elements are obtained from Eq. (3.8) as

$$t_{i(j+1)}\boldsymbol{n}_{i(j+1)} = -\tfrac{1}{2}\rho A_s C_{d_s}\|\,{}^{e}\dot{\boldsymbol{p}}_{ij}\|\,{}^{e}\dot{\boldsymbol{p}}_{ij} + m_{ij}\,{}^{e}\boldsymbol{g} - m_{ij}\,{}^{e}\ddot{\boldsymbol{p}}_{ij} + t_{ij}\boldsymbol{n}_{ij} \tag{3.23}$$

Once the directions of all cable links have been determined, the position of each quadrotor is computed as

$${}^{e}\boldsymbol{p}_{i} = {}^{e}\boldsymbol{p}_{l} + \mathcal{R}_{eb_l}\,{}^{b_l}\boldsymbol{r}_{l_i} - \sum_{j=1}^{P} l_{ij}\boldsymbol{n}_{ij} - \mathcal{R}_{eb_i}\,{}^{b_i}\boldsymbol{r}_{i} \tag{3.24}$$

To determine the positions of the quadrotors, it is therefore also necessary to know their attitude. However, the rotation matrix of each vehicle depends on the acceleration that it must generate [85]. In particular

$$\mathcal{R}_{eb_i} = \begin{bmatrix} \boldsymbol{b}_{1_i} & \boldsymbol{b}_{2_i} & \boldsymbol{b}_{3_i} \end{bmatrix} \tag{3.25}$$

where $\boldsymbol{b}_{1_i}$, $\boldsymbol{b}_{2_i}$, and $\boldsymbol{b}_{3_i}$ correspond to the directions of the body axes. For a quadrotor, $\boldsymbol{b}_{3_i}$ coincides with the thrust direction

$$\boldsymbol{b}_{3_i} = \frac{{}^{e}\boldsymbol{F}_{T_i}}{\|\,{}^{e}\boldsymbol{F}_{T_i}\|} \tag{3.26}$$

since in a quadrotor the thrust is always directed along the body z-axis. Because the required thrust depends on the acceleration that the quadrotor must produce, the determination of $\boldsymbol{b}_{3_i}$ requires knowledge of the vehicle acceleration. As shown in [40], under the assumption of low angular velocities, the attitude variation can be considered constant over a small time interval Δt, leading to the relation

$$ {}^{e}\boldsymbol{p}_i(t+\Delta t) = {}^{e}\boldsymbol{p}_l(t+\Delta t) + \mathcal{R}_{eb_l}(t+\Delta t)\,{}^{b_l}\boldsymbol{r}_{l_i} - \sum_{j=1}^{P} l_{ij}\boldsymbol{n}_{ij}(t+\Delta t) - \mathcal{R}_{eb_i}(t)\,{}^{b_i}\boldsymbol{r}_i \tag{3.27} $$

By differentiating Eq. (3.27) twice, the acceleration of the quadrotors is obtained. Substituting this value into Eq. (3.6) and again assuming low angular velocities for the computation of aerodynamic drag , the expression for the thrust is as follows

$$ {}^{e}\boldsymbol{F}_T = -m_i\,{}^{e}\ddot{\boldsymbol{p}}_i + \mathcal{R}_{eb_i}(\tfrac{1}{2}\rho\mathbf{A}_i|\mathcal{R}_{eb_i}^{T}(t-\Delta t)\,{}^{e}\dot{\boldsymbol{p}}_i|\mathcal{R}_{eb_i}^{T}(t-\Delta t)\,{}^{e}\dot{\boldsymbol{p}}_i) - m_i\,{}^{e}\boldsymbol{g} - t_{iP}\boldsymbol{n}_{iP} \tag{3.28} $$

To determine the desired attitude of the quadrotors, the unit vector $\boldsymbol{b}_{3_i}$ is obtained from Eq. (3.26), while $\boldsymbol{b}_{1_i}$ is calculated as [86]

$$ \boldsymbol{b}_{1_i} = \frac{\boldsymbol{b}_{3_i} \times (\boldsymbol{b}_{3_i} \times \boldsymbol{b}_{1_{i_d}})}{\|\boldsymbol{b}_{3_i} \times \boldsymbol{b}_{1_{i_d}}\|} \tag{3.29} $$

and, finally, the direction $\boldsymbol{b}_{2_i}$ is specified to obtain an orthonormal frame

$$ \boldsymbol{b}_{2_i} = \boldsymbol{b}_{1_i} \times \boldsymbol{b}_{3_i} \tag{3.30} $$

The control moments are then computed from Eq. (3.7) as

$$ {}^{b_i}\boldsymbol{G}_{T_i} = {}^{b_i}\boldsymbol{I}_i\,{}^{b_i}\dot{\boldsymbol{\omega}}_i + {}^{b_i}\boldsymbol{\omega}_i\,{}^{b_i}\boldsymbol{I}_i\,{}^{b_i}\boldsymbol{\omega}_i - {}^{b_i}\hat{\boldsymbol{r}}_i\big(-\mathcal{R}_{eb_i}t_{iP}\boldsymbol{n}_{iP}\big) \tag{3.31} $$

where the expressions of ${}^{b_i}\dot{\boldsymbol{\omega}}_i$ and ${}^{b_i}\boldsymbol{\omega}_i$, derived from the flat outputs and their time derivatives, are provided in the Appendix C.1 for clarity.

The reconstruction process of system states and inputs based on differential flatness is illustrated in Fig. 3.3.

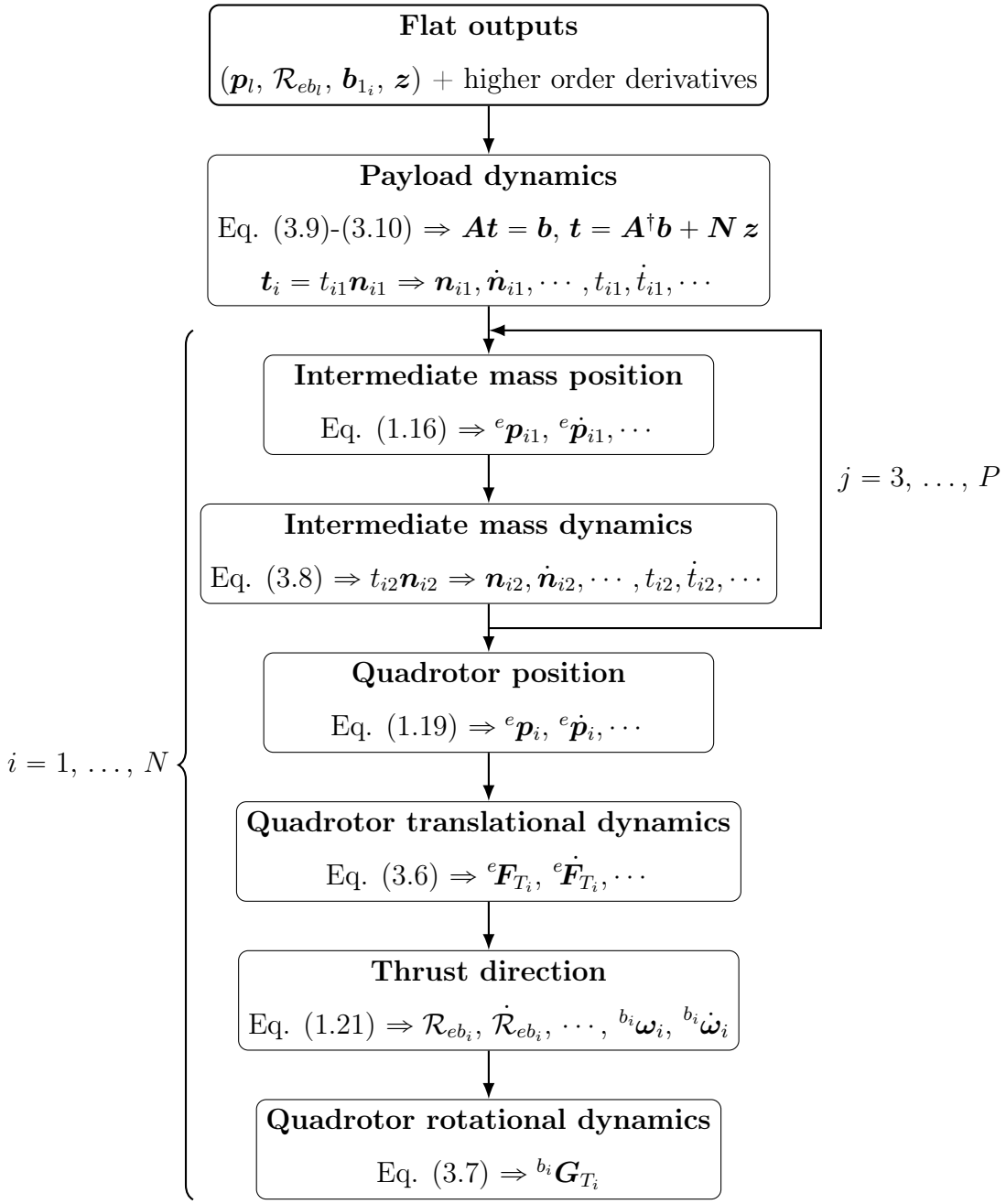

Figure 3.3: Reconstruction of system states and inputs through differential flatness

3.1.3 Time-Varying LQR Control

A finite-horizon time-varying LQR controller is designed to stabilize the linearized error dynamics. The optimal feedback law takes the form

$$\boldsymbol{u}(t) = \boldsymbol{u}_d(t) - \boldsymbol{K}(t)\delta\boldsymbol{x}(t) \tag{3.32}$$

where $\boldsymbol{u}_d(t) = [T_{i_d}, {}^{b_i}\boldsymbol{G}_{T_{i_d}}^{T}]^T$ is the nominal input evaluated from the differential flatness (Eqs. (3.28), (3.31)), and the time-varying state feedback gain $\boldsymbol{K}(t)$ is given by

$$\boldsymbol{K}(t) = \boldsymbol{R}^{-1}\boldsymbol{B}(t)^\top \boldsymbol{P}(t) \tag{3.33}$$

The matrix $\boldsymbol{P}(t)$ is computed by integrating backward in time the continuous-time Riccati differential equation

$$-\dot{\boldsymbol{P}}(t) = \boldsymbol{Q} - \boldsymbol{P}(t)\boldsymbol{B}(t)\boldsymbol{R}^{-1}\boldsymbol{B}(t)^\top \boldsymbol{P}(t) + \boldsymbol{A}(t)^\top \boldsymbol{P}(t) + \boldsymbol{P}(t)\boldsymbol{A}(t) \tag{3.34}$$

with terminal condition $\boldsymbol{P}(T) = \boldsymbol{P}_T$, where $\boldsymbol{P}_T \in \mathbb{R}^{n\times n}$ is a symmetric positive semi-definite matrix penalizing the terminal error. The weighting matrices $\boldsymbol{Q} \in \mathbb{R}^{n\times n}$ and $\boldsymbol{R} \in \mathbb{R}^{m\times m}$ are symmetric positive semi-definite, defined to penalize the state deviation and the control effort, respectively. The matrix $\boldsymbol{P}(t)$, solution of the Riccati differential equation (Eq. (3.34)), is computed offline, since the state-space matrices $\boldsymbol{A}(t)$, and $\boldsymbol{B}(t)$ depend only on the reference trajectory. The resulting values of $\boldsymbol{P}(t)$ are stored in a lookup table for online evaluation of the feedback gain.

3.2 Formation-Centered Control Architecture

In this section, the formation-fixed control architecture is described. A distributed cascaded control architecture is designed to maintain the UAVs in the desired formation while cooperatively transporting a common payload along a prescribed trajectory. To avoid dependence on an accurate model of the constrained dynamics and to eliminate the need for additional sensing, the load dynamics is not explicitly included in the control design. Instead, the payload is treated as an external disturbance acting on the formation, and the controller is designed to be robust to these unmodeled interaction forces.

The architecture features three nested control loops. At the upper control level, the multi-agent system is managed by a distributed leader-follower consensus-based control strategy, where a virtual leader has access to the reference trajectory. The control architecture involves sharing local information on the relative positions and velocities of the agents, while the knowledge of payload position is not necessary. The control inputs for each quadrotor are determined by inner loops on linear acceleration and attitude, based on the INDI method,

which allows for the development of linear controllers without the need to model aerodynamic actions and constraint forces, treated as disturbances [12]. INDI control is robust to neglected or poorly modeled dynamics [72].

The overall cascaded control architecture is sketched in Fig. 3.4. The trajectory controller (outer loop) manages the relative positions of the quadcopters to achieve the desired formation while following the prescribed trajectory realized by the virtual leader (Agent #1 in the figure), which has the same dynamic model as the other agents. Once a reference trajectory, defined in terms of position ${}^e\boldsymbol{p}_r$, velocity ${}^e\boldsymbol{v}_r$, and acceleration ${}^e\boldsymbol{a}_r$ as functions of time, is given to the leader, a distributed control law ${}^e\boldsymbol{a}_{c_i}$ is determined for the desired acceleration vector of each agent by assuming a double-integrator in place of its actual dynamics. Two INDI controllers generate reference commands on the attitude and thrust (middle loop) and manage the rotor rates (inner loop) to execute the acceleration command. Since the INDI-based inner loops compensate for aerodynamic and constraint forces, the translational dynamics of each quadrotor (Eq. (2.58)) is approximated by a double-integrator model, in which the outer-loop input directly governs the commanded acceleration.

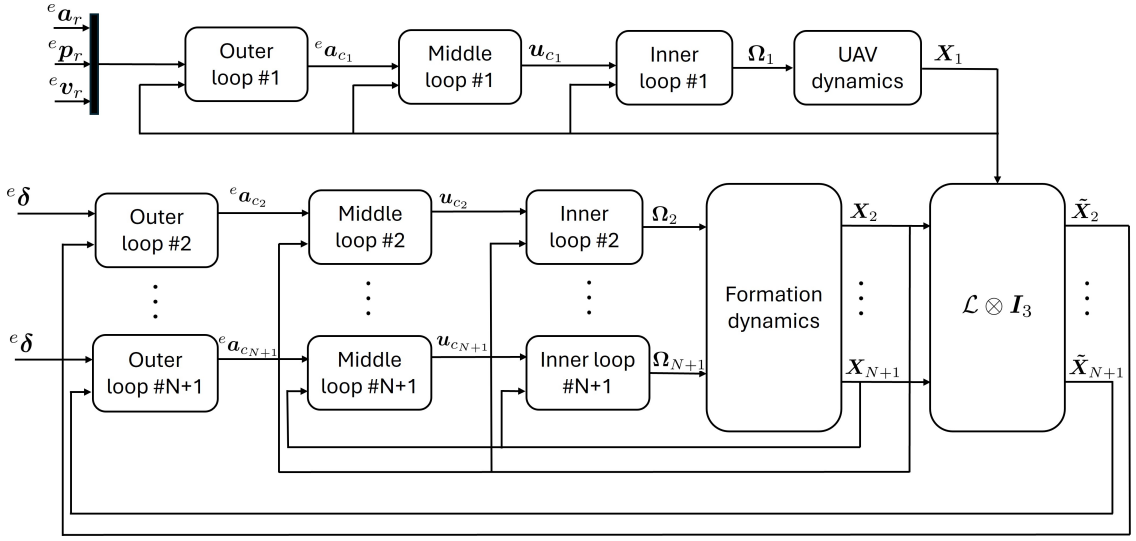

Figure 3.4: Cascaded control architecture for a formation of $N > 2$ agents and a virtual leader

3.2.1 Communication Topology

To achieve cooperative behavior in a consensus-based control strategy, agents need relative information about the state of their neighbors. The communication topology between vehicles is represented as a graph $\mathcal{G} = (\mathcal{V}, \mathcal{E})$, where $\mathcal{V} = \{v_1, v_2, \ldots, v_N\}$ is the set of nodes, and $\mathcal{E} \subseteq \mathcal{V} \times \mathcal{V}$ is the set of edges with ordered pairs of nodes. In this analogy, the nodes correspond to the agents, while the edges indicate the communication links. According to the classical graph theory used in multi-agent systems [87], the following definitions are introduced

- the Adjacency matrix $\mathcal{A} = [a_{ij}]$, that capture the interconnection between the follower agents, where $a_{ij} > 0$ if there is an edge from node j to node i, and 0 otherwise
- the Degree matrix $\mathcal{D}$, which encodes the number of incoming edges for each node. It is a diagonal matrix with entries $d_{ii} = \sum_{j=1}^{N} a_{ij}$
- the Laplacian matrix $\mathcal{L} = \mathcal{D} - \mathcal{A}$, that captures the global structure of the graph
- the Pinning matrix $\mathcal{B} = [b_{ii}]$, that describe the leader–follower interaction. It is a diagonal matrix with $b_{ii} > 0$ if follower i receives information directly from the leader, and 0 otherwise

The coefficients a_{ij} and b_{ii} in the adjacency and pinning matrices define the strength of the communication links among followers and between the followers and the leader, respectively. In the adjacency matrix, the magnitude of a_{ij} determines how strongly agent i reacts to the relative error with agent j. Large values of a_{ij} increase the local cohesion of the formation by emphasizing inter–agent consensus, whereas small values allow more flexibility but may slow down convergence. Similarly, the pinning coefficients b_{ii} specify the influence of the virtual leader on each follower. Increasing b_{ii} strengthens the tracking of the leader but can reduce the smoothness of the collective motion if the communication with neighbors is weak. From a global perspective, the matrices $\mathcal{L}$ and $\mathcal{B}$ jointly determine the overall coupling structure of the formation through the composite term $(\mathcal{L} + \mathcal{B})$. The ratio between inter–agent weights a_{ij} and leader–follower weights b_{ii} defines a trade–off between formation rigidity and responsiveness to the leader motion.

To enhance synchronization among the agents, is assumed that the communication topology among followers is modeled as a connected and undirected graph, while the virtual leader has direct communication links with each follower.

3.2.2 Formation Control

In the outer loop, both the leader and the followers are modeled using double integrator dynamics

$$\begin{cases} {}^{e}\dot{\boldsymbol{p}}_i = {}^{e}\boldsymbol{v}_i \\ {}^{e}\dot{\boldsymbol{v}}_i = \boldsymbol{u}_i \end{cases} \tag{3.35}$$

where $i = 1$ denotes the virtual leader, and $i = 2, \cdots, N+1$ the followers. The virtual leader is not influenced by the real agents and is controlled independently to track a given reference trajectory, using a proportional-derivative controller plus a feedforward term

$$\boldsymbol{u}_1 = -\boldsymbol{k}_{\mathbf{1}_p}({}^{e}\boldsymbol{p}_1 - {}^{e}\boldsymbol{p}_r) - \boldsymbol{k}_{\mathbf{1}_v}({}^{e}\boldsymbol{v}_1 - {}^{e}\boldsymbol{v}_r) + {}^{e}\boldsymbol{a}_r \tag{3.36}$$

The goal of the formation controller is to coordinate the motion of the follower agents so that they maintain a desired spatial configuration with respect to the virtual leader and to each other, while also achieving velocity alignment. Formally, agents are said to be in formation if their relative positions are equal to a set of desired offsets defined by a constant vector ${}^{e}\boldsymbol{\delta} = [{}^{e}\boldsymbol{\delta}_1^T, {}^{e}\boldsymbol{\delta}_2^T, \ldots, {}^{e}\boldsymbol{\delta}_{N+1}^T]^T$, where each ${}^{e}\boldsymbol{\delta}_i \in \mathbb{R}^3$ represents the desired position of agent i in formation, expressed in a fixed inertial frame. The agents converge to the desired formation if the actual relative positions converge to those defined by the formation offsets, i.e., ${}^{e}\boldsymbol{p}_i - {}^{e}\boldsymbol{p}_j \to {}^{e}\boldsymbol{\delta}_i - \boldsymbol{\delta}_j$ and $\boldsymbol{p}_i - {}^{e}\boldsymbol{p}_1 \to {}^{e}\boldsymbol{\delta}_i - {}^{e}\boldsymbol{\delta}_1$, and if velocity consensus is reached, i.e., ${}^{e}\boldsymbol{v}_i - {}^{e}\boldsymbol{v}_j \to 0$ and ${}^{e}\boldsymbol{v}_i - {}^{e}\boldsymbol{v}_1 \to 0$ as $t \to \infty$ [87]. To this end, the following distributed control law is proposed for each follower

$$\begin{aligned} \boldsymbol{u}_i = & -\boldsymbol{k}_p \left\{ \sum_{\substack{j=2 \\ j\neq i}}^{N+1} a_{ij}[({}^{e}\boldsymbol{p}_i - {}^{e}\boldsymbol{p}_j) - ({}^{e}\boldsymbol{\delta}_i - {}^{e}\boldsymbol{\delta}_j)] + b_{ii}\left[({}^{e}\boldsymbol{p}_i - {}^{e}\boldsymbol{p}_1) - ({}^{e}\boldsymbol{\delta}_i - {}^{e}\boldsymbol{\delta}_1)\right] \right\} \\ & -\boldsymbol{k}_v \left\{ \sum_{\substack{j=2 \\ j\neq i}}^{N+1} a_{ij}({}^{e}\boldsymbol{v}_i - {}^{e}\boldsymbol{v}_j) + b_{ii}({}^{e}\boldsymbol{v}_i - {}^{e}\boldsymbol{v}_1) \right\} + b_{ii}\,{}^{e}\dot{\boldsymbol{v}}_1 \end{aligned} \tag{3.37}$$

where ${}^{e}\dot{\boldsymbol{v}}_1 = \boldsymbol{u}_1$, expressed in Eq. (3.36). Defining the shifted positions ${}^{e}\hat{\boldsymbol{p}}_i = {}^{e}\boldsymbol{p}_i - {}^{e}\boldsymbol{\delta}_i$, and

${}^e\hat{\boldsymbol{p}}_1 = {}^e\boldsymbol{p}_1 - {}^e\boldsymbol{\delta}_1$, Eq. (3.37) is rewritten as

$$\begin{aligned}\boldsymbol{u}_i = & -\boldsymbol{k}_p \left\{ \sum_{\substack{j=2 \\ j\neq i}}^{N+1} a_{ij}({}^e\hat{\boldsymbol{p}}_i - {}^e\hat{\boldsymbol{p}}_j) + b_{ii}({}^e\hat{\boldsymbol{p}}_i - {}^e\hat{\boldsymbol{p}}_1) \right\} - \boldsymbol{k}_v \left\{ \sum_{\substack{j=2 \\ j\neq i}}^{N+1} a_{ij}({}^e\boldsymbol{v}_i - {}^e\boldsymbol{v}_j) + b_{ii}({}^e\boldsymbol{v}_i - {}^e\boldsymbol{v}_1) \right\} \\ & + b_{ii}\, {}^e\dot{\boldsymbol{v}}_1 \end{aligned} \tag{3.38}$$

Finally, the formation tracking error for each follower is defined as the deviation of its shifted position and velocity from those of the leader

$$\begin{bmatrix} {}^e\tilde{\hat{\boldsymbol{p}}}_{i1} \\ {}^e\tilde{\boldsymbol{v}}_{i1} \end{bmatrix} = \begin{bmatrix} {}^e\hat{\boldsymbol{p}}_i - {}^e\hat{\boldsymbol{p}}_1 \\ {}^e\boldsymbol{v}_i - {}^e\boldsymbol{v}_1 \end{bmatrix} \tag{3.39}$$

The resulting error dynamics is expressed in matrix form as

$$\begin{aligned} \begin{bmatrix} {}^e\dot{\tilde{\hat{\boldsymbol{p}}}} \\ {}^e\dot{\tilde{\boldsymbol{v}}} \end{bmatrix} &= \boldsymbol{A}_{cl} \begin{bmatrix} {}^e\tilde{\hat{\boldsymbol{p}}} \\ {}^e\tilde{\boldsymbol{v}} \end{bmatrix} + \begin{bmatrix} 0 \\ (\mathcal{B} - I_N) \otimes I_3 \end{bmatrix} {}^e\dot{\boldsymbol{v}}_1 \\ \boldsymbol{A}_{cl} &= \left(\begin{bmatrix} 0 & \mathcal{I} \\ -k_p(\mathcal{L}+\mathcal{B}) & -k_v(\mathcal{L}+\mathcal{B}) \end{bmatrix} \otimes I_3 \right) \end{aligned} \tag{3.40}$$

where $\otimes$ denotes the Kronecker product.

When all followers are directly connected to the virtual leader (i.e., $b_{ii} > 0$ for all i), the error dynamics in Eq. (3.40) reduce to a homogeneous linear system. In this case, the system is asymptotically stable if and only if $\boldsymbol{A}_{cl}$ is Hurwitz. Following Lemma 2.5 in [87], under the assumption of an undirected and connected communication topology among followers, and provided that at least one follower receives information from the leader, the matrix $(\mathcal{L} + \mathcal{B})$ is positive definite. It is worth noting that while the Laplacian matrix $\mathcal{L}$ of a connected follower graph is only positive semi-definite, possessing a single null eigenvalue associated with the consensus mode, the interaction with the leader, introduced by the pinning matrix $\mathcal{B}$, removes this indeterminacy, thus ensuring all eigenvalues of $(\mathcal{L} + \mathcal{B})$ are strictly positive. In the considered scenario, all followers receive information from the leader, so that the above condition is satisfied. It is worth remarking that it is required that at least one quadrotor receives information from the leader, and that the follower network is connected, whereas communication of the virtual leader with all quadrotors is not necessary in principle.

When not all followers are directly connected to the virtual leader, the term $(\mathcal{B} - \alpha I_N)\dot{\boldsymbol{v}}_1$

in Eq. (3.40) acts as an external forcing input proportional to the leader acceleration. In this case, the system is no longer homogeneous but remains input-to-state stable (ISS) with respect to this input, since $\mathcal{L}+\mathcal{B} > 0$. Consequently, if the leader acceleration $\dot{\boldsymbol{v}}_0$ is bounded, the formation tracking errors $\tilde{\hat{\boldsymbol{p}}}$ and $\tilde{\boldsymbol{v}}$ remain bounded.

Let $\lambda_i > 0$ be the i-th eigenvalue of $(\mathcal{L} + \mathcal{B})$. For the homogeneous error dynamics, the associated eigenvalues of the closed loop system are given by

$$\mu_{i\pm} = \frac{-k_v\lambda_i \pm \sqrt{(k_v\lambda_i)^2 - 4k_p\lambda_i}}{2} \tag{3.41}$$

Since all $\lambda_i > 0$ and both control gains (k_p, k_v) are strictly positive, it follows that $\mathrm{Re}(\mu_{i\pm}) < 0$ for all i. Therefore, the state matrix of the closed-loop system is Hurwitz, and the error converges to zero asymptotically.

The closed-loop system described in Eq. (3.40) is a MIMO system, where coupling between agents is introduced by the matrix $(\mathcal{L}+\mathcal{B})$ which, by construction, is symmetric and positive definite. As a result, it admits the eigendecomposition

$$(\mathcal{L} + \mathcal{B}) = Q\Lambda Q^T, \quad \Lambda = \mathrm{diag}(\lambda_1, \ldots, \lambda_N) \tag{3.42}$$

where Q is an orthogonal matrix whose columns are the normalized eigenvectors. The closed-loop matrix $\boldsymbol{A}_{cl}$ is thus written in a block-diagonal form as

$$\bar{\boldsymbol{A}}_{\mathrm{cl}} = \begin{bmatrix} A(\lambda_1) & 0 & \cdots & 0 \\ 0 & A(\lambda_2) & \ddots & \vdots \\ \vdots & \ddots & \ddots & 0 \\ 0 & \cdots & 0 & A(\lambda_N) \end{bmatrix} \otimes I_3 \tag{3.43}$$

where

$$A(\lambda_i) = \begin{bmatrix} 0 & 1 \\ -k_p\lambda_i & -k_v\lambda_i \end{bmatrix} \tag{3.44}$$

which corresponds to a second-order decoupled SISO subsystem, with characteristic equation given by

$$s^2 + \lambda_i(k_v s + k_p) = 0 \tag{3.45}$$

In practical implementations, communication delays may occur within the network. Here, a uniform delay $\tau > 0$ is considered on all communication channels, which corresponds to

$$(\mathcal{L} + \mathcal{B}) \longrightarrow e^{-s\tau}(\mathcal{L} + \mathcal{B}) \tag{3.46}$$

Accordingly, the characteristic equation in Eq. (3.45) becomes for the delayed system

$$s^2 + \lambda_i e^{-s\tau}(k_v s + k_p) = 0 \tag{3.47}$$

The stability of the delayed system is analyzed using the Nyquist criterion [88]. An upper bound on the admissible time-delay can be obtained by finding the smallest value of τ for which the characteristic equation (3.47) admits a purely imaginary root. To do so, substituting $s = j\omega$ ($\omega > 0$) in Eq. (3.47), and separating real and imaginary parts gives

$$\begin{cases} -\omega^2 + \lambda_i(k_p \cos(\omega\tau) + k_v\omega \sin(\omega\tau)) = 0 \\ \\ \lambda_i(k_v\omega \cos(\omega\tau) - k_p \sin(\omega\tau)) = 0 \end{cases} \tag{3.48}$$

From the imaginary part of Eq. (3.48), it follows

$$\tan(\omega\tau) = \frac{k_v}{k_p}\,\omega \tag{3.49}$$

Substituting Eq. (3.49) into the real part of Eq. (3.48) and simplifying leads to

$$\omega^4 = \lambda_i^2\big((k_v\omega)^2 + k_p^2\big) \tag{3.50}$$

Solving Eq. (3.50) for ω yields the crossing frequency

$$\omega_i = \sqrt{\frac{(\lambda_i k_v)^2 + \sqrt{(\lambda_i k_v)^4 + 4\lambda_i^2 k_p^2}}{2}} \tag{3.51}$$

The corresponding critical time-delay is then computed from Eq. (3.49) as

$$\tau_{\max}(\lambda_i) = \frac{1}{\omega_i}\,\arctan\!\left(\frac{k_v}{k_p}\,\omega_i\right) \tag{3.52}$$

The formation system is asymptotically stable if and only if all modal subsystems are stable,

i.e.,

$$\tau < \tau_c = \min_i \tau_{\max}(\lambda_i) = \tau_{\max}(\lambda_{\max}) \tag{3.53}$$

3.2.3 Linear Acceleration Control

The reference acceleration ${}^e\ddot{\boldsymbol{q}}_{i_c}$ ($\boldsymbol{u}_i$ in Eq. (3.37)) is tracked by an INDI controller that determines the commanded roll and pitch angles, as well as the thrust magnitude [12].
To this end, an incremental form of Eq. (2.58) is devised through a first-order Taylor series expansion, assuming that the control input $\boldsymbol{u}_c = [\phi_c, \theta_c, T_c]^T$, changes faster than the state $\boldsymbol{x}$, so that the derivatives with respect to $\boldsymbol{x}$ can be neglected compared to those with respect to $\boldsymbol{u}_c$. The derivatives of aerodynamic and constraint forces with respect to the controls are not included in the control synthesis, to avoid accurate modeling or measurement/estimation of cables and payload states. Although this introduces small errors in the predicted linear and angular accelerations, the measured accelerations depend on the above forces and moments, which are thus implicitly accounted for. In fact, neglecting these derivatives is equivalent to assuming that aerodynamic and constraint forces remain constant over each IMU measurement interval, while fast changes are captured by using a sufficiently high IMU sampling rate [72]. Omitting the subscript i from henceforth for brevity, the result is

$${}^e\ddot{\boldsymbol{q}} \simeq {}^e\ddot{\boldsymbol{q}}_0 + \boldsymbol{D}_u \Delta\boldsymbol{u} \tag{3.54}$$

where $\Delta\boldsymbol{u} = \boldsymbol{u}_c - \boldsymbol{u}_0$ is the control increment, with $\boldsymbol{u}_0$ the control vector at the previous time step, $t_0 = t - T_s$, being T_s the sample time. The Jacobian $\boldsymbol{D}_u$ is defined as

$$\boldsymbol{D}_u = \frac{1}{m}\left[\frac{\partial\, {}^e\boldsymbol{F}_T}{\partial\phi} \quad \frac{\partial\, {}^e\boldsymbol{F}_T}{\partial\theta} \quad \frac{\partial\, {}^e\boldsymbol{F}_T}{\partial T}\right]\Bigg|_{\boldsymbol{\Phi}=\boldsymbol{\Phi}_0, T=T_0} \tag{3.55}$$

which in explicit form reads

$$\boldsymbol{D}_u = \frac{1}{m}\begin{bmatrix} T(s_\phi s_\theta c_\psi - c_\phi s_\psi) & -T(c_\phi c_\theta c_\psi) & -(c_\phi s_\theta c_\psi + s_\phi s_\psi) \\ T(s_\phi s_\theta s_\psi + c_\phi c_\psi) & -T(c_\phi c_\theta s_\psi) & -(c_\phi s_\theta s_\psi - s_\phi c_\psi) \\ T(s_\phi c_\theta) & T(c_\phi s_\theta) & -c_\phi c_\theta \end{bmatrix} \tag{3.56}$$

The INDI control law is thus expressed by the inversion of Eq. (3.54), as

$$\Delta \boldsymbol{u} = \boldsymbol{D}_u^{-1}({}^e\ddot{\boldsymbol{q}}_c - {}^e\ddot{\boldsymbol{q}}_0) \tag{3.57}$$

The feasibility of the INDI control law in Eq. (3.57) depends on the invertibility of the Jacobian matrix $\boldsymbol{D}_u$. For a quadrotor, $\det(\boldsymbol{D}_u)$ is proportional to $T^2 \cos\phi$, which ensures that the inversion is well-defined only for $T > 0$ and $|\phi| < 90^\circ$, conditions that are always satisfied during normal flight. However, the thrust force is highly nonlinear in relation to pitch and roll angles. Consequently, when the commanded acceleration differs significantly from the current one (e.g., during an aggressive maneuver), leading to large input increments, the local linearity assumption used in Eq. (3.57) is no longer valid. In such cases, the control input increment computed by the controller produces an acceleration different from the desired one. This error will appear in the measured acceleration at the next time step, and subsequent input updates will gradually drive the system toward the correct acceleration. Since for a quadrotor the thrust force expression is known and invertible, instead of deriving the INDI controller through a first-order Taylor series expansion, it is preferably to find the increments in the input that provide the desired increment in acceleration by inverting the expression of the thrust [12], [72]. An incremental law for the acceleration can be obtained by subtracting from Eq. (2.58) the same expression evaluated a short time instant earlier

$${}^e\ddot{\boldsymbol{q}} - {}^e\ddot{\boldsymbol{q}}_0 = {}^e\boldsymbol{g} - {}^e\boldsymbol{g}_0 + \frac{1}{m}\left({}^e\boldsymbol{F}_T - {}^e\boldsymbol{F}_{T_0}\right) + \frac{1}{m}\left({}^e\boldsymbol{F}_A - {}^e\boldsymbol{F}_{A_0}\right) + \frac{1}{m}\left({}^e\boldsymbol{F}_{c_m} - {}^e\boldsymbol{F}_{c_{m_0}}\right) \tag{3.58}$$

Assuming that changes in gravity, aerodynamic forces, and constraint forces are small during this time step, which is a reasonable assumption for a sufficiently small sample time T_s, gives

$${}^e\ddot{\boldsymbol{q}} - {}^e\ddot{\boldsymbol{q}}_0 = \frac{1}{m}\left({}^e\boldsymbol{F}_T - {}^e\boldsymbol{F}_{T_0}\right) \tag{3.59}$$

that is rewritten as

$${}^e\boldsymbol{F}_T = m({}^e\ddot{\boldsymbol{q}}_c - {}^e\ddot{\boldsymbol{q}}_0) + {}^e\boldsymbol{F}_{T_0} \tag{3.60}$$

Each thrust component passes through a saturator. The vertical component ${}^eF_{T_z}$ is limited

in the interval

$$^{e}F_{T_z} \in [-T_{max}, k_{T_m}] \tag{3.61}$$

where T_{max} is the nominal maximum thrust that can be generated by a quadrotor and $k_{T_m} < 0$ is a minimum threshold which guarantees $T_c > 0$ and a finite interval for $^{e}F_{T_x}$ and $^{e}F_{T_y}$ (Eqs. (3.62) and (3.63)). The horizontal components $^{e}F_{T_x}$ and $^{e}F_{T_y}$ are limited in

$$^{e}F_{T_x} \in [k_\alpha \, ^{e}F_{T_z}, -k_\alpha \, ^{e}F_{T_z}] \tag{3.62}$$

$$^{e}F_{T_y} \in [k_\alpha \, ^{e}F_{T_z}, -k_\alpha \, ^{e}F_{T_z}] \tag{3.63}$$

where $k_\alpha = tan(\alpha_T)$ with $\alpha_T \in [\, 0, \frac{\pi}{2} \,)$ is a constant which limits the desired angle values. The desired values for the thrust modulus, roll, and pitch angles are now evaluated through a nonlinear inversion of the expression thrust vector projected in $\mathcal{F}_E$, that is

$$^{e}\boldsymbol{F}_T = \mathcal{R}_{EB} \begin{bmatrix} 0 \\ 0 \\ -T \end{bmatrix} = \begin{bmatrix} -T\left(\sin\phi\sin\psi + \cos\phi\cos\psi\sin\theta\right) \\ -T\left(\cos\phi\sin\psi\sin\theta - \cos\psi\sin\phi\right) \\ -T\left(\cos\phi\cos\theta\right) \end{bmatrix} \tag{3.64}$$

giving

$$T_c = \| \, ^{e}\boldsymbol{F}_T \| \tag{3.65}$$

$$\phi_c = \arcsin\left(\frac{-s_{\psi_r} \, ^{e}F_{T_x} + c_{\psi_r} \, ^{e}F_{T_y}}{T_c}\right) \tag{3.66}$$

$$\theta_c = 2\arctan\left(\frac{-c_{\psi_r} \, ^{e}F_{T_x} - s_{\psi_r} \, ^{e}F_{T_y}}{T_c\cos(\phi_c) - \, ^{e}F_{T_z}}\right) \tag{3.67}$$

where ψ_r is defined in the reference trajectory. Regarding the implementation of the discrete time controller, $^{e}\ddot{\boldsymbol{q}}_0$ is the output of a triaxial accelerometer filtered by a discrete low-pass second-order filter $H(s)$

$$H(s) = \frac{\omega_n^2}{s^2 + 2\zeta\omega_n s + \omega_n^2} \tag{3.68}$$

while the thrust force T_0 is evaluated as a quadratic function of the estimated rotor rates (see Eq. (2.67) in Sec. 2.3.2). The input signal $\boldsymbol{u}_0$ is also filtered to avoid time shifts with respect to $^{e}\ddot{\boldsymbol{q}}_0$. The control loop is sketched in Fig. 3.5.

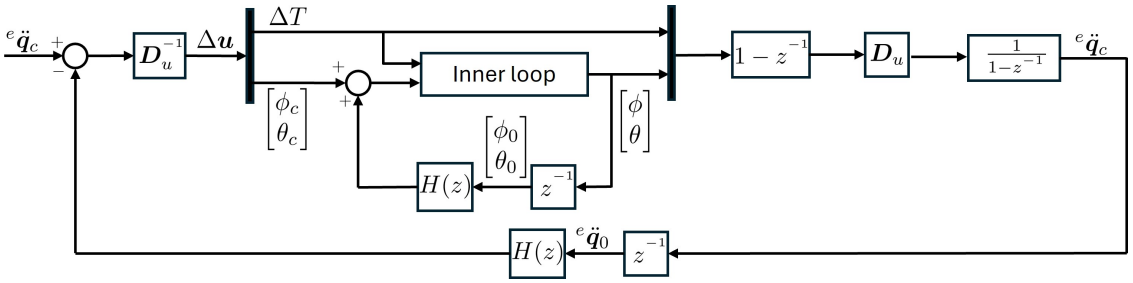

Figure 3.5: Middle control loop

3.2.4 Attitude Control

The inner control loop is designed to track the desired attitude $\boldsymbol{\Phi}_c = [\phi_c, \theta_c, \psi_{ref}]^T$, where the yaw angle ψ_{ref} is specified according to the formation management strategy adopted for the maneuver. The angular rate command is defined as

$$^b\boldsymbol{\omega}_c = \boldsymbol{T}^{-1}(\phi_c, \theta_c)\dot{\boldsymbol{\Phi}}_c \tag{3.69}$$

where $\dot{\boldsymbol{\Phi}}_c = \boldsymbol{K}_\Phi(\boldsymbol{\Phi}_c - \boldsymbol{\Phi})$, so that the reference signal is

$$^b\dot{\boldsymbol{\omega}}_c = \boldsymbol{K}_\omega(^b\boldsymbol{\omega}_c - {}^b\boldsymbol{\omega}) \tag{3.70}$$

being $\boldsymbol{K}_\Phi$ and $\boldsymbol{K}_\omega$ diagonal gain matrices. The expressions of thrust and angular rates are recalled from Sec. 2.3.2 for the design of the controller, as

$$\begin{bmatrix} T \\ {}^b\dot{\boldsymbol{\omega}} \end{bmatrix} = \begin{bmatrix} 0 \\ {}^b\boldsymbol{I}^{-1}\left({}^b\boldsymbol{G}_L\, {}^b + \boldsymbol{G}_{c_m} - {}^b\boldsymbol{\omega} \times {}^b\boldsymbol{I}\, {}^b\boldsymbol{\omega}\right) \end{bmatrix} + \hat{\boldsymbol{U}}(\boldsymbol{\Omega}) \tag{3.71}$$

where the input vector is $\boldsymbol{\Omega} = [\omega_1, \omega_2, \omega_3, \omega_4]^T$, $\hat{\boldsymbol{U}} = (\mathrm{diag}\{1, I_{xx}, I_{yy}, I_{zz}\})^{-1}\boldsymbol{U}$, and the pseudo-control vector $\boldsymbol{U}$ is given in Eq. (2.67). The incremental form of Eq. (3.71) is

$$\begin{bmatrix} T \\ {}^b\dot{\boldsymbol{\omega}} \end{bmatrix} = \begin{bmatrix} T_0 \\ {}^b\dot{\boldsymbol{\omega}}_0 \end{bmatrix} + \boldsymbol{D}_\Omega \Delta\boldsymbol{\Omega}_c \tag{3.72}$$

with $\boldsymbol{D}_\Omega = \partial\hat{\boldsymbol{U}}/\partial\boldsymbol{\Omega}\big|_{\boldsymbol{\Omega}=\boldsymbol{\Omega}_0}$, and $\Delta\boldsymbol{\Omega}_c = \boldsymbol{\Omega}_c - \boldsymbol{\Omega}_0$, while ${}^b\dot{\boldsymbol{\omega}}_0$, T_0, and $\boldsymbol{\Omega}_0$ are the angular acceleration, thrust, and rotor rates, respectively, at the previous time step. The gyroscopic and constraint moment derivatives with respect to the inputs are neglected. The explicit

expression of is given by

$$\boldsymbol{D}_{\Omega} = 2\begin{bmatrix} b\omega_{10} & b\omega_{20} & b\omega_{30} & b\omega_{40} \\ 0 & \frac{lb}{I_{xx}}\omega_{20} & 0 & -\frac{lb}{I_{xx}}\omega_{40} \\ -\frac{lb}{I_{yy}}\omega_{10} & 0 & \frac{lb}{I_{yy}}\omega_{30} & 0 \\ \frac{d}{I_{zz}}\omega_{10} & -\frac{d}{I_{zz}}\omega_{20} & \frac{d}{I_{zz}}\omega_{30} & -\frac{d}{I_{zz}}\omega_{40} \end{bmatrix} \tag{3.73}$$

Solving for the input commands in Eq. (3.72) yields

$$\Delta\boldsymbol{\Omega}_c = \boldsymbol{D}_{\boldsymbol{\Omega}}^{-1}\begin{bmatrix} T - T_0 \\ {}^b\dot{\boldsymbol{\omega}}_c - {}^b\dot{\boldsymbol{\omega}}_0 \end{bmatrix} \tag{3.74}$$

This control law relies on the inversion of $\boldsymbol{D}_{\Omega}$. As can be seen from its expression, the determinant $\det(\boldsymbol{D}_{\Omega})$ is proportional to the product of the individual rotor speeds $(\omega_{10}, \omega_{20}, \omega_{30}, \omega_{40})$. Consequently, the matrix is always invertible except when any one of the rotor speeds is zero. The control law in Eq. (3.74) computes the control increments $\Delta\boldsymbol{\Omega}_c$ by inverting the linearized control effectiveness matrix, $\boldsymbol{D}_{\boldsymbol{\Omega}}$. As shown in Sec. 3.2.3, a more accurate result is achieved by using a nonlinear inversion of the exact control effectiveness function (Eq. (2.67)). To do so, an incremental law for the angular acceleration is first obtained by subtracting from Eq. (2.59) the same expression evaluated a short time instant earlier

$$\begin{aligned} {}^b\dot{\boldsymbol{\omega}} - {}^b\dot{\boldsymbol{\omega}}_0 = {}^b\boldsymbol{I}^{-1}\{&\left({}^b\boldsymbol{G}_L - {}^b\boldsymbol{G}_{L_0}\right) + \left({}^b\boldsymbol{G}_T - {}^b\boldsymbol{G}_{T_0}\right) + \left({}^b\boldsymbol{G}_{c_m} - {}^b\boldsymbol{G}_{c_{m_0}}\right) \\ &- \left[\left({}^b\boldsymbol{\omega} \times {}^b\boldsymbol{I}\,{}^b\boldsymbol{\omega}\right) - \left({}^b\boldsymbol{\omega}_0 \times {}^b\boldsymbol{I}\,{}^b\boldsymbol{\omega}_0\right)\right]\} \end{aligned} \tag{3.75}$$

Assuming that changes in the aerodynamic moment, constraint moments, and angular momentum term are negligible during the sample time, this simplifies to

$${}^b\dot{\boldsymbol{\omega}} - {}^b\dot{\boldsymbol{\omega}}_0 = {}^b\boldsymbol{I}^{-1}\left({}^b\boldsymbol{G}_T - {}^b\boldsymbol{G}_{T_0}\right) \tag{3.76}$$

The control law is then defined by replacing the actual acceleration ${}^b\dot{\boldsymbol{\omega}}$ with its commanded value ${}^b\dot{\boldsymbol{\omega}}_c$, and solving for the desired control moment, ${}^b\boldsymbol{G}_{T_c}$

$${}^b\boldsymbol{G}_{T_c} = {}^b\boldsymbol{G}_{T_0} + {}^b\boldsymbol{I}\left({}^b\dot{\boldsymbol{\omega}}_c - {}^b\dot{\boldsymbol{\omega}}_0\right) \tag{3.77}$$

This desired control moment ${}^b\boldsymbol{G}_{T_c}$, together with the desired thrust module T_c from the outer loop (Section 3.2.3), forms the complete pseudo-control vector $\boldsymbol{U}_c = [T_c, {}^b\boldsymbol{G}_{T_c}^T]^T$. The desired motor speeds $\boldsymbol{\Omega}_c$ are then computed via the nonlinear inversion of Eq. (2.67). For the desired motor speeds to be achievable, each component of $\boldsymbol{\Omega}_c$ must satisfy the motor constraints

$$\omega_i^2 \in \left[0, \frac{T_{max}}{4b}\right] \tag{3.78}$$

In order to guarantee the condition (3.78), the desired pseudo-controls of each agent are saturated in the following intervals

$$T_c \in [0, k_T T_{max}] \tag{3.79}$$

$$|\tau_{\psi_r}| \in 4d\, k_\psi\ \boldsymbol{\Sigma} \tag{3.80}$$

$$|\tau_{\phi_c}| \in 2lb\,(1 - k_\psi)\ \boldsymbol{\Sigma} \tag{3.81}$$

$$|\tau_{\theta_c}| \in 2lb\,(1 - k_\psi)\ \boldsymbol{\Sigma} \tag{3.82}$$

where

$$\boldsymbol{\Sigma} = min\left(\left[0, \tfrac{T_c}{4b}\right], \left[\tfrac{T_c}{4b}, \tfrac{T_{max}}{4b}\right]\right) \tag{3.83}$$

$$0 < k_T < 1 \tag{3.84}$$

$$0 < k_\psi < 1 \tag{3.85}$$

The thresholds k_T and k_ψ ensure the presence of a of $\boldsymbol{\Omega}$ bandwidth dedicated to the attitude control.

The inner loop scheme is sketched in Fig. 3.6, where $\boldsymbol{A}(z)$ is the engine dynamics, and the agent model is given by Eq. (3.72). The angular acceleration is obtained by differentiation of the measured angular velocity provided by the IMU, where the same filter $H(z)$ is used to reduce the noise and for synchronization with the thrust command ($\Delta T = T - T_0$) evaluated in the middle loop. Rotor rates are estimated by assuming a first-order actuator dynamics $\boldsymbol{A}'(z)$ with time constant τ_e.

In the case of an an exact actuator model, that is, $\boldsymbol{A}'(z) = \boldsymbol{A}(z)$, and assuming that all actuators have the same dynamics, the closed-loop transfer function from ${}^b\dot{\boldsymbol{\omega}}_c$ to ${}^b\dot{\boldsymbol{\omega}}$ reduces to the diagonal matrix $\boldsymbol{A}(z) = \boldsymbol{\mathcal{I}}_{4\times4}A(z)$ so that the rotational DoFs are decoupled [71]. The

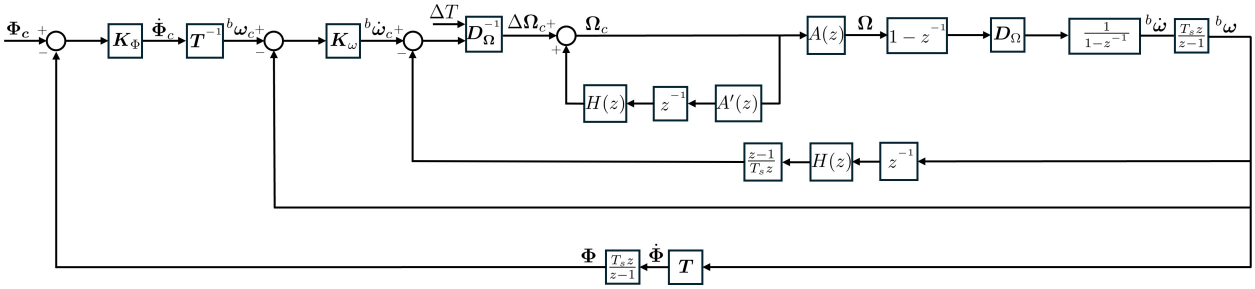

Figure 3.6: Inner control loop

control gain matrices are, therefore, diagonal matrices defined as $\boldsymbol{K}_\omega = \text{diag}\{K_{\omega_1}, K_{\omega_2}, K_{\omega_3}\}$, and $\boldsymbol{K}_\Phi = \text{diag}\{K_{\Phi_1}, K_{\Phi_2}, K_{\Phi_3}\}$, respectively. The transfer function from $\boldsymbol{\Phi}_c$ to $\boldsymbol{\Phi}$ is given, for each axis, by

$$T_{\Phi_{c_i}\to\Phi_i}(z) = \frac{K_{\Phi_i} K_{\omega_i} T_s^2 A(z)}{(z-1)^2 + K_{\omega_i} T_s (z-1) A(z) + K_{\Phi_i} K_{\omega_i} T_s^2 A(z)} \tag{3.86}$$

Since the closed-loop transfer function from the components of the commanded linear acceleration, namely, ${}^e\ddot{q}_{c_i}$ to ${}^e\ddot{q}_i$, is equal to $T_{\Phi_{c_i}\to\Phi_i}(z)$, it follows that translational motion is described by a double-integrator dynamics if the Euler's angles converge to their commanded values.

The attitude controller operates as a quasi-static subsystem within a much slower bandwidth of the formation control, which allows the latter to be designed based on a double-integrator model. Accelerations due to external forces and moments, neglected in Eqs. (3.57) and (3.74), respectively, are treated as external disturbances, expressed as

$$\boldsymbol{d}_{\ddot{\boldsymbol{q}}}(z) = \frac{1}{m}({}^e\boldsymbol{F}_A + {}^e\boldsymbol{F}_{c_m}) \tag{3.87}$$

$$\boldsymbol{d}_{\dot{\boldsymbol{\omega}}}(z) = {}^b\boldsymbol{I}^{-1}\left({}^b\boldsymbol{G}_L + {}^b\boldsymbol{G}_A + {}^b\boldsymbol{G}_{c_m} - {}^b\boldsymbol{\omega} \times {}^b\boldsymbol{I}\,{}^b\boldsymbol{\omega}\right) \tag{3.88}$$

and, according to the schemes in Figs. 3.5 and 3.6, the transfer functions

$$\boldsymbol{T}_{\boldsymbol{d}_{\ddot{\boldsymbol{q}}}\to\ddot{\boldsymbol{q}}}(z) = \boldsymbol{\mathcal{I}}\left[1 - T_{\Phi_c\to\Phi}(z) H(z) z^{-1}\right] \tag{3.89}$$

and

$$\boldsymbol{T}_{\boldsymbol{d}_{\dot{\boldsymbol{\omega}}}\to\dot{\boldsymbol{\omega}}}(z) = \boldsymbol{\mathcal{I}}\left[1 - A(z) H(z) z^{-1}\right] \tag{3.90}$$

show that the disturbances on linear and angular accelerations go to zero, respectively, for

stable attitude dynamics and as long as the actuator and filter dynamics are stable [71].

3.3 Collision/Obstacle Avoidance

In this section, an obstacle-avoidance strategy for the entire formation–payload system is proposed within the formation-centered framework. The underlying idea is that, by ensuring the virtual leader maintains a sufficiently large safety distance from obstacles, the entire formation, including the payload, avoids collisions. Consequently, only the virtual leader needs to have knowledge of the obstacles positions and dimensions.

The proposed approach is implemented within the framework of Control Barrier Functions (CBFs) [89], which provides a rigorous method to impose safety constraints on nonlinear dynamical systems. CBFs ensure the forward invariance of a safe set $\mathcal{C}$, guaranteeing that if the system state begins in $\mathcal{C}$, it remains there for all future time. In the following, CBF–based constraints are formulated for both the virtual leader and the individual quadrotors. The leader–level CBF ensures obstacle avoidance for the entire formation–payload system, while agent–level CBFs prevent inter–agent collisions. In the present framework, the CBFs are incorporated into the outer loop of the cascade control architecture described in Section 3.2.2. Accordingly, each quadrotor and the virtual leader are modeled as a second–order system as in Eq. (3.35). Since the control acceleration $\boldsymbol{u}_i$ appears only in the second derivative of the position, any safety function $h({}^e\boldsymbol{p}_i)$ depending on position has a relative degree two with respect to (3.35). That is, $L_g h({}^e\boldsymbol{p}_i) = 0$ and $L_g L_f h({}^e\boldsymbol{p}_i) \neq 0$, so the standard first–order CBF condition [90] cannot be directly applied. Instead, an Exponential Control Barrier Function (ECBF) [91] is employed, which generalizes the CBF framework to systems with higher relative degree.

Definition 11 (Exponential Control Barrier Function for Relative Degree Two Systems [91])**.** *Consider the affine control system $\dot{x} = f(x) + g(x)u$ with f, g locally Lipschitz. Let $h : \mathcal{D} \to \mathbb{R}$ be twice continuously differentiable and define the safe set $\mathcal{C} = \{x \in \mathcal{D} \mid h(x) \geqslant 0\}$. If h has relative degree two, then h is an* Exponential Control Barrier Function (ECBF) *if there exist constants $k_1, k_2 > 0$ such that*

$$L_f^2 h(x) + L_g L_f h(x)\, u + k_1 L_f h(x) + k_2 h(x) \geqslant 0. \tag{3.91}$$

Any locally Lipschitz feedback law $u(x)$ satisfying (3.91) *renders $\mathcal{C}$ forward invariant.*

The application to inter–agent separation is presented first. For the dynamics (3.35), the pairwise safety constraint between agents i and j is encoded by

$$h_{ij}({}^e\boldsymbol{p}_i, {}^e\boldsymbol{p}_j) = \| {}^e\boldsymbol{p}_i - {}^e\boldsymbol{p}_j\|^2 - \Delta^2, \tag{3.92}$$

where $\Delta > 0$ denotes the prescribed minimum separation distance. Differentiating (3.92) along (3.35) gives

$$\dot{h}_{ij} = 2({}^e\boldsymbol{p}_i - {}^e\boldsymbol{p}_j)^T({}^e\boldsymbol{v}_i - {}^e\boldsymbol{v}_j), \tag{3.93}$$

$$\ddot{h}_{ij} = 2({}^e\boldsymbol{v}_i - {}^e\boldsymbol{v}_j)^T({}^e\boldsymbol{v}_i - {}^e\boldsymbol{v}_j) + 2({}^e\boldsymbol{p}_i - {}^e\boldsymbol{p}_j)^T({}^e\boldsymbol{a}_i - {}^e\boldsymbol{a}_j) \tag{3.94}$$

Substituting (3.93)–(3.94) into (3.91) yields the affine constraint

$$\boldsymbol{A}_{ij}\boldsymbol{u} \geqslant b_{ij}, \tag{3.95}$$

where $\boldsymbol{u} = [\boldsymbol{u}_i^T, \boldsymbol{u}_j^T]^T$

$$\begin{aligned} \boldsymbol{A}_{ij} &= [2({}^e\boldsymbol{p}_i - {}^e\boldsymbol{p}_j)^T, -2({}^e\boldsymbol{p}_i - {}^e\boldsymbol{p}_j)^T] \\ b_{ij} &= -2({}^e\boldsymbol{v}_i - {}^e\boldsymbol{v}_j)^T({}^e\boldsymbol{v}_i - {}^e\boldsymbol{v}_j) - k_1\dot{h}_{ij} - k_2 h_{ij} \end{aligned} \tag{3.96}$$

Equation (3.95) is the centralized ECBF constraint for the pair (i, j). Following the developments in [90], the pairwise safety barrier constraint in Eq. (3.95) is distributed by assigning to each agent one half of the safety requirement

$$2({}^e\boldsymbol{p}_i - {}^e\boldsymbol{p}_j)^T\boldsymbol{u}_i \geqslant \frac{1}{2}b_{ij} \tag{3.97}$$

$$-2({}^e\boldsymbol{p}_i - {}^e\boldsymbol{p}_j)^T\boldsymbol{u}_j \geqslant \frac{1}{2}b_{ij} \tag{3.98}$$

If both agents satisfy their local inequalities, the sum of the two conditions exactly reconstructs the centralized constraint, thereby guaranteeing pairwise safety in a decentralized fashion.

Following [91], the ECBF constraint (3.97) is enforced by solving, at each time step, a

Quadratic Program (QP)

$$\boldsymbol{u}_i^\star = \arg\min_{\boldsymbol{u}_i} \|\boldsymbol{u}_i - \boldsymbol{u}_{i,\text{des}}\|^2 \tag{3.99}$$

$$\text{subject to: } \bar{\boldsymbol{A}}_{ij}\boldsymbol{u}_i \geqslant \bar{b}_{ij}, \quad \forall j \in \mathcal{N}_i, \tag{3.100}$$

$$\|\boldsymbol{u}_i\|_\infty \leqslant u_{i,\max}, \tag{3.101}$$

where $\mathcal{N}_i$ denotes the set of neighboring agents, $\boldsymbol{u}_{i,\text{des}}$ is the nominal acceleration command in Eq. (3.37), $\bar{\boldsymbol{A}}_{ij} = 2({}^e\boldsymbol{p}_i - {}^e\boldsymbol{p}_j)^T$, and $\bar{b}_{ij} = \frac{1}{2}b_{ij}$. The additional constraint (3.101) limits the commanded acceleration within the feasible actuation range of each quadrotor, ensuring physical realizability.

The QP–based ECBF (3.102) acts as a high–level safety filter that modifies the nominal acceleration only when a safety constraint is close to being violated. In practice, however, the decentralized ECBF constraints (3.97) and the actuation limits (3.101) may become conflicting, for instance when the acceleration required to guarantee safety exceeds the physical capabilities of the quadrotor. To avoid infeasibility in such cases, a small slack variable $s_i \geqslant 0$ is introduced as in [89]

$$\boldsymbol{u}_i^\star = \arg\min_{\boldsymbol{u}_i, s_i} \|\boldsymbol{u}_i - \boldsymbol{u}_{i,\text{des}}\|^2 + w_s s_i^2 \tag{3.102}$$

$$\text{subject to: } \bar{\boldsymbol{A}}_{ij}\boldsymbol{u}_i \geqslant \bar{b}_{ij} - s_i, \quad \forall j \in \mathcal{N}_i, \tag{3.103}$$

$$\|\boldsymbol{u}_i\|_\infty \leqslant u_{i,\max}, \tag{3.104}$$

$$s_i \geqslant 0 \tag{3.105}$$

with $w_s \gg 1$.

The same ECBF framework is used to enforce obstacle avoidance for the virtual leader. Let ${}^e\boldsymbol{p}_1$ denote the leader position, and let ${}^e\boldsymbol{p}_{\text{obj}}$ and r_{obj} be the obstacle center and radius, respectively. Define the safety function

$$h_1({}^e\boldsymbol{p}_1) = \|{}^e\boldsymbol{p}_1 - {}^e\boldsymbol{p}_{\text{obj}}\|^2 - (r_{\text{obj}} + \Delta_{\text{safe}})^2,$$

Differentiating h_1 along the leader dynamics yields

$$\dot{h}_1 = 2({}^{e}\boldsymbol{p}_1 - {}^{e}\boldsymbol{p}_{\text{obj}})^T {}^{e}\boldsymbol{v}_1, \tag{3.106}$$

$$\ddot{h}_1 = 2\ {}^{e}\boldsymbol{v}_1^T {}^{e}\boldsymbol{v}_1 + 2({}^{e}\boldsymbol{p}_1 - {}^{e}\boldsymbol{p}_{\text{obj}})^T \boldsymbol{u}_1 \tag{3.107}$$

Substituting into the ECBF condition (3.91) gives the affine constraint

$$\boldsymbol{A}_1 \boldsymbol{u}_1 \geqslant b_1, \tag{3.108}$$

$$\boldsymbol{A}_1 = 2({}^{e}\boldsymbol{p}_1 - {}^{e}\boldsymbol{p}_{\text{obj}})^T, \tag{3.109}$$

$$b_1 = -2\ {}^{e}\boldsymbol{v}_1^T {}^{e}\boldsymbol{v}_1 - k_1 \dot{h}_1 - k_2 h_1. \tag{3.110}$$

This constraint is incorporated into the leader QP in the same fashion as the inter–agent constraints, together with the actuator limits (3.101), ensuring that the safe trajectory generated by the virtual leader remains dynamically feasible for the quadrotors.

Chapter 4

Results and Discussions

In this chapter, the performance of the proposed control architectures is assessed through both numerical simulations and flight tests. The objective is to evaluate the capability of the developed controllers to ensure stable and accurate motion of a cooperative multi–UAV system transporting a rigid-body payload via flexible cables.

A formation of four Parrot Bebop 2 quadcopters is considered. The main parameters of the quadcopters, along with those of the cables and the payload, are reported in Table 4.1.

All numerical simulations are implemented in the MATLAB/Simulink environment using a fixed-step Runge–Kutta (ode4) solver with a time step of 0.005 s.

The consensus-based leader–follower formation control strategy described in Sec. 3.2.2 was experimentally tested in the ISAE–SUPAERO laboratory using Parrot Bebop 2 quadrotors and a motion–capture system.

Table 4.1: System parameters

Name	Parameter	Value	Unit
Quadrotor			
Mass	m	0.608	kg
Inertia on x axis	I_{xx}	1.81×10^{-3}	$\mathrm{kg\,m^2}$
Inertia on y axis	I_{yy}	1.76×10^{-3}	$\mathrm{kg\,m^2}$
Inertia on z axis	I_{zz}	3.33×10^{-3}	$\mathrm{kg\,m^2}$
Thrust coefficient	b	1.9×10^{-6}	$\mathrm{N/(rad/s)^2}$
Torque coefficient	d	2.5×10^{-8}	$\mathrm{Nm/(rad/s)^2}$
Equivalent flat-plate areas	A_x	4.51×10^{-2}	$\mathrm{m^2}$
	A_y	4.51×10^{-2}	$\mathrm{m^2}$
	A_z	0.354	$\mathrm{m^2}$
Rotor inertia	J_r	5.0×10^{-3}	$\mathrm{kg\,m^2}$
Arm length	l	14.5×10^{-2}	m
Cable attachment point	${}^{b_i}\boldsymbol{r}_i$	$[0, 0, -0.03]^T$	m
Maximum thrust	T_{max}	14	N
Load			
Dimensions	$l_x \times l_y \times l_z$	$2 \times 2 \times 0.2$	m
Mass	m_l	1.2	kg
Inertia on x axis	I_{xx_l}	0.41	$\mathrm{kg\,m^2}$
Inertia on y axis	I_{yy_l}	0.41	$\mathrm{kg\,m^2}$
Inertia on z axis	I_{zz_l}	0.81	$\mathrm{kg\,m^2}$
Drag coefficient	C_{d_l}	1.05	
Reference area	A_l	0.4	$\mathrm{m^2}$
1-st cable attachment point	${}^{b_l}\boldsymbol{r}_{l_1}$	$[1, 1, -0.1]^T$	m
2-nd cable attachment point	${}^{b_l}\boldsymbol{r}_{l_2}$	$[-1, 1, -0.1]^T$	m
3-rd cable attachment point	${}^{b_l}\boldsymbol{r}_{l_3}$	$[-1, -1, -0.1]^T$	m
4-th cable attachment point	${}^{b_l}\boldsymbol{r}_{l_4}$	$[1, -1, -0.1]^T$	m
Cable			
no. of links		4	
Mass of the element	$m_{p_{ij}}$	0.01	kg
Drag coefficient (sphere)	$C_{d_{m_{p_{ij}}}}$	0.5	
Reference area	$A_{m_{p_{ij}}}$	0.008	$\mathrm{m^2}$
Cable length	l_c	2	m

4.1 Trim in Hovering

A trim evaluation method is proposed to determine the equilibrium configuration in hovering, which serves as the initial condition for subsequent simulation tests.

The swarm-load dynamics can be rewritten as

$$\dot{\boldsymbol{X}} = f\left(\boldsymbol{X}, \dot{\boldsymbol{X}}, \boldsymbol{\Omega}\right) \tag{4.1}$$

where $\boldsymbol{X}$ is the aggregate state of the swarm-load system composed by $\boldsymbol{X}_i$, $\boldsymbol{X}_l$, and $\boldsymbol{X}_{p_{ij}}$ defined as

$$\boldsymbol{X}_i = \begin{bmatrix} \phi_i & p_i & \theta_i & q_i & \psi_i & r_i & x_i & \dot{x}_i & y_i & \dot{y}_i & z_i & \dot{z}_i \end{bmatrix}^T \tag{4.2}$$

$$\boldsymbol{X}_l = \begin{bmatrix} \phi_l & p_l & \theta_l & q_l & \psi_l & r_l & x_l & \dot{x}_l & y_l & \dot{y}_l & z_l & \dot{z}_l \end{bmatrix}^T \tag{4.3}$$

$$\boldsymbol{X}_{p_{ij}} = \begin{bmatrix} x_{p_{ij}} & \dot{x}_{p_{ij}} & y_{p_{ij}} & \dot{y}_{p_{ij}} & z_{p_{ij}} & \dot{z}_{p_{ij}} \end{bmatrix}^T \tag{4.4}$$

for $i = 1, \cdots, N$, $j = 1, \cdots, P$. The trim condition is the solution of the non-linear system obtained by setting $\dot{\boldsymbol{X}} = 0$

$$\mathbf{0} = f\left(\boldsymbol{X}, \mathbf{0}, \boldsymbol{\Omega}\right) \tag{4.5}$$

and the hovering condition is specified as

$$\boldsymbol{X}_i = \begin{bmatrix} \phi_i & 0 & \theta_i & 0 & \psi_i & 0 & x_i & 0 & y_i & 0 & z_i & 0 \end{bmatrix}^T \tag{4.6}$$

$$\boldsymbol{X}_l = \begin{bmatrix} \phi_l & 0 & \theta_l & 0 & \psi_l & 0 & x_l & 0 & y_l & 0 & z_l & 0 \end{bmatrix}^T \tag{4.7}$$

$$\boldsymbol{X}_{p_{ij}} = \begin{bmatrix} x_{p_{ij}} & 0 & y_{p_{ij}} & 0 & z_{p_{ij}} & 0 \end{bmatrix}^T \tag{4.8}$$

In order to obtain a solution of Eq. (4.5) with conditions (4.6), (4.7) and (4.8), the following assumption are introduced

- The load Euler angles are $\boldsymbol{\Phi}_l = [0, 0, 0]^T$
- The vector ${}^{b_i}\boldsymbol{r}_i$ has the form ${}^{b_i}\boldsymbol{r}_i = [0\ 0\ w]^T$ with $w > 0$ and ${}^{b_i}\boldsymbol{r}_i \in \Pi_{i_Z}$, where Π_{i_Z} is the vertical plane passing through the attachment point of the i-th cable on the load and the c.g. of the i-th agent.
- ${}^{e}\boldsymbol{p}_{p_{ij}} \in \Pi_{i_Z}$
- The yaw angles of the agents are $\psi_i = 0$
- All the point masses are equal, $m_{p_{ij}} = m_p$
- Each agent carries $1/N$ of the load weight
- The swarm geometry is such that the trim with the above conditions is possible

The positions of the agents ${}^e\boldsymbol{p}_i$ and the load ${}^e\boldsymbol{p}_l$ are fixed while the unknowns are the angles ϕ_i, θ_i, the positions of the element masses ${}^e\boldsymbol{p}_{p_{ij}}$, and the control vector $\boldsymbol{\Omega}$. The problem of finding a solution is simplified by considering the geometry of the i-th cable in Π_{i_Z} (Fig. 4.1), and setting the length of the cable elements l_{c_p} and the side constraint force α, parallel to the $x-y$ plane, as unknowns.

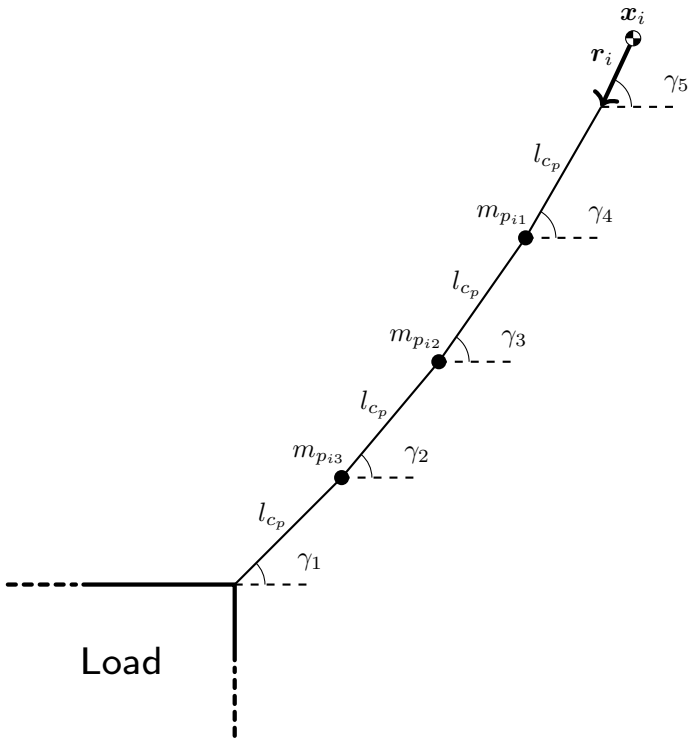

Figure 4.1: Geometry of the i-th cable in Π_{i_Z}

The system (4.5) then becomes

$$\begin{cases} l_{c_p}\left(sin\gamma_1 + sin\gamma_2 + sin\gamma_3 + sin\gamma_4\right) + \|{}^{b_i}\boldsymbol{r}_i\| sin\gamma_5 = |z_l + r_{z_{l_i}} - z_i| \\ l_{c_p}\left(cos\gamma_1 + cos\gamma_2 + cos\gamma_3 + cos\gamma_4\right) + \|{}^{b_i}\boldsymbol{r}_i\| cos\gamma_5 = \|\hat{\boldsymbol{x}}_l + \hat{\boldsymbol{r}}_{l_i} - \hat{\boldsymbol{x}}_i\| \end{cases} \tag{4.9}$$

where

$$\gamma_k = tan^{-1}\frac{\frac{\|{}^e\boldsymbol{F}_{g_l}\|}{N} + (k-1)\|{}^e\boldsymbol{F}_{g_p}\|}{|\alpha|} \quad \text{with } k = 1, \cdots, 4 \tag{4.10}$$

$$\gamma_5 = tan^{-1}\frac{\frac{\|{}^e\boldsymbol{F}_{g_l}\|}{N} + 3\|{}^e\boldsymbol{F}_{g_p}\| + \|{}^e\boldsymbol{F}_{g_i}\|}{|\alpha|} \tag{4.11}$$

$$\hat{\boldsymbol{x}}_l = [x_l, y_l]^T \tag{4.12}$$

$$\hat{\boldsymbol{r}}_{l_i} = \left[r_{x_{l_i}}, r_{y_{l_i}}\right]^T \tag{4.13}$$

$$\hat{\boldsymbol{x}}_i = [x_i, y_i]^T \tag{4.14}$$

and the solution is obtained trough the non-linear Matlab solver $fsolve$.

Now, the problem is to obtain ϕ_i, θ_i, $\boldsymbol{x}_{p_{ij}}$, and $\boldsymbol{\Omega}$ from α and l_{c_p}. The position vector $\boldsymbol{r}_i$ of the attachment point, known in $\mathcal{F}_B$, is expressed in $\mathcal{F}_E$ as

$$
{}^{e}\boldsymbol{r}_i = -\|{}^{b_i}\boldsymbol{r}_i\| \begin{bmatrix} s_{l_i}\sqrt{\frac{1-sin^2\gamma_5}{1+\beta_i^2}} \\ \beta_i\, s_{l_i}\sqrt{\frac{1-sin^2\gamma_5}{1+\beta_i^2}} \\ -sin\gamma_5 \end{bmatrix} \tag{4.15}
$$

where

$$
\beta_i = \left(\frac{r_{y_{l_i}} - y_l}{r_{x_{l_i}} - x_l}\right) \tag{4.16}
$$

$$
s_{l_i} = \text{sign}(r_{x_{l_i}}) \tag{4.17}
$$

The comparison between ${}^{e}\boldsymbol{r}_i$ and ${}^{b_i}\boldsymbol{r}_i$, given by

$$
{}^{e}\boldsymbol{r}_i = \mathcal{R}_{EB_i}\, {}^{b_i}\boldsymbol{r}_i \tag{4.18}
$$

provides the initial Euler angles for the i-th agent as

$$
\phi_{i_0} = sin^{-1}\left(-\frac{{}^{e}r_{y_i}}{\|{}^{b_i}\boldsymbol{r}_i\|}\right) \tag{4.19}
$$

$$
\theta_{i_0} = sin^{-1}\left(\frac{-\,{}^{e}r_{x_i}}{\|{}^{b_i}\boldsymbol{r}_i\| cos\phi_i}\right) \tag{4.20}
$$

while the initial positions for the point masses are given by

$$
\boldsymbol{x}_{p_{i3_0}} = \boldsymbol{x}_l + \boldsymbol{r}_{l_i} + l_{c_p} \begin{bmatrix} s_{l_i}\sqrt{\frac{1-sin^2\gamma_1}{1+\beta_i^2}} \\ \beta_i\, s_{l_i}\sqrt{\frac{1-sin^2\gamma_1}{1+\beta_i^2}} \\ -sin\gamma_1 \end{bmatrix} \tag{4.21}
$$

$$
\boldsymbol{x}_{p_{ij_0}} = \boldsymbol{x}_{p_{ij+1}} + l_{c_p} \begin{bmatrix} s_{l_i}\sqrt{\frac{1-sin^2\gamma_j}{1+\beta_i^2}} \\ \beta_i\, s_{l_i}\sqrt{\frac{1-sin^2\gamma_j}{1+\beta_i^2}} \\ -sin\gamma_j \end{bmatrix} \quad \text{for } j = 1, 2 \tag{4.22}
$$

Finally, the initial thrust for the i-th agent is

$$
T_{i_0} = \sqrt{\left(\frac{\|{}^{e}\boldsymbol{F}_{g_l}\|}{N} + 3\|{}^{e}\boldsymbol{F}_{g_p}\| + \|{}^{e}\boldsymbol{F}_{g_i}\|\right)^2 + \alpha^2} \tag{4.23}
$$

while the initial control moments components are

$$\begin{bmatrix} \tau_{\phi_{i_0}} \\ \tau_{\theta_{i_0}} \\ \tau_{\psi_{i_0}} \end{bmatrix} = \mathcal{R}_{B_i E} \left\{ {}^{e}\boldsymbol{r}_i \times \left(\sqrt{\left(\frac{\| {}^{e}\boldsymbol{F}_{g_l} \|}{N} + 3 \| {}^{e}\boldsymbol{F}_{g_p} \| \right)^2 + \alpha^2} \begin{bmatrix} s_{l_i} \sqrt{\frac{1-sin^2\gamma_4}{1+\beta_i^2}} \\ \beta_i \, s_{l_i} \sqrt{\frac{1-sin^2\gamma_4}{1+\beta_i^2}} \\ -sin\gamma_4 \end{bmatrix} \right) \right\} \tag{4.24}$$

Equations (2.67) with Eqs. (4.23) and (4.24), provide the initial control vector $\boldsymbol{\omega}_{c_{i_0}}$.

4.2 Load-Leading Control

The performance of the LQR controller are analyzed in this section. The simulations are carried out using the nonlinear model developed on the manifold presented in Sec. 2.5. The analysis is conducted both in nominal condition, and taking into account the effects of parameter uncertainties, and communication delays. Two representative scenarios are considered. In the first case, the controller is tasked with stabilizing the payload from an initial condition characterized by large angular deviations of both the load and suspension cables. In the second case, the controller tracking performance is evaluated by imposing a time-varying reference trajectory for the payload center of mass. The following weights are used in the LQR synthesis

$$\boldsymbol{Q} = 0.5\mathcal{I}_{(12+6PN+6N)} \tag{4.25}$$

$$\boldsymbol{R} = 0.2\mathcal{I}_{(4N)} \tag{4.26}$$

$$\boldsymbol{P}_T = 0.01\mathcal{I}_{(12+6PN+6N)} \tag{4.27}$$

To evaluate the controller performance, the position and attitude errors of the payload, together with the deviations of the cable directions and the quadrotor attitudes from their equilibrium values, are analyzed. Since the equations of motion are written on the configuration manifold, configuration errors, as described in Sec. 2.4, are considered.
The payload position error is defined as the Euclidean norm of the difference between the actual and desired payload positions

$$\boldsymbol{e}_{p_l} = \| {}^{e}\boldsymbol{p}_l - {}^{e}\boldsymbol{p}_{l_d} \| \tag{4.28}$$

The attitude error of each link, denoted by $\Psi_{n_{ij}}$, is defined in Eq. (2.133), whereas the

attitude error of the quadrotors and the payload, $\Psi_{\mathcal{R}}$, is defined in Eq. (2.100). For clarity of presentation, instead of showing the four individual link errors for each cable, the mean links attitude error for the i-th cable is considered, defined as

$$\bar{\Psi}_{n_i}(t) = \frac{1}{4}\sum_{j=1}^{4} \Psi_{n_{ij}}(t) \tag{4.29}$$

4.2.1 Payload Stabilization

The performance of the LQR controller is first evaluated in terms of its capability to stabilize the rigid-body payload under significant initial configuration errors. The objective of the controller is to drive the payload to its nominal equilibrium configuration, corresponding to the origin of the inertial frame and a level attitude, while maintaining the cables aligned along the vertical direction. To this end, the system is initialized with large orientation errors of both the payload and the suspension cables, defined by the following initial conditions

$$\begin{aligned}
{}^{e}\boldsymbol{p}_l &= [0,0,0]^T, \;\; {}^{e}\dot{\boldsymbol{p}}_l = [0,0,0]^T, \;\; \mathbf{R}_{eb_l} = \mathbf{R}_{eb_{l,x}}(30^\circ) \\
\boldsymbol{n}_{1j} &= [-\cos(15^\circ), 0, \sin(15^\circ)]^T, \;\; \boldsymbol{n}_{2j} = [-\cos(30^\circ), 0, \sin(30^\circ)]^T \\
\boldsymbol{n}_{3j} &= [-\cos(45^\circ), 0, \sin(45^\circ)]^T, \;\; \boldsymbol{n}_{4j} = [-\cos(60^\circ), 0, \sin(60^\circ)]^T \\
\boldsymbol{\omega}_{ij} &= [0,0,0]^T \\
\mathbf{R}_{eb_i} &= \mathcal{I}
\end{aligned}$$

The time-histories of the load position error, load attitude error, mean link attitude errors, and quadrotor attitude errors are reported in Figs. 4.2, 4.3, 4.4, and 4.5, respectively.

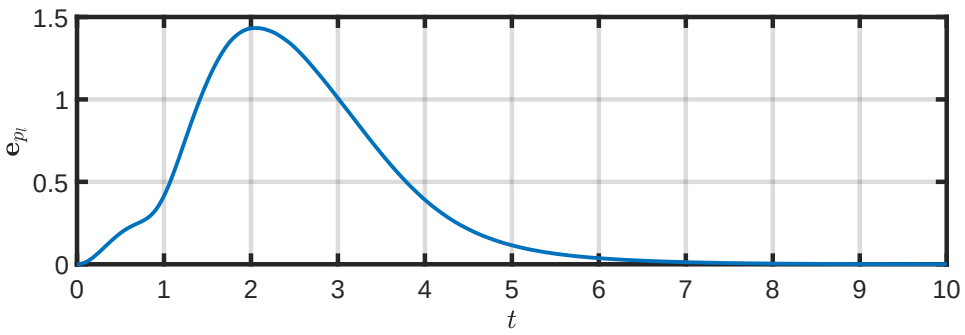

Figure 4.2: Time history of load position error

It is apparent that all error components asymptotically converge to zero, confirming that the controller effectively stabilizes the payload at the desired equilibrium.

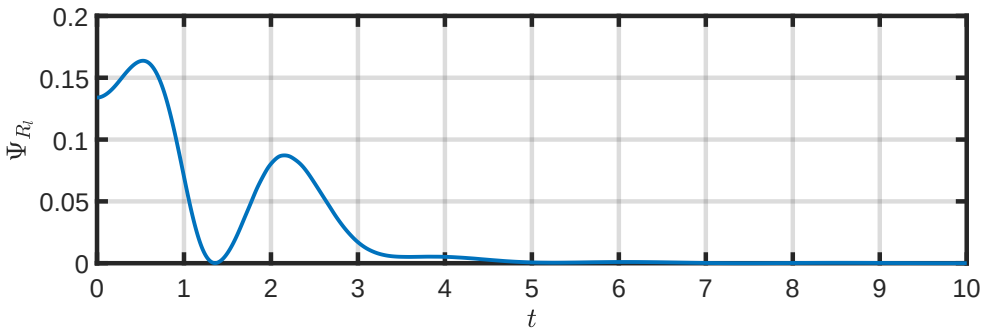

Figure 4.3: Time history of load attitude error

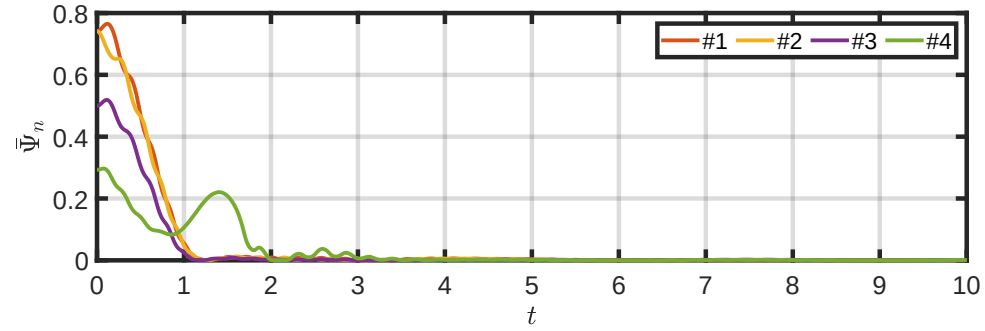

Figure 4.4: Time-histories of cables attitude errors

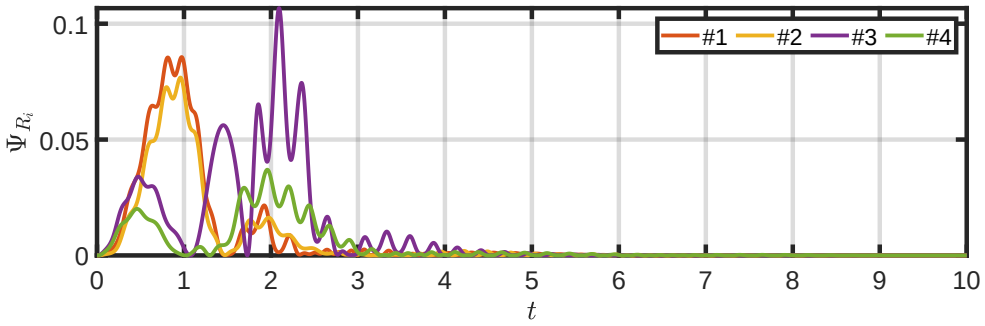

Figure 4.5: Time-histories of quadrotors attitude errors

To assess the feasibility of the considered maneuver, the thrust magnitude and the Euler angles of the quadrotors are analyzed and shown in Figs. 4.6 and 4.7, respectively. For simplicity of representation, only the pitch angle is shown in Fig. 4.7, as it is the most excited among the three Euler angles during the maneuver.

Both the thrust commands and the pitch angles remain within operationally acceptable ranges throughout the maneuver, and exhibit small oscillations, due to the residual vibrations of the suspension cables, which are effectively damped by the controller.

Snapshots of the system configuration at different instants during the stabilization maneuver are reported in Fig. 4.8. The sequence illustrates the progressive reduction of the large initial

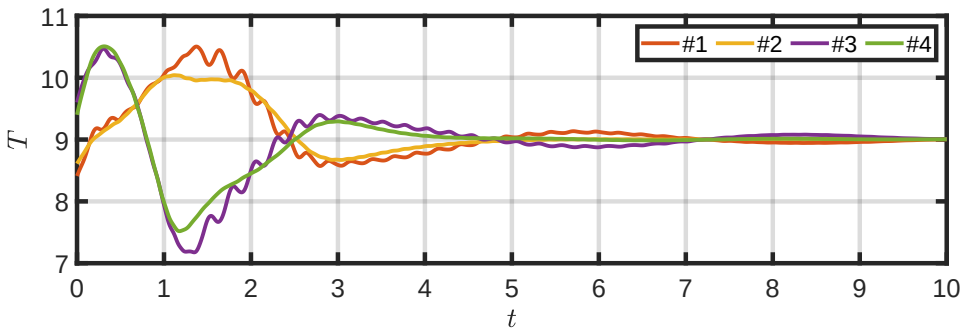

Figure 4.6: Time-histories of quadrotor thrust commands

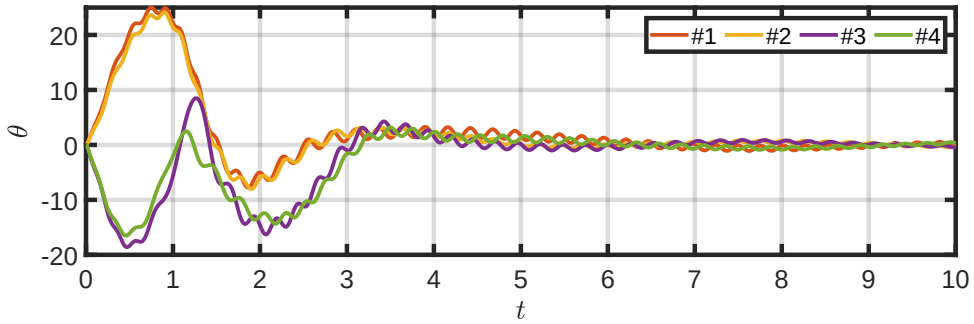

Figure 4.7: Time-histories of quadrotor pitch angles

orientation errors of both the payload and the suspension cables, leading to the restored equilibrium configuration.

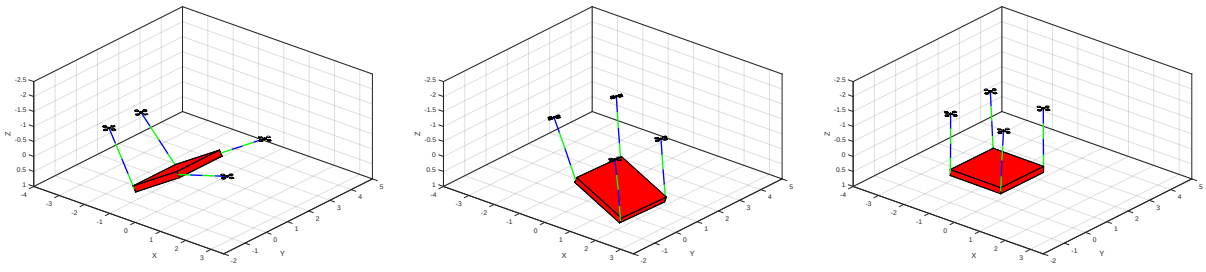

(a) $t = 0$ s **(b)** $t = 2$ s **(c)** $t = 8$ s

Figure 4.8: Sanpshot of the stabilization maneuver

4.2.2 Trajectory Tracking

The capability of the LQR controller to track a time-varying reference trajectory for the payload is evaluated. In particular, a lemniscate trajectory is prescribed for the payload center of mass, while a null attitude is imposed as desired orientation. The desired yaw

angles of the quadrotors are set to zero, together with the free parameter $\boldsymbol{z}$, corresponding to vertically aligned cables. The choice of vertically aligned cables is motivated by the fact that, in this configuration, all quadrotors effectively contribute to the horizontal motion of the payload. The following flat output trajectory is specified

$$
\begin{aligned}
{}^{e}\boldsymbol{p}_l &= \Big[1.2\sin(2\omega t), -4.2\cos(\omega t) + 4.2, -6\Big]^T \\
\mathbf{R}_{eb_l} &= \mathcal{I} \\
\boldsymbol{b}_{1_i} &= [1, 0, 0]^T \\
\boldsymbol{z} &= 0
\end{aligned}
$$

with $\omega = 0.2\ \pi$. The remaining state variables and control input, used as feedforward terms in the LQR, are obtained from the flat outputs by exploiting the differential-flatness property of the system, as described in Sec. 3.1.2. The system starts from rest, with all quadrotors and cables initially at equilibrium. The payload center of mass is initialized with a position error of 1 m along both the x- and y-axes with respect to the reference trajectory, while its velocity and attitude are set to zero.

The time-histories of position and velocity components in the horizontal plane, computed at $\omega = 0.2\ \pi$ rad/s, are reported in Figs. 4.9 and 4.10, respectively, for the quadrotors and the load together with the reference values (dashed black lines). It appears that the load rapidly converge to the desired trajectory.

The effect of the maneuver velocity on control system performance is investigated by varying the frequency in the range $\omega = 0.1\ \pi$ - $0.3\ \pi$ rad/s. To evaluate the tracking performance, the same error metrics defined for the stabilization test are considered. The time-histories of the load position error, load attitude error, mean link attitude errors, and quadrotor attitude errors are reported in Figs. 4.11, 4.12 and 4.13, respectively, where all errors ar shown to converge to zero.

Control robustness is evaluated against modeling errors, considering a perturbation in the mass of the load as $\bar{m} = m \pm \Delta_m$ in both the reference state generation, computed via differential flatness, and the linearized error dynamics. Load position error, evaluated for $\Delta m = \pm 0.2m$ kg on the lemniscate trajectory at $\omega = 0.2\ \pi$ rad/s and the same initial conditions as above, is reported in Fig. 4.14.

the error remains bounded ($\simeq 0.5$ m), demonstrating that the proposed controller is robust

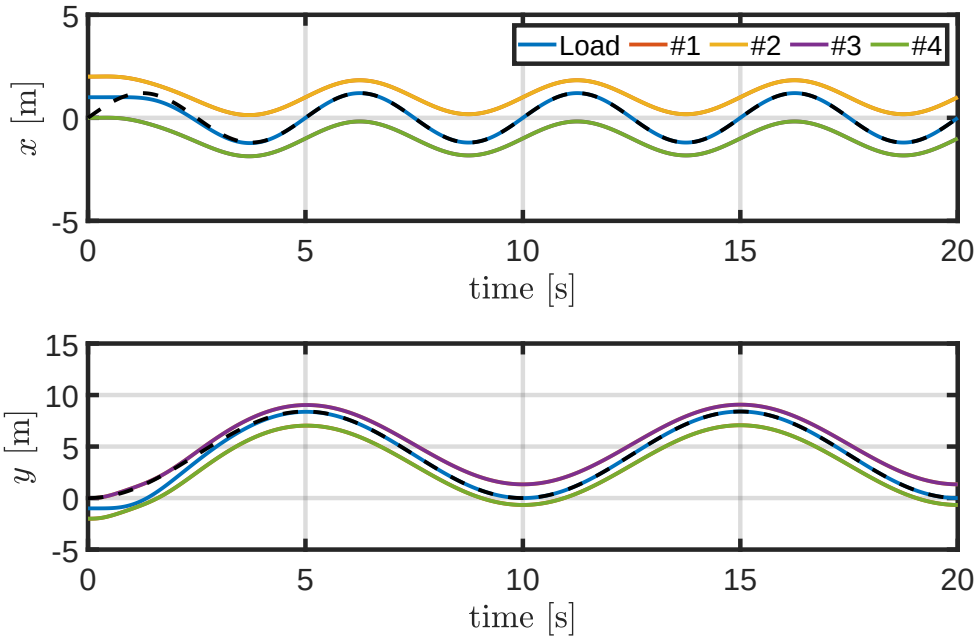

Figure 4.9: Coordinates of payload and quadrotor c.g. vs. time, $\omega = 0.2\pi$ rad/s; the dashed black line indicates reference values

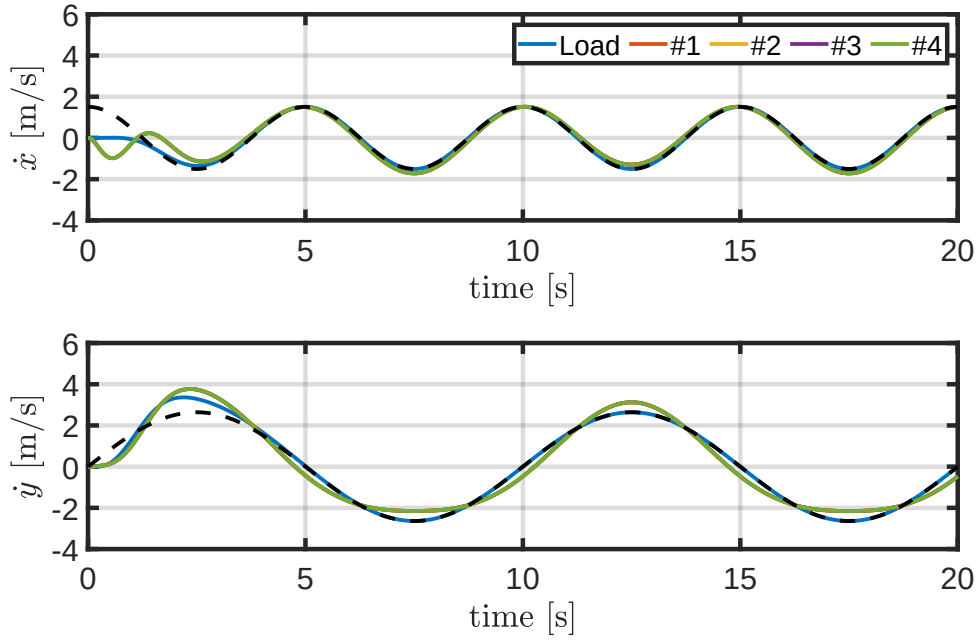

Figure 4.10: Velocity components of payload and quadrotors vs. time, $\omega = 0.2\pi$ rad/s; the dashed black line indicates reference values

to the considered model uncertainties. However, asymptotic tracking is not realized because the feedforward terms computed through differential flatness are based on an incorrect value of the load mass.

The effect of a 50% uncertainty in the aerodynamic drag coefficient of the payload is also

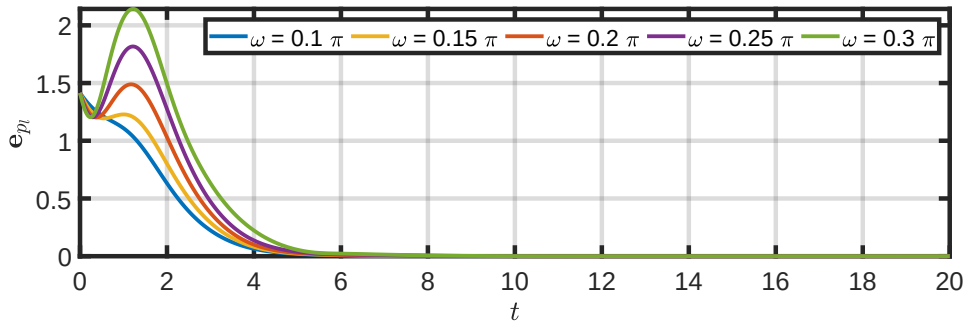

Figure 4.11: Time-history of load position error for varying ω

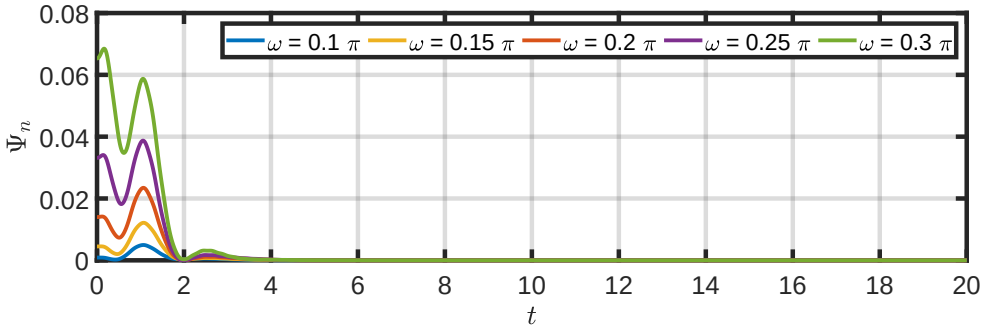

Figure 4.12: Time-histories of cables attitude errors for varying ω

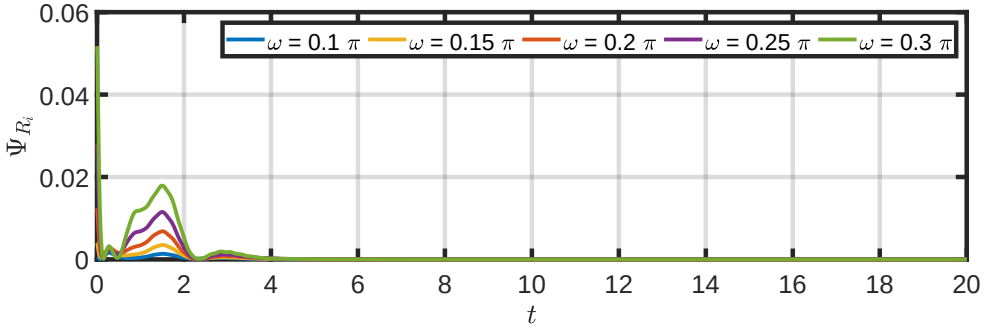

Figure 4.13: Time-histories of quadrotors attitude errors for varying ω

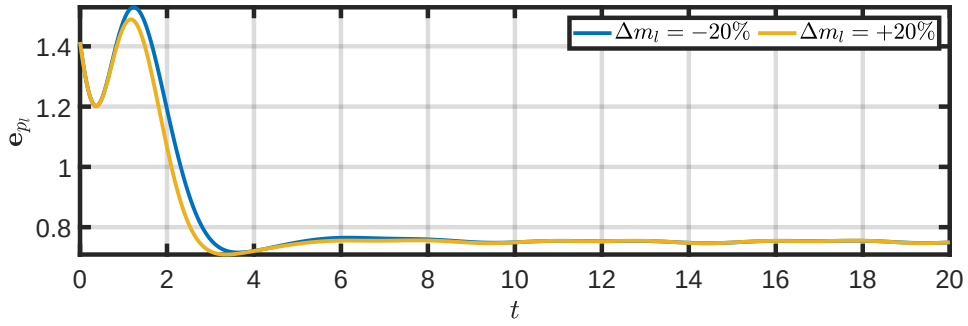

Figure 4.14: Time-histories of load position error in presence of model uncertainties

examined. The controller remains stable under the considered uncertainty, with peak values of approximately 1 m in the load position error.

As for the effect of communication delay, a latency is introduced in the transmission of the control inputs to the quadrotors. It is observed that the system becomes unstable for time delays larger than 0.01 s.

4.3 Formation-Centered Control

The performance of the controller presented in Sec. 4.3 is here evaluated through simulations. The simulations are carried out using the nonlinear model developed based on the Udwadia-Kalaba formulation presented in Sec. 2.3. A square formation is designed to have the same payload size, as in the previous section. This gives

$$^{e}\boldsymbol{\delta} = \Big[0, 0, 0, 1, -1, 0, 1, 1, 0, -1, 1, 0, -1, -1, 0\Big]^{T} \tag{4.30}$$

where the first three coordinates refer to the virtual leader.
The communication topology among followers is modeled as a connected and undirected graph, where the virtual leader has direct communication links with each follower.

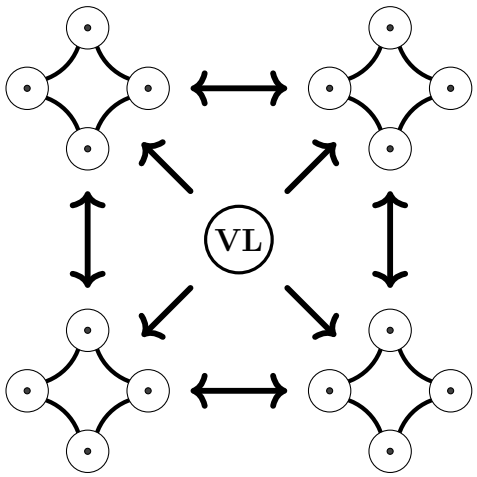

Figure 4.15: Communication scheme

The structure of the weighted Laplacian matrix (Sec. 3.2.1) is specified to ensure a balanced response to formation errors. In particular, an error between a follower and the virtual leader is corrected only by the follower, and is therefore assigned a unit weight. Conversely, errors between followers are corrected cooperatively. To preserve the overall magnitude of the corrective action, the inter-follower weights are normalized by the number of neighboring followers so that the total corrective effort associated with a given inter-follower error also

sums up to one. The result is

$$\mathcal{L} = \begin{bmatrix} 0 & 0 & 0 & 0 & 0 \\ -1 & 2 & -\frac{1}{3} & -\frac{1}{3} & -\frac{1}{3} \\ -1 & -\frac{1}{3} & 2 & -\frac{1}{3} & -\frac{1}{3} \\ -1 & -\frac{1}{3} & -\frac{1}{3} & 2 & -\frac{1}{3} \\ -1 & -\frac{1}{3} & -\frac{1}{3} & -\frac{1}{3} & 2 \end{bmatrix} \tag{4.31}$$

The saturation parameters, as defined in Sec. 3.2.3, are set as

$$k_{T_m} = -3\mathrm{m\,s^{-2}}, \quad k_T = 0.9, \quad k_\psi = 0.08$$

The attitude controller gains are designed such that the attitude response is at least three times lower than the actuator dynamics, ensuring proper bandwidth separation. The actuators are modeled as a first-order system with a time constant of $\tau = 0.015$ s, which corresponds to a bandwidth of approximately 66.7 rad/s. Subsequently, the gains are tuned through a pole–zero analysis to achieve a fast response with minimal overshoot. The resulting gain matrices are

$$\boldsymbol{K}_\Phi = \mathrm{diag}\{12, 12, 14\}; \quad \boldsymbol{K}_\omega = \mathrm{diag}\{30, 30, 17\}$$

The resulting bandwidth for the roll and pitch axes are approximately 16.77 rad/s, and 18.7 rad/s for the yaw axis, respectively, which are within the limits. The gains of the formation controller, k_p, and k_v, are determined next. Following the cascade control theory, the formation control loop is designed to have a bandwidth less than one-third that of the attitude control loop.

As shown in Sec. 3.2.2, the formation error dynamics is expressed in modal coordinates as a set of independent second-order SISO subsystems, each governed by the characteristic equation (Eq. (3.45)). The bandwidth of each SISO subsystem is evaluated through a Bode plot analysis and to guarantee appropriate bandwidth separation, k_p, and k_v, are specified so that the highest bandwidth of the formation controller, which corresponds to the highest eigenvalue λ_{max}, remains below one-third of the attitude control bandwidth. In addition, the same gains are verified to guarantee robustness to communication delays, by ensuring that the corresponding critical delay τ_c, computed according to Eq. (3.53), remains higher

than the maximum expected communication latency in the network. Finally, the gains are fine-tuned to achieve a satisfactory transient response to a step in the formation error.
The gains k_{0_p}, and k_{0_v}, associated with the tracking performance of the virtual leader, are selected next, considering that formation control and reference tracking tasks are coupled. Therefore, their values are such that the tracking response timescale is comparable to the formation response while maintaining a small overshoot.
The gains are

$$k_p = 20; \quad k_v = 8, \quad k_{0_p} = 18, \quad k_{0_v} = 6$$

so that, the bandwidth of the formation controller is approximately 3 rad/s. Furthermore, the maximum admissible uniform delay on all communication channels, evaluated as in Eq. (3.53), is of 0.075 s. The formation controller operates at 50 Hz, whereas the inner-loop controllers run at 200 Hz.

4.3.1 Trajectory Tracking

In the first tests, the formation must track, at increasing frequency, the same lemniscate trajectory described in Sec. 4.2.2, to which only the virtual leader has access, given by

$$^e\boldsymbol{p}_r = \Big[1.2\sin(2\omega t), -4.2\cos(\omega t) + 4.2, -6\Big]^T \tag{4.32}$$

The agents are at rest at the initial time with positions $^e\boldsymbol{p}_2 = [2, -2, 6]^T$ m, $^e\boldsymbol{p}_3 = [2, 2, 6]^T$ m, $^e\boldsymbol{p}_4 = [-2, 2, 6]^T$ m, and $^e\boldsymbol{p}_5 = [-2, -2, 6]^T$ m, while the virtual leader is in the origin. The load initial position is $^e\boldsymbol{p}_l = [0, 0, 4]^T$ m. The simulation starts with large initial errors (formation and trajectory). Specifically, the virtual leader has an error of 1 m in the x- and y-coordinates, and 2 $\mathrm{m\,s^{-1}}$ and 1.65 $\mathrm{m\,s^{-2}}$ on $\dot{x}$ and $\ddot{y}$, respectively, while the initial shape of the formation is a square with sides of 4 m.
The time-histories of position and velocity components in the horizontal plane, computed at $\omega = 0.2\pi$ rad/s, are reported in Figs. 4.16 and 4.17, respectively, for the agents and the virtual leader, together with the reference values (dashed black lines). It appears that the virtual leader and agents rapidly converge to the desired trajectory and specified formation, respectively, and the quadcopters track the leader with negligible delay and overshoot.

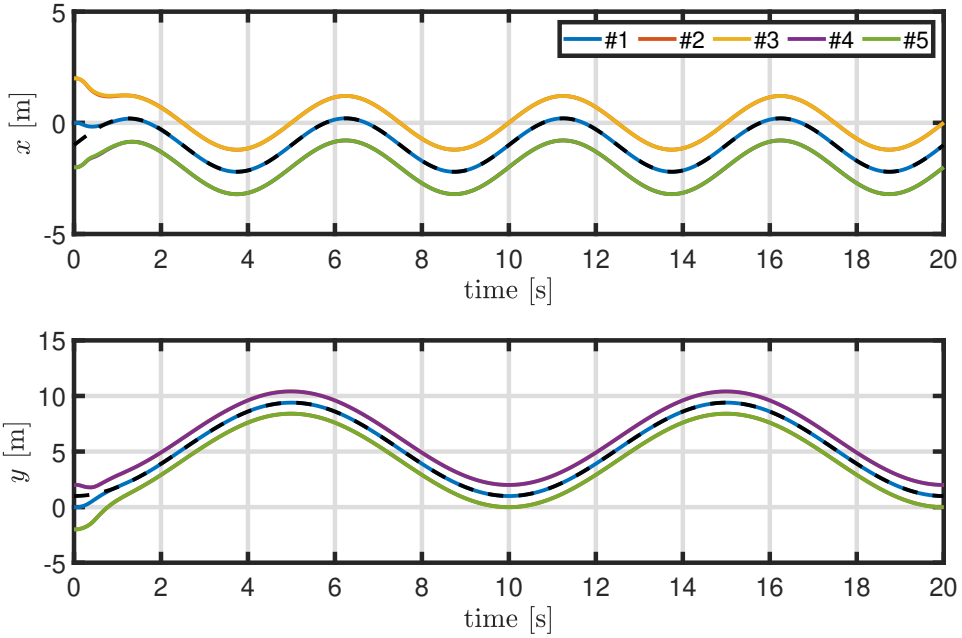

Figure 4.16: Coordinates of virtual leader (#1) and agent c.g. vs. time, $\omega = 0.2\pi$ rad/s; the dashed black line indicates reference values

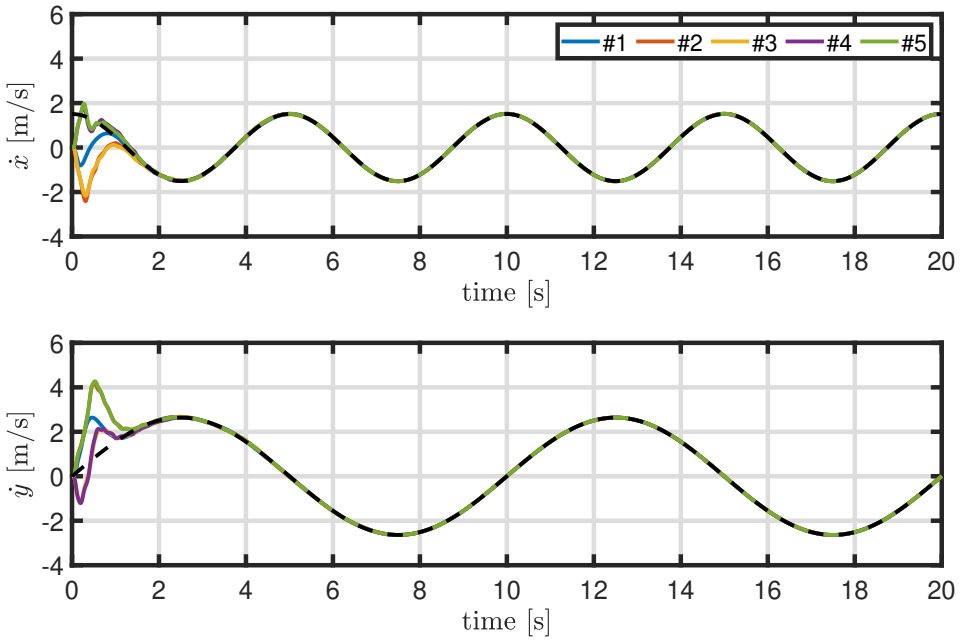

Figure 4.17: Velocity components of virtual leader (#1) and agents vs. time, $\omega = 0.2\pi$ rad/s; the dashed black line indicates reference values

Formation errors among followers and those relative to the virtual leader are analyzed, as the former quantify the accuracy with which agents maintain their relative spatial configuration, while the latter measure how well they track the target trajectory. The formation error ϵ_{ij},

for $i = 1, ..., 5$, with $i \neq j$, is expressed as

$$\epsilon_{ij} = \|({}^e\boldsymbol{p}_i - {}^e\boldsymbol{p}_j) - ({}^e\boldsymbol{\delta}_i - {}^e\boldsymbol{\delta}_j)\|_1 \tag{4.33}$$

where $i = 1$ indicates the virtual leader, and $\epsilon_{ij} = \epsilon_{ji}$, while the trajectory tracking error ϵ_{tr} is defined as the distance between the virtual leader c.g. and the reference path. The results are evaluated in terms of the RMS value of the errors, computed over the duration of the simulation. In the considered maneuver, the virtual leader accurately tracks the reference trajectory with an RMS tracking error of 0.005 m, while the RMS values of the formation error of each agent with respect to the virtual leader (ϵ_{1j}, $j = 2, \cdots, 5$) are below 0.01 m. Figure 4.18, where the maneuver of the quadrotors and the load with a few snapshots at $t = 0$ (right), $t = 2.5$ s (middle) and $t = 5$ (left), are depicted, confirms that the large initial error on the position of the agents is quickly reduced and the formation is maintained with adequate accuracy. The synchronized behavior of the agents ensures that the payload attitude angles exhibit minimal oscillations during the maneuver. Note that the figure also shows the cable elements (in green and blue colors)

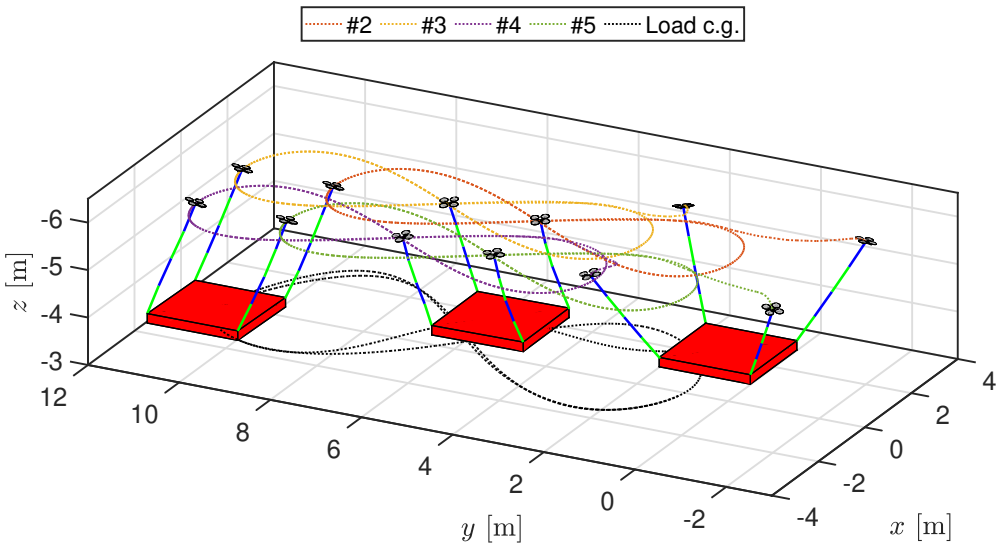

Figure 4.18: Snapshots of the maneuver, $\omega = 0.2\pi$

The plots of tensile forces acting on the agents in Fig. 4.19 show that the relevant perturbations in the initial phase of the maneuver, caused by the formation error, are rapidly damped. In the later phase of flight, they maintain modest variations due to the relatively small effect

of inertial actions in the case considered. The high-frequency oscillations in the first phase of flight are due to the cable vibrations, which are progressively damped by aerodynamic resistance.

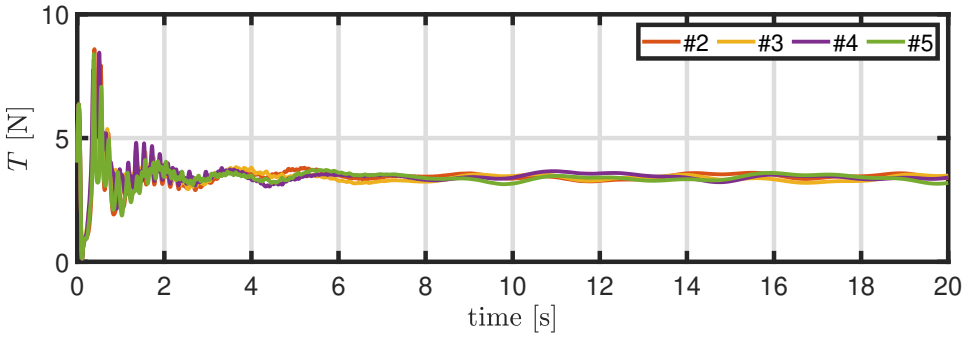

Figure 4.19: Tensile forces on the agents, $\omega = 0.2\pi$

As for the computational burden of the code, the time required for simulations performed in MATLAB on a computer with an Intel® Core™ i7-7700HQ CPU @ 2.80 GHz increases approximately linearly with the number P of cable elements from 10 s ($P = 3$) to 45 s ($P = 10$). The computational latency of the controller, evaluated using the Simulink Profiler, is 100 μs in all cases. Since no code optimization has been performed, the above times should be regarded as conservative upper bounds.

The evaluation of the mean formation errors, $\bar{\epsilon}_1 = \left[\sum_{2 \leqslant i < j \leqslant 5} \epsilon_{ij}\right] /6$, and the mean leader-follower error, $\bar{\epsilon}_2 = \left[\sum_{j=2}^{5} \epsilon_{1j}\right] /4$, for 3 values of P show that a negligible effect of the number of cable segments on the controller performance is apparent. Varying the number of elements mainly induces a change in the magnitude and frequency content of the tensile forces along the cables, and hence in the external forces transmitted to the quadrotors. However, the INDI inner control loops are robust to unmodeled external forces and moments, which are implicitly accounted for through the measured acceleration as long as the dominant cable frequencies are less than half the IMU sampling rate. Moreover, aerodynamic actions on cables and payload introduce additional damping, further limiting the high-frequency content of the oscillations.

The effect of maneuver velocity on control system performance is investigated by varying the frequency in the range $\omega = 0.1\pi$ - 0.3π rad/s. At $t = 0$ the agents are at rest and in formation, located at ${}^e\boldsymbol{p}_1 = [0, 0, 6]^T$ m, ${}^e\boldsymbol{p}_2 = [1, -1, 6]^T$ m, ${}^e\boldsymbol{p}_3 = [1, 1, 6]^T$ m, ${}^e\boldsymbol{p}_4 = [-1, 1, 6]^T$ m, and ${}^e\boldsymbol{p}_5 = [-1, -1, 6]^T$ m. Load position and velocity are ${}^e\boldsymbol{p}_l = [0, 0, 4]^T$ m, and ${}^e\boldsymbol{v}_l = [0, 0, 0]^T$ m/s, respectively. The results, computed for five values of ω, are reported in Figs. 4.20, 4.21,

and 4.22, that show the time-histories of, respectively, the mean formation errors, $\bar{\epsilon}_1$, the mean leader-follower error, $\bar{\epsilon}_2$, and the tracking error $\epsilon_{tr} = \| {}^e\boldsymbol{p}_r - {}^e\boldsymbol{p}_1 \|$.

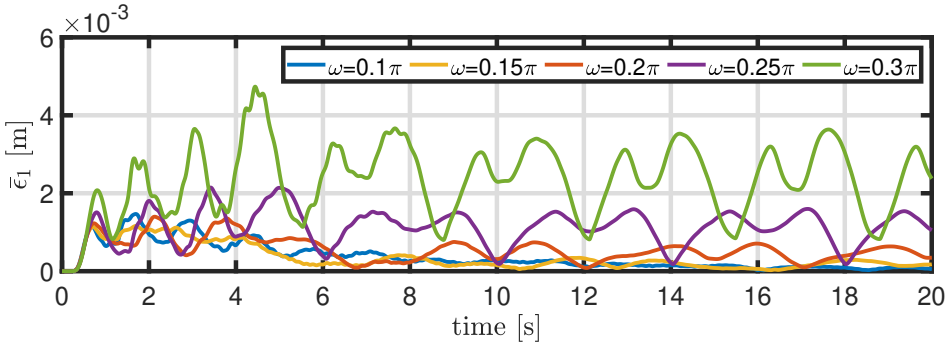

Figure 4.20: Time-histories of mean formation error at different values of ω

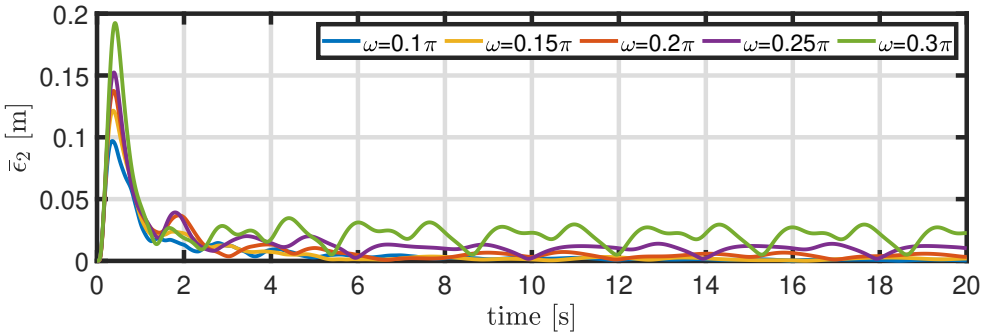

Figure 4.21: Time-histories of mean leader-follower error at different values of ω

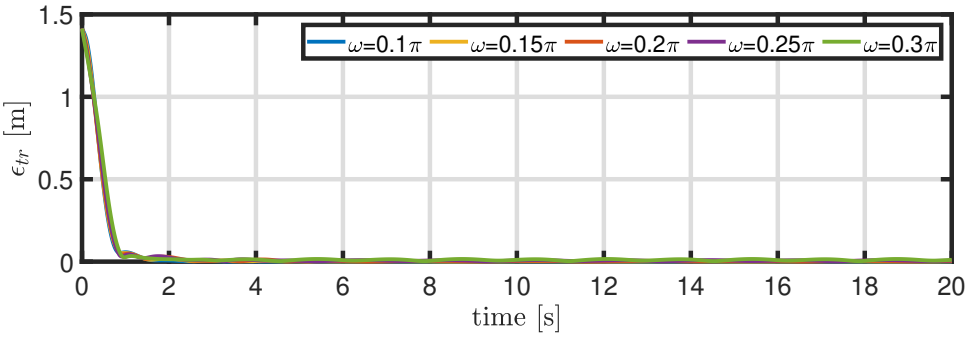

Figure 4.22: Time-histories of trajectory tracking error at different values of ω

It is apparent that all the error metrics increase only slightly with ω, demonstrating the good performance of the controller in trajectory tracking. It is remarkable that, although load inertia has a greater effect when agents move faster along the trajectory, the formation error is marginally affected by whether agents carry the load or not, which is explained by the robustness of the INDI control to external forces. In particular, for $\omega = 0.3\pi$ rad/s, the agents experience peak tensile forces larger than 7 N, with maximum increments of mean

inter-agent formation error lower than 0.003 m. The above also explains the reason for the negligible inter-agent position error ($\bar{\epsilon}_1$ in Fig. 4.20) because, once the variations in tension force along the trajectory are handled very effectively by the INDI controllers, the formation behaves as a whole where disturbances on individual agents are in fact eliminated. The large initial error on ϵ_{tr} in Fig. 4.22 is related to the initial position of the virtual leader, while $\bar{\epsilon}_2$ and ϵ_{tr} are of the same order of magnitude and show a similar trends at increasing ω.

Control robustness is evaluated against modeling errors, considering a perturbation in the mass of the first quadrotor (Agent #2) as $\bar{m} = m + \Delta_m$ in Eq. (3.57). Mean formation error ($\bar{\epsilon}_1$) and leader-followers error ($\bar{\epsilon}_2$), evaluated for $\Delta m = \pm 0.2m$ kg on the lemniscate at $\omega = 0.2\pi$ rad/s and the same initial conditions as above, show increments lower than 0.01 m.

As for the effect of communication delay, a 50 ms latency is introduced in the transmission of the virtual leader position, velocity, and acceleration to the agents. When the reference trajectory is tracked at the same frequency of 0.2π rad/s as above, $\bar{\epsilon}_1$ is bounded with a maximum of about 0.2 m. In a second test, the same transmission delay is considered in the communication of Agent #2 to the other agents. Again, the formation errors are bounded and lower than 0.18 m.

Up to this point, a square formation with dimensions equal to those of the payload has been considered. This configuration ensures that all quadrotors contribute uniformly to the load translation, resulting in lower and more uniform cable tensions. In this case, the payload swing is not directly actuated, but it is effectively limited by properly shaping the virtual leader trajectory with bounded acceleration and jerk.

When the formation is wider than the payload, the cables are no longer aligned with the vertical direction. In this case, the horizontal components of the cable tensions can be exploited to influence the payload swing. However, this configuration leads to higher and less regular tension levels during motion, mainly due to alternating slack and re-tension phases in the cables connected to the rear quadrotors. These effects are particularly evident at the beginning of the maneuver, when the formation starts moving slightly before the payload as a result of its inertia. These variations in cable tension excite oscillations of the payload, whose amplitude depends on the relative size of the payload with respect to the formation. Larger payloads exhibit more pronounced oscillations, whereas this effect becomes less significant for smaller payloads, where shorter moment arms limit the induced motion. However, in such cases, a wider formation is required to ensure adequate spatial

separation among the quadrotors.

The same lemniscate trajectory used in the previous simulation is here considered, with $\omega = 0.2\pi$ rad/s. To account for the wider formation, the constant offset vector ${}^{e}\boldsymbol{\delta}$ is redefined accordingly to increase the relative spacing between the agents with respect to the payload, giving

$$ {}^{e}\boldsymbol{\delta} = \Big[0, 0, 0, 1.5, -1.5, 0, 1.5, 1.5, 0, -1.5, 1.5, 0, -1.5, -1.5, 0\Big]^{T} \tag{4.34} $$

The agents are at rest at the initial time with positions ${}^{e}\boldsymbol{p}_2 = [2.5, -2.5, 6]^T$ m, ${}^{e}\boldsymbol{p}_3 = [2.5, 2.5, 6]^T$ m, ${}^{e}\boldsymbol{p}_4 = [-2.5, 2.5, 6]^T$ m, and ${}^{e}\boldsymbol{p}_5 = [-2.5, -2.5, 6]^T$ m, while the virtual leader is in the origin. The load initial position is ${}^{e}\boldsymbol{p}_l = [0, 0, 4]^T$ m.

The cable tension time-histories for the case of vertically aligned cables (Fig. 4.23a) and for inclined cables (Fig. 4.23b) are compared in Figure 4.23. Note that, in the vertical configuration, the tension magnitudes are lower and more evenly distributed among the quadrotors, and their variations remain small and regular throughout the maneuver. Conversely, when the cables are inclined, the overall tension levels increase and exhibit larger fluctuations, indicating a less uniform load sharing among the agents.

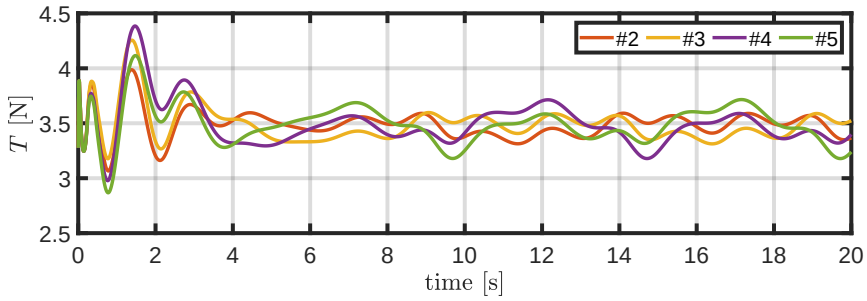

(a) Vertically aligned cables

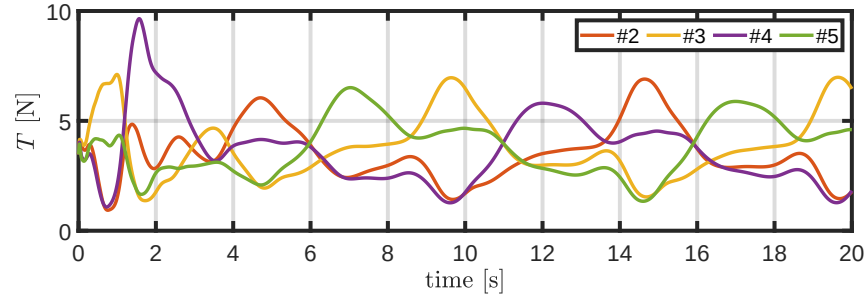

(b) Inclined cables

Figure 4.23: Comparison of cable tension time-histories for vertical and inclined cable configurations

Figure 4.24 illustrates the load configuration during the maneuver with inclined cables. The front quadrotors generate cable tensions inclined in the direction of motion, thus providing the horizontal components required to pull the payload forward. Conversely, the rear quadrotors exhibit nearly vertical cables, contributing predominantly to the vertical support of the load.

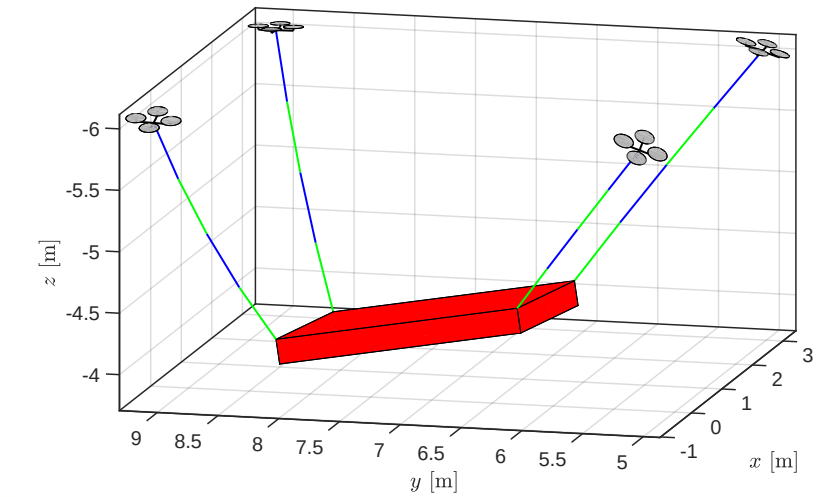

Figure 4.24: Snapshot of the maneuver with inclined cables, $\omega = 0.2\pi$

Figure 4.25, which shows two snapshots of the maneuver at $t = 5.5$ s (left) and $t = 10.5$ s (right), confirms that also in this configuration the system accurately tracks the reference trajectory described in the previous section. The payload exhibits small swing during the maneuver and attitude oscillations of about $\pm 10°$, as shown in Fig. 4.26, demonstrating that the control scheme effectively compensates for the more variable tension distribution among the cables.

4.3.2 Take-off and Landing

The control strategy is evaluated during the take-off and landing phases, starting from hovering. At the initial time, the agent location is specified as

$$^{e}\boldsymbol{\delta} = \Big[0, 0, 0, 1.1, -1.1, 0, 1.1, 1.1, 0, -1.1, 1.1, 0, -1.1, -1.1, 0\Big]^{T} \tag{4.35}$$

The trim values of the system states are computed following the procedure described in Sec. 4.1.

In the first test scenario, the agents are commanded to perform a coordinated take-off to

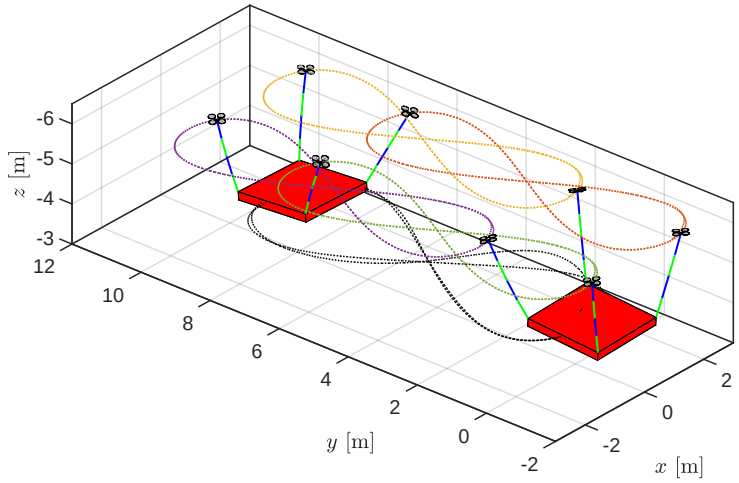

Figure 4.25: Snapshots of the maneuver with inclined cables at $t = 5.5$ s (left), and $t = 10.5$ s (right), $\omega = 0.2\pi$

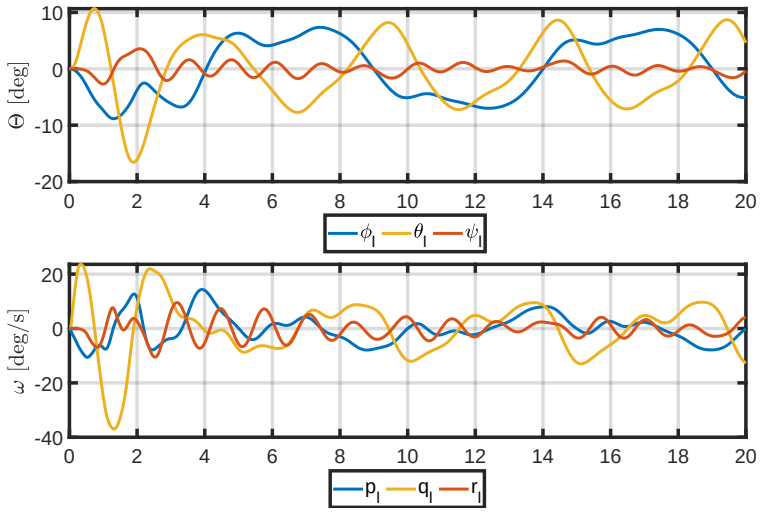

Figure 4.26: Payload Euler angles, $\omega = 0.2\pi$

lift the payload from the ground while maintaining the desired formation. The same control gains used in the previous cases are adopted. The agents start at an altitude of $z = -1$ m, corresponding to a configuration in which all cables are slack.

Considering the reference trajectory for the virtual leader, specified as

$$z_r = z_0 + (z_f - z_0)\left(10s^3 - 15s^4 + 6s^5\right) \tag{4.36}$$

$$\dot{z}_r = \frac{(z_f - z_0)}{T}\left(30s^2 - 60s^3 + 30s^4\right) \tag{4.37}$$

with $s = \frac{t}{T}$, and $T = 6$, the plots of the tensile forces on the agents in Fig. 4.27 show that the cable tension, initially due to the weight of the cable elements, rapidly increases as the

agents start to lift the payload. Transient oscillations due to the motions of cable elements are visible, which are rapidly damped by the aerodynamic drag.

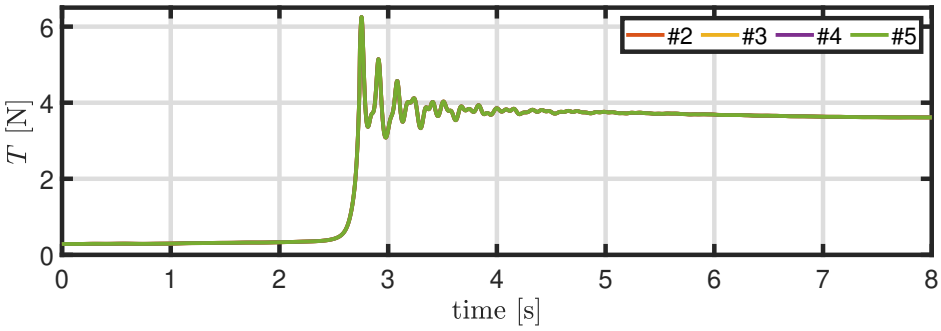

Figure 4.27: Time-histories of cable tensions during take-off

Figure 4.28 shows the formation errors among the agents. At the moment of lift-off, the sudden increase in cable tension induces a brief perturbation in the inter-agent distances. This transient effect results in small formation errors, with maximum deviations of approximately 0.015 m, which are rapidly compensated for as the system stabilizes. The rapid decay of these errors demonstrates the capability of the proposed controller to effectively counteract the physical coupling effects introduced by the cables and to maintain tight formation coherence throughout the maneuver.

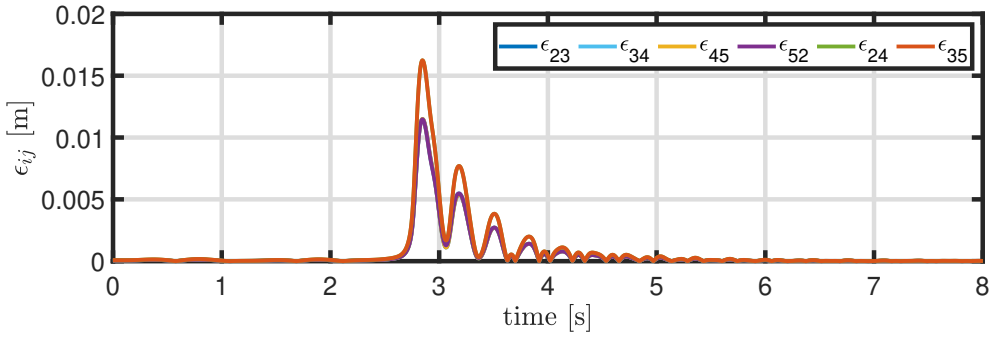

Figure 4.28: Time-histories of formation errors during take-off

The tracking errors between followers and virtual leader remain very small throughout the maneuver, with a maximum deviation of approximately 0.02 m, confirming the high precision achieved by the formation-centered control strategy, even in situations where the tensile forces suddenly increase. The controller is synthesized without an explicit modeling of the constraint forces, their influence is only indirectly accounted for through the acceleration measurements. This demonstrates the ability of the INDI approach to effectively handle unmodeled external forces.

Snapshots of the take-off maneuver are shown in Fig. 4.29.

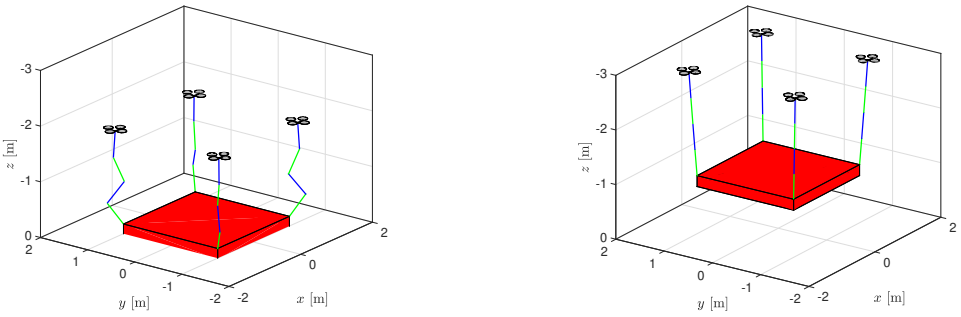

Figure 4.29: Sanpshots of the take-off maneuver

In the second test scenario, the agents perform a coordinated landing to drop the load on a massless platform to avoid any discontinuity in the load velocity at the touchdown, (see Sec. 2.3). It is located at $z = -0.1$m and anchored to the ground through a mechanical spring of stiffness $k = 100$ and a damper with damping coefficient $c = 2m_l\sqrt{k/m_l}$. Note that the rotational motion of cable elements takes place since each cable at the initial time is slightly inclined with respect to the z-axis. The agents start at an altitude of $z = -3$ m, corresponding to a configuration in which all cables are taut, and the reference trajectory is given in Eq. (4.36).

When the load touches the ground, the tensile forces (Fig. 4.30) drop sharply and then stabilize at the weight of the cables.

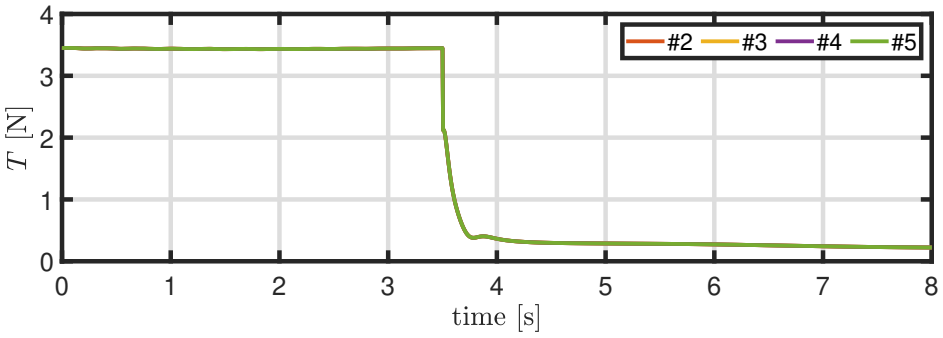

Figure 4.30: Time-histories of cable tensions during landing

As for the formation errors in Fig 4.31, the sudden decrease in cable tension when the load touches the ground (platform) induces a brief perturbation in the inter-agent distances that causes small formation errors, with maximum deviations of approximately 0.01 m.

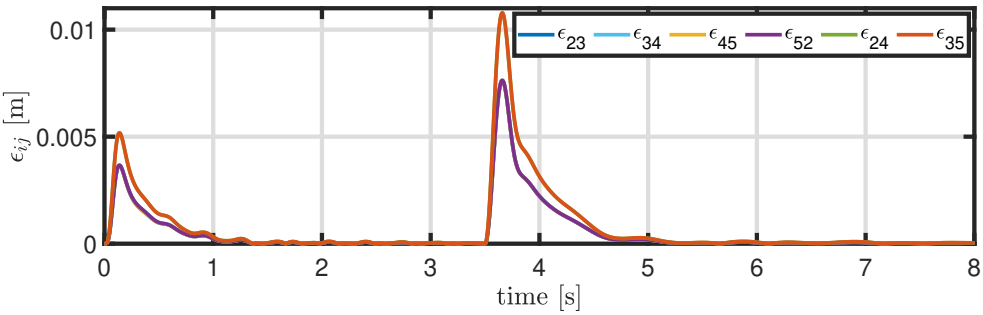

Figure 4.31: Time-histories of formation error during landing

The leader-follower errors are again very small, with maximum values of the order of 0.01 m.

Snapshots of the landing maneuver are shown in Fig. 4.32.

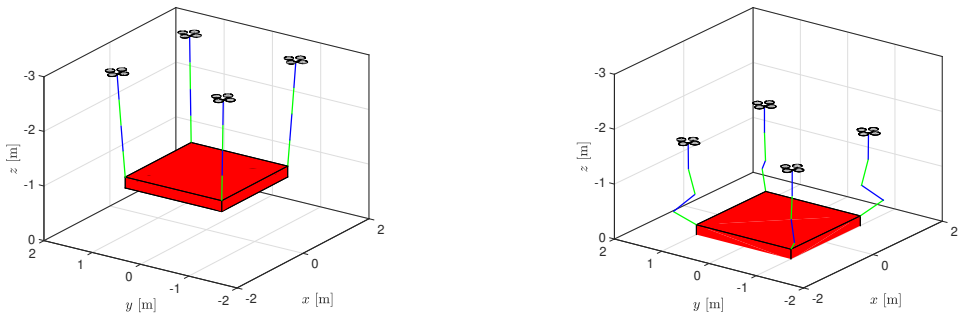

Figure 4.32: Sanpshots of the landing maneuver

4.3.3 Wind Gust Rejection

The effects of a wind gust are discussed next to assess the effect of external perturbations on control performance. The formation is defined as

$$ {}^{e}\boldsymbol{\sigma_p} = \Big[0, 0, 0, 2.25, -2.25, 0, 2.25, 2.25, 0, -2.25, 2.25, 0, -2.25, -2.25, 0\Big]^T \tag{4.38} $$

A horizontal wind gust is simulated at $t = 1$ s, with a peak intensity of 8 m/s and a direction of 30° with respect to the x-axis. The wind speed smoothly increases from 0 to 8 m/s over an interval of 2 s, according to a standard $1 - \cos$ profile, is constant at its maximum value for 4 s, and then decreases to zero at $t = 9$ s.

The results, in terms of the time-histories of the formation errors, are reported in Figs. 4.33 and 4.34. When the gust occurs, all errors increase. Due to the gust direction, the pitch

angle of the upwind Agent #5 saturates at 45 deg, to counteract both the gust and the tension induced by the payload, which leads to large, although bounded, formation errors.

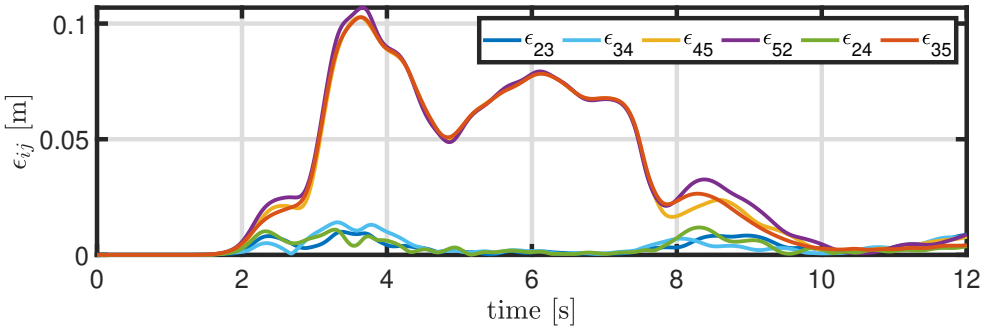

Figure 4.33: Gust response: time-histories of formation error

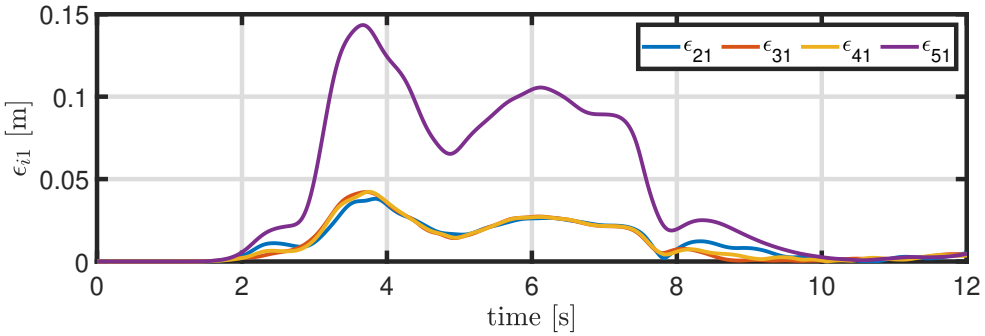

Figure 4.34: Gust response: time-histories of formation error

The time-histories of the tensile forces in Fig. 4.35 show that most of the payload weight is initially carried by Agent #5 when the gust occurs. Once its pitch angle reaches the saturation limit, Agent #5 can no longer reorient its thrust to provide the required force component along the cable, so that its load is mainly transferred to Agent #4.

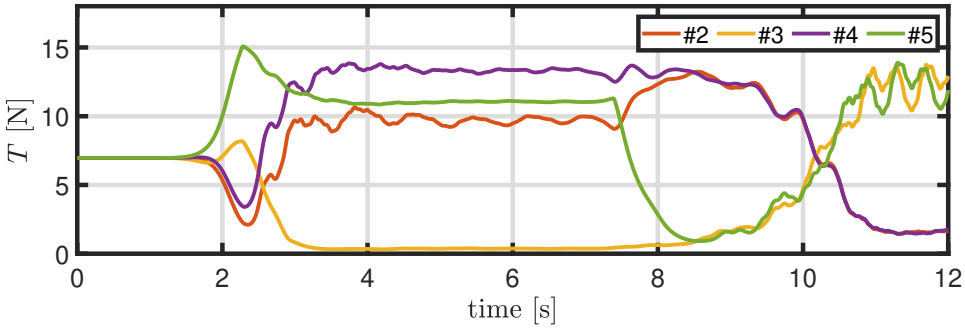

Figure 4.35: Gust response: time-histories of tensile forces

Snapshots of the gust disturbance rejection are reported in Fig. 4.36.

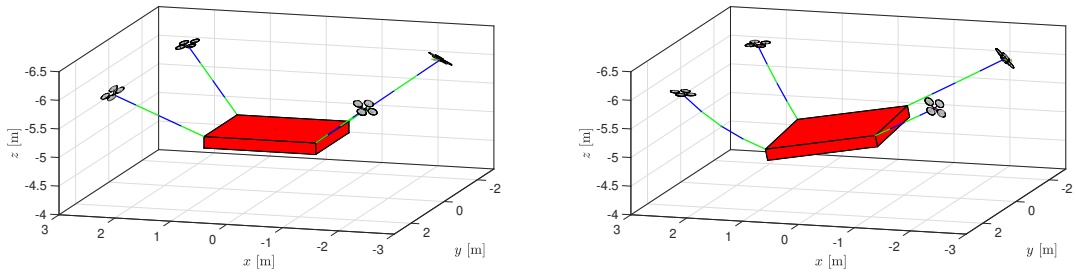

Figure 4.36: Sanpshot of the gust disturbance rejection

4.3.4 Obstacle/Collision Avoidance

In the case of obstacle avoidance, the formation must avoid a 6 m high cylinder with radius $r_{obj} = 0.3\,\text{m}$, located at $x = 0$ m and $y = 12$ m.

To ensure that the whole formation–payload system avoids the obstacle, the minimum safe distance between the virtual leader and the obstacle is set to $\Delta_{min} = 2\,\text{m}$. Since the virtual leader is located at the center of the square formation, maintaining this minimum clearance ensures that all agents and the payload remain at a safe distance from the obstacle. The initial conditions and desired formation are the same as in the previous cases (specified for the maneuvers at increasing ω), while the virtual leader follows a rectilinear trajectory along the y-axis.

Figure 4.37 shows the distances (d) between the obstacle and the virtual leader (# 1), Agents # 2, # 3 and load, (blue, red, yellow and purple lines, respectively). The obstacle radius r_{obj} (black dashed line) and the minimum allowed distance for the virtual leader Δ_{min} (black dotted line) are also drawn for the sake of clarity. The avoidance law is effective to prevent the agents from colliding with the obstacle, the minimum distance not being lower than 0.75 m.

Snapshots of the avoidance maneuver are reported in Fig. 4.38. Before entering the detection region, the agents fly at a constant velocity of $4\,\text{m}\,\text{s}^{-1}$, according to the virtual leader motion. Approaching the obstacle, the formation decelerates and deviates laterally to the left (along the negative x-axis), starting the avoidance maneuver. After passing the obstacle, the reference trajectory is recovered with minimal overshoot, including the specified flight speed.

One issue associated with this approach is that while the formation deviates laterally to avoid the obstacle, the time-based reference trajectory of the virtual leader continues to

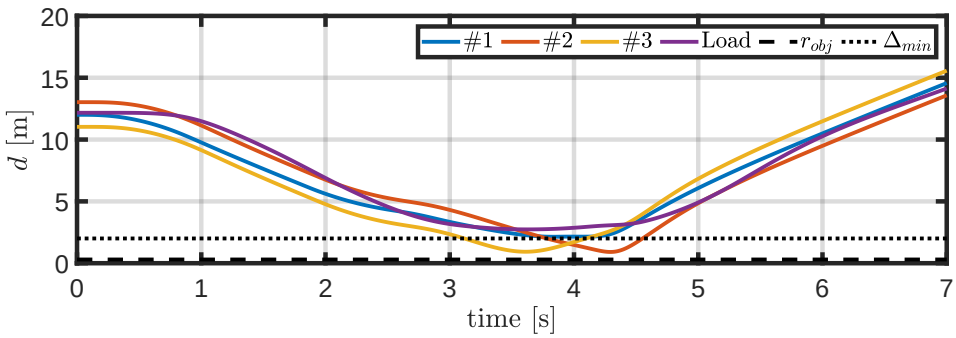

Figure 4.37: Distances between virtual leader (#1), agents (#2 and #3), payload, and obstacle vs. time

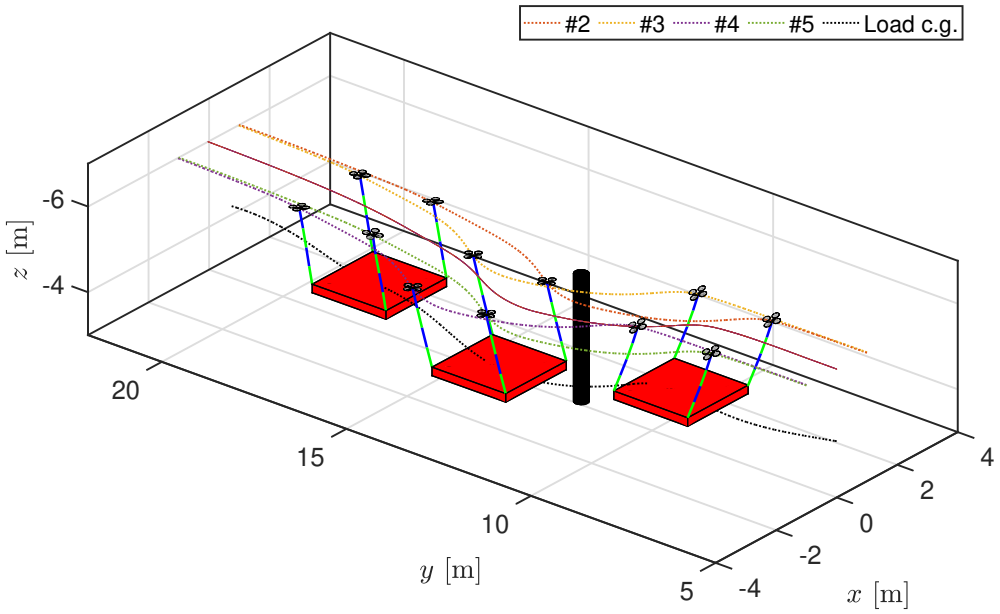

Figure 4.38: Snapshots of the avoidance maneuver

evolve along the y-axis. As a result, once the obstacle is cleared, a significant tracking error may have accumulated, leading the controller to generate large accelerations in order to recover the nominal trajectory. This effect becomes more pronounced when the minimum safety distance from the obstacle is increased, resulting in a wider deviation, or when the reference trajectory velocity is higher, since the reference advances more rapidly in time. A possible solution is to either redefine the reference trajectory upon obstacle detection or to formulate the reference in the spatial domain, rather than as an explicit function of time, so that progress along the path naturally adapts to the vehicle motion.

The CBFs are also implemented on the individual quadrotors to prevent inter-agent collisions. To assess the effectiveness of the collision avoidance strategy, a simulation is carried out with

two agents moving along the same line but in opposite directions. The inner control loops are identical to those described in the previous sections, while the outer loop generates the reference acceleration according to Eq. (3.100).

At the initial time, both agents are at rest with positions ${}^e\boldsymbol{p}_1 = [4, 0, -6]^T$, and ${}^e\boldsymbol{p}_2 = [0, 0, -6]^T$. During the maneuver, the CBFs modify the nominal control inputs whenever the inter-agent distance approaches the safety limit, set to 0.7m, ensuring collision-free motion. Snapshots of the avoidance maneuver are reported in Fig. 4.39.

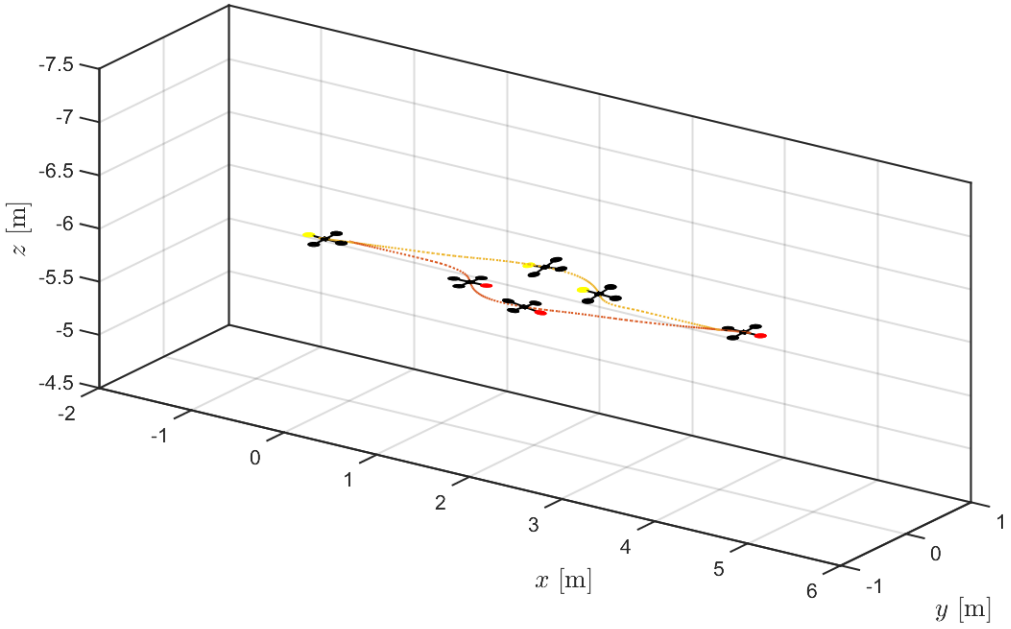

Figure 4.39: Snapshots of the collision avoidance maneuver

4.4 Flight Tests

In this section, the feasibility and effectiveness of the consensus-based leader-follower formation control strategy described in Sec. 3.2.2, for both formation maintenance and cooperative transportation task, is investigated through experiments.

The experiments have been conducted in the drone facility of ISAE-SUPAERO, a $10 \times 10 \times 4$ m indoor laboratory that allows the testing of high-performance control laws based on the Simulink software framework. The laboratory is equipped with 12 OptiTrack Prime 17w cameras [1], which provide precise 3D position and from which the velocity of each drone is

[1] `https://www.optitrack.com/cameras/`

estimated at a frequency of 50 Hz, with an accuracy of 0.01 m. The experimental setup is sketched in Fig. 4.40.

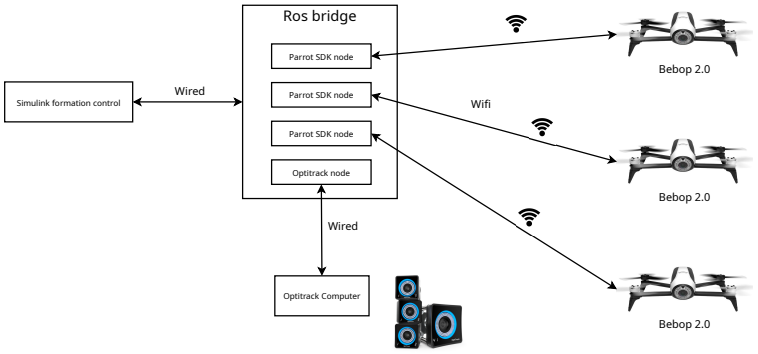

Figure 4.40: Experimental setup [1]

High-level guidance and navigation algorithms are implemented and executed externally from the quadrotor, on a ground-based computer, using Simulink. Simulink operates as a monitoring and control ground station, performing real-time data acquisition and logging, and transmitting attitude and vertical velocity commands to the quadrotor. Communication with the UAV is achieved via a WI-FI connection through a ROS Bridge interface [2]. The designed control law and path generation are computed in real time in Matlab at a frequency of 50 Hz, which is also the overall sampling time of the experimental system.

Indoor experimental validation is conducted using Parrot Bebop 2 quadrotors, whose main parameters are the same as the ones reported in Tab. 4.1. The Parrot Bebop 2 quadrotor is equipped with an onboard flight controller that handles low-level attitude and vertical velocity stabilization using proportional-derivative (PD) control laws with added feedforward terms. The controller accepts control inputs for roll and pitch angles (in radians), vertical speed (in meters per second), and yaw rate (in radians per second), and operates at 200 Hz. State evaluation for the control loops relies on onboard sensors, including an inertial measurement unit (IMU) for attitude data and an ultrasonic sensor for altitude and vertical velocity measurements. The limited accuracy and low update rates of the ultrasonic sensor (15 Hz) limit the performance of the embedded vertical control.

Since low-level stabilization is already managed internally by the Bebop flight controller, the formation controller is implemented in a cascade architecture, as shown in Fig. 4.41

[2]ROS (Robot Operating System) `https://www.ros.org/`

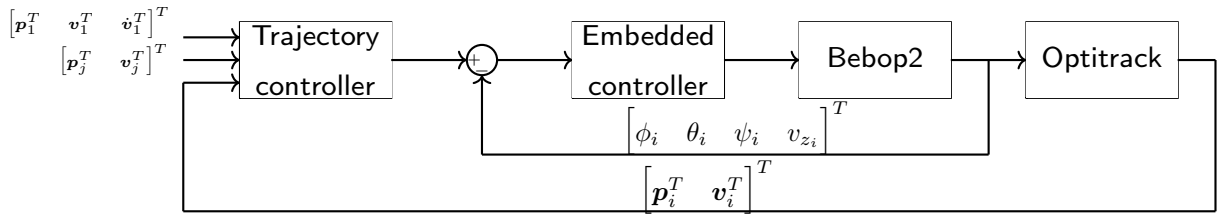

Figure 4.41: Cascade control architecture

The trajectory controller (outer loop) manages the relative positions of the quadrotors to achieve the desired formation while following the prescribed trajectory realized by the virtual leader. Once a reference trajectory, defined in terms of position $\boldsymbol{p}_r$, velocity $\boldsymbol{v}_r$, and acceleration $\boldsymbol{a}_r$ as functions of time, is given to the leader, the distributed control law in Eq. is employed to calculate the desired acceleration vector of each follower agent, while the control inputs for each quadrotor are determined by a back-stepping technique. In particular, the desired angles ϕ_d, θ_d are computed from the desired acceleration components for the agent. Setting $[a_{i_{d_x}}, a_{i_{d_y}}, a_{i_{d_z}}]^T = \boldsymbol{u}_i$, and $\psi_d = \psi_r$, where ψ_r is the reference yaw angle defined by the reference trajectory, yields

$$\theta_{d_i} = \arctan\left(\frac{a_{i_{d_x}} \cos\psi_d + a_{i_{d_y}} \sin\psi_d}{a_{i_{d_z}} - g}\right) \tag{4.39}$$

$$\phi_{d_i} = \arctan\left(\frac{(-a_{i_{d_x}} \sin\psi_d + a_{i_{d_y}} \cos\psi_d)\cos\theta_{d_i}}{-a_{i_{d_z}} + g}\right) \tag{4.40}$$

The desired vertical velocity is obtained by integrating the commanded vertical acceleration, whereas the desired yaw velocity is generated by a proportional control loop on the desired yaw angle ψ_d.

The control methodology is first evaluated through simulations using the Simulink Project SimoDrones, developed at ISAE-Supaero [1]. It features a high-fidelity 6-DoF model of the Parrot Bebop 2 quadrotor, including the brushless motor dynamics, battery consumption, onboard flight controller, and communication delays. The models of IMU, ultrasonic, and OptiTrack sensors are also considered. Environmental disturbances, such as those caused by airflow perturbations in the facility, are not included in the simulation model.

To evaluate the feasibility of the control architecture for cooperative transport tasks, the simulation environment is extended to include the dynamics of the payload and cables, modeled as multi-element systems, and the associated constraint forces, evaluated through

the Udwadia-Kalaba formulation, as shown in Sec. 2.3. The distributed control strategy described in Section 3.2.2 is implemented to control a formation of three quadrotors. The same software framework is used also for flight tests. A mode switch allows selection between simulation and experimental operation. In simulation mode, the control inputs generated by the formation controller are applied to the quadrotor model. In experimental mode, the same inputs are transmitted to the real drones, while the state feedback is acquired from the OptiTrack system via ROS blocks in Simulink.

In the experiments, we assume that the communication topology among followers is modeled as a connected and undirected graph, while the virtual leader has direct communication links with each follower. For the specific case considered, involving three follower agents and one virtual leader, the corresponding matrices are:

$$\mathcal{A} = \begin{bmatrix} 0 & 1 & 1 \\ 1 & 0 & 1 \\ 1 & 1 & 0 \end{bmatrix}, \quad \mathcal{D} = \begin{bmatrix} 2 & 0 & 0 \\ 0 & 2 & 0 \\ 0 & 0 & 2 \end{bmatrix}, \quad \mathcal{L} = \begin{bmatrix} 2 & -1 & -1 \\ -1 & 2 & -1 \\ -1 & -1 & 2 \end{bmatrix}, \quad \mathcal{B} = \begin{bmatrix} 1 & 0 & 0 \\ 0 & 1 & 0 \\ 0 & 0 & 1 \end{bmatrix}$$

The bandwidth of the Bebop 2 onboard attitude controller is estimated from the step response of the simulation model using the relation $\omega_{3\text{dB}} = \frac{3}{T_s}$, where T_s is the settling time. The resulting bandwidth is about $\omega_{3dB} = 1.4$ rad/s.

Following the same tuning procedure as described in Sec. 4.3, the gains are set to $k_p = 0.6$ and $k_v = 2$, also to guarantee stability in the presence of constant communication delays up to 0.1 s, measured during the experiments. These delays occur in the transmission of command inputs to the quadcopters and in the reception of position and speed measurements from the OptiTrack system to the guidance controller. With these gain values, the bandwidth of the formation controller is about 0.35 rad/s, which satisfies the frequency separation requirement for cascaded controllers. Furthermore, the resulting critical time-delay is approximately 0.19 s, which is above the 0.1 s delays measured in the experimental setup. In the next section, the results of the formation flight and cooperative load transportation are reported.

4.4.1 Results

In the first test (dubbed Case 1), the agents must take off simultaneously, maintaining a constant formation. When an altitude of 1.5 m is reached, ${}^{e}\boldsymbol{\delta}$ is updated to specify an equilateral triangular configuration. Once the trajectories converge on the new formation,

with errors on the agent positions lower than 0.05 m, the virtual leader starts to follow a circular trajectory with radius $R = 0.75$ m and frequency $\omega = 2$ rad/s. The maximum velocity on the reference trajectory is equal to 1.5 m/s. The agent initial positions are ${}^e\boldsymbol{p}_2 = [0, -2, 0]^T$ m, ${}^e\boldsymbol{p}_3 = [0, 2, 0]^T$ m, ${}^e\boldsymbol{p}_4 = [0, 0, 0]^T$ m, while the virtual leader is in the origin, ${}^e\boldsymbol{p}_1 = [0, 0, 0]^T$ m. The agent trajectories, acquired during the flight test, are reported in Fig. 4.42.

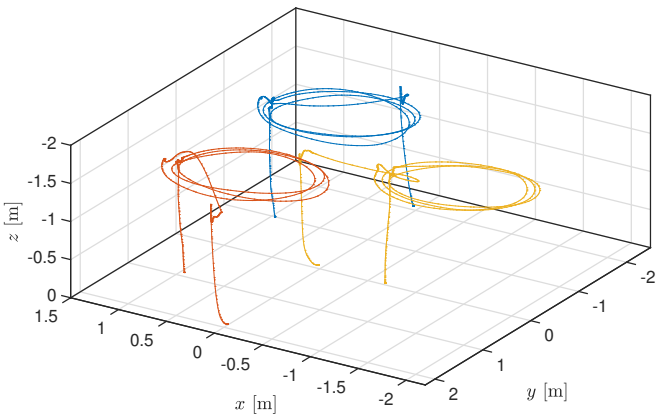

Figure 4.42: Case 1: Quadrotor trajectories

After take-off, the agents converge to the desired formation and track the virtual leader while maintaining the prescribed relative positions.

Formation errors among followers and those relative to the virtual leader are evaluated to assess the control system performance, as the former quantify the accuracy with which agents maintain their relative spatial configuration, while the latter measure how well they track the target trajectory. The formation error ϵ_{ij}, for $i = 1, ..., 4$, with $i \neq j$, is expressed as

$$\epsilon_{ij} = \|({}^e\boldsymbol{p}_i - {}^e\boldsymbol{p}_j) - ({}^e\boldsymbol{\delta}_i - {}^e\boldsymbol{\delta}_j)\|_1 \tag{4.41}$$

where $\epsilon_{ij} = \epsilon_{ji}$, while the trajectory tracking error ϵ_{tr} is defined as the distance between the virtual leader and the reference path. Given the aforementioned limited control accuracy along the vertical axis, and since the reference trajectory evolves in the horizontal plane, only the x-y components of the formation error are considered, as shown in Fig. 4.43. It is apparent that during take-off, the agents maintain the formation with minimal error, reaching a peak deviation of 0.03 m. At t =13.7 s, the step variation of the offset vector $\boldsymbol{\delta}$ causes a significant increase in the formation error, quickly canceled by the controller. The formation error remains low during the trajectory tracking phase, with a peak value

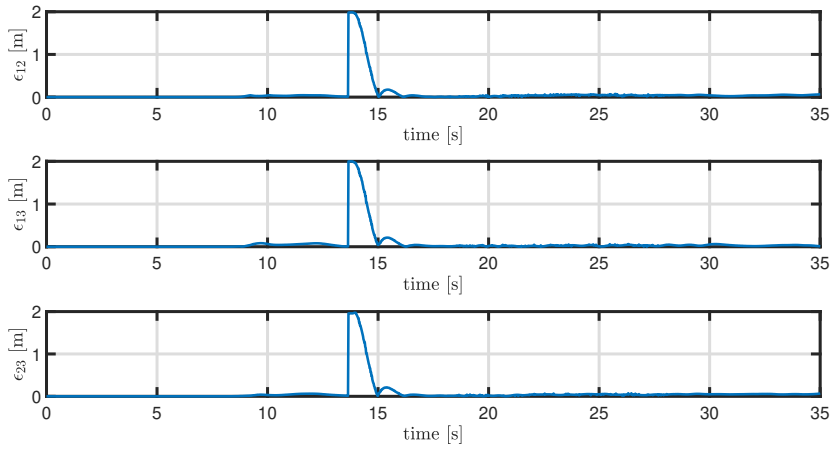

Figure 4.43: Case 1: time-histories of formation error

around 0.05 m, indicating good perturbation rejection with respect to aerodynamic effects not accounted for in the design of the control law. The leader-follower error plot, reported in Fig. 4.44, shows that all followers exhibit identical formation errors with respect to the

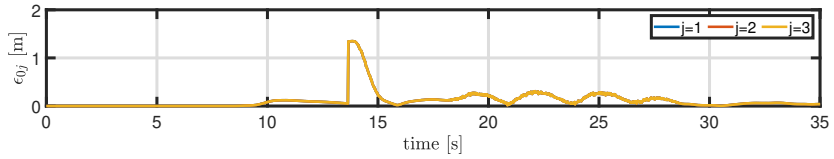

Figure 4.44: Case 1: time-histories of leader-follower formation error

virtual leader, the maximum deviation from the virtual leader being approximately 0.3 m, with a tracking delay of about 0.15 s and an overshoot of 0.05 m. The tracking delay is primarily due to the limited bandwidth of the onboard attitude controller, which constrains the responsiveness of the formation control loop. The root mean square value of the virtual leader tracking error with respect to the reference trajectory is approximately 0.04 m. A frame selected from the video acquired during the experiment is reported in Fig.4.45.

In the second test (Case 2), a load is attached to the quadrotors to evaluate the robustness of the formation control strategy under the disturbances introduced by the payload, not accounted for in the design of the control law, and to investigate its suitability for cooperative transportation tasks. The load is a cylinder with a radius of 0.1 m and a height of 0.2 m. It is connected to the quadrotors by cables of length 1.5 m, all attached to a single point on the upper base of the cylinder. The total mass of the payload and the connecting cables is 0.154 kg. The same circular trajectory used in Case 1 is the reference path for the virtual leader. Since the ultrasonic sensor used by the internal flight control system of the Bebop 2

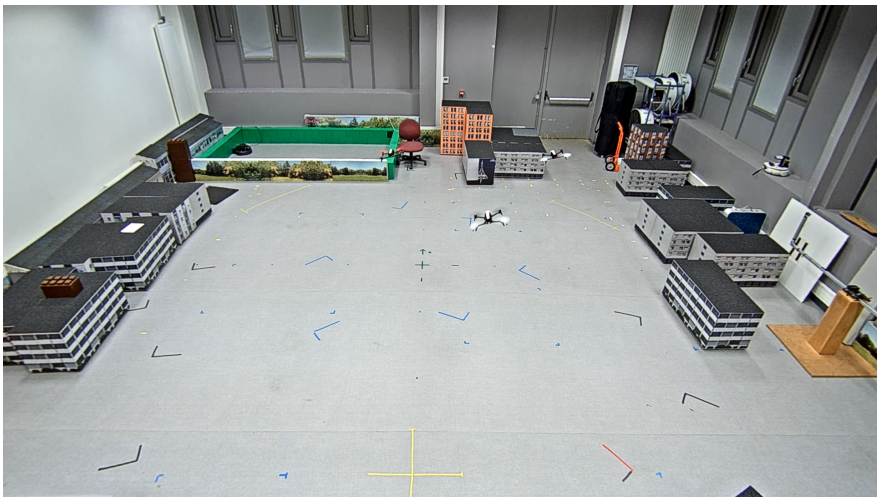

Figure 4.45: Case 1: Video frame of the test

drone for altitude estimation is below the c.g., the cable attachment point is located near the front of each drone, which generates a moment due to the load. As in the previous test, the quadrotors take-off simultaneously, starting from an initial triangular configuration. Upon reaching the target altitude, the formation is adjusted to form an equilateral triangle, which closely corresponds to the initial configuration. The trajectories of the quadrotors and the load in Fig. 4.46 show some oscillations in the altitude, due to the limited performance of the vertical control.

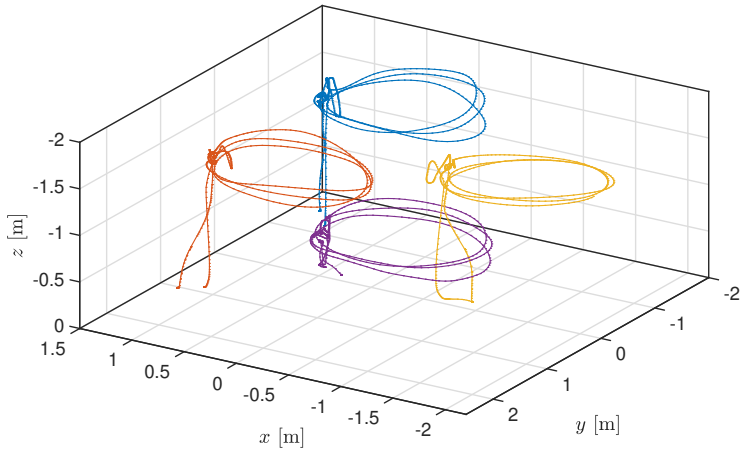

Figure 4.46: Case 2: quadrotor and load (purple line) trajectories

The results in terms of formation errors are reported in Fig. 4.47

Payload lifting causes an increase in the formation errors due to the tensile forces transmitted through the cables. Once the reference height is reached and the formation geometry is updated, the controller successfully stabilizes the agents in hovering with a small formation

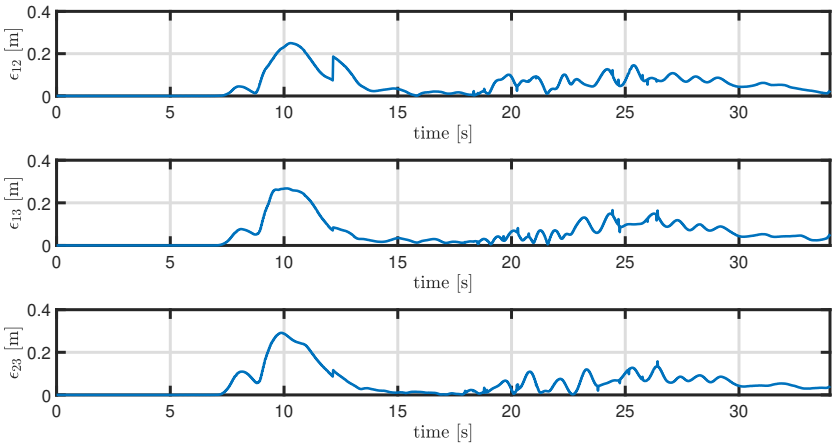

Figure 4.47: Case 2: time-histories of formation error

error. At t =17 s, the virtual leader begins to follow the reference trajectory. During this phase, the formation error remains bounded, with maximum values of approximately 0.16 m. The offset of the cable attachment point with respect to the c.g. contributes to larger formation errors. Fig.4.48 shows a video frame of the experiment.

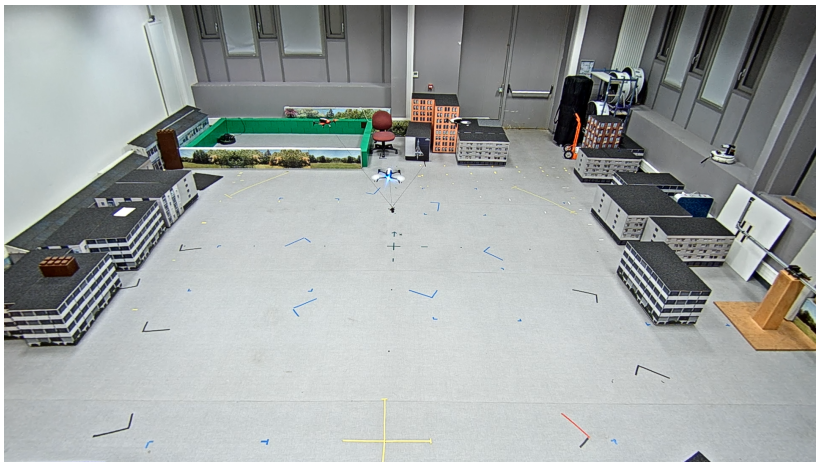

Figure 4.48: Case 2: Video frame of the test

As a conclusion, the results demonstrate the effectiveness of the approach in both formation maintenance and cooperative transport scenarios, as the system achieves accurate position tracking and stable formation flight, with bounded errors despite disturbances and communication delays.

Chapter 5

Conclusions

In this thesis, a transportation system composed of multiple quadrotors carrying a suspended load has been dealt with, focusing on modeling and control system design.

5.1 Slung-Load Modeling

A first mathematical model, based on the Udwadia–Kalaba formulation, was developed and implemented to account for the physical constraints between quadrotors and the load. To obtain a model suitable for dealing with a wide range of motions and maneuvers, including take-off and landing, a multi-element cable model was adopted. The Udwadia–Kalaba formulation, providing a closed-form expression for the constrained accelerations, is simple to implement and to adapt whenever the agent dynamics changes. Since the constraint forces are computed from the unconstrained dynamics of each subsystem, it allows to first define the unconstrained dynamics of each subsystem with any desired level of detail, including effects such as actuator dynamics, saturation, delays, and external disturbances, and then to impose the physical constraints among them. In other words, the Udwadia–Kalaba approach separates the modeling of individual subsystems from the enforcement of constraints; once the accurate free dynamics are established, the constraint equations can be applied without modifying the original models. Consequently, any change in a subsystem, for instance, replacing the quadrotor model with that of a helicopter, only requires updating its free dynamics, while the overall constraint formulation remains unchanged. For the same reason, this approach scales efficiently with the number of quadrotors in the system. Moreover, the explicit computation of the constraint forces enables the analysis of maximum allowable

stresses within the system. The Braun–Goldfarb algorithm was employed in the implementation of the simulation model to limit the accumulation of position and velocity errors over time. As the main drawback, it was found that the system could not be linearized when using this formulation.

A second mathematical model, based on a Lagrangian formulation on the configuration manifold, was derived and implemented. This model captures the constrained dynamics of the entire multi–body system, accounts for the offset attachment points on the quadrotors, and includes aerodynamic effects, while neglects actuator dynamics. To account for cable flexibility, a multi-element cable model has been employed. The resulting equations of motion provide a compact and elegant representation of the system dynamics. This formulation avoids cumbersome trigonometric expressions and does not rely on local coordinates, thereby eliminating singularities such as those associated with Euler angles. When derived within the Lagrangian framework, the system dynamics can be analytically linearized around equilibrium points or along desired trajectories, thus allowing the design of linear controllers. As a drawback, however, this formulation requires a large number of algebraic steps, and even minor errors can propagate throughout the entire derivation.

5.2 Cooperative Control

The control objective is to transport the payload with minimal swing and without collisions between quadrotors. In defining suitable control approaches for cooperative transportation, the analysis considered both load–centered and formation–centered strategies.

In the first approach, a time-varying LQR controller was designed based on the linearized dynamics of the coupled system, explicitly incorporating the coupling effects between the rigid payload, flexible cables, and multiple quadrotors in the control design. The reference states of the system, along with the feedforward control terms, were obtained by exploiting the differential flatness property of the system, with the payload position and attitude and the quadrotor yaw serving as flat outputs. An additional flat output can also be defined to impose constraints on the cable tensions required to track the reference trajectory, for instance, to identify configurations that minimize the forces exerted on the quadrotors during cooperative transportation.

In this approach, the payload position and attitude are directly controlled, enabling active stabilization of the payload and effective suppression of swing during transportation. Sim-

ulation results demonstrated that the controller is capable of stabilizing the payload even in the presence of large initial errors. Moreover, it achieves zero steady-state tracking error when following a lemniscate trajectory at a frequency of 0.3 π rad/s, corresponding to a maximum payload speed of 4 m/s and acceleration of 0.4 g.

Being a model-based approach, it requires accurate knowledge of the system parameters. Simulation results showed that the controller is able to stabilize the system when a $\pm 20\%$ uncertainty is introduced in the payload mass, although a maximum tracking error of about 0.5 m is observed. Moreover, when a 50% uncertainty is applied to the aerodynamic drag coefficient of the payload, the controller still maintains stability, although peak load position errors of about 1 m are observed. Being a centralized approach, it requires a ground station that computes the control commands for all agents simultaneously and transmits them to each individual quadrotor. This approach requires high-speed communication with the individual agents to enable active control of the payload. In outdoor applications, ensuring such fast communication with a ground station may be challenging. As an alternative, one of the quadrotors can act as the ground station, although this solution demands higher onboard computational capability. Simulation results showed that the system remains stable for communication delays between the controller and the agents of up to 0.01 s.

In the second approach, a cooperative formation control strategy with a leader–follower structure was adopted. A virtual leader tracks the prescribed trajectory, while the follower quadrotors maintain a desired relative configuration with respect to the leader and to each other, keeping the inter-agent distances fixed during transportation.

In this approach, the control design intentionally avoided the use of load motion information, in order to reduce the dependence on the mathematical model and avoid the need for additional sensors. The payload was treated as an external disturbance acting on the formation. To ensure robustness against these unmodeled forces and moments, a cascaded control architecture was adopted, in which the outer loop regulates the formation, while two INDI-based inner loops control the thrust and the attitude of the quadrotors. The robust INDI control law compensates for the neglected cable tension forces, as assumed in the formation control designs.

When three or more agents are employed, and under the assumption of non-collinear attachment points and always taut cables, the position and attitude of the payload are uniquely determined by the positions of the quadrotors. However, as observed in the simulations, when the cables are flexible, this assumption no longer holds and the payload exhibits oscil-

lations. During forward motion, the front quadrotors generate the horizontal forces required to tow the payload, while the rear quadrotors provide vertical lift. It is observed that the rear cables often become slack, since the formation moves faster than the payload due to its inertia. Since the payload swing is not directly controlled, the application of this approach is limited to low-speed maneuvers.

The results demonstrate the suitability of the proposed control architecture that, at the highest frequency in tracking the prescribed trajectory, achieves a moderate tracking error of the order of 0.3 m and negligible inter-agent errors with top speed and acceleration of 4 m/s and 0.4 g, respectively. Control system robustness to mass variation and communication delays is also satisfactory. In particular, the controller remains stable in the presence of a 20% uncertainty in the payload mass, with a maximum tracking error of approximately 0.01 m, and it tolerates communication delays up to 0.05 s without loss of stability.

The leader-follower formation controller has been experimentally tested using Parrot Bebop 2 quadrotors and a motion capture system. The experimental results demonstrated the effectiveness of the approach in formation maintenance. The system achieved accurate position tracking and stable formation flight, with bounded errors despite disturbances, such as unmodeled aerodynamic effects and constraint forces, and actuation delays. Compared to simulations where INDI-based inner loops are adopted, the tracking errors result in higher values.

5.3 Future Work

Future work will focus on the experimental validation of the proposed cascaded control architecture, which relies exclusively on GPS and IMU measurements and does not require information on the payload state. An experimental setup with four quadrotors in the 10 kg mass class is currently under development for outdoor flight demonstrations.

Although the models developed in this thesis already include aerodynamic drag on all subsystems, aerodynamic interactions among the vehicles and downwash effects acting on the cables and payload are also important. While the INDI-based controllers provide a robust framework capable of rejecting external disturbances, explicitly modeling downwash will allow for a more accurate prediction of internal disturbances and will support the design of system parameters, such as suitable cable lengths or minimum inter-vehicle spacing, to mitigate these effects.

For the centralized control architecture, future developments will focus on designing state estimation algorithms for both the payload and the cables states. Recent advances in onboard hardware now make it possible to run computationally demanding perception algorithms directly on the quadrotors, enabling real-time estimation of the payload state during flight. In particular, integrating onboard vision for real-time load state estimation will be pursued. Another direction for future work is the synthesis of robust linear controllers, such as H_∞ control or model predictive control (MPC), to replace the LQR and improve performance in the presence of model uncertainties and external disturbances.

Finally, future work may also explore learning-based control strategies to enhance system autonomy and performance. In particular, reinforcement learning (RL) could be investigated as a tool to derive control policies that map sensor measurements directly to actuator commands, with the potential to reduce load swing and tracking errors beyond what is achievable with classical tuning.

Bibliography

[1] José A Macés-Hernández, François Defaÿ, and Corentin Chauffaut. Autonomous landing of an uav on a moving platform using model predictive control. In *2017 11th Asian Control Conference (ASCC)*, pages 2298–2303. IEEE, 2017.

[2] Disha Amrutlal Gandhi and Munmun Ghosal. Novel low cost quadcopter for surveillance application. In *2018 International Conference on Inventive Research in Computing Applications (ICIRCA)*, pages 412–414. IEEE, 2018.

[3] Yiheng Liu, Honglun Wang, and Jiaxuan Fan. Novel docking controller for autonomous aerial refueling with probe direct control and learning-based preview method. *Aerospace science and technology*, 94:105403, 2019.

[4] Mihail Pivtoraiko, Daniel Mellinger, and Vijay Kumar. Incremental micro-uav motion replanning for exploring unknown environments. In *2013 IEEE international conference on robotics and automation*, pages 2452–2458. IEEE, 2013.

[5] Sofia Karma, Eleni Zorba, GC Pallis, G Statheropoulos, I Balta, Katerina Mikedi, Julia Vamvakari, Athina Pappa, Michail Chalaris, Gavriil Xanthopoulos, et al. Use of unmanned vehicles in search and rescue operations in forest fires: Advantages and limitations observed in a field trial. *International journal of disaster risk reduction*, 13:307–312, 2015.

[6] Jose Alfredo Guerrero. Flight formation control strategies for mini uavs. *Flight Formation Control*, pages 135–163, 2012.

[7] Yuxuan Liu, Hu Liu, Yongliang Tian, and Cong Sun. Reinforcement learning based two-level control framework of uav swarm for cooperative persistent surveillance in an unknown urban area. *Aerospace Science and Technology*, 98:105671, 2020.

[8] Jan Willmann, Federico Augugliaro, Thomas Cadalbert, Raffaello D'Andrea, Fabio Gramazio, and Matthias Kohler. Aerial robotic construction towards a new field of architectural research. *International journal of architectural computing*, 10(3):439–459, 2012.

[9] Kristian Klausen, Chris Meissen, Thor I Fossen, Murat Arcak, and Tor Arne Johansen. Cooperative control for multirotors transporting an unknown suspended load under environmental disturbances. *IEEE Transactions on Control Systems Technology*, 28(2):653–660, 2018.

[10] Daniel KD Villa, Alexandre S Brandao, and Mário Sarcinelli-Filho. A survey on load transportation using multirotor uavs. *J. Intell. Robot. Syst.*, 98:267–296, 2020.

[11] Yu Herng Tan, Shupeng Lai, Kangli Wang, and Ben M. Chen. Cooperative control of multiple unmanned aerial systems for heavy duty carrying. *Annu. Rev. Control*, 46:44–57, 2018.

[12] Ewoud JJ Smeur, Guido CHE de Croon, and Qiping Chu. Cascaded incremental nonlinear dynamic inversion for mav disturbance rejection. *Control Eng. Pract.*, 73:79–90, 2018.

[13] Taeyoung Lee. Geometric control of quadrotor uavs transporting a cable-suspended rigid body. *IEEE Transactions on Control Systems Technology*, 26(1):255–264, 2017.

[14] Guanrui Li and Giuseppe Loianno. Nonlinear model predictive control for cooperative transportation and manipulation of cable suspended payloads with multiple quadrotors. In *2023 IEEE/RSJ International Conference on Intelligent Robots and Systems (IROS)*, pages 5034–5041. IEEE, 2023.

[15] Wen-Chieh Chen, Michihiro Kawanishi, Chian-Yu Lu, Syu-You Ciou, Chun-Liang Lin, and Cheng-Hsin Hsu. Cooperative load transportation of multi-drones based on disturbance observer and formation control. *IEEE Access*, 12:77393–77405, 2024.

[16] Junyi Geng and Jack W Langelaan. Cooperative transport of a slung load using load-leading control. *Journal of Guidance, Control, and Dynamics*, 43(7):1313–1331, 2020.

[17] Koushil Sreenath and Vijay Kumar. Dynamics, control and planning for cooperative manipulation of payloads suspended by cables from multiple quadrotor robots. *rn*, 1(r2):r3, 2013.

[18] Julian Estevez, Gorka Garate, Jose Manuel Lopez-Guede, and Mikel Larrea. Review of aerial transportation of suspended-cable payloads with quadrotors. *Drones*, 8(2):35, 2024.

[19] Kristian Klausen, Thor I Fossen, Tor Arne Johansen, and A Pedro Aguiar. Cooperative path-following for multirotor uavs with a suspended payload. In *2015 IEEE Conference on Control Applications (CCA)*, pages 1354–1360. IEEE, 2015.

[20] Gaetano Tartaglione, Egidio D'Amato, Marco Ariola, Pierluigi Salvo Rossi, and Tor Arne Johansen. Model predictive control for a multi-body slung-load system. *Robot. Auton. Syst.*, 92:1–11, 2017.

[21] Hyun-Shik Oh, Dong-Wan Yoo, Byung-Yoon Lee, Gun-Hee Moon, and Min-Jea Tahk. Leader steering method for the guidance and control of multi-lift transportation system. *Int. J. Robot. Autom.*, 32, 09 2017.

[22] Byung-Yoon Lee, Gun hee Moon, Dong-Yeon Lee, Min-Jea Tahk, and Hyun-Shik Oh. Modeling and parameter identification of the slung load system of an unmanned rotorcraft using a flexible cable. *Int. J. Aeronaut. Space Sci.*, 18:365–377, 2017.

[23] Farhad Goodarzi and Taeyoung Lee. Dynamics and control of quadrotor uavs transporting a rigid body connected via flexible cables. *Proceedings of the American Control Conference*, 01 2015.

[24] Yihua Cao, Wensong Nie, Zhaorui Wang, and Shaofeng Wan. Dynamic modeling of helicopter-slung load system under the flexible sling hypothesis. *Aerosp. Sci. Technol.*, 99:105770, 2020.

[25] Morten Bisgaard, Jan Dimon Bendtsen, and Anders la Cour-Harbo. Modeling of generic slung load system. *Journal of guidance, control, and dynamics*, 32(2):573–585, 2009.

[26] GA Cardona, D Tellez-Castro, and E Mojica-Nava. Cooperative transportation of a cable-suspended load by multiple quadrotors. *IFAC-Pap*, 52(20):145–150, 2019.

[27] Patricio J. Cruz and Rafael Fierro. Autonomous lift of a cable-suspended load by an unmanned aerial robot. *2014 IEEE Conference on Control Applications (CCA)*, pages 802–807, 2014.

[28] Patricio J. Cruz and Rafael Fierro. Cable-suspended load lifting by a quadrotor uav: hybrid model, trajectory generation, and control. *Auton. Robots*, 41:1629–1643, 2017.

[29] Behzad Shirani, Majdeddin Najafi, and Iman Izadi. Cooperative load transportation using multiple uavs. *Aerosp. Sci. Technol.*, 84(1):158–169, 2019.

[30] Fabio Polese, Giovanni Di Monaco, Alessandro Zavoli, and Guido De Matteis. Limitations of switching dynamics in the modeling of cooperative slung load transportation system. In *2025 American Control Conference (ACC)*, pages 5148–5153, 2025.

[31] Taeyoung Lee. *Computational geometric mechanics and control of rigid bodies*. PhD thesis, University of Michigan, 2008.

[32] Firdaus E Udwadia and Robert E Kalaba. A new perspective on constrained motion. *Proc. R. Soc. Lond., Ser. A Math. Phys. Sci.*, 439(1906):407–410, 1992.

[33] Rui Ying Zhao, Meng Li, Qiang Niu, and Ye hwa Chen. Udwadia–kalaba constraint-based tracking control for artificial swarm mechanical systems: dynamic approach. *Nonlinear Dyn.*, 100:2381 – 2399, 2020.

[34] Conghua Wang, Jinchen Ji, Zhonghua Miao, and Jin Zhou. Formation tracking of multi-robot systems with switching directed topologies based on udwadia-kalaba approach. *Appl. Math. Model.*, 126:147–158, 2024.

[35] Mikkel Cornelius Nielsen, Ole Alexander Eidsvik, Mogens Blanke, and Ingrid Schjølberg. Constrained multi-body dynamics for modular underwater robots — theory and experiments. *Ocean Eng.*, 149:358–372, 2018.

[36] Taeyoung Lee. Geometric control of quadrotor uavs transporting a cable-suspended rigid body. *IEEE Trans. Control Syst. Technol.*, 26(1):255–264, 2018.

[37] Richard M Murray, Muruhan Rathinam, and Willem Sluis. Differential flatness of mechanical control systems: A catalog of prototype systems. In *ASME international mechanical engineering congress and exposition*, pages 349–357. San Francisco CA, 1995.

[38] Koushil Sreenath, Taeyoung Lee, and Vijay Kumar. Geometric control and differential flatness of a quadrotor uav with a cable-suspended load. In *52nd IEEE conference on decision and control*, pages 2269–2274. IEEE, 2013.

[39] Prasanth Kotaru, Guofan Wu, and Koushil Sreenath. Differential-flatness and control of quadrotor (s) with a payload suspended through flexible cable (s). In *2018 Indian Control Conference (ICC)*, pages 352–357. IEEE, 2018.

[40] Jun Zeng and Koushil Sreenath. Geometric control of a quadrotor with a load suspended from an offset. In *2019 American Control Conference (ACC)*, pages 3044–3050. IEEE, 2019.

[41] Koushil Sreenath, Nathan Michael, and Vijay Kumar. Trajectory generation and control of a quadrotor with a cable-suspended load - a differentially-flat hybrid system. In *2013 IEEE International Conference on Robotics and Automation*, pages 4888–4895, 2013.

[42] Koushil Sreenath and Vijay Kumar. Dynamics, control and planning for cooperative manipulation of payloads suspended by cables from multiple quadrotor robots. In *Proceedings of Robotics: Science and Systems*, Berlin, Germany, June 2013.

[43] Carlo Masone and Paolo Stegagno. Shared control of an aerial cooperative transportation system with a cable-suspended payload. *Journal of Intelligent & Robotic Systems*, 103(3):40, 2021.

[44] M Takahashi, M Whalley, Marcos G Berrios, and GJ Schulein. A system for autonomous rotorcraft dual-lift flight research. In *74th Annual Forum of the American Helicopter Society*, pages 1–18. American Helicopter Society Phoenix, AZ, 2018.

[45] ZuQun Li, Joseph F Horn, and Jack W Langelaan. Coordinated transport of a slung load by a team of autonomous rotorcraft. In *AIAA Guidance, Navigation, and Control Conference*, page 0968, 2014.

[46] Venkata Naga Prasanth Kotaru. *Dynamics and Control for Collaborative Aerial Manipulation*. PhD thesis, University of California, Berkeley, 2022.

[47] Markus Zürn, Kye Morton, Alexander Heckmann, Aaron McFadyen, Stefan Notter, and Felipe Gonzalez. Mpc controlled multirotor with suspended slung load: System

architecture and visual load detection. In *2016 IEEE Aerospace Conference*, pages 1–11, 2016.

[48] Kuldeep K Dhiman, Mangal Kothari, and Abhishek. Autonomous control and transportation of underslung load with single and dual lift helicopter systems. *Journal of Dynamic Systems, Measurement, and Control*, 144(4):041001, 2022.

[49] Emanuele Luigi de Angelis, Elia Costantini, and Fabrizio Giulietti. Swing state estimation and control of series-connected slung payloads in rotorcraft transportation. *Available at SSRN 5521525*.

[50] Taeyoung Lee, Koushil Sreenath, and Vijay Kumar. Geometric control of cooperating multiple quadrotor uavs with a suspended payload. In *52nd IEEE Conference on Decision and Control*, pages 5510–5515, 2013.

[51] Taeyoung Lee. Geometric control of multiple quadrotor uavs transporting a cable-suspended rigid body. In *53rd IEEE Conference on Decision and Control*, pages 6155–6160, 2014.

[52] Junyi Geng and Jack W. Langelaan. Cooperative transport of a slung load using load-leading control. *J. Guid. Control Dyn.*, 43(7):1313–1331, 2020.

[53] Khaled Wahba and Wolfgang Hönig. Efficient optimization-based cable force allocation for geometric control of a multirotor team transporting a payload. *IEEE Robotics and Automation Letters*, 9(4):3688–3695, 2024.

[54] Prasanth Kotaru and Koushil Sreenath. Multiple quadrotors carrying a flexible hose: dynamics, differential flatness and control. *IFAC-PapersOnLine*, 53(2):8832–8839, 2020.

[55] Qijie Chen, Yao Wang, Yuqiang Jin, Taoyu Wang, Xinhua Nie, and Tinglong Yan. A survey of an intelligent multi-agent formation control. *Appl. Sci.*, 13(10), 2023.

[56] Yefeng Liu, Jingjing Liu, Zengpeng He, Zhenhong Li, Qichun Zhang, and Zhengtao Ding. A survey of multi-agent systems on distributed formation control. *Unmanned Syst.*, 12(05):913–926, 2024.

[57] Wei Ren and Randal W Beard. *Distributed consensus in multi-vehicle cooperative control*, volume 27. Springer, 2008.

[58] Toru Namerikawa, Yasuhiro Kuriki, and Ahmed Khalifa. Consensus-based cooperative formation control for multiquadcopter system with unidirectional network connections. *Journal of Dynamic Systems, Measurement, and Control*, 140(4):044502, 2018.

[59] Jianan Wang, Zhengyang Zhou, Chunyan Wang, and Jiayuan Shan. Multiple quadrotors formation flying control design and experimental verification. *Unmanned Systems*, 7(01):47–54, 2019.

[60] Anthony Oliveira Pinto, Harrison Neves Marciano, Vinicius Pacheco Bacheti, Mauro Sergio Mafra Moreira, Alexandre Santos Brandão, and Mario Sarcinelli-Filho. High-level modeling and control of the bebop 2 micro aerial vehicle. In *2020 International Conference on Unmanned Aircraft Systems (ICUAS)*, pages 939–947. IEEE, 2020.

[61] Bocheng Yu, Xiwang Dong, Zongying Shi, and Yisheng Zhong. Formation control for quadrotor swarm systems: Algorithms and experiments. In *Proceedings of the 32nd Chinese control conference*, pages 7099–7104. IEEE, 2013.

[62] Juan Antonio Vazquez Trejo, Manuel Adam-Medina, Carlos Daniel Garcia-Beltran, Gerardo Vicente Guerrero Ramírez, Betty yolanda lópez Zapata, Eduardo-Mael Sanchez-Coronado, and Didier Theilliol. Robust formation control based on leader-following consensus in multi-agent systems with faults in the information exchange: Application in a fleet of unmanned aerial vehicles. *IEEE Access*, 9:104940–104949, 2021.

[63] Valentim Ernandes Neto, Alexandre Santos Brandão, and Mário Sarcinelli-Filho. Load manipulation by a triangular formation of quadrotors. In *2020 International Conference on Unmanned Aircraft Systems (ICUAS)*, pages 744–753. IEEE, 2020.

[64] Giovanny Ortega, Filiberto Muñoz, ES Espinoza Quesada, Luis R Garcia, and Patricio Ordaz. Implementation of leader-follower linear consensus algorithm for coordination of multiple aircrafts. In *2015 Workshop on Research, Education and Development of Unmanned Aerial Systems (RED-UAS)*, pages 25–32. IEEE, 2015.

[65] Giovanni Di Monaco, Alessandro Zavoli, Guido De Matteis, and Giulio Avanzini. Optimal formation control for cooperative slung load transportation. In *AIAA SCITECH 2024 Forum*, page 2743, 2024.

[66] Hector Garcia De Marina and Ewoud Smeur. Flexible collaborative transportation by a team of rotorcraft. In *2019 International Conference on Robotics and Automation (ICRA)*, pages 1074–1080, 2019.

[67] Kento Kotani, Zhiqin Guo, Toru Namerikawa, and Zhihua Qu. Cooperative transport control by a multicopter system. *IET Control Theory & Applications*, 15(6):861–876, 2021.

[68] Afef Hfaiedh, Ahmed Chemori, and Afef Abdelkrim. Observer-based robust integral of the sign of the error control of class i of underactuated mechanical systems: Theory and real-time experiments. *Transactions of the Institute of Measurement and Control*, 44:014233122110313, 08 2021.

[69] Morten Bisgaard. Modeling, estimation, and control of helicopter slung load system. 2008.

[70] Guofan Wu and Koushil Sreenath. Variation-based linearization of nonlinear systems evolving on $so(3)$ and s^2. *IEEE Access*, 3:1592–1604, 2015.

[71] Ewoud JJ Smeur, Qiping Chu, and Guido CHE De Croon. Adaptive incremental nonlinear dynamic inversion for attitude control of micro air vehicles. *J. Guid. Control Dyn.*, 39(3):450–461, 2016.

[72] Ezra Tal and Sertac Karaman. Accurate tracking of aggressive quadrotor trajectories using incremental nonlinear dynamic inversion and differential flatness. *IEEE Transactions on Control Systems Technology*, 29(3):1203–1218, 2020.

[73] Farhad A Goodarzi and Taeyoung Lee. Stabilization of a rigid body payload with multiple cooperative quadrotors. *Journal of Dynamic Systems, Measurement, and Control*, 138(12):121001, 2016.

[74] Joachim Baumgarte. Stabilization of constraints and integrals of motion in dynamical systems. *Computer methods in applied mechanics and engineering*, 1(1):1–16, 1972.

[75] Morten Bisgaard. *Modeling, Estimation, Andcontrol of Helicopterslung Load System*. Department of Electronic Systems, Section for Automation and Control ..., 2007.

[76] David J. Braun and Michael Goldfarb. Simulation of constrained mechanical systems — part i: An equation of motion. *J. Appl. Mech.*, 79:041017, 2012.

[77] Bernard Etkin and Lloyd Duff Reid. *Dynamics of Flight Stability and Control*, chapter 1,4. John Wiley & Sons, Inc, USA, 3 edition, 1996.

[78] Samir Bouabdallah. Design and control of quadrotors with application to autonomous flying. Technical report, Epfl, 2007.

[79] John M Lee. Smooth manifolds. In *Introduction to smooth manifolds*, pages 1–29. Springer, 2003.

[80] Francesco Bullo and Andrew D Lewis. *Geometric control of mechanical systems: modeling, analysis, and design for simple mechanical control systems*, volume 49. Springer, 2019.

[81] Taeyoung Lee, Melvin Leok, and N Harris McClamroch. Control of complex maneuvers for a quadrotor uav using geometric methods on se (3). *arXiv preprint arXiv:1003.2005*, 2010.

[82] Taeyoung Lee, Melvin Leok, and N Harris McClamroch. Stable manifolds of saddle points for pendulum dynamics on s^ 2 and so (3). *arXiv preprint arXiv:1103.2822*, 2011.

[83] Taeyoung Lee, Melvin Leok, and N. Harris McClamroch. Global formulations of lagrangian and hamiltonian mechanics on two-spheres. In *2015 54th IEEE Conference on Decision and Control (CDC)*, pages 6010–6015, 2015.

[84] Taeyoung Lee, Melvin Leok, and N Harris McClamroch. *Global formulations of Lagrangian and Hamiltonian dynamics on manifolds*. Springer, 2018.

[85] Koushil Sreenath, Nathan Michael, and Vijay Kumar. Trajectory generation and control of a quadrotor with a cable-suspended load-a differentially-flat hybrid system. In *2013 IEEE international conference on robotics and automation*, pages 4888–4895. IEEE, 2013.

[86] Farhad Goodarzi, Daewon Lee, and Taeyoung Lee. Geometric nonlinear pid control of a quadrotor uav on se (3). In *2013 European control conference (ECC)*, pages 3845–3850. IEEE, 2013.

[87] Jianan Wang, Chunyan Wang, Ming Xin, Zhengtao Ding, and Jiayuan Shan. *Cooperative control of multi-agent systems: An optimal and robust perspective*. Academic Press, 2020.

[88] Reza Olfati-Saber and Richard M Murray. Consensus problems in networks of agents with switching topology and time-delays. *IEEE Transactions on automatic control*, 49(9):1520–1533, 2004.

[89] Aaron D Ames, Samuel Coogan, Magnus Egerstedt, Gennaro Notomista, Koushil Sreenath, and Paulo Tabuada. Control barrier functions: Theory and applications. In *2019 18th European control conference (ECC)*, pages 3420–3431. Ieee, 2019.

[90] Li Wang, Aaron D Ames, and Magnus Egerstedt. Safety barrier certificates for collisions-free multirobot systems. *IEEE Transactions on Robotics*, 33(3):661–674, 2017.

[91] Quan Nguyen and Koushil Sreenath. Exponential control barrier functions for enforcing high relative-degree safety-critical constraints. In *2016 American Control Conference (ACC)*, pages 322–328. IEEE, 2016.

Appendix A

A.1 Moore-Penrose Inverse

A square matrix $\boldsymbol{A} \in \mathbb{R}^{n \times n}$ is invertible if and only if $\det(\boldsymbol{A}) \neq 0$. In this case, there exists a unique matrix $\boldsymbol{A}^{-1} \in \mathbb{R}^{n \times n}$, referred to as the inverse of $\boldsymbol{A}$, such that

$$\boldsymbol{A}^{-1}\boldsymbol{A} = \boldsymbol{A}\boldsymbol{A}^{-1} = \boldsymbol{I}, \tag{A.1}$$

where $\boldsymbol{I} \in \mathbb{R}^{n \times n}$ denotes the identity matrix.
Now, consider a rectangular matrix $\boldsymbol{A} \in \mathbb{R}^{m \times n}$ with $m \neq n$. By definition, such a matrix does not admit an inverse. Nevertheless, by defining

$$\boldsymbol{B} = (\boldsymbol{A}^T\boldsymbol{A})^{-1}\boldsymbol{A}^T \in \mathbb{R}^{n \times m}, \tag{A.2}$$

one obtains

$$\boldsymbol{B}\boldsymbol{A} = (\boldsymbol{A}^T\boldsymbol{A})^{-1}\boldsymbol{A}^T\boldsymbol{A} = \boldsymbol{I}. \tag{A.3}$$

In general, however,

$$\boldsymbol{A}\boldsymbol{B} \neq \boldsymbol{I}. \tag{A.4}$$

The matrix $\boldsymbol{B}$ is called the *left pseudo-inverse* of $\boldsymbol{A}$. It is obtained by pre-multiplying $\boldsymbol{A} \in \mathbb{R}^{m \times n}$ with its transpose $\boldsymbol{A}^T \in \mathbb{R}^{n \times m}$, which produces the square matrix $\boldsymbol{A}^T\boldsymbol{A} \in \mathbb{R}^{n \times n}$. Under the assumption that $\det(\boldsymbol{A}^T\boldsymbol{A}) \neq 0$, this matrix is invertible, and multiplication by $(\boldsymbol{A}^T\boldsymbol{A})^{-1}$ leads directly to the identity $\boldsymbol{I} \in \mathbb{R}^{n \times n}$.
As previously said, the existence of $\boldsymbol{B}$ is guaranteed if and only if $\det(\boldsymbol{A}^T\boldsymbol{A}) \neq 0$. In general, however, the matrix $\boldsymbol{A}^T\boldsymbol{A}$ is only positive semidefinite, that is, all of its eigenvalues are non–negative, but some of them may be zero, in which case the matrix is not invertible.

To see this, consider the eigenvalue problem

$$\boldsymbol{A}^T\boldsymbol{A}\boldsymbol{v} = \lambda\boldsymbol{v}. \tag{A.5}$$

from which it follows that

$$\boldsymbol{v}^T\boldsymbol{A}^T\boldsymbol{A}\boldsymbol{v} = \boldsymbol{w}^T\boldsymbol{w} \geqslant 0, \qquad w = \boldsymbol{A}\boldsymbol{v}. \tag{A.6}$$

which can also be written as

$$\boldsymbol{v}^T\boldsymbol{A}^T\boldsymbol{A}\boldsymbol{v} = \boldsymbol{v}^T\lambda\boldsymbol{v} = (\boldsymbol{v}^T\boldsymbol{v})\,\lambda. \tag{A.7}$$

Equating the two expressions gives

$$(\boldsymbol{v}^T\boldsymbol{v})\,\lambda = \boldsymbol{w}^T\boldsymbol{w} \geqslant 0, \tag{A.8}$$

showing that $\lambda \geqslant 0$. Hence, $\boldsymbol{A}^T\boldsymbol{A}$ has non–negative eigenvalues and may fail to be invertible if any $\lambda = 0$. In order to guarantee invertibility, a small regularization term (δ) is introduced and the *left pseudo-inverse* is defined as

$$\widehat{B} = \boldsymbol{A}^T\boldsymbol{A} + \delta^2\boldsymbol{I}, \qquad \delta \neq 0. \tag{A.9}$$

The corresponding eigenvalue problem becomes

$$\widehat{B}\,\hat{\boldsymbol{v}} = \hat{\lambda}\,\hat{\boldsymbol{v}}, \tag{A.10}$$

$$\boldsymbol{A}^T\boldsymbol{A}\,\hat{\boldsymbol{v}} + \delta^2\hat{\boldsymbol{v}} = \hat{\lambda}\,\hat{\boldsymbol{v}}, \tag{A.11}$$

which implies $\hat{\boldsymbol{v}} = \boldsymbol{v}$ and $\hat{\lambda} = \lambda + \delta^2 > 0$. Therefore, $\widehat{B}$ is positive definite and thus always invertible. The same reasoning applies to the *right pseudo-inverse*, defined as $\boldsymbol{C} = \boldsymbol{A}^T(\boldsymbol{A}\boldsymbol{A}^T)^{-1} \in \mathbb{R}^{n\times m}$, by considering instead the perturbed matrix $\widehat{C} = \boldsymbol{A}\boldsymbol{A}^T + \delta^2\boldsymbol{I}$.
The Moore-Penrose pseudoinverse is a generalization of both $\boldsymbol{B}$ and $\boldsymbol{C}$, and is defined as

$$\boldsymbol{A}^+ = \lim_{\delta\to 0}(\boldsymbol{A}^T\boldsymbol{A} + \delta^2\boldsymbol{I})^{-1}\boldsymbol{A}^T = \lim_{\delta\to 0}\boldsymbol{A}^T(\boldsymbol{A}\boldsymbol{A}^T + \delta^2\boldsymbol{I})^{-1}. \tag{A.12}$$

This matrix exists and is unique for any $\boldsymbol{A} \in \mathbb{R}^{m\times n}$, and satisfies the following four properties:

1. $\boldsymbol{A}\boldsymbol{A}^{+}\boldsymbol{A} = \boldsymbol{A}$

2. $\boldsymbol{A}^{+}\boldsymbol{A}\boldsymbol{A}^{+} = \boldsymbol{A}^{+}$

3. $(\boldsymbol{A}\boldsymbol{A}^{+})^{T} = \boldsymbol{A}\boldsymbol{A}^{+}$

4. $(\boldsymbol{A}^{+}\boldsymbol{A})^{T} = \boldsymbol{A}^{+}\boldsymbol{A}$

In particular, $\boldsymbol{A}^{+}\boldsymbol{A} = \boldsymbol{I}$ if $m \geqslant n$ and $\text{rank}(\boldsymbol{A}) = n$, while $\boldsymbol{A}\boldsymbol{A}^{+} = \boldsymbol{I}$ if $m \leqslant n$ and $\text{rank}(\boldsymbol{A}) = m$. In these cases, the Moore-Penrose pseudoinverse reduces to the left pseudoinverse $\boldsymbol{B}$ or to the right pseudoinverse $\boldsymbol{C}$, respectively. Finally, when $m = n$ and $\text{rank}(\boldsymbol{A}) = n$, one recovers the classical inverse, namely $\boldsymbol{A}^{+} = \boldsymbol{A}^{-1}$.

A.1.1 Computation via SVD

The definition given in Eq. (A.12) does not directly provide a practical way to compute the Moore–Penrose pseudoinverse. A standard approach is to employ the Singular Value Decomposition (SVD). For any $\boldsymbol{A} \in \mathbb{R}^{m\times n}$, there exists a factorization

$$\boldsymbol{A} = \boldsymbol{U}\,\boldsymbol{\Sigma}\,\boldsymbol{V}^{T} \tag{A.13}$$

where $\boldsymbol{U} \in \mathbb{R}^{m\times m}$ and $\boldsymbol{V} \in \mathbb{R}^{n\times n}$ are orthonormal matrices, obtained respectively from the eigenvectors of $\boldsymbol{A}\boldsymbol{A}^{T}$ and $\boldsymbol{A}^{T}\boldsymbol{A}$. The matrix $\boldsymbol{\Sigma} \in \mathbb{R}^{m\times n}$ is diagonal, with non–zero entries σ_{ii}, known as the *singular values* of $\boldsymbol{A}$. These singular values are equal to the square roots of the $s = \min(m, n)$ largest eigenvalues of $\boldsymbol{A}\boldsymbol{A}^{T}$, ordered as $\lambda_1 \geqslant \lambda_2 \geqslant \cdots \geqslant \lambda_s \geqslant \cdots \geqslant \lambda_m$. Applying the pseudo-inverse operator to Eq. (A.13), and exploiting the properties of orthonormal matrices, yields

$$\boldsymbol{A}^{+} = \boldsymbol{V}\,\boldsymbol{\Sigma}^{+}\,\boldsymbol{U}^{T} \tag{A.14}$$

where $\boldsymbol{\Sigma}^{+} \in \mathbb{R}^{n\times m}$ is a diagonal matrix whose non–zero entries satisfy $\hat{\sigma}_{ii} = \frac{1}{\sigma_{ii}}$, while all other elements are zero.

It is worth noting that this SVD–based procedure is the one implemented in `MATLAB` through the command `pinv`.

A.1.2 Solution of Linear Systems

The Moore-Penrose inverse provides a powerful framework for the solution of linear systems of the form

$$\boldsymbol{A}\boldsymbol{x} = \boldsymbol{b} \tag{A.15}$$

where $\boldsymbol{A} \in \mathbb{R}^{m\times n}$, $\boldsymbol{x} \in \mathbb{R}^n$, and $\boldsymbol{b} \in \mathbb{R}^m$. When $\boldsymbol{A}$ is square and nonsingular, the unique solution is $\boldsymbol{x} = \boldsymbol{A}^{-1}\boldsymbol{b}$, and in this case the pseudoinverse reduces to the inverse. In the more general case, where $\boldsymbol{A}$ may be rectangular or rank-deficient, the system is either underdetermined or overdetermined, and the Moore-Penrose pseudoinverse provides a systematic way to construct solutions.

The general solution of Eq. (A.15) can be expressed as

$$\boldsymbol{x} = \boldsymbol{A}^{+}\boldsymbol{b} + (\boldsymbol{I} - \boldsymbol{A}^{+}\boldsymbol{A})\boldsymbol{z} \tag{A.16}$$

where $\mathrm{Im}(\boldsymbol{I} - \boldsymbol{A}^{+}\boldsymbol{A}) = \ker(\boldsymbol{A})$, and $\boldsymbol{z} \in \mathbb{R}^k$. The additional term $(\boldsymbol{I} - \boldsymbol{A}^{+}\boldsymbol{A})\boldsymbol{z}$ lies in $\ker(\boldsymbol{A})$, and thus does not affect the satisfaction of Eq. (A.15).

If the system is underdetermined ($m < n$), there are infinitely many admissible solutions. Among them, the pseudoinverse selects the one with minimum Euclidean norm, namely

$$\boldsymbol{x}_{\mathrm{ln}} = \boldsymbol{A}^{+}\boldsymbol{b} = \arg\min_{\boldsymbol{x}} \|\boldsymbol{x}\|_2, \tag{A.17}$$

Conversely, if the system is overdetermined ($m > n$) and no exact solution exists, the pseudoinverse provides the least-squares solution

$$\boldsymbol{x}_{\mathrm{ls}} = \boldsymbol{A}^{+}\boldsymbol{b} = \arg\min_{\boldsymbol{x}} \|\boldsymbol{A}\boldsymbol{x} - \boldsymbol{b}\|_2, \tag{A.18}$$

which minimizes the residual in the Euclidean sense.

A.2 Proof of the Udwadia-Kalaba Equation (Eq. (2.7))

According to Gauss' principle of least constraint, the admissible acceleration $\ddot{\boldsymbol{q}}$ of a constrained mechanical system is the one that minimizes, at each time instant, the quadratic

functional $\mathcal{G}(\ddot{\boldsymbol{q}})$

$$\begin{aligned} \underset{\ddot{\boldsymbol{q}}}{\text{minimize}} \quad & \mathcal{G}(\ddot{\boldsymbol{q}}) = (\ddot{\boldsymbol{q}} - \ddot{\boldsymbol{q}}_u)^T \boldsymbol{M} (\ddot{\boldsymbol{q}} - \ddot{\boldsymbol{q}}_u) \\ \text{subject to} \quad & \boldsymbol{A}(\boldsymbol{q}, \dot{\boldsymbol{q}}, t)\, \ddot{\boldsymbol{q}} = \boldsymbol{b}(\boldsymbol{q}, \dot{\boldsymbol{q}}, t). \end{aligned} \tag{A.19}$$

Since $\boldsymbol{M}$ is the mass matrix of the system, it is symmetric positive definite, and therefore admits a symmetric square root such that $\boldsymbol{M}^{1/2} = \boldsymbol{M}^{\frac{1}{2}^T}$, and $\boldsymbol{M} = \boldsymbol{M}^{\frac{1}{2}^T} \boldsymbol{M}^{1/2}$. Substituting this definition of $\boldsymbol{M}$ in the expression of $\mathcal{G}(\ddot{\boldsymbol{q}})$ one get

$$\mathcal{G}(\ddot{\boldsymbol{q}}) = (\ddot{\boldsymbol{q}} - \ddot{\boldsymbol{q}}_u)^T \boldsymbol{M}^{\frac{1}{2}^T} \boldsymbol{M}^{\frac{1}{2}} (\ddot{\boldsymbol{q}} - \ddot{\boldsymbol{q}}_u) = \boldsymbol{\gamma}^T \boldsymbol{\gamma} = \|\boldsymbol{\gamma}\|_2^2. \tag{A.20}$$

where $\boldsymbol{\gamma} = \boldsymbol{M}^{\frac{1}{2}} (\ddot{\boldsymbol{q}} - \ddot{\boldsymbol{q}}_u)$, and the identity $(\boldsymbol{D}\boldsymbol{v})^T = \boldsymbol{v}^T A^T$, for a generic matrix $\boldsymbol{D}$ and vector $\boldsymbol{v}$, has been used. From the definition of $\boldsymbol{\gamma}$ it follows that

$$\ddot{\boldsymbol{q}} = \boldsymbol{M}^{-\frac{1}{2}} \boldsymbol{\gamma} + \ddot{\boldsymbol{q}}_u \tag{A.21}$$

substituting Eq. (A.21) into Eq. (A.19) one gets

$$\hat{\boldsymbol{A}}\, \boldsymbol{\gamma} = \hat{\boldsymbol{b}}, \tag{A.22}$$

where $\hat{\boldsymbol{A}} := \boldsymbol{A}\boldsymbol{M}^{-1/2}$, and $\hat{\boldsymbol{b}} := \boldsymbol{b} - \boldsymbol{A}\ddot{\boldsymbol{q}}_u$. As discussed in Sec. A.1.2, the solution of Eq. (A.22) that minimizes $\|\boldsymbol{\gamma}\|_2^2$, and thereby satisfies Gauss' principle in Eq. (A.19), is obtained through the Moore–Penrose pseudoinverse as

$$\boldsymbol{\gamma} = \hat{\boldsymbol{A}}^+ \hat{\boldsymbol{b}} \tag{A.23}$$

Substituting the definitions of $\boldsymbol{\gamma}$, $\hat{\boldsymbol{A}}$ and $\hat{\boldsymbol{b}}$ into (A.22) yields

$$\boldsymbol{M}^{1/2} \ddot{\boldsymbol{q}} - \boldsymbol{M}^{1/2} \ddot{\boldsymbol{q}}_u = (\boldsymbol{A}\boldsymbol{M}^{-1/2})^+ (\boldsymbol{b} - \boldsymbol{A}\ddot{\boldsymbol{q}}_u). \tag{A.24}$$

Finally, solving for $\ddot{\boldsymbol{q}}$ gives

$$\ddot{\boldsymbol{q}} = \ddot{\boldsymbol{q}}_u + \boldsymbol{M}^{-1/2} (\boldsymbol{A}\boldsymbol{M}^{-1/2})^+ (\boldsymbol{b} - \boldsymbol{A}\ddot{\boldsymbol{q}}_u), \tag{A.25}$$

and the associated generalized constraint force is

$$Q_c = M(\ddot{\boldsymbol{q}} - \ddot{\boldsymbol{q}}_u) = M^{1/2}(\boldsymbol{A}M^{-1/2})^{+}(\boldsymbol{b} - \boldsymbol{A}\ddot{\boldsymbol{q}}_u), \tag{A.26}$$

which corresponds to Eq. (2.7).

A.3 Mass and Constraint Matrices in the Multi-Element Cable Model

The mass matrix in Eq. (2.10) is expressed as

$$\boldsymbol{M}_m = \begin{bmatrix} \boldsymbol{M}_{m_1} & \cdots & \boldsymbol{0}_{\mu\times\mu} & \cdots & \boldsymbol{0}_{\mu\times\mu} & \boldsymbol{0}_{\mu\times 3} & \boldsymbol{0}_{\mu\times 3} \\ \vdots & \ddots & \vdots & \vdots & \vdots & \vdots & \vdots \\ \boldsymbol{0}_{\mu\times\mu} & \cdots & \boldsymbol{M}_{m_i} & \cdots & \boldsymbol{0}_{\mu\times\mu} & \boldsymbol{0}_{\mu\times 3} & \boldsymbol{0}_{\mu\times 3} \\ \vdots & \vdots & \vdots & \ddots & \vdots & \vdots & \vdots \\ \boldsymbol{0}_{\mu\times\mu} & \cdots & \boldsymbol{0}_{\mu\times\mu} & \cdots & \boldsymbol{M}_{m_N} & \boldsymbol{0}_{\mu\times 3} & \boldsymbol{0}_{\mu\times 3} \\ \boldsymbol{0}_{3\times\mu} & \cdots & \boldsymbol{0}_{3\times\mu} & \cdots & \boldsymbol{0}_{3\times\mu} & m_l\boldsymbol{\mathcal{I}} & \boldsymbol{0}_{3\times 3} \\ \boldsymbol{0}_{3\times\mu} & \cdots & \boldsymbol{0}_{3\times\mu} & \cdots & \boldsymbol{0}_{3\times\mu} & \boldsymbol{0}_{3\times 3} & {}^{b_l}\boldsymbol{I}_l \end{bmatrix} \tag{A.27}$$

with $\mu = 6 + 3P$, and where

$$\boldsymbol{M}_{m_i} = \begin{bmatrix} m_i\boldsymbol{\mathcal{I}} & \boldsymbol{0}_{3\times 3} & \boldsymbol{0}_{3\times 3} & \cdots & \boldsymbol{0}_{3\times 3} & \cdots & \boldsymbol{0}_{3\times 3} \\ \boldsymbol{0}_{3\times 3} & {}^{b_i}\boldsymbol{I}_i & \boldsymbol{0}_{3\times 3} & \cdots & \boldsymbol{0}_{3\times 3} & \cdots & \boldsymbol{0}_{3\times 3} \\ \boldsymbol{0}_{3\times 3} & \boldsymbol{0}_{3\times 3} & m_{p_{i1}}\boldsymbol{\mathcal{I}} & \cdots & \boldsymbol{0}_{3\times 3} & \cdots & \boldsymbol{0}_{3\times 3} \\ \vdots & \vdots & \vdots & \ddots & \vdots & \vdots & \vdots \\ \boldsymbol{0}_{3\times 3} & \boldsymbol{0}_{3\times 3} & \boldsymbol{0}_{3\times 3} & \cdots & m_{p_{ij}}\boldsymbol{\mathcal{I}} & \cdots & \boldsymbol{0}_{3\times 3} \\ \vdots & \vdots & \vdots & \vdots & \vdots & \ddots & \vdots \\ \boldsymbol{0}_{3\times 3} & \boldsymbol{0}_{3\times 3} & \boldsymbol{0}_{3\times 3} & \cdots & \boldsymbol{0}_{3\times 3} & \cdots & m_{p_{iP}}\boldsymbol{\mathcal{I}} \end{bmatrix} \tag{A.28}$$

A.4 Expression of matrix C in Eq. (2.55)

The translational and rotational kinematics are written in the concise form of Eq. (2.55) using the matrix $\boldsymbol{C}$, defined as

$$\boldsymbol{C} = \begin{bmatrix} \boldsymbol{C}_1 & \cdots & \mathbf{0}_{\mu\times\mu} & \cdots & \mathbf{0}_{\mu\times\mu} & \mathbf{0}_{\mu\times 3} & \mathbf{0}_{\mu\times 3} \\ \vdots & \ddots & \vdots & \vdots & \vdots & \vdots & \vdots \\ \mathbf{0}_{\mu\times\mu} & \cdots & \boldsymbol{C}_i & \cdots & \mathbf{0}_{\mu\times\mu} & \mathbf{0}_{\mu\times 3} & \mathbf{0}_{\mu\times 3} \\ \vdots & \vdots & \vdots & \ddots & \vdots & \vdots & \vdots \\ \mathbf{0}_{\mu\times\mu} & \cdots & \mathbf{0}_{\mu\times\mu} & \cdots & \boldsymbol{C}_N & \mathbf{0}_{\mu\times 3} & \mathbf{0}_{\mu\times 3} \\ \mathbf{0}_{3\times\mu} & \cdots & \mathbf{0}_{3\times\mu} & \cdots & \mathbf{0}_{3\times\mu} & \boldsymbol{\mathcal{I}} & \mathbf{0}_{3\times 3} \\ \mathbf{0}_{3\times\mu} & \cdots & \mathbf{0}_{3\times\mu} & \cdots & \mathbf{0}_{3\times\mu} & \mathbf{0}_{3\times 3} & \boldsymbol{T}_l \end{bmatrix} \tag{A.29}$$

where

$$\boldsymbol{C}_i = \begin{bmatrix} \boldsymbol{\mathcal{I}} & \mathbf{0}_{3\times 3} & \mathbf{0}_{3\times 3} & \cdots & \mathbf{0}_{3\times 3} & \cdots & \mathbf{0}_{3\times 3} \\ \mathbf{0}_{3\times 3} & \boldsymbol{T}_i & \mathbf{0}_{3\times 3} & \cdots & \mathbf{0}_{3\times 3} & \cdots & \mathbf{0}_{3\times 3} \\ \mathbf{0}_{3\times 3} & \mathbf{0}_{3\times 3} & \boldsymbol{\mathcal{I}} & \cdots & \mathbf{0}_{3\times 3} & \cdots & \mathbf{0}_{3\times 3} \\ \vdots & \vdots & \vdots & \ddots & \vdots & \vdots & \vdots \\ \mathbf{0}_{3\times 3} & \mathbf{0}_{3\times 3} & \mathbf{0}_{3\times 3} & \cdots & \boldsymbol{\mathcal{I}} & \cdots & \mathbf{0}_{3\times 3} \\ \vdots & \vdots & \vdots & \vdots & \vdots & \ddots & \vdots \\ \mathbf{0}_{3\times 3} & \mathbf{0}_{3\times 3} & \mathbf{0}_{3\times 3} & \cdots & \mathbf{0}_{3\times 3} & \cdots & \boldsymbol{\mathcal{I}} \end{bmatrix} \tag{A.30}$$

for $i = 1, \ldots, N$.

Appendix B

B.1 Hat Operator

The hat map $\widehat{\cdot}: \mathbb{R}^3 \to \mathfrak{so}(3)$ is defined as

$$\hat{x} = \begin{bmatrix} 0 & -x_3 & x_2 \\ x_3 & 0 & -x_1 \\ -x_2 & x_1 & 0 \end{bmatrix} \tag{B.1}$$

for $x = [x_1, x_2, x_3]^T \in \mathbb{R}^3$. This identifies the Lie algebra $\mathfrak{so}(3)$ with $\mathbb{R}^3$ using the vector cross product in $\mathbb{R}^3$. Consider $x, y \in \mathbb{R}^3$, $A \in \mathbb{R}^{3\times 3}$, then the following identities hold [84]

$$\hat{x}y = x \times y = -y \times x = -\hat{y}x \tag{B.2}$$

$$\hat{x}^T\hat{x} = (x^T x)I - xx^T \tag{B.3}$$

$$\hat{x}\hat{y}\hat{x} = -(y^T x)\hat{x} \tag{B.4}$$

$$-\tfrac{1}{2}\mathrm{tr}[\hat{x}\hat{y}] = x^T y \tag{B.5}$$

$$x \times y = \hat{x}y = \hat{y}^T x = yx^T - xy^T \tag{B.6}$$

$$\mathrm{tr}[\hat{x}A] = \tfrac{1}{2}\mathrm{tr}\big[\hat{x}(A - A^T)\big] \tag{B.7}$$

$$\widehat{Ax} = \hat{x}\big(\tfrac{1}{2}\mathrm{tr}[A]I - A\big) + \big(\tfrac{1}{2}\mathrm{tr}[A]I - A\big)^T\hat{x} \tag{B.8}$$

$$\hat{x}A + A^T\hat{x} = \big(\{\mathrm{tr}[A]I_{3\times 3} - A\}x\big)^{\wedge} \tag{B.9}$$

B.2 Lagrangian

The Lagrangian is defined as $\mathcal{L} = \mathcal{K} - \mathcal{U}$. The kinetic energy is obtained by summing the contributions of the payload, the quadrotors, and the cable links, and consists of both translational and rotational terms. The potential energy accounts for the gravitational effects

on all components of the system. Explicitly, one has

$$\mathcal{K} = \frac{1}{2}\left(m_l \| {}^e\dot{\boldsymbol{p}}_l \|^2 + \sum_{i=1}^{N}\sum_{j=1}^{P-1} m_{ij} \| {}^e\dot{\boldsymbol{p}}_{p_{ij}} \|^2 + \sum_{i=1}^{N} m_i \| {}^e\dot{\boldsymbol{p}}_i \|^2 + \sum_{i=1}^{N} {}^{b_i}\boldsymbol{\omega}_i \cdot \mathbf{J}_i \, {}^{b_i}\boldsymbol{\omega}_i + {}^{b_l}\boldsymbol{\omega}_l \cdot \mathbf{J}_l \, {}^{b_l}\boldsymbol{\omega}_l \right) \tag{B.10}$$

$$\mathcal{U} = -m_l g \mathbf{e}_3 \cdot {}^e\boldsymbol{p}_l - \sum_{i=1}^{N} m_i g \mathbf{e}_3 \cdot {}^e\boldsymbol{p}_i - \sum_{i=1}^{N}\sum_{j=1}^{P-1} m_{ij} g \mathbf{e}_3 \cdot {}^e\boldsymbol{p}_{p_{ij}} \tag{B.11}$$

By substituting Eq. (3.27) into Eqs. (B.10), (B.11), and recalling that the position of the j-th link of the i-th cable is given by

$${}^e\boldsymbol{p}_{ij} = {}^e\boldsymbol{p}_l + \mathcal{R}_{eb_l} \, {}^{b_l}\boldsymbol{r}_{l_i} - \sum_{a=1}^{j} l_{ia} \boldsymbol{n}_{ia} \tag{B.12}$$

The expressions for the kinetic and potential energies can thus be written as

$$\begin{aligned}
\mathcal{K} = \frac{1}{2}(& m_l \| {}^e\dot{\boldsymbol{p}}_l \|^2 + \sum_{i=1}^{N}\sum_{j=1}^{P-1} m_{ij} \| {}^e\dot{\boldsymbol{p}}_l + \dot{\mathcal{R}}_{eb_l} \, {}^{b_l}\boldsymbol{r}_{l_i} - \sum_{a=1}^{j} l_{ia} \dot{\boldsymbol{n}}_{ia} \|^2 + \\
& + \sum_{i=1}^{N} m_i \| {}^e\dot{\boldsymbol{p}}_l + \dot{\mathcal{R}}_{eb_l} \, {}^{b_l}\boldsymbol{r}_{l_i} - \sum_{j=1}^{P} l_{ij} \dot{\boldsymbol{n}}_{ij} - \dot{\mathcal{R}}_{eb_i} \, {}^{b_i}\boldsymbol{r}_i \|^2 + \\
& + \sum_{i=1}^{N} {}^{b_i}\boldsymbol{\omega}_i \cdot \mathbf{J}_i \, {}^{b_i}\boldsymbol{\omega}_i + {}^{b_l}\boldsymbol{\omega}_l \cdot \mathbf{J}_l \, {}^{b_l}\boldsymbol{\omega}_l)
\end{aligned} \tag{B.13}$$

$$\begin{aligned}
\mathcal{U} = & -m_l g \mathbf{e}_3 \cdot {}^e\boldsymbol{p}_l - \sum_{i=1}^{N} m_i g \mathbf{e}_3 \cdot ({}^e\boldsymbol{p}_l + \mathcal{R}_{eb_l} \, {}^{b_l}\boldsymbol{r}_{l_i} - \sum_{j=1}^{P} l_{ij} \boldsymbol{n}_{ij} - \mathcal{R}_{eb_i} \, {}^{b_i}\boldsymbol{r}_i) \\
& - \sum_{i=1}^{N}\sum_{j=1}^{P-1} m_{ij} g \mathbf{e}_3 \cdot ({}^e\boldsymbol{p}_l + \mathcal{R}_{eb_l} \, {}^{b_l}\boldsymbol{r}_{l_i} - \sum_{a=1}^{j} l_{ia} \boldsymbol{n}_{ia})
\end{aligned} \tag{B.14}$$

Finally, substituting into the expression of the kinetic energy the kinematic relations defined in Eqs. (2.88), (2.106), using the identity $\|\boldsymbol{x}+\boldsymbol{y}-\boldsymbol{z}\|^2 = \|\boldsymbol{x}\|^2+\|\boldsymbol{y}\|^2+\|\boldsymbol{z}\|^2+2\boldsymbol{x}\cdot\boldsymbol{y}-2\boldsymbol{x}\cdot\boldsymbol{z}-2\boldsymbol{y}\cdot\boldsymbol{z}$,

and collecting terms, it follows

$$\begin{aligned}
\mathcal{K} = &\frac{1}{2}(m_l + \sum_{i=1}^{N}\sum_{j=1}^{P-1} m_{ij} + \sum_{i=1}^{N} m_i)\| {}^{e}\dot{\boldsymbol{p}}_l\|^2 + \frac{1}{2}\sum_{i=1}^{N}(\sum_{j=1}^{P-1} m_{ij} + m_i)\|(-\mathcal{R}_{eb_l}\,{}^{b_l}\hat{\boldsymbol{r}}_{l_i}\,{}^{b_l}\boldsymbol{\omega}_l)\|^2 + \\
&+ \frac{1}{2}\sum_{i=1}^{N}(\sum_{j=1}^{P-1} m_{ij}\|\sum_{a=1}^{j} l_{ia}\dot{\boldsymbol{n}}_{ia}\|^2 + m_i\|\sum_{a=1}^{P} l_{ia}\dot{\boldsymbol{n}}_{ia}\|^2) + \frac{1}{2}\sum_{i=1}^{N} m_i\|(-\mathcal{R}_{eb_i}\,{}^{b_i}\hat{\boldsymbol{r}}_i\,{}^{b_i}\boldsymbol{\omega}_i)\|^2 + \\
&+ \sum_{i=1}^{N}(\sum_{j=1}^{P-1} m_{ij} + m_i)\,{}^{e}\dot{\boldsymbol{p}}_l \cdot (-\mathcal{R}_{eb_l}\,{}^{b_l}\hat{\boldsymbol{r}}_{l_i}\,{}^{b_l}\boldsymbol{\omega}_l) - \sum_{i=1}^{N}(\sum_{j=1}^{P-1} m_{ij}\,{}^{e}\dot{\boldsymbol{p}}_l \cdot \sum_{a=1}^{j} l_{ia}\dot{\boldsymbol{n}}_{ia} + m_i\,{}^{e}\dot{\boldsymbol{p}}_l \cdot \sum_{j=1}^{P} l_{ij}\dot{\boldsymbol{n}}_{ij}) + \\
&- \sum_{i=1}^{N}(\sum_{j=1}^{P-1} m_{ij}(-\mathcal{R}_{eb_l}\,{}^{b_l}\hat{\boldsymbol{r}}_{l_i}\,{}^{b_l}\boldsymbol{\omega}_l) \cdot \sum_{a=1}^{j} l_{ia}\dot{\boldsymbol{n}}_{ia} - m_i(\mathcal{R}_{eb_l}\,{}^{b_l}\hat{\boldsymbol{r}}_{l_i}\,{}^{b_l}\boldsymbol{\omega}_l) \cdot \sum_{a=1}^{P} l_{ia}\dot{\boldsymbol{n}}_{ia}) + \\
&- \sum_{i=1}^{N} m_i({}^{e}\dot{\boldsymbol{p}}_l \cdot (-\mathcal{R}_{eb_i}\,{}^{b_i}\hat{\boldsymbol{r}}_i\,{}^{b_i}\boldsymbol{\omega}_i) + (\mathcal{R}_{eb_l}\,{}^{b_l}\hat{\boldsymbol{r}}_{l_i}\,{}^{b_l}\boldsymbol{\omega}_l) \cdot (\mathcal{R}_{eb_i}\,{}^{b_i}\hat{\boldsymbol{r}}_i\,{}^{b_i}\boldsymbol{\omega}_i) \\
&+ + \sum_{j=1}^{P} l_{ij}\dot{\boldsymbol{n}}_{ij} \cdot (\mathcal{R}_{eb_i}\,{}^{b_i}\hat{\boldsymbol{r}}_i\,{}^{b_i}\boldsymbol{\omega}_i)) + \frac{1}{2}\sum_{i=1}^{N} {}^{b_i}\boldsymbol{\omega}_i \cdot \mathbf{J}_i\,{}^{b_i}\boldsymbol{\omega}_i + \frac{1}{2}\,{}^{b_l}\boldsymbol{\omega}_l \cdot \mathbf{J}_l\,{}^{b_l}\boldsymbol{\omega}_l
\end{aligned} \tag{B.15}$$

By defining $m_t = (m_l + \sum_{i=1}^{N}\sum_{j=1}^{P-1} m_{ij} + \sum_{i=1}^{N} m_i)$, $m_{iT} = \sum_{j=1}^{P-1} m_{ij} + m_i$, and $m_{0ij} = \sum_{a=j}^{P-1} m_{ij} + m_i$, Eq. (B.15) is simplified as

$$\begin{aligned}
\mathcal{K} = &\frac{1}{2}m_t\| {}^{e}\dot{\boldsymbol{p}}_l\|^2 + \frac{1}{2}\sum_{i=1}^{N} m_{iT}\| - \mathcal{R}_{eb_l}\,{}^{b_l}\hat{\boldsymbol{r}}_{l_i}\,{}^{b_l}\boldsymbol{\omega}_l\|^2 + \frac{1}{2}\sum_{i=1}^{N}\sum_{j,k=1}^{P} m_{0ij} l_{ij} l_{ik}\dot{\boldsymbol{n}}_{ij} \cdot \dot{\boldsymbol{n}}_{ik} \\
&+ \frac{1}{2}\sum_{i=1}^{N} m_i\| - \mathcal{R}_{eb_i}\,{}^{b_i}\hat{\boldsymbol{r}}_i\,{}^{b_i}\boldsymbol{\omega}_i\|^2 + \sum_{i=1}^{N} m_{iT}\,{}^{e}\dot{\boldsymbol{p}}_l \cdot (-\mathcal{R}_{eb_l}\,{}^{b_l}\hat{\boldsymbol{r}}_{l_i}\,{}^{b_l}\boldsymbol{\omega}_l) \\
&- \sum_{i=1}^{N}{}^{e}\dot{\boldsymbol{p}}_l \cdot \sum_{j=1}^{P} m_{0ij} l_{ij}\dot{\boldsymbol{n}}_{ij} - \sum_{i=1}^{N}(-\mathcal{R}_{eb_l}\,{}^{b_l}\hat{\boldsymbol{r}}_{l_i}\,{}^{b_l}\boldsymbol{\omega}_l) \cdot \sum_{j=1}^{P} m_{0ij} l_{ij}\dot{\boldsymbol{n}}_{ij} \\
&- \sum_{i=1}^{N} m_i\,{}^{e}\dot{\boldsymbol{p}}_l \cdot (-\mathcal{R}_{eb_i}\,{}^{b_i}\hat{\boldsymbol{r}}_i\,{}^{b_i}\boldsymbol{\omega}_i) - \sum_{i=1}^{N} m_i(\mathcal{R}_{eb_l}\,{}^{b_l}\hat{\boldsymbol{r}}_{l_i}\,{}^{b_l}\boldsymbol{\omega}_l) \cdot (\mathcal{R}_{eb_i}\,{}^{b_i}\hat{\boldsymbol{r}}_i\,{}^{b_i}\boldsymbol{\omega}_i) \\
&- \sum_{i=1}^{N}(-\mathcal{R}_{eb_i}\,{}^{b_i}\hat{\boldsymbol{r}}_i\,{}^{b_i}\boldsymbol{\omega}_i) \cdot \sum_{j=1}^{P} l_{ij}\dot{\boldsymbol{n}}_{ij} + \frac{1}{2}\sum_{i=1}^{N} {}^{b_i}\boldsymbol{\omega}_i \cdot \mathbf{J}_i\,{}^{b_i}\boldsymbol{\omega}_i + \frac{1}{2}\,{}^{b_l}\boldsymbol{\omega}_l \cdot \mathbf{J}_l\,{}^{b_l}\boldsymbol{\omega}_l
\end{aligned} \tag{B.16}$$

B.3 Derivatives of the Lagrangian

In this section, the derivatives of the Lagrangian required for the derivation of the equations of motion are computed.

- **Derivative with respect to the payload attitude $\mathcal{R}_{eb_l}$**

$$\frac{\partial \mathcal{L}}{\partial \mathcal{R}_{eb_l}} = -\sum_{i=1}^{N} m_{iT}\, {}^{e}\dot{\boldsymbol{p}}_l ({}^{b_l}\hat{\boldsymbol{r}}_{l_i}\, {}^{b_l}\boldsymbol{\omega}_l)^T + \sum_{i=1}^{N}\sum_{j=1}^{P} m_{0ij} l_{ij} \dot{\boldsymbol{n}}_{ij} ({}^{b_l}\hat{\boldsymbol{r}}_{l_i}\, {}^{b_l}\boldsymbol{\omega}_l)^T$$
$$- \sum_{i=1}^{N} m_i (\mathcal{R}_{eb_i}\, {}^{b_i}\hat{\boldsymbol{r}}_i\, {}^{b_i}\boldsymbol{\omega}_i)({}^{b_l}\hat{\boldsymbol{r}}_{l_i}\, {}^{b_l}\boldsymbol{\omega}_l)^T + \sum_{i=1}^{N} m_{iT} g \boldsymbol{e}_3\, {}^{b}_{l}\boldsymbol{r}_{l_i}^T \tag{B.17}$$

$$\frac{\partial \mathcal{L}}{\partial \mathcal{R}_{eb_l}} \cdot \mathcal{R}_{eb_l}\hat{\boldsymbol{\eta}}_l = \Big[-\sum_{i=1}^{N} m_{iT} \widehat{{}^{b_l}\hat{\boldsymbol{r}}_{l_i}\, {}^{b_l}\boldsymbol{\omega}_l} \mathcal{R}_{eb_l}^T\, {}^{e}\dot{\boldsymbol{p}}_l + \sum_{i=1}^{N}\sum_{j=1}^{P} m_{0ij} \widehat{{}^{b_l}\hat{\boldsymbol{r}}_{l_i}\, {}^{b_l}\boldsymbol{\omega}_l} \mathcal{R}_{eb_l}^T l_{ij} \dot{\boldsymbol{n}}_{ij}$$
$$- \sum_{i=1}^{N} m_i \widehat{{}^{b_l}\hat{\boldsymbol{r}}_{l_i}\, {}^{b_l}\boldsymbol{\omega}_l} \mathcal{R}_{eb_l}^T \mathcal{R}_{eb_i}\, {}^{b_i}\hat{\boldsymbol{r}}_i\, {}^{b_i}\boldsymbol{\omega}_i + \sum_{i=1}^{N} m_{iT} g\, {}^{b_l}\hat{\boldsymbol{r}}_{l_i}\, \mathcal{R}_{eb_l}^T \boldsymbol{e}_3 \Big] \cdot \boldsymbol{\eta}_l$$
$$:= \nabla_L \mathcal{L}(\mathcal{R}_{eb_l}) \cdot \boldsymbol{\eta}_l \tag{B.18}$$

- **Derivative with respect to the payload angular velocity ${}^{b_l}\boldsymbol{\omega}_l$**

$$\frac{\partial \mathcal{L}}{\partial\, {}^{b_l}\boldsymbol{\omega}_l} = \sum_{i=1}^{N} m_{iT}\, {}^{b_l}\hat{\boldsymbol{r}}_{l_i} \mathcal{R}_{eb_l}^T\, {}^{e}\dot{\boldsymbol{p}}_l - \sum_{i=1}^{N}\sum_{j=1}^{P} m_{0ij}\, {}^{b_l}\hat{\boldsymbol{r}}_{l_i} \mathcal{R}_{eb_l}^T l_{ij} \dot{\boldsymbol{n}}_{ij}$$
$$+ \sum_{i=1}^{N} m_i\, {}^{b_l}\hat{\boldsymbol{r}}_{l_i} \mathcal{R}_{eb_l}^T \mathcal{R}_{eb_i}\, {}^{b_i}\hat{\boldsymbol{r}}_i\, {}^{b_i}\boldsymbol{\omega}_i + (\mathbf{J}_l - \sum_{i=1}^{N} m_{iT}\, {}^{b_l}\hat{\boldsymbol{r}}_{l_i}^2)\, {}^{b_l}\boldsymbol{\omega}_l \tag{B.19}$$

$$\frac{d}{dt}\Big(\frac{\partial \mathcal{L}}{\partial\, {}^{b_l}\boldsymbol{\omega}_l}\Big) = \sum_{i=1}^{N} m_{iT}\, {}^{b_l}\hat{\boldsymbol{r}}_{l_i} \mathcal{R}_{eb_l}^T\, {}^{e}\ddot{\boldsymbol{p}}_l - \sum_{i=1}^{N} m_{iT}\, {}^{b_l}\hat{\boldsymbol{r}}_{l_i}\, {}^{b_l}\hat{\boldsymbol{\omega}}_l \mathcal{R}_{eb_l}^T\, {}^{e}\dot{\boldsymbol{p}}_l + \bar{\boldsymbol{J}}_l\, {}^{b_l}\dot{\boldsymbol{\omega}}_l$$
$$- \sum_{i=1}^{N}\sum_{j=1}^{P} m_{0ij}\, {}^{b_l}\hat{\boldsymbol{r}}_{l_i} \mathcal{R}_{eb_l}^T l_{ij} \ddot{\boldsymbol{n}}_{ij} + \sum_{i=1}^{N}\sum_{j=1}^{P} m_{0ij}\, {}^{b_l}\hat{\boldsymbol{r}}_{l_i}\, {}^{b_l}\hat{\boldsymbol{\omega}}_l \mathcal{R}_{eb_l}^T l_{ij} \dot{\boldsymbol{n}}_{ij}$$
$$+ \sum_{i=1}^{N} m_i\, {}^{b_l}\hat{\boldsymbol{r}}_{l_i} \mathcal{R}_{eb_l}^T \mathcal{R}_{eb_i}\, {}^{b}_{i}\hat{\boldsymbol{r}}_i\, {}^{b}_{i}\dot{\boldsymbol{\omega}}_i - \sum_{i=1}^{N} m_i\, {}^{b_l}\hat{\boldsymbol{r}}_{l_i}\, {}^{b_l}\boldsymbol{\omega}_l \mathcal{R}_{eb_l}^T \mathcal{R}_{eb_i}\, {}^{b}_{i}\hat{\boldsymbol{r}}_i\, {}^{b}_{i}\boldsymbol{\omega}_i$$
$$+ \sum_{i=1}^{N} m_i\, {}^{b_l}\hat{\boldsymbol{r}}_{l_i} \mathcal{R}_{eb_l}^T \mathcal{R}_{eb_i}\, {}^{b}_{i}\hat{\boldsymbol{\omega}}_i\, {}^{b}_{i}\hat{\boldsymbol{r}}_i\, {}^{b}_{i}\boldsymbol{\omega}_i \tag{B.20}$$

- **Derivative with respect to the cable-link attitude $\boldsymbol{n}_{ij}$**

$$\frac{\partial \mathcal{L}}{\partial \boldsymbol{n}_{ij}} = -m_{0ij} l_{ij} g \boldsymbol{e}_3 \tag{B.21}$$

- **Derivative with respect to the cable-link angular velocity $\dot{\boldsymbol{n}}_{ij}$**

$$\begin{aligned}\frac{\partial \mathcal{L}}{\partial \dot{\boldsymbol{n}}_{ij}} = &\sum_{j=1}^{P} m_{0ij} l_{ij} l_{ik} \dot{\boldsymbol{n}}_{ik} - \sum_{i=1}^{N} m_{0ij} l_{ij}\, {}^{b_l}\dot{\boldsymbol{p}}_l + \sum_{i=1}^{N} m_{0ij} l_{ij} \mathcal{R}_{eb_l}\, {}^{b_l}\hat{\boldsymbol{r}}_{l_i}\, {}^{b_l}\boldsymbol{\omega}_l \\ &- \sum_{i=1}^{N} m_i l_{ij} \mathcal{R}_{eb_i}\, {}^{b_i}\hat{\boldsymbol{r}}_i\, {}^{b_i}\boldsymbol{\omega}_i \end{aligned} \tag{B.22}$$

$$\begin{aligned}\frac{d}{dt}\Big(\frac{\partial \mathcal{L}}{\partial \dot{\boldsymbol{n}}_{ij}}\Big) = &\sum_{j=1}^{P} m_{0ij} l_{ij} l_{ik} \ddot{\boldsymbol{n}}_{ik} - m_{0ij} l_{ij}\, {}^{e}\ddot{\boldsymbol{p}}_l + m_{0ij} l_{ij} \mathcal{R}_{eb_l}\, {}^{b_l}\hat{\boldsymbol{r}}_{l_i}\, {}^{b_l}\dot{\boldsymbol{\omega}}_l \\ &+ m_{0ij} l_{ij} \mathcal{R}_{eb_l}\, {}^{b_l}\hat{\boldsymbol{\omega}}_l\, {}^{b_l}\hat{\boldsymbol{r}}_{l_i}\, {}^{b_l}\boldsymbol{\omega}_l - m_i l_{ij} \mathcal{R}_{eb_i}\, {}^{b_i}\hat{\boldsymbol{r}}_i\, {}^{b_i}\dot{\boldsymbol{\omega}}_i \\ &- m_i l_{ij} \mathcal{R}_{eb_i}\, {}^{b_i}\hat{\boldsymbol{\omega}}_i\, {}^{b_i}\hat{\boldsymbol{r}}_i\, {}^{b_i}\boldsymbol{\omega}_i \end{aligned} \tag{B.23}$$

- **Derivative with respect to the payload position ${}^{e}\boldsymbol{p}_l$**

$$\frac{\partial \mathcal{L}}{\partial\, {}^{e}\boldsymbol{p}_l} = m_t g \boldsymbol{e}_3 \tag{B.24}$$

- **Derivative with respect to the payload velocity ${}^{e}\dot{\boldsymbol{p}}_l$**

$$\begin{aligned}\frac{\partial \mathcal{L}}{\partial\, {}^{e}\dot{\boldsymbol{p}}_l} = &\, m_t\, {}^{e}\dot{\boldsymbol{p}}_l - \sum_{i=1}^{N} m_{iT} \mathcal{R}_{eb_l}\, {}^{b_l}\hat{\boldsymbol{r}}_{l_i}\, {}^{b_l}\boldsymbol{\omega}_l - \sum_{i=1}^{N}\sum_{j=1}^{P-1} m_{0ij} l_{ij} \dot{\boldsymbol{n}}_{ij} \\ &+ \sum_{i=1}^{N} m_i \mathcal{R}_{eb_i}\, {}^{b_i}\hat{\boldsymbol{r}}_i\, {}^{b_i}\boldsymbol{\omega}_i \end{aligned} \tag{B.25}$$

$$\begin{aligned}\frac{d}{dt}\Big(\frac{\partial \mathcal{L}}{\partial\, {}^{e}\dot{\boldsymbol{p}}_l}\Big) = &\, m_t\, {}^{e}\ddot{\boldsymbol{p}}_l - \sum_{i=1}^{N} m_{iT} \mathcal{R}_{eb_l}\Big({}^{b_l}\hat{\boldsymbol{r}}_{l_i}\, {}^{b_l}\dot{\boldsymbol{\omega}}_l + \hat{\boldsymbol{\omega}}_l\, {}^{b_l}\hat{\boldsymbol{r}}_{l_i}\, {}^{b_l}\boldsymbol{\omega}_l \Big) \\ &- \sum_{i=1}^{N}\sum_{j=1}^{P} m_{0ij} l_{ij} \ddot{\boldsymbol{n}}_{ij} + \sum_{i=1}^{N} m_i \mathcal{R}_{eb_i}\Big({}^{b_i}\hat{\boldsymbol{r}}_i\, {}^{b_i}\dot{\boldsymbol{\omega}}_i + \hat{\boldsymbol{\omega}}_i\, {}^{b_i}\hat{\boldsymbol{r}}_i\, {}^{b_i}\boldsymbol{\omega}_i \Big) \end{aligned} \tag{B.26}$$

- **Derivative with respect to the quadrotor attitude $\mathcal{R}_{eb_i}$**

$$\frac{\partial \mathcal{L}}{\partial \mathcal{R}_{eb_i}} = m_i \, {}^{e}\dot{\boldsymbol{p}}_l \, ({}^{b_i}\hat{\boldsymbol{r}}_i \, {}^{b_i}\boldsymbol{\omega}_i)^T - m_i \sum_{j=1}^{P} l_{ij} \dot{\boldsymbol{n}}_{ij} ({}^{b_i}\hat{\boldsymbol{r}}_i \, {}^{b_i}\boldsymbol{\omega}_i)^T$$
$$- m_i \mathcal{R}_{eb_l} \, {}^{b_l}\hat{\boldsymbol{r}}_{l_i} \, {}^{b_l}\boldsymbol{\omega}_l ({}^{b_i}\hat{\boldsymbol{r}}_i \, {}^{b_i}\boldsymbol{\omega}_i)^T - m_i g \boldsymbol{e}_3 \, {}^{b_i}\boldsymbol{r}_i^T \tag{B.27}$$

$$\frac{\partial \mathcal{L}}{\partial \mathcal{R}_{eb_i}} \cdot \mathcal{R}_{eb_i} \hat{\boldsymbol{\eta}}_i = \Big[m_i \widehat{{}^{b_i}\hat{\boldsymbol{r}}_i \, {}^{b_i}\boldsymbol{\omega}_i} \, \mathcal{R}_{eb_i}^T \, {}^{e}\dot{\boldsymbol{p}}_l - m_i \widehat{{}^{b_i}\hat{\boldsymbol{r}}_i \, {}^{b_i}\boldsymbol{\omega}_i} \, \mathcal{R}_{eb_i}^T \sum_{j=1}^{P} l_{ij} \dot{\boldsymbol{n}}_{ij}$$
$$- m_i \widehat{{}^{b_i}\hat{\boldsymbol{r}}_i \, {}^{b_i}\boldsymbol{\omega}_i} \, \mathcal{R}_{eb_i}^T \mathcal{R}_{eb_l} \, {}^{b_l}\hat{\boldsymbol{r}}_{l_i} \, {}^{b_l}\boldsymbol{\omega}_l - m_i g \, {}^{b_i}\hat{\boldsymbol{r}}_i \mathcal{R}_{eb_i}^T \boldsymbol{e}_3 \Big] \cdot \boldsymbol{\eta}_i$$
$$:= \nabla_L \mathcal{L}(\mathcal{R}_{eb_i}) \cdot \boldsymbol{\eta}_i \tag{B.28}$$

- **Derivative with respect to the quadrotor angular velocities** ${}^{b_i}\boldsymbol{\omega}_i$

$$\frac{\partial \mathcal{L}}{\partial \, {}^{b_i}\boldsymbol{\omega}_i} = -m_i \, {}^{b_i}\hat{\boldsymbol{r}}_i \mathcal{R}_{eb_i}^T \, {}^{e}\dot{\boldsymbol{p}}_l + m_i \, {}^{b_i}\hat{\boldsymbol{r}}_i \mathcal{R}_{eb_i}^T \mathcal{R}_{eb_l} \, {}^{b_l}\hat{\boldsymbol{r}}_{l_i} \, {}^{b_l}\boldsymbol{\omega}_l$$
$$+ m_i \, {}^{b_i}\hat{\boldsymbol{r}}_i \mathcal{R}_{eb_i}^T \sum_{j=1}^{P} l_{ij} \dot{\boldsymbol{n}}_{ij} + (\boldsymbol{J}_i - m_i \, {}^{b_i}\hat{\boldsymbol{r}}_i^2) \, {}^{b_i}\boldsymbol{\omega}_i \tag{B.29}$$

$$\frac{d}{dt}\Big(\frac{\partial \mathcal{L}}{\partial \, {}^{b_i}\boldsymbol{\omega}_i}\Big) = m_i \, {}^{b_i}\hat{\boldsymbol{r}}_i \, {}^{b_i}\hat{\boldsymbol{\omega}}_i \mathcal{R}_{eb_i}^T \, {}^{e}\dot{\boldsymbol{p}}_l - m_i \, {}^{b_i}\hat{\boldsymbol{r}}_i \mathcal{R}_{eb_i}^T \, {}^{e}\ddot{\boldsymbol{p}}_l$$
$$- m_i \, {}^{b_i}\hat{\boldsymbol{r}}_i \, {}^{b_i}\hat{\boldsymbol{\omega}}_i \mathcal{R}_{eb_i}^T \sum_{j=1}^{P} l_{ij} \dot{\boldsymbol{n}}_{ij} + m_i \, {}^{b_i}\hat{\boldsymbol{r}}_i \mathcal{R}_{eb_i}^T \sum_{j=1}^{P} l_{ij} \ddot{\boldsymbol{n}}_{ij}$$
$$- m_i \, {}^{b_i}\hat{\boldsymbol{r}}_i \, {}^{b_i}\hat{\boldsymbol{\omega}}_i \mathcal{R}_{eb_i}^T \mathcal{R}_{eb_l} \, {}^{b_l}\hat{\boldsymbol{r}}_{l_i} \, {}^{b_l}\boldsymbol{\omega}_l + m_i \, {}^{b_i}\hat{\boldsymbol{r}}_i \mathcal{R}_{eb_i}^T \mathcal{R}_{eb_l} \, {}^{b_l}\hat{\boldsymbol{\omega}}_l \, {}^{b_l}\hat{\boldsymbol{r}}_{l_i} \, {}^{b_l}\boldsymbol{\omega}_l$$
$$+ m_i \, {}^{b_i}\hat{\boldsymbol{r}}_i \mathcal{R}_{eb_i}^T \mathcal{R}_{eb_l} \, {}^{b_l}\hat{\boldsymbol{r}}_{l_i} \, {}^{b_l}\dot{\boldsymbol{\omega}}_l + (\boldsymbol{J}_i - m_i \, {}^{b_i}\hat{\boldsymbol{r}}_i^2) \, {}^{b_i}\dot{\boldsymbol{\omega}}_i \tag{B.30}$$

B.4 Derivation of Lagrange equations of motion

In this section, the explicit form of the equations of motion is derived, following the developments in [73].

- **Payload translational dynamics**

By substituting the derivatives of the Lagrangian into Eq. (2.129), the translational dynamics of the payload c.g. is written as

$$
\begin{aligned}
& m_t\ {}^{e}\ddot{\boldsymbol{p}}_l - \sum_{i=1}^{N} m_{iT} \mathcal{R}_{eb_l}\ {}^{b_l}\hat{\boldsymbol{r}}_{l_i}\ {}^{b_l}\dot{\boldsymbol{\omega}}_l + \sum_{i=1}^{N} m_i\, \mathcal{R}_{eb_i}\ {}^{b_i}\hat{\boldsymbol{r}}_i\ {}^{b_i}\dot{\boldsymbol{\omega}}_i - \sum_{i=1}^{N}\sum_{j=1}^{P} m_{0ij} l_{ij} \ddot{\boldsymbol{n}}_{ij} \\
& = \sum_{i=1}^{N} m_{iT} \mathcal{R}_{eb_l}\ {}^{b_l}\hat{\boldsymbol{\omega}}_l\ {}^{b_l}\hat{\boldsymbol{r}}_{l_i}\ {}^{b_l}\boldsymbol{\omega}_l - \sum_{i=1}^{N} m_i\, \mathcal{R}_{eb_i}\ {}^{b_i}\hat{\boldsymbol{\omega}}_i\ {}^{b_i}\hat{\boldsymbol{r}}_i\ {}^{b_i}\boldsymbol{\omega}_i + m_t g\, \boldsymbol{e}_3 \\
& + \sum_{i=1}^{N} {}^{e}\boldsymbol{F}_{T_i} + \sum_{i=1}^{N} {}^{e}\boldsymbol{F}_{A_i} + \sum_{i=1}^{N}\sum_{j=1}^{P-1} {}^{e}\boldsymbol{F}_{A_{m_{ij}}} + {}^{e}\boldsymbol{F}_{A_l}
\end{aligned}
\tag{B.31}
$$

This expression is rewritten in terms of the angular velocities of the cable links. Taking the time derivative of the link kinematic relation $\dot{\boldsymbol{n}}_{ij} = \widehat{\boldsymbol{\omega}}_{ij}\, \boldsymbol{n}_{ij}$ and using the vector triple–product identity, together with the orthogonality condition $\boldsymbol{\omega}_{ij} \cdot \boldsymbol{n}_{ij} = 0$, gives

$$
\ddot{\boldsymbol{n}}_{ij} = -\,\widehat{\boldsymbol{n}}_{ij}\, \dot{\boldsymbol{\omega}}_{ij} - \|\boldsymbol{\omega}_{ij}\|^2 \boldsymbol{n}_{ij}
\tag{B.32}
$$

Substituting this expression into Eq. (B.31) yields

$$
\begin{aligned}
& m_t\ {}^{e}\ddot{\boldsymbol{p}}_l - \sum_{i=1}^{N} m_{iT} \mathcal{R}_{eb_l}\ {}^{b_l}\hat{\boldsymbol{r}}_{l_i}\ {}^{b_l}\dot{\boldsymbol{\omega}}_l + \sum_{i=1}^{N} m_i\, \mathcal{R}_{eb_i}\ {}^{b_i}\hat{\boldsymbol{r}}_i\ {}^{b_i}\dot{\boldsymbol{\omega}}_i + \sum_{i=1}^{N}\sum_{j=1}^{P} m_{0ij} l_{ij} \hat{\boldsymbol{n}}_{ij} \dot{\boldsymbol{\omega}}_{ij} \\
& = \sum_{i=1}^{N} m_{iT} \mathcal{R}_{eb_l}\ {}^{b_l}\hat{\boldsymbol{\omega}}_l\ {}^{b_l}\hat{\boldsymbol{r}}_{l_i}\ {}^{b_l}\boldsymbol{\omega}_l - \sum_{i=1}^{N} m_i \mathcal{R}_{eb_i}\ {}^{b_i}\hat{\boldsymbol{\omega}}_i\ {}^{b_i}\hat{\boldsymbol{r}}_i\ {}^{b_i}\boldsymbol{\omega}_i - \sum_{i=1}^{N}\sum_{j=1}^{P} m_{0ij} l_{ij} \|\boldsymbol{\omega}_{ij}\|^2 \boldsymbol{n}_{ij} \\
& + m_t g\, \boldsymbol{e}_3 + \sum_{i=1}^{N} {}^{e}\boldsymbol{F}_{T_i} + \sum_{i=1}^{N} {}^{e}\boldsymbol{F}_{A_i} + \sum_{i=1}^{N}\sum_{j=1}^{P-1} {}^{e}\boldsymbol{F}_{A_{m_{ij}}} + {}^{e}\boldsymbol{F}_{A_l}
\end{aligned}
\tag{B.33}
$$

which corresponds to Eq. (2.133) in Section 2.5.

- **Link dynamics**

The link dynamics in Eq. (2.130) is expressed as

$$
\begin{aligned}
& \sum_{j=1}^{P} m_{0ij} l_{ij} l_{ik} \hat{\boldsymbol{n}}_{ij}^2 \ddot{\boldsymbol{n}}_{ij} - m_{0ij} l_{ij} \hat{\boldsymbol{n}}_{ij}^2\ {}^{e}\ddot{\boldsymbol{p}}_l + m_{0ij} l_{ij} \hat{\boldsymbol{n}}_{ij}^2 \mathcal{R}_{eb_l} \left({}^{b_l}\hat{\boldsymbol{\omega}}_l\ {}^{b_l}\hat{\boldsymbol{r}}_{l_i}\ {}^{b_l}\boldsymbol{\omega}_l + {}^{b_l}\hat{\boldsymbol{r}}_{l_i}\ {}^{b_l}\dot{\boldsymbol{\omega}}_l \right) \\
& - m_i l_{ij} \hat{\boldsymbol{n}}_{ij}^2 \mathcal{R}_{eb_i} \left({}^{b_i}\hat{\boldsymbol{\omega}}_i\ {}^{b_i}\hat{\boldsymbol{r}}_i\ {}^{b_i}\boldsymbol{\omega}_i + {}^{b_i}\hat{\boldsymbol{r}}_i\ {}^{b_i}\dot{\boldsymbol{\omega}}_i \right) + m_{0ij} l_{ij} g \hat{\boldsymbol{n}}_{ij}^2 \boldsymbol{e}_3 \\
& = -\, l_{ij}\, \hat{\boldsymbol{n}}_{ij}^2 \left({}^{e}\boldsymbol{F}_{T_i} + {}^{e}\boldsymbol{F}_{A_i} + {}^{e}\boldsymbol{F}_{A_{m_{ij}}} \right)
\end{aligned}
\tag{B.34}
$$

Since $\boldsymbol{n}_{ij}\cdot\dot{\boldsymbol{n}}_{ij}=0$, it follows $\boldsymbol{n}_{ij}\cdot\ddot{\boldsymbol{n}}_{ij}+\dot{\boldsymbol{n}}_{ij}\cdot\dot{\boldsymbol{n}}_{ij}=0$, which implies

$$-\hat{\boldsymbol{n}}_{ij}^2\ddot{\boldsymbol{n}}_{ij}=-(\boldsymbol{n}_{ij}\cdot\ddot{\boldsymbol{n}}_{ij})\boldsymbol{n}_{ij}+(\boldsymbol{n}_{ij}\cdot\boldsymbol{n}_{ij})\ddot{\boldsymbol{n}}_{ij}=(\dot{\boldsymbol{n}}_{ij}\cdot\dot{\boldsymbol{n}}_{ij})\boldsymbol{n}_{ij}+\ddot{\boldsymbol{n}}_{ij} \tag{B.35}$$

By using the above expression, the first term in Eq. (B.34) is rewritten as

$$\sum_{j=1}^{P} m_{0ij}l_{ij}l_{ik}\hat{\boldsymbol{n}}_{ij}^2\ddot{\boldsymbol{n}}_{ij}=\sum_{k=1,k\neq j}^{P} m_{0ij}l_{ij}l_{ik}\hat{\boldsymbol{n}}_{ij}^2\ddot{\boldsymbol{n}}_{ik}-m_{0ij}l_{ij}^2\ddot{\boldsymbol{n}}_{ij}-m_{0ij}l_{ij}^2\|\dot{\boldsymbol{n}}_{ij}\|^2\boldsymbol{n}_{ij} \tag{B.36}$$

Next, using $\ddot{\boldsymbol{n}}_{ij}=-\hat{\boldsymbol{n}}_{ij}\dot{\boldsymbol{\omega}}_{ij}-\|\boldsymbol{\omega}_{ij}\|^2\boldsymbol{n}_{ij}$, and projecting the above equation along the direction $\boldsymbol{n}_{ij}$, recalling that $\hat{\boldsymbol{n}}_{ij}^3=-\hat{\boldsymbol{n}}_{ij}$, and using the vector triple-product identity, yields

$$\begin{aligned}
&\sum_{k=1,k\neq j}^{P} m_{0ij}l_{ij}l_{ik}\,\hat{\boldsymbol{n}}_{ij}\hat{\boldsymbol{n}}_{ik}\,\dot{\boldsymbol{\omega}}_{ik}+m_{0ij}l_{ij}^2\dot{\boldsymbol{\omega}}_{ij}+m_{0ij}l_{ij}\hat{\boldsymbol{n}}_{ij}\,{}^{e}\ddot{\boldsymbol{p}}_{l}\\
&\quad-m_{0ij}l_{ij}\hat{\boldsymbol{n}}_{ij}\mathcal{R}_{eb_l}({}^{b_l}\hat{\boldsymbol{r}}_{l_i}\,{}^{b_l}\dot{\boldsymbol{\omega}}_{l})+m_{i}l_{ij}\hat{\boldsymbol{n}}_{ij}\mathcal{R}_{eb_i}({}^{b_i}\hat{\boldsymbol{r}}_{i}\,{}^{b_i}\dot{\boldsymbol{\omega}}_{i})\\
&=-\sum_{k\neq j} m_{0ij}l_{ij}l_{ik}\,\|\boldsymbol{\omega}_{ik}\|^2\hat{\boldsymbol{n}}_{ij}\boldsymbol{n}_{ik}+m_{0ij}l_{ij}\hat{\boldsymbol{n}}_{ij}\mathcal{R}_{eb_l}({}^{b_l}\hat{\boldsymbol{\omega}}_{l}\,{}^{b_l}\hat{\boldsymbol{r}}_{l_i}\,{}^{b_l}\boldsymbol{\omega}_{l})\\
&\quad-m_{i}l_{ij}\hat{\boldsymbol{n}}_{ij}\mathcal{R}_{eb_i}({}^{b_i}\hat{\boldsymbol{\omega}}_{i}\,{}^{b_i}\hat{\boldsymbol{r}}_{i}\,{}^{b_i}\boldsymbol{\omega}_{i})-m_{0ij}l_{ij}g\hat{\boldsymbol{n}}_{ij}\boldsymbol{e}_3\\
&\quad+l_{ij}\,\hat{\boldsymbol{n}}_{ij}({}^{e}\boldsymbol{F}_{T_i}+{}^{e}\boldsymbol{F}_{A_i}+{}^{e}\boldsymbol{F}_{A_{m_{ij}}})
\end{aligned} \tag{B.37}$$

which corresponds to Eq. (2.134) in Section 2.5.

- **Payload attitude dynamics**

Using the algebraic identity $\hat{\boldsymbol{\omega}}\hat{\boldsymbol{r}}-\hat{\boldsymbol{r}}\hat{\boldsymbol{\omega}}=\widehat{\boldsymbol{\omega}\times\boldsymbol{r}}$, the rotational dynamics of the payload can be written as

$$\begin{aligned}
&\bar{\boldsymbol{J}}_l\,{}^{b_l}\dot{\boldsymbol{\omega}}_{l}+\sum_{i=1}^{N} m_{iT}\,{}^{b_l}\hat{\boldsymbol{r}}_{l_i}\,\mathcal{R}_{eb_l}^{T}\,{}^{e}\ddot{\boldsymbol{p}}_{l}-\sum_{i=1}^{N}\sum_{j=1}^{P} m_{0ij}\,{}^{b_l}\hat{\boldsymbol{r}}_{l_i}\mathcal{R}_{eb_l}^{T}l_{ij}\ddot{\boldsymbol{n}}_{ij}\\
&+\sum_{i=1}^{N} m_i\,{}^{b_l}\hat{\boldsymbol{r}}_{l_i}\,\mathcal{R}_{eb_l}^{T}\mathcal{R}_{eb_i}\,{}^{b_i}\hat{\boldsymbol{r}}_{i}\,{}^{b_i}\dot{\boldsymbol{\omega}}_{i}=\sum_{i=1}^{N}\sum_{j=1}^{P-1}{}^{b_l}\widehat{\boldsymbol{r}}_{l_i}\,\mathcal{R}_{eb_l}^{T}\left({}^{e}\boldsymbol{F}_{T_i}+{}^{e}\boldsymbol{F}_{A_i}+{}^{e}\boldsymbol{F}_{A_{m_{ij}}}\right)\\
&+\sum_{i=1}^{N} m_{iT}g\,{}^{b_l}\hat{\boldsymbol{r}}_{l_i}\,\mathcal{R}_{eb_l}^{T}\boldsymbol{e}_3-{}^{b_l}\hat{\boldsymbol{\omega}}_{l}\bar{\boldsymbol{J}}_l\,{}^{b_l}\boldsymbol{\omega}_{l}
\end{aligned} \tag{B.38}$$

Next, substituting the relation $\ddot{\boldsymbol{n}}_{ij} = -\hat{\boldsymbol{n}}_{ij}\dot{\boldsymbol{\omega}}_{ij} - \|\boldsymbol{\omega}_{ij}\|^2\boldsymbol{n}_{ij}$, the dynamics become

$$\begin{aligned}
&\bar{\boldsymbol{J}}_l\, {}^{b_l}\dot{\boldsymbol{\omega}}_l + \sum_{i=1}^{N} m_{iT}\, {}^{b_l}\hat{\boldsymbol{r}}_{l_i}\, \mathcal{R}_{eb_l}^T\, {}^{e}\ddot{\boldsymbol{p}}_l + \sum_{i=1}^{N} m_i\, {}^{b_l}\hat{\boldsymbol{r}}_{l_i}\, \mathcal{R}_{eb_l}^T \mathcal{R}_{eb_i}\, {}^{b_i}\hat{\boldsymbol{r}}_i\, {}^{b_i}\dot{\boldsymbol{\omega}}_i \\
&\quad + \sum_{i=1}^{N}\sum_{j=1}^{P} m_{0ij}\, {}^{b_l}\hat{\boldsymbol{r}}_{l_i}\, \mathcal{R}_{eb_l}^T\, l_{ij}\, \hat{\boldsymbol{n}}_{ij}\, \dot{\boldsymbol{\omega}}_{ij} = \sum_{i=1}^{N}\sum_{j=1}^{P-1} {}^{b_l}\widehat{\boldsymbol{r}}_{l_i}\, \mathcal{R}_{eb_l}^T({}^{e}\boldsymbol{F}_{T_i} + {}^{e}\boldsymbol{F}_{A_i} + {}^{e}\boldsymbol{F}_{A_{m_{ij}}}) \\
&\quad - \sum_{i=1}^{N}\sum_{j=1}^{P} m_{0ij}\, {}^{b_l}\hat{\boldsymbol{r}}_{l_i}\, \mathcal{R}_{eb_l}^T\, l_{ij}\, \|\boldsymbol{\omega}_{ij}\|^2\boldsymbol{n}_{ij} + \sum_{i=1}^{N} m_{iT} g\, {}^{b_l}\hat{\boldsymbol{r}}_{l_i}\, \mathcal{R}_{eb_l}^T \boldsymbol{e}_3 - {}^{b_l}\hat{\boldsymbol{\omega}}_l \bar{\boldsymbol{J}}_l\, {}^{b_l}\boldsymbol{\omega}_l
\end{aligned} \tag{B.39}$$

which corresponds to Eq. (2.135) in Section 2.5.

- **Quadrotor attitude dynamics**

The attitude dynamics of each quadrotor are expressed as

$$\begin{aligned}
&-m_i\, {}^{b_i}\hat{\boldsymbol{r}}_i^2\, {}^{b_i}\dot{\boldsymbol{\omega}}_i - m_i\, {}^{b_i}\hat{\boldsymbol{r}}_i \mathcal{R}_{eb_i}^T\, {}^{e}\ddot{\boldsymbol{p}}_l + m_i\, {}^{b_i}\hat{\boldsymbol{r}}_i \mathcal{R}_{eb_i}^T \sum_{j=1}^{P} l_{ij}\ddot{\boldsymbol{n}}_{ij} + m_i\, {}^{b_i}\hat{\boldsymbol{r}}_i \mathcal{R}_{eb_i}^T \mathcal{R}_{eb_l}\, {}^{b_l}\hat{\boldsymbol{r}}_{l_i}\, {}^{b_l}\dot{\boldsymbol{\omega}}_l \\
&\quad = -\, {}^{b_i}\widehat{\boldsymbol{r}}_i \mathcal{R}_{eb_i}^T\, ({}^{e}\boldsymbol{F}_{T_i} + {}^{e}\boldsymbol{F}_{A_i}) + {}^{b}\boldsymbol{G}_i - m_i g\, {}^{b_i}\hat{\boldsymbol{r}}_i \mathcal{R}_{eb_i}^T \boldsymbol{e}_3 + m_i\, {}^{b_i}\hat{\boldsymbol{\omega}}_i\, {}^{b_i}\hat{\boldsymbol{r}}_i^2\, {}^{b_i}\boldsymbol{\omega}_i
\end{aligned} \tag{B.40}$$

By substituting the relation $\ddot{\boldsymbol{n}}_{ij} = -\hat{\boldsymbol{n}}_{ij}\dot{\boldsymbol{\omega}}_{ij} - \|\boldsymbol{\omega}_{ij}\|^2\boldsymbol{n}_{ij}$, the above equation can be rewritten as

$$\begin{aligned}
&m_i\, {}^{b_i}\hat{\boldsymbol{r}}_i^2\, {}^{b_i}\dot{\boldsymbol{\omega}}_i + m_i\, {}^{b_i}\hat{\boldsymbol{r}}_i \mathcal{R}_{eb_i}^T\, {}^{e}\ddot{\boldsymbol{p}}_l + m_i\, {}^{b_i}\hat{\boldsymbol{r}}_i \mathcal{R}_{eb_i}^T \sum_{j=1}^{P} l_{ij}\hat{\boldsymbol{n}}_{ij}\dot{\boldsymbol{\omega}}_{ij} - m_i\, {}^{b_i}\hat{\boldsymbol{r}}_i \mathcal{R}_{eb_i}^T \mathcal{R}_{eb_l}\, {}^{b_l}\hat{\boldsymbol{r}}_{l_i}\, {}^{b_l}\dot{\boldsymbol{\omega}}_l \\
&= {}^{b_i}\widehat{\boldsymbol{r}}_i \mathcal{R}_{eb_i}^T\, ({}^{e}\boldsymbol{F}_{T_i} - {}^{e}\boldsymbol{F}_{A_i}) - {}^{b}\boldsymbol{G}_i + m_i g\, {}^{b_i}\hat{\boldsymbol{r}}_i \mathcal{R}_{eb_i}^T \boldsymbol{e}_3 - m_i\, {}^{b_i}\hat{\boldsymbol{\omega}}_i\, {}^{b_i}\hat{\boldsymbol{r}}_i^2\, {}^{b_i}\boldsymbol{\omega}_i \\
&\quad - m_i\, {}^{b_i}\hat{\boldsymbol{r}}_i \mathcal{R}_{eb_i}^T \sum_{j=1}^{P} l_{ij}\|\boldsymbol{\omega}_{ij}\|^2\boldsymbol{n}_{ij}
\end{aligned} \tag{B.41}$$

which corresponds to Eq. (2.136) in Section 2.5.

Appendix C

C.1 Expressions of ${}^{b_i}\dot{\boldsymbol{\omega}}_i$ and ${}^{b_i}\boldsymbol{\omega}_i$ from Differential Flatness

The angular velocity and angular acceleration of the quadrotors are derived from the rotation matrix $\mathcal{R}_{eb_i}$. The angular velocity in the body frame is computed as

$$ {}^{b_i}\boldsymbol{\omega}_i = \left(\mathcal{R}_{eb_i}^T \dot{\mathcal{R}}_{eb_i}\right)^\vee \tag{C.1} $$

where the time derivative of the rotation matrix is given by

$$ \dot{\mathcal{R}}_{eb_i} = \begin{bmatrix} \dot{\boldsymbol{b}}_1 & \dot{\boldsymbol{b}}_2 & \dot{\boldsymbol{b}}_3 \end{bmatrix} \tag{C.2} $$

The derivative of the third body axis is expressed as

$$ \dot{\boldsymbol{b}}_3 = \frac{{}^e\dot{\boldsymbol{F}}_T \,\|\, {}^e\boldsymbol{F}_T\| - {}^e\boldsymbol{F}_T \,\|\, {}^e\dot{\boldsymbol{F}}_T\|}{\|\, {}^e\boldsymbol{F}_T\|^2} \tag{C.3} $$

while the derivative of the first axis is obtained as

$$ \begin{aligned} \dot{\boldsymbol{b}}_1 = &- \frac{\dot{\boldsymbol{b}}_3 \times (\boldsymbol{b}_3 \times \boldsymbol{b}_{1d})}{\|\boldsymbol{b}_3 \times \boldsymbol{b}_{1d}\|} - \frac{\boldsymbol{b}_3 \times \left[(\dot{\boldsymbol{b}}_3 \times \boldsymbol{b}_{1d}) + (\boldsymbol{b}_3 \times \dot{\boldsymbol{b}}_{1d})\right]}{\|\boldsymbol{b}_3 \times \boldsymbol{b}_{1d}\|} \\ &- \frac{\boldsymbol{b}_1(\boldsymbol{b}_3 \times \boldsymbol{b}_{1d})\left[(\dot{\boldsymbol{b}}_3 \times \boldsymbol{b}_{1d}) + (\boldsymbol{b}_3 \times \dot{\boldsymbol{b}}_{1d})\right]}{\|\boldsymbol{b}_3 \times \boldsymbol{b}_{1d}\|} \end{aligned} \tag{C.4} $$

The derivative of the second axis follows from the orthogonality condition

$$ \dot{\boldsymbol{b}}_2 = \dot{\boldsymbol{b}}_3 \times \boldsymbol{b}_1 + \boldsymbol{b}_3 \times \dot{\boldsymbol{b}}_1 \tag{C.5} $$

The angular acceleration is then obtained as

$$ {}^{b_i}\dot{\boldsymbol{\omega}}_i = \left(\dot{\mathcal{R}}_{eb_i}^T \dot{\mathcal{R}}_{eb_i} + \mathcal{R}_{eb_i}^T \ddot{\mathcal{R}}_{eb_i}\right)^\vee \tag{C.6} $$

where

$$ \ddot{\mathcal{R}}_{eb_i} = \begin{bmatrix} \ddot{\boldsymbol{b}}_1 & \ddot{\boldsymbol{b}}_2 & \ddot{\boldsymbol{b}}_3 \end{bmatrix} \tag{C.7} $$

and

$$ \ddot{\boldsymbol{b}}_3 = \frac{({}^e\ddot{\boldsymbol{F}}_T\| \, {}^e\boldsymbol{F}_T\| - {}^e\boldsymbol{F}_T\| \, {}^e\ddot{\boldsymbol{F}}_T\|)\| \, {}^e\boldsymbol{F}_T\|^2 - \dot{\boldsymbol{b}}_3\| \, {}^e\boldsymbol{F}_T\|^2 \, 2\| \, {}^e\boldsymbol{F}_T\|\| \, {}^e\dot{\boldsymbol{F}}_T\|}{\| \, {}^e\boldsymbol{F}_T\|^4} \tag{C.8} $$

$$ \begin{aligned} \ddot{\boldsymbol{b}}_1 = \{ & -\ddot{\boldsymbol{b}}_3 \times (\boldsymbol{b}_3 \times \boldsymbol{b}_{1d}) - 2[\dot{\boldsymbol{b}}_3 \times (\dot{\boldsymbol{b}}_3 \times \boldsymbol{b}_{1d} + \boldsymbol{b}_3 \times \dot{\boldsymbol{b}}_{1d})] \\ & - \boldsymbol{b}_3 \times [\ddot{\boldsymbol{b}}_3 \times \boldsymbol{b}_{1_d} + 2(\dot{\boldsymbol{b}}_3 \times \dot{\boldsymbol{b}}_{1d}) + \boldsymbol{b}_3 \times \ddot{\boldsymbol{b}}_{1d}] \\ & - \dot{\boldsymbol{b}}_1[(\boldsymbol{b}_3 \times \boldsymbol{b}_{1d})(\dot{\boldsymbol{b}}_3 \times \boldsymbol{b}_{1d} + \boldsymbol{b}_3 \times \dot{\boldsymbol{b}}_{1d})] - \boldsymbol{b}_1\|\boldsymbol{b}_3 \times \ddot{\boldsymbol{b}}_{1d}\|\} \frac{1}{\|\boldsymbol{b}_3 \times \boldsymbol{b}_{1d}\|} \\ & - \dot{\boldsymbol{b}}_1 \frac{\|\boldsymbol{b}_3 \times \dot{\boldsymbol{b}}_{1d}\|}{\|\boldsymbol{b}_3 \times \boldsymbol{b}_{1d}\|} \end{aligned} \tag{C.9} $$

$$ \ddot{\boldsymbol{b}}_2 = \ddot{\boldsymbol{b}}_3 \times \boldsymbol{b}_1 + 2(\dot{\boldsymbol{b}}_3 \times \dot{\boldsymbol{b}}_1) + \boldsymbol{b}_3 \times \ddot{\boldsymbol{b}}_1 \tag{C.10} $$

C.2 First-Order Approximation of Configuration Errors on $SO(3)$ and S^2

This section presents the first-order approximations of the configuration errors on $SO(3)$ and S^2, which serve as the foundation for the derivation of the linearized dynamics presented in Sec. 3.1.1.

C.2.1 Linearized error on SO(3)

On $SO(3)$, the infinitesimal variation of R with respect to a reference R_d is given, according to Eq. (2.97), by

$$\delta\mathcal{R}(t) = \mathcal{R}_d(t)\hat{\boldsymbol{\eta}}(t) \tag{C.11}$$

con $\boldsymbol{\eta} \in \mathbb{R}^3$. Assuming that the system state is sufficiently close to the reference, variations with respect to the reference trajectory provide a first-order approximation of the error. The configuration error for a point is $SO(3)$ is defined in Eq. (2.104). If $\mathcal{R}$ is close enough to $\mathcal{R}_d$, there exists $\boldsymbol{\eta} \in \mathbb{R}^3$ with small norm such that

$$\mathcal{R}(t) = \mathcal{R}_d(t)\exp(\hat{\boldsymbol{\eta}})(t) \tag{C.12}$$

hence, taking the first-order approximation of $\exp(\hat{\boldsymbol{\eta}})$, defined in Eq. (2.91), it follows

$$\mathcal{R}_d^T(t)\mathcal{R}(t) = \mathcal{I} + \hat{\boldsymbol{\eta}}(t) + O(\|\boldsymbol{\eta}(t)\|^2) \tag{C.13}$$

Substituting into the definition of $\boldsymbol{e}_{\mathcal{R}}(t)$ yields

$$\boldsymbol{e}_{\mathcal{R}}(t) \simeq \tfrac{1}{2}((\mathcal{I} + \hat{\boldsymbol{\eta}}(t)) - (\mathcal{I} - \hat{\boldsymbol{\eta}}(t)))^{\vee} = \boldsymbol{\eta}(t) \tag{C.14}$$

For the body angular velocity the infinitesimal variation with respect to a reference is written as in Eq. (2.99)

$$\delta\,{}^b\boldsymbol{\omega} = {}^{b_d}\hat{\boldsymbol{\omega}}_d\boldsymbol{\eta} + \dot{\boldsymbol{\eta}} \tag{C.15}$$

The corresponding error is given in Eq. (2.105). Substituting Eq. (C.13) it follows

$$\boldsymbol{e}_{\omega} \simeq ({}^{b_d}\boldsymbol{\omega}_d + \delta\,{}^b\boldsymbol{\omega}) - (\mathcal{I} + \hat{\boldsymbol{\eta}})\,{}^b\boldsymbol{\omega} = \delta\,{}^b\boldsymbol{\omega} + \hat{\boldsymbol{\eta}}\,{}^{b_d}\boldsymbol{\omega}_d = \dot{\boldsymbol{\eta}} \tag{C.16}$$

C.2.2 Linearized error on S^2

For a variable in S^2 the infinitesimal variation with respect to a reference is

$$\delta \boldsymbol{n}(t) = \hat{\boldsymbol{\xi}}(t)\boldsymbol{n}_d(t) \tag{C.17}$$

The configuration error is defined as

$$\boldsymbol{e}_n = \hat{\boldsymbol{n}}_d(t)\boldsymbol{n}(t) \tag{C.18}$$

If $\boldsymbol{n}$ is close enough to $\boldsymbol{n}_d$ it follows that

$$\boldsymbol{n} = \exp(\hat{\boldsymbol{\xi}})\boldsymbol{n}_d \tag{C.19}$$

from which it follows that

$$\boldsymbol{e}_n \simeq \hat{\boldsymbol{n}}_d(\mathcal{I} + \hat{\boldsymbol{\xi}})\boldsymbol{n}_d = \boldsymbol{\xi} \tag{C.20}$$

Similarly, for the associated angular velocity the infinitesimal variation is

$$\delta \boldsymbol{\omega} = \hat{\boldsymbol{\omega}}_d \boldsymbol{\xi} + \dot{\boldsymbol{\xi}} \tag{C.21}$$

and the velocity error is defined as

$$\boldsymbol{e}_\omega = \boldsymbol{\omega} - (\mathcal{I} - \boldsymbol{n}\boldsymbol{n}^T)\,\boldsymbol{\omega}_d, \tag{C.22}$$

which, under the first-order approximation $\boldsymbol{n} \simeq \boldsymbol{n}_d$, reduces to

$$\boldsymbol{e}_\omega \simeq \delta \boldsymbol{\omega} \tag{C.23}$$

C.3 Linearized Dynamics

The linearized equations of motion, derived by applying variation-based linearization to the nonlinear equations presented in Eqs. [...], are reported below, following the developments in [70].

- **Linearized Payload translational dynamics**

$$
\begin{aligned}
\delta(m_t\, {}^{e}\ddot{\boldsymbol{p}}_l) &= m_t\, {}^{e}\delta\ddot{\boldsymbol{p}}_l,\\
\delta\left(-\sum_{i=1}^{N} m_{iT}\,\boldsymbol{\mathcal{R}}_{eb_l}\, {}^{b_l}\hat{\boldsymbol{r}}_{l_i}\, {}^{b_l}\dot{\boldsymbol{\omega}}_l\right) &= -\sum_{i=1}^{N} m_{iT}\Big[\boldsymbol{\mathcal{R}}_{eb_l,d}\, {}^{b_l}\hat{\boldsymbol{r}}_{l_i}\, {}^{b_l}\delta\dot{\boldsymbol{\omega}}_l + \boldsymbol{\mathcal{R}}_{eb_l,d}\,\widehat{\left({}^{b_l}\hat{\boldsymbol{r}}_{l_i}\, {}^{b_l}\boldsymbol{\omega}_{l,d}\right)}\,\boldsymbol{\eta}_l\Big],\\
\delta\left(\sum_{i=1}^{N} m_i\,\boldsymbol{\mathcal{R}}_{eb_i}\, {}^{b_i}\hat{\boldsymbol{r}}_i\, {}^{b_i}\dot{\boldsymbol{\omega}}_i\right) &= \sum_{i=1}^{N} m_i\Big[\boldsymbol{\mathcal{R}}_{eb_i,d}\, {}^{b_i}\hat{\boldsymbol{r}}_i\, {}^{b_i}\delta\dot{\boldsymbol{\omega}}_i + \boldsymbol{\mathcal{R}}_{eb_i,d}\,\widehat{\left({}^{b_i}\hat{\boldsymbol{r}}_i\, {}^{b_i}\boldsymbol{\omega}_{i,d}\right)}\,\boldsymbol{\eta}_i\Big],\\
\delta\left(\sum_{i=1}^{N}\sum_{j=1}^{P} m_{0ij}\, l_{ij}\,\hat{\boldsymbol{n}}_{ij}\,\dot{\boldsymbol{\omega}}_{ij}\right) &= \sum_{i=1}^{N}\sum_{j=1}^{P} m_{0ij}\, l_{ij}\Big[\hat{\boldsymbol{n}}_{ij,d}\,\delta\dot{\boldsymbol{\omega}}_{ij} + \hat{\dot{\boldsymbol{\omega}}}_{ij,d}\,\hat{\boldsymbol{n}}_{ij,d}\,\xi_{ij}\Big],\\
\delta\left(\sum_{i=1}^{N} m_{iT}\,\boldsymbol{\mathcal{R}}_{eb_l}\,\hat{\boldsymbol{\omega}}_l\, {}^{b_l}\hat{\boldsymbol{r}}_{l_i}\, {}^{b_l}\boldsymbol{\omega}_l\right) &= \sum_{i=1}^{N} m_{iT}\Big[\boldsymbol{\mathcal{R}}_{eb_l,d}\big({}^{b_l}\hat{\delta\boldsymbol{\omega}}_l\, {}^{b_l}\hat{\boldsymbol{r}}_{l_i}\, {}^{b_l}\boldsymbol{\omega}_{l,d} + \hat{\boldsymbol{\omega}}_{l,d}\, {}^{b_l}\hat{\boldsymbol{r}}_{l_i}\, {}^{b_l}\delta\boldsymbol{\omega}_l\big)\\
&\qquad + \boldsymbol{\mathcal{R}}_{eb_l,d}\,\widehat{\left(\hat{\boldsymbol{\omega}}_{l,d}\, {}^{b_l}\hat{\boldsymbol{r}}_{l_i}\, {}^{b_l}\boldsymbol{\omega}_{l,d}\right)}\,\boldsymbol{\eta}_l\Big],\\
\delta\left(-\sum_{i=1}^{N} m_i\,\boldsymbol{\mathcal{R}}_{eb_i}\,\hat{\boldsymbol{\omega}}_i\, {}^{b_i}\hat{\boldsymbol{r}}_i\, {}^{b_i}\boldsymbol{\omega}_i\right) &= -\sum_{i=1}^{N} m_i\Big[\boldsymbol{\mathcal{R}}_{eb_i,d}\big({}^{b_i}\hat{\delta\boldsymbol{\omega}}_i\, {}^{b_i}\hat{\boldsymbol{r}}_i\, {}^{b_i}\boldsymbol{\omega}_{i,d} + \hat{\boldsymbol{\omega}}_{i,d}\, {}^{b_i}\hat{\boldsymbol{r}}_i\, {}^{b_i}\delta\boldsymbol{\omega}_i\big)\\
&\qquad + \boldsymbol{\mathcal{R}}_{eb_i,d}\,\widehat{\left(\hat{\boldsymbol{\omega}}_{i,d}\, {}^{b_i}\hat{\boldsymbol{r}}_i\, {}^{b_i}\boldsymbol{\omega}_{i,d}\right)}\,\boldsymbol{\eta}_i\Big],\\
\delta\left(-\sum_{i=1}^{N}\sum_{j=1}^{P} m_{0ij}\, l_{ij}\,\|\boldsymbol{\omega}_{ij}\|^2\,\boldsymbol{n}_{ij}\right) &= \sum_{i=1}^{N}\sum_{j=1}^{P} m_{0ij}\, l_{ij}\Big[-2\,\boldsymbol{n}_{ij,d}\,\boldsymbol{\omega}_{ij,d}^{\top}\,\delta\boldsymbol{\omega}_{ij} + \|\boldsymbol{\omega}_{ij,d}\|^2\,\widehat{\boldsymbol{n}}_{ij,d}\,\boldsymbol{\xi}_{ij}\Big],\\
\delta(m_t g\,\boldsymbol{e}_3) &= 0,\\
\delta\, {}^{e}\boldsymbol{F}_{T_i} &= -\mathcal{R}_{eb_{i,d}}\boldsymbol{e}_3\delta T_i + T_{i,d}\mathcal{R}_{eb_{i,d}}\hat{\boldsymbol{e}}_3\, {}^{b_i}\delta\dot{\boldsymbol{\omega}}_i,\\
\delta^{e}\boldsymbol{F}_{A_l} &= \mathcal{R}_{eb_{l,d}}\left(-\widehat{{}^{b_l}\boldsymbol{F}_{A_{l,d}}} + \left.\frac{\partial\, {}^{b_l}\boldsymbol{F}_{A_l}}{\partial\, {}^{b_l}\boldsymbol{v}_l}\right|_{{}^{b_l}\boldsymbol{v}_l = {}^{b_l}\boldsymbol{v}_{l,d}}\left(\mathcal{R}^{T}_{eb_{l,d}}\, {}^{e}\dot{\boldsymbol{p}}_{l,d}\right)\widehat{\ }\right)\boldsymbol{\eta}_l\\
&\qquad + \left(\mathcal{R}_{eb_{l,d}}\left.\frac{\partial\, {}^{b_l}\boldsymbol{F}_{A_l}}{\partial\, {}^{b_l}\boldsymbol{v}_l}\right|_{{}^{b_l}\boldsymbol{v}_l = {}^{b_l}\boldsymbol{v}_{l,d}}\mathcal{R}^{T}_{eb_{l,d}}\right)\, {}^{e}\delta\dot{\boldsymbol{p}}_l,\\
\delta^{e}\mathbf{F}_{A_{m_{ij}}} &= -\tfrac{1}{2}\rho A_s C_{d_s}\left(\|{}^{e}\dot{\boldsymbol{p}}_{ij,d}\|\,\mathcal{I}_3 + \frac{{}^{e}\dot{\boldsymbol{p}}_{ij,d}\,{}^{e}\dot{\boldsymbol{p}}^{T}_{ij,d}}{\|{}^{e}\dot{\boldsymbol{p}}_{ij,d}\|}\right)\\
&\qquad \left[\delta\dot{\mathbf{p}}^{e}_{l} - R_d\,\widehat{{}^{b_l}\mathbf{r}_{l_i}}\,\boldsymbol{\eta}_l + \sum_{a=1}^{j} l_{ia}\Big(\widehat{\mathbf{n}}_{ia,d}\,\delta\boldsymbol{\omega}_{ia} + (\mathbf{n}_{ia,d}\boldsymbol{\omega}^{T}_{ia,d})\,\boldsymbol{\xi}_{ia}\Big)\right]
\end{aligned}
$$

- **Linearized link dynamics**

$$\delta\left(\sum_{k\neq j} m_{0ij} l_{ij} l_{ik}\, \hat{\boldsymbol{n}}_{ij} \hat{\boldsymbol{n}}_{ik} \dot{\boldsymbol{\omega}}_{ik}\right) = \sum_{k\neq j} m_{0ij} l_{ij} l_{ik} \Big[\hat{\boldsymbol{n}}_{ij,d} \hat{\boldsymbol{n}}_{ik,d}\, \delta\dot{\boldsymbol{\omega}}_{ik} + \big(\widehat{\boldsymbol{n}}_{ik,d} \dot{\boldsymbol{\omega}}_{ik,d}\big)^{\widehat{}}\ \hat{\boldsymbol{n}}_{ij,d}\, \boldsymbol{\xi}_{ij} + \hat{\boldsymbol{n}}_{ij,d}\, \widehat{\dot{\boldsymbol{\omega}}}_{ik,d}\, \hat{\boldsymbol{n}}_{ik,d}$$

$$\delta\big(m_{0ij} l_{ij}^2 \dot{\boldsymbol{\omega}}_{ij}\big) = m_{0ij} l_{ij}^2\, \delta\dot{\boldsymbol{\omega}}_{ij},$$

$$\delta(m_{0ij} l_{ij}\, \hat{\boldsymbol{n}}_{ij}\, {}^{e}\ddot{\boldsymbol{p}}_l) = m_{0ij} l_{ij}\, \hat{\boldsymbol{n}}_{ij,d}\, {}^{e}\delta\ddot{\boldsymbol{p}}_l + m_{0ij} l_{ij}\, {}^{e}\widehat{\ddot{\boldsymbol{p}}}_{l,d}\, \hat{\boldsymbol{n}}_{ij,d}\, \boldsymbol{\xi}_{ij},$$

$$\begin{aligned}\delta(-m_{0ij} l_{ij}\, \hat{\boldsymbol{n}}_{ij}\, \boldsymbol{\mathcal{R}}_{eb_l}(\hat{\boldsymbol{r}}_{l_i} \dot{\boldsymbol{\omega}}_l)) &= -m_{0ij} l_{ij}\, \hat{\boldsymbol{n}}_{ij,d}\, \boldsymbol{\mathcal{R}}_{eb_l,d}\, \hat{\boldsymbol{r}}_{l_i}\, \delta\dot{\boldsymbol{\omega}}_l + m_{0ij} l_{ij}\, \boldsymbol{\mathcal{R}}_{eb_l,d}\, \big(\hat{\boldsymbol{r}}_{l_i} \dot{\boldsymbol{\omega}}_{l,d}\big)^{\widehat{}}\ \hat{\boldsymbol{n}}_{ij,d}\, \boldsymbol{\xi}_{ij} \\ &\quad + m_{0ij} l_{ij}\, \hat{\boldsymbol{n}}_{ij,d}\, \boldsymbol{\mathcal{R}}_{eb_l,d}\, \big(\hat{\boldsymbol{r}}_{l_i} \dot{\boldsymbol{\omega}}_{l,d}\big)^{\widehat{}}\ \boldsymbol{\eta}_l,\end{aligned}$$

$$\begin{aligned}\delta(m_i l_{ij}\, \hat{\boldsymbol{n}}_{ij}\, \boldsymbol{\mathcal{R}}_{eb_i}(\hat{\boldsymbol{r}}_i \dot{\boldsymbol{\omega}}_i)) &= m_i l_{ij}\, \hat{\boldsymbol{n}}_{ij,d}\, \boldsymbol{\mathcal{R}}_{eb_i,d}\, \hat{\boldsymbol{r}}_i\, \delta\dot{\boldsymbol{\omega}}_i - m_i l_{ij}\, \boldsymbol{\mathcal{R}}_{eb_i,d}\, \big(\hat{\boldsymbol{r}}_i \dot{\boldsymbol{\omega}}_{i,d}\big)^{\widehat{}}\ \hat{\boldsymbol{n}}_{ij,d}\, \boldsymbol{\xi}_{ij} \\ &\quad - m_i l_{ij}\, \hat{\boldsymbol{n}}_{ij,d}\, \boldsymbol{\mathcal{R}}_{eb_i,d}\, \big(\hat{\boldsymbol{r}}_i \dot{\boldsymbol{\omega}}_{i,d}\big)^{\widehat{}}\ \boldsymbol{\eta}_i,\end{aligned}$$

$$\begin{aligned}\delta\left(-\sum_{k\neq j} m_{0ij} l_{ij} l_{ik}\, \|\boldsymbol{\omega_{ik}}\|^2\, \hat{\boldsymbol{n}}_{ij}\, \boldsymbol{n}_{ik}\right) &= \sum_{k\neq j} m_{0ij} l_{ij} l_{ik} \Big[-2\, \hat{\boldsymbol{n}}_{ij,d}\, \boldsymbol{n}_{ik,d}\, \boldsymbol{\omega}_{ik,d}^{\top} \delta\boldsymbol{\omega}_{ik} \\ &\quad + \|\boldsymbol{\omega}_{ik,d}\|^2\, \hat{\boldsymbol{n}}_{ik,d}\, \hat{\boldsymbol{n}}_{ij,d}\, \boldsymbol{\xi}_{ij} + \|\boldsymbol{\omega}_{ik,d}\|^2\, \hat{\boldsymbol{n}}_{ij,d}\, \hat{\boldsymbol{n}}_{ik,d}\, \boldsymbol{\xi}_{ik}\Big],\end{aligned}$$

$$\begin{aligned}\delta(m_{0ij} l_{ij}\, \hat{\boldsymbol{n}}_{ij}\, \boldsymbol{\mathcal{R}}_{eb_l}(\hat{\boldsymbol{\omega}}_l \hat{\boldsymbol{r}}_{l_i} \boldsymbol{\omega}_l)) &= m_{0ij} l_{ij}\, \hat{\boldsymbol{n}}_{ij,d}\, \boldsymbol{\mathcal{R}}_{eb_l,d}\big(\hat{\boldsymbol{\omega}}_{l,d}\, \hat{\boldsymbol{r}}_{l_i} \boldsymbol{\omega}_{l,d} + \hat{\boldsymbol{\omega}}_{l,d} \hat{\boldsymbol{r}}_{l_i}\big)\delta\boldsymbol{\omega}_l \\ &\quad - m_{0ij} l_{ij}\, \boldsymbol{\mathcal{R}}_{eb_l,d}\, \big(\hat{\boldsymbol{\omega}}_{l,d} \hat{\boldsymbol{r}}_{l_i} \boldsymbol{\omega}_{l,d}\big)^{\widehat{}}\ \hat{\boldsymbol{n}}_{ij,d}\, \boldsymbol{\xi}_{ij} \\ &\quad - m_{0ij} l_{ij}\, \hat{\boldsymbol{n}}_{ij,d}\, \boldsymbol{\mathcal{R}}_{eb_l,d}\, \big(\hat{\boldsymbol{\omega}}_{l,d} \hat{\boldsymbol{r}}_{l_i} \boldsymbol{\omega}_{l,d}\big)^{\widehat{}}\ \boldsymbol{\eta}_l,\end{aligned}$$

$$\begin{aligned}\delta(-m_i l_{ij}\, \hat{\boldsymbol{n}}_{ij}\, \boldsymbol{\mathcal{R}}_{eb_i}(\hat{\boldsymbol{\omega}}_i \hat{\boldsymbol{r}}_i \boldsymbol{\omega}_i)) &= -m_i l_{ij}\, \hat{\boldsymbol{n}}_{ij,d}\, \boldsymbol{\mathcal{R}}_{eb_i,d}\big(\hat{\boldsymbol{\omega}}_{i,d}\, \hat{\boldsymbol{r}}_i \boldsymbol{\omega}_{i,d} + \hat{\boldsymbol{\omega}}_{i,d} \hat{\boldsymbol{r}}_i\big)\delta\boldsymbol{\omega}_i \\ &\quad + m_i l_{ij}\, \boldsymbol{\mathcal{R}}_{eb_i,d}\, \big(\hat{\boldsymbol{\omega}}_{i,d} \hat{\boldsymbol{r}}_i \boldsymbol{\omega}_{i,d}\big)^{\widehat{}}\ \hat{\boldsymbol{n}}_{ij,d}\, \boldsymbol{\xi}_{ij} \\ &\quad + m_i l_{ij}\, \hat{\boldsymbol{n}}_{ij,d}\, \boldsymbol{\mathcal{R}}_{eb_i,d}\, \big(\hat{\boldsymbol{\omega}}_{i,d} \hat{\boldsymbol{r}}_i \boldsymbol{\omega}_{i,d}\big)^{\widehat{}}\ \boldsymbol{\eta}_i,\end{aligned}$$

$$\delta(-m_{0ij} l_{ij} g\, \hat{\boldsymbol{n}}_{ij}\, \boldsymbol{e}_3) = m_{0ij} l_{ij} g\, \hat{\boldsymbol{e}}_3\, \hat{\boldsymbol{n}}_{ij,d}\, \boldsymbol{\xi}_{ij},$$

$$\delta(l_{ij}\, \hat{\boldsymbol{n}}_{ij}\, {}^{e}\boldsymbol{F}) = l_{ij}\, \hat{\boldsymbol{n}}_{ij,d}\, {}^{e}\delta\boldsymbol{F} - l_{ij}\, {}^{e}\hat{\boldsymbol{F}}_d\, \hat{\boldsymbol{n}}_{ij,d}\, \boldsymbol{\xi}_{ij}.$$

- **Linearized Payload attitude dynamics**

$$\delta\big(\bar{\boldsymbol{J}}_l\,{}^{b_l}\dot{\boldsymbol{\omega}}_l\big) = \bar{\boldsymbol{J}}_l\,{}^{b_l}\delta\dot{\boldsymbol{\omega}}_l,$$

$$\delta\left(\sum_{i=1}^{N} m_{iT}\,{}^{b_l}\hat{\boldsymbol{r}}_{l_i}\,\boldsymbol{\mathcal{R}}_{eb_l}^{T}\,{}^{e}\ddot{\boldsymbol{p}}_l\right) = \sum_{i=1}^{N} m_{iT}\Big[{}^{b_l}\hat{\boldsymbol{r}}_{l_i}\,\boldsymbol{\mathcal{R}}_{eb_l,d}^{T}\,{}^{e}\delta\ddot{\boldsymbol{p}}_l + {}^{b_l}\hat{\boldsymbol{r}}_{l_i}\,\boldsymbol{\mathcal{R}}_{eb_l,d}^{T}\,{}^{e}\hat{\ddot{\boldsymbol{p}}}_{l,d}\,\boldsymbol{\eta}_l\Big],$$

$$\begin{aligned}\delta\left(\sum_{i=1}^{N} m_i\,{}^{b_l}\hat{\boldsymbol{r}}_{l_i}\,\boldsymbol{\mathcal{R}}_{eb_l}^{T}\boldsymbol{\mathcal{R}}_{eb_i}\,{}^{b_i}\hat{\boldsymbol{r}}_i\,{}^{b_i}\dot{\boldsymbol{\omega}}_i\right) = \sum_{i=1}^{N} m_i\Big[&{}^{b_l}\hat{\boldsymbol{r}}_{l_i}\,\boldsymbol{\mathcal{R}}_{eb_l,d}^{T}\boldsymbol{\mathcal{R}}_{eb_i,d}\,{}^{b_i}\hat{\boldsymbol{r}}_i\,{}^{b_i}\delta\dot{\boldsymbol{\omega}}_i\\ &- {}^{b_l}\hat{\boldsymbol{r}}_{l_i}\,\boldsymbol{\mathcal{R}}_{eb_l,d}^{T}\,\widehat{\big(\boldsymbol{\mathcal{R}}_{eb_i,d}\,{}^{b_i}\hat{\boldsymbol{r}}_i\,{}^{b_i}\dot{\boldsymbol{\omega}}_{i,d}\big)}\,\boldsymbol{\eta}_i\\ &+ {}^{b_l}\hat{\boldsymbol{r}}_{l_i}\,\boldsymbol{\mathcal{R}}_{eb_l,d}^{T}\,\widehat{\big(\boldsymbol{\mathcal{R}}_{eb_i,d}\,{}^{b_i}\hat{\boldsymbol{r}}_i\,{}^{b_i}\dot{\boldsymbol{\omega}}_{i,d}\big)}\,\boldsymbol{\eta}_l\Big],\end{aligned}$$

$$\begin{aligned}\delta\left(\sum_{i=1}^{N}\sum_{j=1}^{P} m_{0ij}\,{}^{b_l}\hat{\boldsymbol{r}}_{l_i}\,\boldsymbol{\mathcal{R}}_{eb_l}^{T}\,l_{ij}\,\hat{\boldsymbol{n}}_{ij}\,\dot{\boldsymbol{\omega}}_{ij}\right) = \sum_{i=1}^{N}\sum_{j=1}^{P} m_{0ij}\Big[&{}^{b_l}\hat{\boldsymbol{r}}_{l_i}\,\boldsymbol{\mathcal{R}}_{eb_l,d}^{T}\,l_{ij}\,\hat{\boldsymbol{n}}_{ij,d}\,\delta\dot{\boldsymbol{\omega}}_{ij}\\ &+ {}^{b_l}\hat{\boldsymbol{r}}_{l_i}\,\boldsymbol{\mathcal{R}}_{eb_l,d}^{T}\,l_{ij}\,\hat{\dot{\boldsymbol{\omega}}}_{ij,d}\,\hat{\boldsymbol{n}}_{ij,d}\,\boldsymbol{\xi}_{ij}\\ &+ {}^{b_l}\hat{\boldsymbol{r}}_{l_i}\,\boldsymbol{\mathcal{R}}_{eb_l,d}^{T}\,\widehat{\big(\,l_{ij}\hat{\boldsymbol{n}}_{ij,d}\dot{\boldsymbol{\omega}}_{ij,d}\,\big)}\,\boldsymbol{\eta}_l\Big],\end{aligned}$$

$$\delta\big({}^{b_l}\hat{\boldsymbol{r}}_{l_i}\,\boldsymbol{\mathcal{R}}_{eb_l}^{T}\,{}^{e}\boldsymbol{F}\big) = \big({}^{b_l}\hat{\boldsymbol{r}}_{l_i}\,\boldsymbol{\mathcal{R}}_{eb_l,d}^{T}\delta^{e}\boldsymbol{F} + {}^{b_l}\hat{\boldsymbol{r}}_{l_i}\,\boldsymbol{\mathcal{R}}_{eb_l,d}^{T}\,{}^{e}\hat{\boldsymbol{F}}_d\,\boldsymbol{\eta}_l\big),$$

$$\begin{aligned}\delta\left(-\sum_{i=1}^{N}\sum_{j=1}^{P} m_{0ij}\,{}^{b_l}\hat{\boldsymbol{r}}_{l_i}\,\boldsymbol{\mathcal{R}}_{eb_l}^{T}\,l_{ij}\,\|\boldsymbol{\omega}_{ij}\|^2\boldsymbol{n}_{ij}\right) = \sum_{i=1}^{N}\sum_{j=1}^{P} m_{0ij}\Big[&-2\,{}^{b_l}\hat{\boldsymbol{r}}_{l_i}\,\boldsymbol{\mathcal{R}}_{eb_l,d}^{T}\,l_{ij}\,\boldsymbol{n}_{ij,d}\,\boldsymbol{\omega}_{ij,d}^{\top}\,\delta\boldsymbol{\omega}_{ij}\\ &+ {}^{b_l}\hat{\boldsymbol{r}}_{l_i}\,\boldsymbol{\mathcal{R}}_{eb_l,d}^{T}\,l_{ij}\,\|\boldsymbol{\omega}_{ij,d}\|^2\,\hat{\boldsymbol{n}}_{ij,d}\,\boldsymbol{\xi}_{ij}\\ &- {}^{b_l}\hat{\boldsymbol{r}}_{l_i}\,\boldsymbol{\mathcal{R}}_{eb_l,d}^{T}\,\widehat{\big(\,l_{ij}\|\boldsymbol{\omega}_{ij,d}\|^2\boldsymbol{n}_{ij,d}\,\big)}\,\boldsymbol{\eta}_l\Big],\end{aligned}$$

$$\delta\left(\sum_{i=1}^{N} m_{iT}g\,{}^{b_l}\hat{\boldsymbol{r}}_{l_i}\,\boldsymbol{\mathcal{R}}_{eb_l}^{T}\boldsymbol{e}_3\right) = \sum_{i=1}^{N} m_{iT}g\,{}^{b_l}\hat{\boldsymbol{r}}_{l_i}\,\boldsymbol{\mathcal{R}}_{eb_l,d}^{T}\,\hat{\boldsymbol{e}}_3\,\boldsymbol{\eta}_l,$$

$$\delta\big(-\,{}^{b_l}\hat{\boldsymbol{\omega}}_l\,\bar{\boldsymbol{J}}_l\,{}^{b_l}\boldsymbol{\omega}_l\big) = \big(\widehat{(\bar{\boldsymbol{J}}_l\,{}^{b_l}\boldsymbol{\omega}_{l,d})} - {}^{b_l}\hat{\boldsymbol{\omega}}_{l,d}\,\bar{\boldsymbol{J}}_l\big)\,{}^{b_l}\delta\boldsymbol{\omega}_l.$$

- **Linearized quadrotor attitude dynamics**

$$
\begin{aligned}
\delta\big(m_i\,{}^{b_i}\hat{\boldsymbol{r}}_i^{\,2}\,{}^{b_i}\dot{\boldsymbol{\omega}}_i\big) &= m_i\,{}^{b_i}\hat{\boldsymbol{r}}_i^{\,2}\,{}^{b_i}\delta\dot{\boldsymbol{\omega}}_i,\\
\delta\big(m_i\,{}^{b_i}\hat{\boldsymbol{r}}_i\,\boldsymbol{\mathcal{R}}_{eb_i}^{T}\,{}^{e}\ddot{\boldsymbol{p}}_l\big) &= m_i\Big[{}^{b_i}\hat{\boldsymbol{r}}_i\,\boldsymbol{\mathcal{R}}_{eb_i,d}^{T}\,{}^{e}\delta\ddot{\boldsymbol{p}}_l + {}^{b_i}\hat{\boldsymbol{r}}_i\,\boldsymbol{\mathcal{R}}_{eb_i,d}^{T}\,{}^{e}\hat{\ddot{\boldsymbol{p}}}_{l,d}\,\boldsymbol{\eta}_i\Big],\\
\delta\left(m_i\,{}^{b_i}\hat{\boldsymbol{r}}_i\,\boldsymbol{\mathcal{R}}_{eb_i}^{T}\sum_{j=1}^{P} l_{ij}\,\hat{\boldsymbol{n}}_{ij}\,\dot{\boldsymbol{\omega}}_{ij}\right) &= m_i\sum_{j=1}^{P} l_{ij}\Big[{}^{b_i}\hat{\boldsymbol{r}}_i\,\boldsymbol{\mathcal{R}}_{eb_i,d}^{T}\,\hat{\boldsymbol{n}}_{ij,d}\,\delta\dot{\boldsymbol{\omega}}_{ij}\\
&\quad + {}^{b_i}\hat{\boldsymbol{r}}_i\,\boldsymbol{\mathcal{R}}_{eb_i,d}^{T}\,\hat{\dot{\boldsymbol{\omega}}}_{ij,d}\,\hat{\boldsymbol{n}}_{ij,d}\,\boldsymbol{\xi}_{ij}\\
&\quad + {}^{b_i}\hat{\boldsymbol{r}}_i\,\boldsymbol{\mathcal{R}}_{eb_i,d}^{T}\,\widehat{(\hat{\boldsymbol{n}}_{ij,d}\dot{\boldsymbol{\omega}}_{ij,d})}\,\boldsymbol{\eta}_i\Big],\\
\delta\big(-m_i\,{}^{b_i}\hat{\boldsymbol{r}}_i\,\boldsymbol{\mathcal{R}}_{eb_i}^{T}\boldsymbol{\mathcal{R}}_{eb_l}\,{}^{b_l}\hat{\boldsymbol{r}}_{l_i}\,{}^{b_l}\dot{\boldsymbol{\omega}}_l\big) &= -m_i\Big[{}^{b_i}\hat{\boldsymbol{r}}_i\,\boldsymbol{\mathcal{R}}_{eb_i,d}^{T}\boldsymbol{\mathcal{R}}_{eb_l,d}\,{}^{b_l}\hat{\boldsymbol{r}}_{l_i}\,{}^{b_l}\delta\dot{\boldsymbol{\omega}}_l\\
&\quad - {}^{b_i}\hat{\boldsymbol{r}}_i\,\boldsymbol{\mathcal{R}}_{eb_i,d}^{T}\,\widehat{\big(\boldsymbol{\mathcal{R}}_{eb_l,d}\,{}^{b_l}\hat{\boldsymbol{r}}_{l_i}\,{}^{b_l}\dot{\boldsymbol{\omega}}_{l,d}\big)}\,\boldsymbol{\eta}_i\\
&\quad + {}^{b_i}\hat{\boldsymbol{r}}_i\,\boldsymbol{\mathcal{R}}_{eb_i,d}^{T}\,\widehat{\big(\boldsymbol{\mathcal{R}}_{eb_l,d}\,{}^{b_l}\hat{\boldsymbol{r}}_{l_i}\,{}^{b_l}\dot{\boldsymbol{\omega}}_{l,d}\big)}\,\boldsymbol{\eta}_l\Big],\\
\delta\big({}^{b_i}\hat{\boldsymbol{r}}_i\,\boldsymbol{\mathcal{R}}_{eb_i}^{T}({}^{e}\boldsymbol{F}_{T_i} - {}^{e}\boldsymbol{F}_{A_i})\big) &= {}^{b_i}\hat{\boldsymbol{r}}_i\,\boldsymbol{\mathcal{R}}_{eb_i,d}^{T}\,({}^{e}\delta\boldsymbol{F}_{T_i} - {}^{e}\delta\boldsymbol{F}_{A_i}) + {}^{b_i}\hat{\boldsymbol{r}}_i\,\boldsymbol{\mathcal{R}}_{eb_i,d}^{T}\,\widehat{({}^{e}\boldsymbol{F}_{T_i,d} - {}^{e}\boldsymbol{F}_{A_i,d})}\,\boldsymbol{\eta}_i,\\
\delta\big(-{}^{b}\boldsymbol{G}_{T_i}\big) &= -\,\delta({}^{b}\boldsymbol{G}_{T_i}),\\
\delta\big(m_i g\,{}^{b_i}\hat{\boldsymbol{r}}_i\,\boldsymbol{\mathcal{R}}_{eb_i}^{T}\boldsymbol{e}_3\big) &= m_i g\,{}^{b_i}\hat{\boldsymbol{r}}_i\,\boldsymbol{\mathcal{R}}_{eb_i,d}^{T}\,\hat{\boldsymbol{e}}_3\,\boldsymbol{\eta}_i,\\
\delta\big(-m_i\,{}^{b_i}\hat{\boldsymbol{\omega}}_i\,{}^{b_i}\hat{\boldsymbol{r}}_i^{\,2}\,{}^{b_i}\boldsymbol{\omega}_i\big) &= m_i\Big(\,\widehat{\big({}^{b_i}\hat{\boldsymbol{r}}_i^{\,2}\,{}^{b_i}\boldsymbol{\omega}_{i,d}\big)} - {}^{b_i}\hat{\boldsymbol{\omega}}_{i,d}\,{}^{b_i}\hat{\boldsymbol{r}}_i^{\,2}\Big)\,{}^{b_i}\delta\boldsymbol{\omega}_i,\\
\delta\left(-m_i\,{}^{b_i}\hat{\boldsymbol{r}}_i\,\boldsymbol{\mathcal{R}}_{eb_i}^{T}\sum_{j=1}^{P} l_{ij}\|\boldsymbol{\omega}_{ij}\|^2\boldsymbol{n}_{ij}\right) &= m_i\sum_{j=1}^{P} l_{ij}\Big[-2\,{}^{b_i}\hat{\boldsymbol{r}}_i\,\boldsymbol{\mathcal{R}}_{eb_i,d}^{T}\,\boldsymbol{n}_{ij,d}\,\boldsymbol{\omega}_{ij,d}^{\top}\,\delta\boldsymbol{\omega}_{ij}\\
&\quad + {}^{b_i}\hat{\boldsymbol{r}}_i\,\boldsymbol{\mathcal{R}}_{eb_i,d}^{T}\,\|\boldsymbol{\omega}_{ij,d}\|^2\,\hat{\boldsymbol{n}}_{ij,d}\,\boldsymbol{\xi}_{ij}\\
&\quad - {}^{b_i}\hat{\boldsymbol{r}}_i\,\boldsymbol{\mathcal{R}}_{eb_i,d}^{T}\,\big(\,\|\boldsymbol{\omega}_{ij,d}\|^2\boldsymbol{n}_{ij,d}\,\big)\widehat{\ }\,\boldsymbol{\eta}_i\Big].
\end{aligned}
$$